b-Tagging and Evidence for the Standard Model $H \rightarrow b\bar{b}$ Decay with the ATLAS Experiment

Andrew Stuart Bell
University College London

Submitted to University College London in fulfilment
of the requirements for the award of the
degree of **Doctor of Philosophy**

July 2, 2019

Declaration

I, Andrew Stuart Bell, confirm that the work presented in this thesis is my own. Where information has been derived from other sources, I confirm that this has been indicated in the thesis.

Andrew Bell ________________________________

Abstract

The observation of a new particle consistent with the Standard Model Higgs boson by the ATLAS and CMS experiments in 2012 heralded a new era in the understanding of the Standard Model. To date, the direct couplings of the Higgs boson to the bosonic and leptonic sectors of the Standard Model have been observed with a significance of at least 5 standard deviations. With a mass of 125 GeV, the largest decay mode of the Higgs boson is predicted to be to a pair of bottom-quarks, $H \to b\bar{b}$, accounting for approximately 58% of all decays.

A search for the Standard Model $H \to b\bar{b}$ decay has been conducted in the $VH \to Vb\bar{b}$ production channel, with V corresponding to either a W or Z boson, using 36.1 fb^{-1} of Run-2 pp collisions, recorded by the ATLAS detector at the Large Hadron Collider. Three channels are considered to target each of the leptonic decays of the vector boson, $Z \to \nu\nu$, $W \to \ell\nu$ and $Z \to \ell\ell$, known as the 0-lepton, 1-lepton and 2-lepton channels, respectively.

The identification of the $H \to b\bar{b}$ candidate is a vital aspect of the analysis, with techniques known as b-tagging algorithms used to identify the b-quark content of jets. Understanding the performance of b-tagging algorithms in collision data is necessary to correctly model the performance in simulated processes. A measurement of the b-jet tagging efficiency in data has been conducted using a likelihood fitting procedure in $t\bar{t}$ events. Multivariate analysis techniques have been implemented to reduce the dominant systematic uncertainties in the measurement of the b-jet tagging efficiency, which improved the sensitivity of the $VH \to Vb\bar{b}$ analysis.

To enhance the $VH \to Vb\bar{b}$ analysis, studies have been carried out to improve the understanding of the modelling of background processes in the 1-lepton channel, with the development and implementation of a dedicated control region for events where a W boson is produced in association with a b- or c-quark. A boosted decision tree has been trained to improve the signal sensitivity of the $VH \to Vb\bar{b}$ analysis in the 1-lepton channel, and numerous cross-checks have been carried out to improve the performance.

From the analysis of the Run-2 dataset, an observed signal significance of 3.5 standard deviations for the $VH \to Vb\bar{b}$ process over the background-only model, compared to an expectation of 3.0 standard deviations, is measured. This corresponds to a ratio of the signal yield to the Standard Model expectation of $1.20^{+0.24}_{-0.23}(\text{stat.})^{+0.34}_{-0.28}(\text{syst.})$. The combination of this result with the Run-1 analysis yields an observed signal significance of 3.6 standard deviations, compared to an expectation of 4.0 standard deviations, with the ratio of the measured signal yield to the Standard Model expectation is equal to $0.90 \pm 0.18(\text{stat.})^{+0.21}_{-0.19}(\text{syst.})$. This result is the first single-experiment evidence for the $H \to b\bar{b}$ decay and the VH production mode.

Acknowledgements

The work presented in this thesis would not have been possible without the help and encouragement of countless people. First and foremost, I would like to thank my supervisor, Tim, whose guidance, advice and support during my PhD made all of the work presented in this thesis possible.

I would like to thank all the members, past and present, of the ATLAS Flavour Tagging and $H \to b\bar{b}$ groups I have had the pleasure to work with. Thank you also to all the PhD students, post-docs and academics at UCL who have helped to create a friendly and nurturing environment. In particular I would like to thank Stephen and Laurie, not only for helping with my numerous questions, but for their friendship during long evenings in the UCL office at CERN. I would also like to thank Kristian and Inês for their help introducing me to the world of ATLAS when I first joined UCL.

Thank you to the friends I made during my time on LTA at CERN. Without you, my time there would have been significantly less enjoyable. I would also like to thank to my friends from Cambridge and Camberley who have all played a vital part in helping me through university and my PhD, and providing me with many much-needed distractions over the years.

Thank you also to Mum, Dad and Mark. Your unconditional support has been with me since the day I was born, and has resulted in the person I am today.

Lastly, I would like to thank Hannah, whose ability to put a smile on my face after a tiring day, even when separated by 10,000 km, is what made it all worthwhile.

Contents

List of Figures

List of Tables

Chapter 1

Introduction

This thesis describes the work carried out by the author between September 2014 and September 2017 as a member of the ATLAS collaboration at the Large Hadron Collider (LHC). The structure of the thesis is outlined below.

Chapter 2 presents an overview of the relevant background theory, briefly covering the Standard Model and Higgs mechanism.

Chapter 3 presents an overview of the LHC, the ATLAS detector, and the physics objects used in the analyses described in this thesis.

Chapter 4 presents a measurement of the muon isolation efficiency in data using a Tag and Probe procedure on events where a Z boson decays to a muon pair, $Z \rightarrow \mu\mu$, for a new isolation working point derived for the $VH \rightarrow Vb\bar{b}$ analysis.

Chapter 5 presents the b-tagging algorithms used by ATLAS for data collected in 2015 and 2016.

Chapter 6 presents the measurement of the performance of b-tagging algorithms in data, carried out using the pair production of top-quarks, $t\bar{t}$, and a likelihood method.

Chapter 7 presents an analysis searching for the decay of the Standard Model Higgs boson to a pair of bottom-quarks, in association with the production of a vector boson, $VH \rightarrow Vb\bar{b}$, using 36.1 fb^{-1} of pp collision data recorded by ATLAS during 2015 and 2016.

Chapter 8 presents a summary and outlook for future work.

The author's contribution to the work presented in the thesis is as follows.

***b*-tagging:** The author has been an active member of the ATLAS Flavour Tagging group since September 2014. The author played a key role in the commissioning of b-tagging algorithms in the build up to Run-2 data-taking, with the performance of b-tagging algorithms validated and optimised. The installation of the Insertable B-Layer (IBL) as the innermost pixel layer of the ATLAS inner-detector between 2012 and 2015 offered a significant boost to the performance of b-tagging algorithms, along with algorithm improvements, with studies carried out to determine the improvement in b-tagging performance between Run-1[1] and Run-2[2] of the LHC. The results were included in a public note on the expected performance of b-tagging algorithms for Run-2 [1].

The author carried out the first Run-2 data-driven b-jet efficiency measurement using a $t\bar{t}$ based likelihood method, developed during Run-1. The author implemented a machine learning technique in this method to improve the b-jet purity, and reduce systematic uncertainties arising from the modelling of $t\bar{t}$ processes. The simulation-to-data corrections derived using this method are used as the default b-jet tagging efficiency correction for all ATLAS analyses that use b-tagging. The author was the editor for the internal documentation of the $t\bar{t}$ likelihood method, and is an editor on a forthcoming paper on Run-2 ATLAS b-jet calibrations.

Higgs: The author has been an active member of the ATLAS Higgs group since October 2015, and has contributed to two iterations of the search for the decay of the Standard Model Higgs boson to a pair of bottom-quarks, in association with the production of a vector boson, $VH \rightarrow Vb\bar{b}$. In the first iteration of the analysis (results not presented) [2], the author helped develop the necessary analysis code for the 1-lepton channel, conducted background modelling studies and was an editor for the internal documentation of the analysis.

In the second iteration of the analysis (the results presented in this thesis) [3], the author's contribution included the training and optimisation of the multivariate discriminant used in the 1-lepton channel, development of new background control regions and background modelling studies. The author also produced the 1-lepton inputs to the fit model, requiring the inclusion of new simulated data samples and updating the recommendations for physics tools, along with their systematic uncertainties. Studies were also carried out to cross-check the profile likelihood fit model, and production of the final fit results. Additionally, the author was an editor for the internal documentation of the analysis.

Lepton Isolation and Fake Forum: The author has contributed to the ATLAS Lepton Isolation and Fake Forum in the derivation of muon isolation scale factors. A new dedicated muon isolation working point was developed for the Standard Model $VH \rightarrow Vb\bar{b}$ analysis, and the author worked to evaluate the corresponding isolation efficiencies in data using a Tag and Probe approach with $Z \rightarrow \mu\mu$ events. The derived simulation to data scale factors were approved by the Lepton Isolation and Fake Forum, and are used as the recommended correction for the new working point throughout ATLAS.

Event Display: The maintenance of the ATLANTIS Event Display in the ATLAS control room was undertaken as part of the author's service work. Work was carried out to maintain the operation of the event display, including on-call shifts, as well as the production of event displays produced by beam-splash tests in March of 2016.

---

[1] Run-1 of the LHC lasted from 2010-2012, and collected pp collision data at $\sqrt{s} = 7$ TeV and $\sqrt{s} = 8$ TeV.

[2] Run-2 of the LHC is scheduled for 2015-2018, collecting pp collision data at $\sqrt{s} = 13$ TeV.

Chapter 2

Theoretical Framework

The Standard Model (SM) of particle physics [4–6] is one of the most thoroughly tested theories of modern physics. Developed during the second half of the 20th century, the SM has been shown to explain existing experimental observations of particle physics to a high degree of precision, as well as providing a road map for the discovery of new particles. The discovery of the top quark by the CDF and DØ experiments at the Tevatron $p\bar{p}$ collider in 1995 [7, 8], and the tau neutrino in 2000 [9] were both predictions made by the SM, later confirmed with experimental observation. The most recent development in our understanding of the SM was via the observation of the Higgs boson by the ATLAS and CMS experiments at the LHC in 2012 [10, 11]. This new particle was the last missing piece in the completion of the SM.

Whilst our understanding of the SM is almost complete, there remains a large number of experimental observations which are not explained by the SM, and which will require it to be further modified or extended. For example, the origin of dark matter [12], the origin of neutrino mass and oscillations [13], and the origin of the matter anti-matter asymmetry in the universe [14] to name but a few.

The Higgs sector can be studied to both explain the origins of electroweak symmetry breaking, the Higgs self-interaction, and other properties of this unique particle, while also providing a new opportunity to search for physics beyond the Standard Model (BSM). For example, dark matter candidates are known to be massive, and could therefore couple to the Higgs boson. By precisely measuring the coupling of the Higgs to the SM, one can use this as a probe of BSM physics.

In this thesis, work is carried out with the aim of measuring the branching ratio of the $H \to b\bar{b}$ decay mode. This chapter covers a brief overview of the necessary theoretical background of the SM in Section 2.1 and the Higgs Mechanism is Section 2.2. A more complete description of the SM and Higgs Mechanism can be found in Refs. [4, 15].

2.1 The Standard Model

The Standard Model of particle physics is a Quantum Field Theory (QFT) based on a $SU(3)_c \times SU(2)_L \times U(1)_Y$ gauge symmetry where, by Noether's theorem, each symmetry has a corresponding conserved quantity. Interactions of the SM are considered in terms of the fields, ψ, of half-integer spin fermions with integer spin bosons. Fermions are broken into two categories, the colourless leptons, and the colour charged quarks. Fermions are further categorised into three generations, with each generation having identical properties, except for the fermion's mass, as summarised in Table 2.1. Bosons are the mediators of the three fundamental interactions included in the SM[1], the weak, strong and electromagnetic interactions. The properties of these bosons, along with the Higgs boson, are summarised in Table 2.2.

	Leptons				Quarks			
Generation	Particle		Charge	Mass [GeV]	Particle		Charge	Mass [GeV]
First	electron neutrino	ν_e	0	$< 2 \times 10^{-9}$	up	u	$+\frac{2}{3}$	0.002
	electron	e^-	-1	0.0005	down	d	$-\frac{1}{3}$	0.005
Second	muon neutrino	ν_μ	0	$< 1.9 \times 10^{-4}$	charm	c	$+\frac{2}{3}$	1.27
	muon	μ^-	-1	0.1057	strange	s	$-\frac{1}{3}$	0.096
Third	tau neutrino	ν_τ	0	$< 18.2 \times 10^{-3}$	top	t	$+\frac{2}{3}$	173.21
	tau	τ^-	-1	1.777	bottom	b	$-\frac{1}{3}$	4.66

Table 2.1: Summary of the properties of the half-integer spin fermions of the Standard Model [6]. Anti-fermions have identical properties, with the exception of charge which is inverted, and are denoted with an overbar, i.e. $\bar{f}$.

Name	Boson	J^P	Mass [GeV]
Photon	γ	1^{-1}	0
Weak	$W^\pm$	1^{-1}	80.4
Weak	Z	1^{-1}	91.2
Strong	g ($\times$8)	1^{-1}	0
Higgs	H	0^{+1}	125.0 [16]

Table 2.2: Summary of the properties of the integer spin bosons of the Standard Model [6].

The basics of the symmetries and interactions of the SM are summarised below, with the exception of the Higgs mechanism, which is summarised in Section 2.2. Consider the Dirac Lagrangian density

$$\mathcal{L}_{\text{Dirac}} = \overline{\psi}(i\gamma^\mu \partial_\mu - m)\psi, \tag{2.1}$$

---

[1] A theory of gravitation is not currently included in the SM.

where $\psi = \psi(x)$ is the Dirac spinor of a spin $\frac{1}{2}$ fermion, $\overline{\psi} = \psi^{\dagger}\gamma^0$ and γ^{μ} are the Dirac gamma matrices. Under the $U(1)$ gauge transformation

$$\psi \rightarrow \psi' = e^{i\alpha(x)}\psi, \tag{2.2}$$

where $\alpha(x)$ is a spacetime dependent phase, the Dirac Lagrangian now becomes

$$\mathcal{L}_{\text{Dirac}} \rightarrow \mathcal{L}'_{\text{Dirac}} = \mathcal{L}_{\text{Dirac}} - \overline{\psi}\gamma^{\mu}\partial_{\mu}\alpha(x)\psi. \tag{2.3}$$

In order to conserve the $U(1)$ symmetry of the Lagrangian under this transformation, the partial derivative ∂_{μ} is replaced with the covariant derivative, D_{μ}. This implies that, to conserve the symmetry, D_{μ} must satisfy

$$D_{\mu}\psi(x) \rightarrow D'_{\mu}\psi(x)' = e^{i\alpha(x)}D_{\mu}\psi(x), \tag{2.4}$$

which is satisfied for

$$D_{\mu} = \partial_{\mu} + ieA_{\mu}, \tag{2.5}$$

with

$$A_{\mu} \rightarrow A'_{\mu} = A_{\mu} - \frac{1}{e}\partial_{\mu}\alpha(x). \tag{2.6}$$

In terms of quantum electrodynamics (QED), A_{μ} is interpreted as the gauge field for the electromagnetic interaction with interaction strength e. One can then write the QED Lagrangian as

$$\mathcal{L}_{\text{QED}} = -\frac{1}{4}F_{\mu\nu}F^{\mu\nu} + \overline{\psi}(i\gamma^{\mu}\partial_{\mu} - m)\psi, \tag{2.7}$$

where $F_{\mu\nu}$ represents the kinetic energy term of the excitation of the gauge field. $F_{\mu\nu}$ can also be defined in terms of D_{μ} to generalise the interaction as an Abelian gauge group,

$$[D_{\mu}, D_{\nu}]\psi \equiv ieF_{\mu\nu}\psi. \tag{2.8}$$

Expanding this procedure to include non-Abelian gauge groups, one can introduce the strong interaction as the symmetry of the $SU(3)_c$ group, describing the colour charged strong interactions of quantum chromodynamics (QCD). The unified electromagnetic and weak forces are introduced by requiring an $SU(2)_L \times\ U(1)_Y$ symmetry of the SM Lagrangian. Under the $SU(2)_L$ local gauge transformation

$$\psi \rightarrow \psi' = e^{i\boldsymbol{\alpha}(x)\cdot\frac{\boldsymbol{\sigma}}{2}}\psi, \tag{2.9}$$

with $\boldsymbol{\sigma}$ the vector of Pauli spin matrices (the generators of the $SU(2)$ symmetry group). It is then necessary to introduce an additional 3 gauge fields to conserve the symmetry of the Lagrangian,

$W_1^\mu, W_2^\mu, W_3^\mu$, analogous to A^μ in the above QED example, with coupling g. From studies of the β^- decays of ^{60}Co [17], it was observed that parity is violated in the weak interaction. In order to explain this in terms of a Lagrangian gauge symmetry, the weak interaction has both a vector and axial-vector ($V - A$) component. By the nature of the $V - A$ interaction, only the left handed (right handed) component of (anti-) particle spinors partake in the charged weak current interaction.

To describe the weak interaction, it is necessary to introduce the weak isospin quantum number, I_W. Left handed fermions are in weak isospin doublets with $I_W = \frac{1}{2}$, whilst right handed fermions are in weak isospin singlets with $I_W = 0$. Particle wave functions couple to these bosons dependent on the third component of the weak isospin charge, I_W^3, with $I_W^3 = \pm\frac{1}{2}$ for the left handed doublet, and $I_W^3 = 0$ for the right handed singlet. The charged flavour changing current is expressed as a linear combination of W_1^μ and W_2^μ,

$$W^{\pm\mu} = \frac{1}{\sqrt{2}}(W_1^\mu \mp iW_2^\mu). \tag{2.10}$$

Whilst it seems tempting to associate the Z boson with W_3, experimental observations indicate that the Z boson couples to both left and right handed electrons. Instead, the weak neutral current and photon are expressed as the product of the mixing of W_3^μ and B^μ, the boson of the $U(1)_Y$ symmetry, with coupling g'. In the $U(1)_Y$ symmetry, the weak hypercharge is defined as

$$Y = 2Q - 2I_W^3, \tag{2.11}$$

with Q the charge of the fermion. The mixing of W_3^μ and B^μ is defined in terms of the electroweak mixing angle θ_W,

$$\begin{pmatrix} A^\mu \\ Z^\mu \end{pmatrix} = \begin{pmatrix} \cos\theta_W & \sin\theta_W \\ -\sin\theta_W & \cos\theta_W \end{pmatrix} \begin{pmatrix} B^\mu \\ W_3^\mu \end{pmatrix}. \tag{2.12}$$

From equating the $SU(2)_L$ and $U(1)_Y$ currents with the known interaction current of the photon, A_μ, the following relations are obtained

$$e = g' \cos\theta_W \tag{2.13}$$

$$e = g\sin\theta_W. \tag{2.14}$$

In the description of the SM thus far, all fermions and bosons are massless. To explain the origin of mass within the SM, without breaking gauge symmetry, the Higgs mechanism is introduced.

2.2 The Higgs Mechanism

The Higgs (Brout-Englert-Higgs) mechanism is introduced to the SM to explain the masses of the gauge bosons through a process of spontaneous symmetry breaking [18–23]. This section first describes the generation of boson masses in the $SU(2)_L \times U(1)_Y$ sector, and then the expansion to the masses of the fermionic sector of the SM.

Consider the complex isospin doublet, with $I_W = \frac{1}{2}$ and $Y = 1$, of the Higgs field

$$\boldsymbol{\Phi} = \begin{pmatrix} \phi^+ \\ \phi^0 \end{pmatrix}, \tag{2.15}$$

which can be written in terms of real scalar fields as

$$\phi^+ = \frac{\phi_1 + i\phi_2}{\sqrt{2}}, \ \phi^0 = \frac{\phi_3 + i\phi_4}{\sqrt{2}}, \tag{2.16}$$

and introduces four additional degrees of freedom to the SM Lagrangian. The $SU(2)_L \times U(1)_L$ covariant derivative is defined as

$$D_\mu = \left(\partial_\mu + i\frac{g}{2}\boldsymbol{\sigma}\cdot\boldsymbol{W_\mu} + iY\frac{g^{'}}{2}B_\mu\right). \tag{2.17}$$

The most general Lagrangian for the field can be expressed as

$$\mathcal{L}_{\boldsymbol{\Phi}} = (D_\mu\boldsymbol{\Phi})^\dagger(D^\mu\boldsymbol{\Phi}) - V(\boldsymbol{\Phi}), \tag{2.18}$$

with

$$V(\boldsymbol{\Phi}) = \lambda(\boldsymbol{\Phi}^\dagger\boldsymbol{\Phi})^2 - \mu^2\boldsymbol{\Phi}^\dagger\boldsymbol{\Phi}, \tag{2.19}$$

where μ and λ are scalar constants. It can be seen that $V(\boldsymbol{\Phi})$ has minima specified by

$$\frac{\partial V}{\partial(\boldsymbol{\Phi}^\dagger\boldsymbol{\Phi})} = \mu^2 - 2\lambda\boldsymbol{\Phi}^\dagger\boldsymbol{\Phi} \tag{2.20}$$

$$\implies \boldsymbol{\Phi}^\dagger\boldsymbol{\Phi} = \frac{\mu^2}{2\lambda} \tag{2.21}$$

$$\implies \frac{1}{2}(\phi_1^2 + \phi_2^2 + \phi_3^2 + \phi_4^2) = \frac{\mu^2}{2\lambda}, \tag{2.22}$$

with real solutions for $\mu^2 > 0$. Figure 2.1 presents the Higgs potential in the cases without spontaneous symmetry breaking, $\mu^2 \leq 0$, (a), and where the symmetry is broken with $\mu^2 > 0$ (b).

The solutions to Equation 2.21 are degenerate, meaning that by a phase rotation, it is possible to set $\phi_1^2 = \phi_2^2 = \phi_4^2 = 0$ and $\phi_3^2 = \frac{\mu^2}{\lambda}$. Expanding around this minimum, and setting $\phi_3 = v + H(x)$,

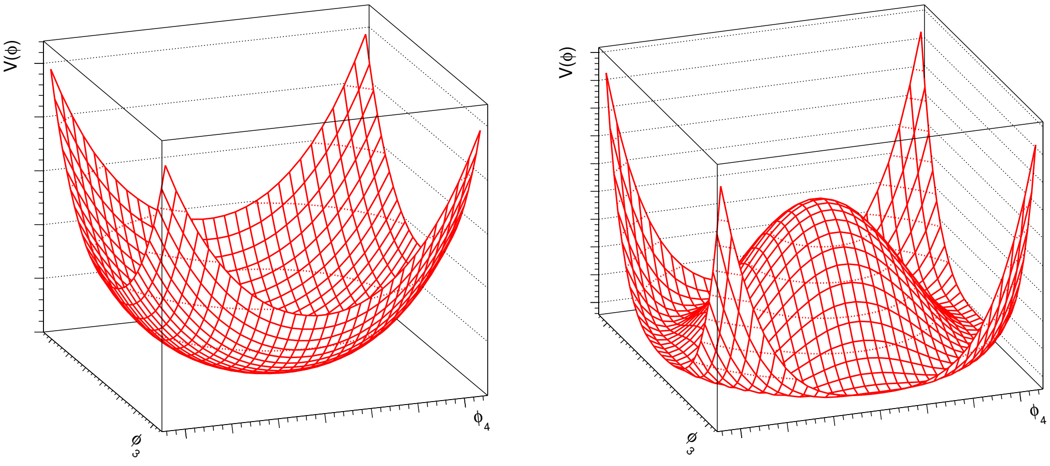

(a) **(b)**

Figure 2.1: Representation of the 2D Higgs potential without spontaneous symmetry breaking, $\mu^2 \leq 0$, (a), and where the symmetry is broken with $\mu^2 > 0$ (b). In (b), the minimum of the Higgs potential is degenerate, with solutions in the circle $\phi_3^2 + \phi_4^2 = \frac{\mu^2}{\lambda}$.

with $v^2 = \frac{\mu^2}{\lambda}$, $\mathbf{\Phi}$ can be expressed as

$$\mathbf{\Phi} = \frac{1}{\sqrt{2}} \begin{pmatrix} 0 \\ v + H(x) \end{pmatrix}. \tag{2.23}$$

Substituting Equation 2.23 into Equation 2.17, one finds

$$\begin{aligned} \mathcal{L}_{\mathbf{\Phi}} = &\frac{1}{2}(\partial_\mu H)(\partial^\mu H) + \frac{g^2}{4}(v+H)^2(W_\mu^+ W^{\mu -}) \\ &+ \frac{1}{8}(g^2 + g'^2)Z_\mu Z^\mu (v+H) \\ &+ \frac{\mu^2}{2}(v+H)^2 - \frac{\lambda}{4}(v+H)^4. \end{aligned} \tag{2.24}$$

From this, the masses of the bosons can be interpreted as

$$m_W = \frac{1}{2} g v \tag{2.25}$$

$$m_Z = \frac{1}{2}\sqrt{(g^2 + g'^2)}v = \frac{m_W}{\cos\theta_W} \tag{2.26}$$

$$m_A = 0 \tag{2.27}$$

$$m_H = \sqrt{-2\mu^2} = \sqrt{-2\lambda v^2}. \tag{2.28}$$

It can therefore be seen that by the method of spontaneous symmetry breaking in the $SU(2)_L \times U(1)_Y$ sector, masses can be given to the W and Z bosons, whilst ensuring the photon remains massless. The W and Z bosons have absorbed three of the additional degrees of freedom by becoming massive and gaining three polarisation degrees of freedom. The remaining degree of freedom results in a massive Goldstone boson, the Higgs boson. The only possible way to measure μ is through a direct measurement of the Higgs boson mass.

2.2.1 Yukawa Coupling to the Fermionic Sector

Electroweak symmetry breaking only results in the generation of mass terms for the electroweak sector. An expansion of the Higgs mechanism is now required to give masses to the fermionic sector of the SM, requiring the addition of Yukawa coupling terms

$$\mathcal{L}_{\text{Yukawa}} = -G_f(\overline{\mathbf{\Psi}}_L \mathbf{\Phi} \mathbf{\Psi}_R + \overline{\mathbf{\Psi}}_R \overline{\mathbf{\Phi}} \mathbf{\Psi}_L), \tag{2.29}$$

where G_f is the Yukawa coupling term to be determined from experiment for a fermion f, $\mathbf{\Psi}_{L(R)}$ the left (right) handed fermion isospin doublet (singlet) and $\mathbf{\Phi}$ the complex scalar Higgs field. Whilst the Yukawa term is applicable to all fermions, consider as an example the case of the first generation of leptons. It is found that

$$\begin{aligned}
\mathcal{L}_e &= -\frac{G_e}{\sqrt{2}} \left[(\overline{\nu}_e, \overline{e})_L \begin{pmatrix} 0 \\ v + H(x) \end{pmatrix} e_R + \overline{e}_R \Big(0, v + H(x)\Big) \begin{pmatrix} \nu_e \\ e \end{pmatrix}_L \right] && (2.30) \\
&= -\frac{G_e(v + H(x))}{\sqrt{2}} \left(\overline{e}e\right). && (2.31)
\end{aligned}$$

The term $\frac{G_e v}{\sqrt{2}}$ is interpreted as the electron mass term, m_e, with G_e to be determined from a measurement of v and m_e. Furthermore, the interaction term, $\frac{G_e}{\sqrt{2}}$, is proportional to the electron mass. This formalism can equally be applied to the second and third generation of fermions, with a corresponding G_f term required for each fermion flavour.

The above formalism only gives masses to the 'down' type fermions, meaning another term must be added to the Lagrangian to include masses for the 'up' type quarks. Adding an additional term to the Yukawa Lagrangian of the form

$$\mathcal{L}_{\text{Yukawa,up}} = -G_f(\overline{\mathbf{\Psi}}_L \tilde{\mathbf{\Phi}}^c \mathbf{\Psi}_R + h.c.), \tag{2.32}$$

with $h.c.$ the Hermitian conjugate and

$$\tilde{\mathbf{\Phi}}^c = -i\sigma_2 \mathbf{\Phi}^* = -\frac{1}{\sqrt{2}} \begin{pmatrix} v + H(x) \\ 0 \end{pmatrix}. \tag{2.33}$$

From this, masses are introduced for the 'up' type quarks.

2.2.2 Higgs Boson Production and Branching Fractions

In order to introduce the masses of the bosonic and leptonic sectors of the SM, as described in Section 2.2, interaction terms between the Higgs boson and other particles of the SM are introduced. Each of these couplings are proportional to v, and are therefore dependent on the measured mass of the Higgs boson. From measurements of the decays $H \to \gamma\gamma$ and $H \to ZZ \to 4\ell$, m_H has been measured to be $m_H = 124.98 \pm 0.19(\text{stat.}) \pm 0.21(\text{syst.})$ GeV [16].

The corresponding production cross-section for the dominant production modes is presented in Figure 2.2 (a) as a function of m_H. The largest production mode of the Higgs boson in pp collisions at $\sqrt{s} = 13$ TeV is via gluon-gluon fusion ($pp \to H$), with the cross-section for the production of a Higgs boson in association with a vector boson ($pp \to WH$, $pp \to ZH$) approximately 20 times smaller. In Figure 2.2 (b), the Higgs branching fractions are presented as a function of m_H. For $m_H = 124.98$ GeV, the dominant decay mode is predicted by the SM to be $H \to b\bar{b}$, with a branching ratio of $0.582^{+0.007}_{-0.007}$ [24].

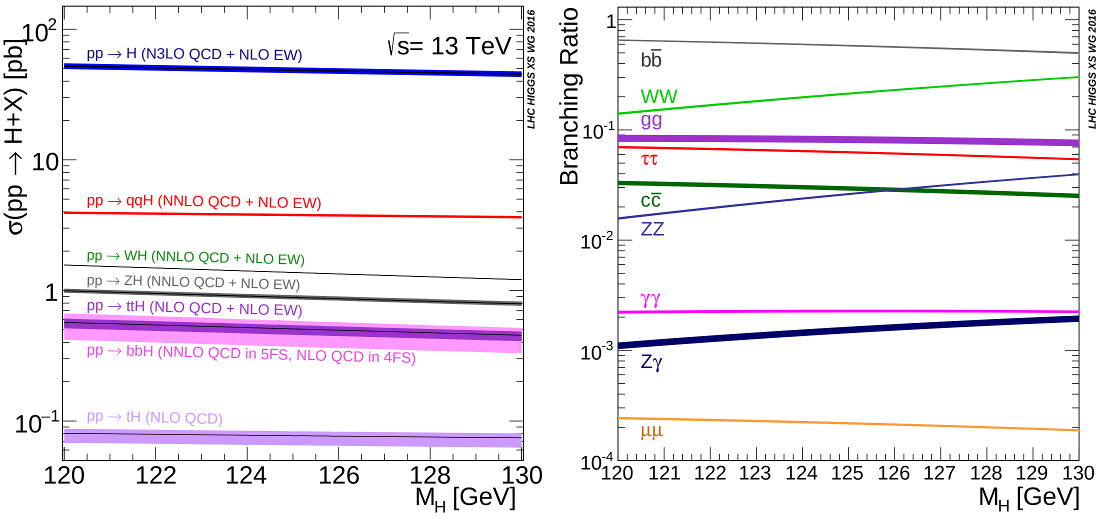

(a) **(b)**

Figure 2.2: Expected production cross-sections by channel in pp collisions at $\sqrt{s} = 13$ TeV (a) and branching ratios (b) of the Standard Model Higgs boson as a function of m_H [24].

Chapter 3

The Large Hadron Collider and the ATLAS Detector

The work presented in this thesis relies on data recorded by the ATLAS detector in high energy proton-proton collisions. This chapter provides an overview of the experimental apparatus and analysis techniques used throughout this thesis. Section 3.1 provides an overview of the Large Hadron Collider particle accelerator, which is used to generate the high energy collisions. Section 3.2 provides an overview of the design and operation of the ATLAS detector. Section 3.3 details the size of the recorded dataset used for analyses presented in this thesis, and Section 3.4 presents the pile-up conditions in the recorded dataset. Section 3.5 presents an overview of the reconstructed physics objects used for analysis. Lastly, Section 3.6 presents an overview of multivariate techniques used in analyses presented in this thesis.

3.1 The Large Hadron Collider

The Large Hadron Collider (LHC) [25] at the European Organisation for Nuclear Research (CERN) is the world's largest and most powerful particle accelerator. Constructed in the tunnel previously used for the Large Electron-Positron Collider (LEP) [26], the LHC accelerates two beams of protons in a 27 km ring in opposite directions using powerful superconducting magnets (the LHC is also capable of accelerating lead ions, although all studies and results presented will focus on *pp* collisions), before colliding them at several interaction points.

An overview of the LHC complex is presented in Figure 3.1. Hydrogen gas is ionised using an electric field. The first accelerator in the chain, Linac 2, accelerates these protons to 50 MeV. The Proton Synchrotron Booster then accelerates the protons to 1.4 GeV, before they are accelerated to 25 GeV by the Proton Synchrotron. The energy of the beam is further increased to 450 GeV by the Super Proton Synchrotron, before it is split into the two beampipes of the LHC. At this final stage, the beams are accelerated to an energy of 6.5 TeV (for Run-2) [25, 27]. Proton bunches are spaced by 25 ns, with each bunch containing up to 1.1×10^{11} protons.

During Run-1 of the LHC, 2010-2012, protons were collided with centre of mass energies ($\sqrt{s}$) of 7 TeV and 8 TeV. During the long-shutdown of 2012-2015, the superconducting beampipe magnets were upgraded in order to reach $\sqrt{s} = 13$ TeV, meaning an average magnetic field strength of ~ 5 T. Run-2 of the LHC is scheduled to last from 2015-2018, collecting up to 150 fb^{-1} of pp collision data.

At the end of Run-2, the LHC will be shutdown between 2019 and 2020 to allow upgrades in preparation for Run-3, scheduled to last from 2021 to 2023. During Run-3, it is aimed to collide protons at $\sqrt{s} = 14$ TeV, and at twice the Run-2 instantaneous luminosity, collecting a predicted 300 fb^{-1} of pp collision data. Between 2024 and 2026, further upgrades to the LHC will facilitate instantaneous luminosities seven times larger than the current Run-2 luminosity, referred to as the High Luminosity LHC (HL-LHC) era. The HL-LHC physics programme is scheduled to last until 2035-37, collecting a total of $3000 - 4000$ fb^{-1} of pp collision data with ~ 200 collisions expected in each bunch crossing [28].

Situated around the ring are the four main physics experiments of the LHC; ALICE [29], CMS [30], LHC*b* [31] and ATLAS [32], located at crossing points where the two proton beams are collided.

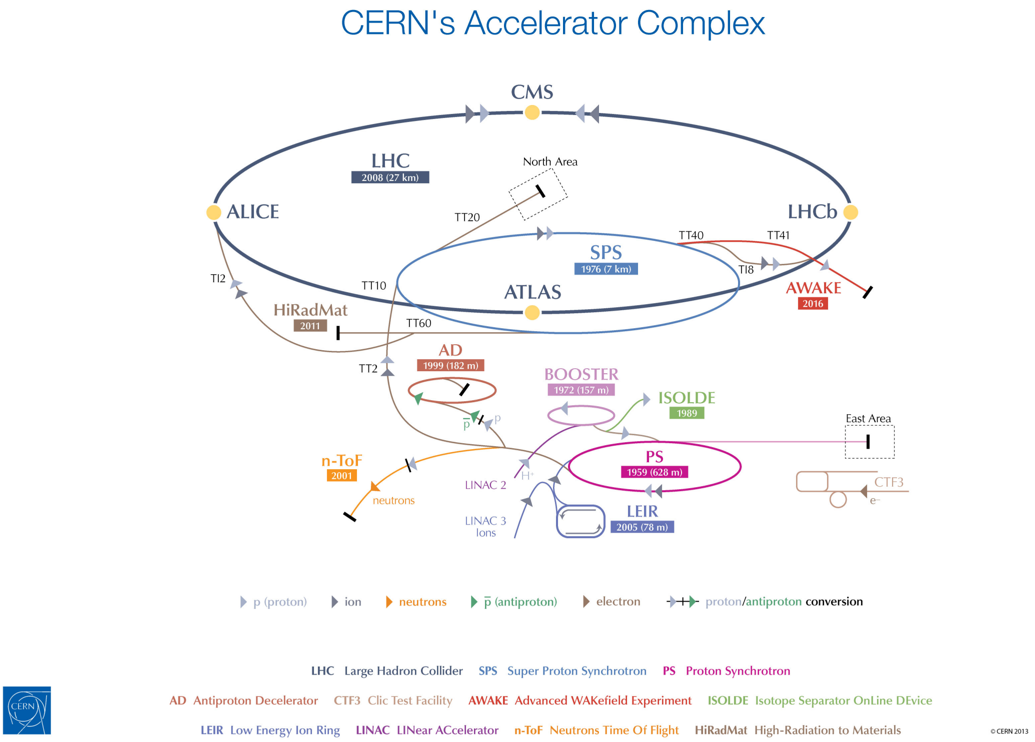

Figure 3.1: Overview of the CERN accelerator complex and the LHC [27].

3.2 The ATLAS Detector

The ATLAS (A Toroidal LHC ApparatuS) detector is one of the four main physics experiments on the LHC ring. In this section, a brief description of the ATLAS detector is presented, with a full description available in Ref. [32].

Proton-proton collisions take place at the centre of the detector, producing showers of particles. It is from the measurement of these particles that the underlying physics process is probed. The detector is cylindrically shaped around the beampipe, with a diameter of 25 m and length of 44 m. The detector weighs approximately 7,000 tonnes. The main components and subsystems of the ATLAS detector are presented in Figure 3.2. The main subsystems are cylindrically symmetric layers around the beampipe. End-caps, perpendicular to the beampipe, are situated at either end of the detector to improve the detector coverage in the forward regions.

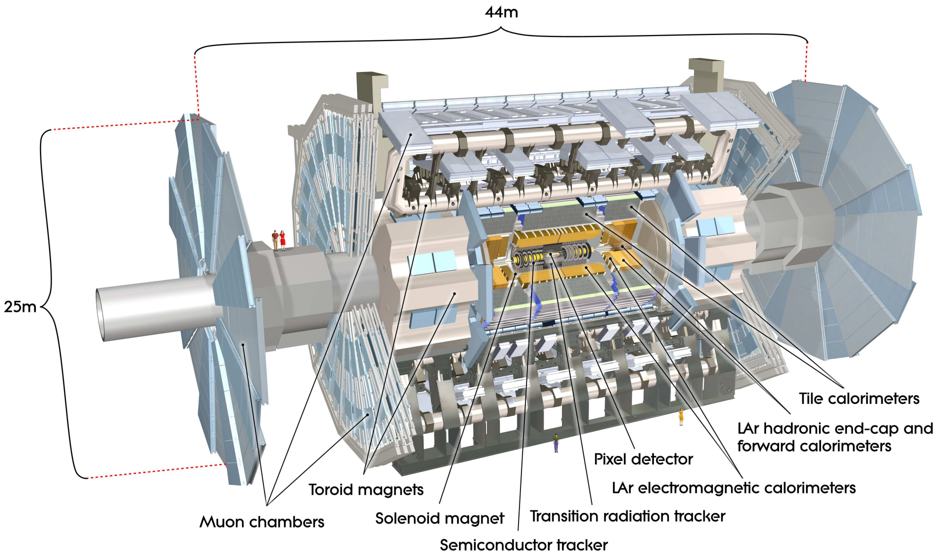

Figure 3.2: Overview of the ATLAS detector with a section cutaway to show details of the inner components [32].

3.2.1 Coordinate System

The ATLAS coordinate system is defined as a right-handed Cartesian system, with the z-axis along the beampipe, the positive x-axis pointing towards the centre of the LHC ring, and the positive y-axis pointing upwards. The $x - y$ plane is defined as the transverse plane. The azimuthal angle ϕ is the angle around the beam axis, starting from the x-axis. The polar angle θ is the angle from the beampipe. The distance r is defined as the radial distance in the transverse plane from the centre of the detector outwards.

The momentum of an object is expressed in Cartesian coordinates as

$$\boldsymbol{p} = (p_x, p_y, p_z), \tag{3.1}$$

with p_x, p_y and p_z the momentum in the x, y and z directions. The transverse momentum of an object, p_{T}, is defined as the projection of the momentum into the $x - y$ plane, with $p_{\mathrm{T}} = |\boldsymbol{p}| \sin\theta$.

A frequently used transformation of the polar angle, is to define the pseudorapidity

$$\eta = -\log\left(\tan\left(\frac{\theta}{2}\right)\right), \tag{3.2}$$

where in the massless particle limit, this is equivalent to the rapidity, $y = \frac{1}{2}\log\left(\frac{E+p_z}{E-p_z}\right)$. Differences in rapidity are invariant under Lorentz boosts along the beampipe. A particle with $\eta = 0$ is travelling perpendicular to the beampipe ($\theta = 90^\circ$), whilst in the limit of $\theta \to 0^\circ, 180^\circ$ (i.e. parallel to the beampipe), $\eta \to \infty$. Distances between objects are defined in the azimuthal-pseudorapidity space as

$$\Delta R^2 = \Delta\eta^2 + \Delta\phi^2. \tag{3.3}$$

3.2.2 Inner Detector

The inner detector (ID) is designed to measure tracks from charged particles, and consists of four main sub-sections. The Insertable B-Layer (IBL) was installed during the first long shut-down of the LHC, and is the inner-most pixel layer of the ATLAS detector, at a radius of approximately 30 mm [33]. The IBL uses silicon pixels to measure the trajectories of charged particles, offering a coverage of $|\eta| < 2.5$. The IBL is designed to improve: the robustness of tracking due to dead pixel modules; the tracking precision; and the resilience of tracking performance in higher instantaneous luminosity conditions.

The next sub-section is the ATLAS pixel detector. The pixel detector consists of three cylindrical pixel layers in the central barrel region, and two sets (one at either end) of three disks. In the barrel region, the layers occupy the radial space $50.5 < r < 122.5$ mm, again giving a coverage of $|\eta| < 2.5$. Pixels are 50×400 $\mu\mathrm{m}^2$ in $r - \phi \times z$, giving a resolution of 10 μm in the transverse direction and 115 μm in the longitudinal direction in the barrel region.

The next layer is the semiconductor tracker (SCT). The SCT consists of four layers of silicon microstrip pairs, covering $255 < r < 549$ mm in the barrel region. In the end-cap region, the SCT consists of two sets of 9 disk layers, covering $275 < r < 560$ mm for $839 < |z| < 2735$ mm, with intrinsic uncertainties of 17 μm in the transverse direction, and 580 μm in the longitudinal direction.

The last and outermost-layer of the ID is the transition radiation tracker (TRT). The TRT is constructed from 2 mm radius straw trackers, filled with xenon gas. Charged particles ionise the xenon. The wall of the straws is kept at a negative voltage, creating an electric field which means the ionised electrons are accelerated towards the central anode. In the barrel, straws are parallel to the beampipe, and cover $560 < r < 1080$ mm for $|z| < 720$ mm. In the end-cap, straws are perpendicular to the beampipe, in a fan-like arrangement, covering $617 < r < 1106$ mm and $827 < z < 2774$ mm. The TRT covers $|\eta| < 2.0$, providing $r - \phi$ information, with an accuracy of 130 μm per straw and ~ 35 hits per track. The space between tracker straws is filled with materials of various refractive indices, which cause particles passing through to radiate photons. For particles with the same momentum, lighter particles have a larger Lorentz factor, meaning that particles such as electrons are likely to radiate more photons than heavier hadrons, aiding in their identification.

In order to measure the momentum and charge of a particle, the entirety of the ID is submerged in a 2 T magnetic field, generated by a solenoid magnet. By measuring the curvature of the path of charged particles from hits in the ID, it is possible to determine a particle's momentum. The target track momentum resolution, σ_{p_T}, for the ATLAS ID as a function of the track transverse momentum p_T, is given by

$$\frac{\sigma_{p_\mathrm{T}}}{p_\mathrm{T}} = 0.05\%\ p_\mathrm{T} \oplus 1\%. \tag{3.4}$$

3.2.3 Calorimeters

Calorimeters are situated outside of the inner detector, designed to measure the energy of particles produced in a collision. The ATLAS calorimeters consist of two types of sampling calorimeters; the Electromagnetic (ECAL) and Hadronic (HCAL) calorimeters. These are designed to precisely measure the energies of electrons/photons and hadrons, respectively.

In many analyses, excellent energy resolution is required. The ATLAS calorimeter energy resolutions, determined from beam-test data, are summarised in Table 3.1.

	Detector component	Required resolution
EM	Barrel and end-cap	$\sigma_E/E = 10\%/\sqrt{E} \oplus 0.7\%$
Hadronic	Barrel and end-cap	$\sigma_E/E = 50\%/\sqrt{E} \oplus 3\%$
	Forward	$\sigma_E/E = 100\%/\sqrt{E} \oplus 10\%$

Table 3.1: ATLAS calorimetry energy resolution, as obtained from beam-test data.

3.2.3.1 Electromagnetic Calorimeter

The ECAL is a liquid argon (LAr) calorimeter, with lead as the absorber, and LAr as the active material. The LAr is ionised to measure the energy of the shower. The ECAL has an accordion geometry to provide complete coverage in ϕ without any cracks. The barrel region covers $|\eta| < 1.475$, whilst the end-cap consists of two pairs of concentric wheels (one at either end of the detector), covering $1.375 < |\eta| < 2.5$ and $2.5 < |\eta| < 3.2$.

The evolution of an electromagnetic shower is characterised by the material's radiation length, X_0, and is the distance over which an electromagnetically interacting particle loses all but $1/e$ of its energy. In order to contain a large fraction of the electromagnetic shower, the ECAL is $> 22\ X_0$ in the barrel, and $> 24\ X_0$ in the end caps.

3.2.3.2 Hadronic Calorimeter

The interaction of a hadron with detector material is fundamentally different to that of an electron or photon, as it can interact by the strong force as well as the electromagnetic force. The characteristic depth of a material, λ, is the distance over which a hadron loses all but $1/e$ of its energy. The barrel HCAL consists of steel absorbers and scintillating tiles (tile calorimeter), divided into two sections covering $|\eta| < 1.0$ and $0.8 < |\eta| < 1.7$. In the central barrel region, the calorimeter consists of three layers of thickness 1.5 λ, 4.1 λ and 1.8 λ. In the extended barrel region, the thicknesses are 1.5 λ, 2.6 λ and 3.3 λ.

The hadronic end-cap calorimeter (HEC) and forward calorimeters provide additional coverage at high $|\eta|$, and both use LAr technology. The hadronic end-cap calorimeter consists of two wheels per end-cap using a copper absorber, approximately 12 λ deep, and covers $1.5 < |\eta| < 3.2$. The forward calorimeter consists of three layers of absorber (one of copper, two of tungsten), approximately 10 λ deep, and covers $3.1 < |\eta| < 4.9$.

3.2.4 Muon Spectrometer

The outermost and largest system of the ATLAS detector is the muon system. Due to the larger mass of muons over electrons, the effect of bremsstrahlung is reduced, and muons are therefore able to pass through the ATLAS calorimeters with minimal interactions. Tracking chambers are used to measure the paths of muons. A series of toroidal magnets are used to generate a strong magnetic field in the barrel and end-cap regions, from which the muon momentum can be measured. Monitored drift tubes cover $|\eta| < 2.7$, whilst cathode strip chambers cover $2.0 < |\eta| < 2.7$.

The muon trigger system uses resistive place chambers to cover $|\eta| < 1.05$, and thin gap chambers in the end cap region $1.05 < |\eta| < 2.4$. The trigger system for the muon spectrometer achieves timing resolutions of 1.5-4 ns, and can therefore also be used for bunch crossing association.

The muon spectrometer is designed to offer a high transverse momentum resolution for muons. Typically, the muon spectrometer can reconstruct a 100 GeV muon track with a 3% momentum uncertainty [34].

3.2.5 Trigger System

Each bunch crossing in the detector is called an event. With 25 ns bunch spacing, events occur at a rate of 40 MHz. This rate is clearly too high to record every event, and thus a trigger system is used in ATLAS in order to identify events of interest to record. The trigger system must balance having a good rejection of background events, whilst also ensuring that events of interest are kept with a high efficiency. For Run-2, the ATLAS trigger system has two levels; the Level 1 (L1) hardware trigger and the Higher Level Trigger (HLT) software trigger, designed to reduce the event rate to 1 kHz [35].

The L1 trigger is a hardware based trigger, designed to reduce the event rate from 40 MHz to 100 kHz. Due to limited latencies, the L1 trigger only has information from the calorimeters and muon spectrometers. Regions of Interest (RoIs) are identified by the L1 trigger, selecting regions which could contain high p_{T} jets, leptons or photons. To reduce processing time, RoIs are passed to the HLT.

The HLT is a software based trigger, designed to reduce the event rate from 100 kHz to 1 kHz. The HLT uses a farm of computers to reconstruct events. By targeting just the RoIs, the event processing rate can be increased, reducing latency. The reconstruction of the event also uses offline techniques which allows for more accurate selections over the reduced granularity of the L1 trigger, improving the triggering efficiency.

A number of different triggers are in use in ATLAS, making up the “trigger menu”. In order to ensure the HLT output rate is limited to 1 kHz, thresholds of triggers in the menu are either increased, so as to reduce the rate of events passing the selection, or are “prescaled”, meaning that only a set fraction of events passing the HLT are kept. The trigger menu is modified to take into account changes of the instantaneous luminosity.

3.3 Luminosity

The total luminosity, L, of collisions recorded by a detector can be considered in terms of the number of recorded events, N, and the total inelastic cross section, σ, which in the case of the LHC is the proton-proton inelastic cross-section,

$$N = \sigma L = \sigma \int \mathcal{L}\, dt, \tag{3.5}$$

with $\mathcal{L}$ the instantaneous luminosity. The instantaneous luminosity can be expressed as

$$\mathcal{L} = f_r n_b \frac{N_1 N_2}{2\pi \Sigma_x \Sigma_y}, \tag{3.6}$$

with f_r the beam revolution frequency, n_b the number of bunches, $N_{1(2)}$ the number of particles in bunch 1 (2), and $\Sigma_{x(y)}$ the mean beam width in the $x(y)$ direction. The calibration of $\Sigma_{x(y)}$ is conducted using van-der-Meer beam-separation scans [36, 37]. The instantaneous luminosity is determined using a series of sub-detectors which measure the inelastic rate.

Figure 3.3 presents the cumulative luminosity delivered by the LHC and recorded by ATLAS for the 2015 and 2016 data-taking periods at a centre of mass energy of $\sqrt{s} = 13$ TeV. The recorded luminosity is lower than the delivered luminosity due to inefficiencies in data acquisition.

From the 2015 and 2016 datasets, a total of 36.1 ± 1.2 fb^{-1} has been collected, and corresponds to a quarter of the total expected Run-2 dataset, where up to 150 fb^{-1} is expected to be delivered by the end of 2018.

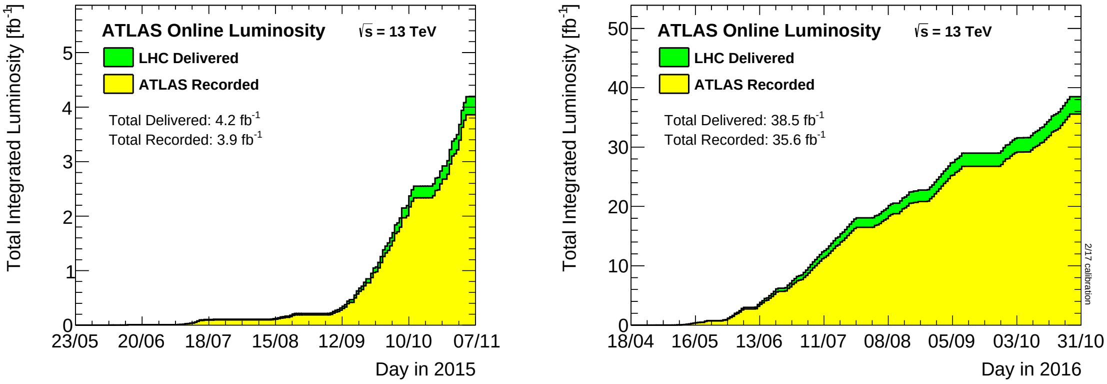

(a) **(b)**

Figure 3.3: Cumulative pp luminosity by day delivered by the LHC (green) and recorded by ATLAS (yellow) for the 2015 (a) and 2016 (b) data-taking periods at a centre of mass energy of $\sqrt{s} = 13$ TeV [38].

3.4 Pile-Up

At the LHC, bunches of up to 10^{11} protons collide in each event. Whilst there is generally one hard scattering process of interest, there are also a large number of softer collisions taking place in the same bunch crossing, referred to as pile-up. The level of pile-up is evaluated by considering the number of collisions present in an event. The average number of interactions per bunch crossing, μ, is calculated as

$$\mu = \frac{\mathcal{L}\sigma}{n_b f_r}, \tag{3.7}$$

with $\mathcal{L}$ the instantaneous luminosity, σ the inelastic cross section, n_b the number of bunches and f_r the LHC revolution frequency. Figure 3.4 presents the mean number of interactions per bunch crossing for the 2015 and 2016 datasets, with a mean $\langle\mu\rangle$ of 23.7 [38]. Simulated Monte Carlo samples are scaled by a correction factor of 1.09 to improve the agreement between simulation and data, and then reweighted to match the pile-up profile of data in all analyses presented in this thesis.

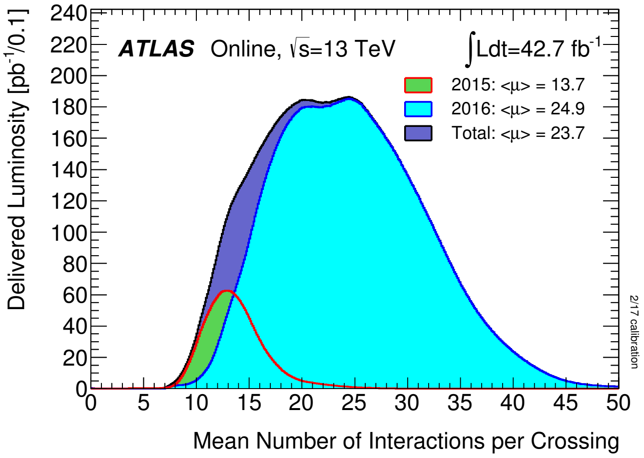

Figure 3.4: Mean number of interactions per bunch crossing for the 2015 and 2016 ATLAS *pp* datasets [38]. The higher instantaneous luminosities achieved during 2016 results in a higher average number of interactions per bunch crossing than in 2015.

3.5 Object Reconstruction

In order to perform physics analyses, it is necessary to reconstruct the signals recorded by the detector into meaningful physics objects. The reconstruction and identification procedures for each type of physics object used in this thesis are described in this section.

3.5.1 Tracks

The tracks of charged particles are reconstructed using energy deposits recorded in multiple detector elements [39]. As a charged particle passes through each detector layer, it will leave energy deposits. These energy deposits are reconstructed as hits, which correspond to a 3D space-point where the charged particle traversed the sensor.

Track seeds are formed from 3 hits, in either the pixel layers or SCT, which are compatible with a track. The track is grown by adding hits which are consistent with the trajectory of the initial track seed.

In the track reconstruction, it is possible that a hit can be associated to more than one track, meaning it is necessary to resolve these ambiguities. Tracks are ranked based on the number of associated hits, the number of “holes” (expected hits which are missing), track momentum and the χ^2 of the track fit. Hits assigned to multiple tracks are associated to the highest ranked track, and tracks with either less than 7 hits or $p_{\mathrm{T}} < 400$ MeV are removed. The TRT information is added by extrapolating the track, and refitting to the pixel, SCT and TRT information.

3.5.1.1 Primary Vertex Reconstruction

In any given bunch crossing, due to the high instantaneous luminosities achieved by the LHC, multiple pp interactions can occur. Interaction vertices are reconstructed by first identifying a vertex seed position from the reconstructed tracks [40]. Tracks which are not compatible with the vertex position are removed, and the vertex position recomputed. Once the vertex position passes set quality requirements, no further tracks are removed, and the vertex position is fixed. The process is repeated, with the tracks which have been removed used in the determination of another vertex. The primary vertex is determined as the vertex with the highest sum of squared transverse momenta of all associated tracks, and is the vertex where the hard scattering is most likely to have originated from. In a $t\bar{t}$ sample, the reconstruction and identification efficiency for the primary vertex is larger than 99% for $\mu = 30$.

3.5.2 Electrons

3.5.2.1 Reconstruction

In the offline reconstruction of electrons, candidate tracks are matched to clusters in the EM calorimeter. The following procedure is employed [41]:

- **Seed cluster reconstruction**: Seed clusters in the EM calorimeter are identified using a sliding window of size 3×5 units of 0.025×0.025 (corresponding to the granularity of the middle layer of the EM calorimeter) in $\eta \times \phi$. Clusters are required to have an energy deposit greater than 2.5 GeV.

- **Track reconstruction**: The ATLAS track reconstruction uses a pion hypothesis to account for detector material interactions (up to 30% momentum loss at each layer). If a track seed with transverse momentum $p_{\mathrm{T}} > 1$ GeV cannot be extended to at least 7 hits using the pion hypothesis, and falls within the region of interest of one EM cluster, then a second attempt is made using the electron hypothesis (which allows for higher momentum loss at each layer).

- **Electron specific track fit**: Tracks are matched to EM clusters, requiring $\Delta\phi < 0.05$ and $\Delta\eta < 0.05$ between the track and the centre of the EM cluster.

- **Electron candidate reconstruction**: If several tracks are matched to the EM cluster, then one track is chosen as the "primary" track. Tracks are ranked based on the ΔR separation of the track and cluster, along with the number of pixel hits and holes. The highest ranked track is chosen as the electron track.

The electron is also required to be consistent with the primary vertex. Two quantities are used to asses the compatibility of the tracks with the primary vertex. The transverse impact parameter, d_0, is defined as the distance of closest approach of the track to the primary vertex, and σ_{d_0} is the uncertainty on d_0. It is required that the transverse impact parameter significance satisfies $|d_0|/\sigma_{d_0} < 5$. The distance along the beam-line (i.e. the longitudinal direction) between d_0 and the reconstructed primary vertex, Δz_0, and the polar angle of the track, θ, are required to satisfy $|\Delta z_0 \sin\theta| < 0.5$ mm. Due to the detector layout, electrons are only considered for $|\eta| < 2.5$. Electrons in the transition region between the barrel and endcap EM calorimeter ($1.37 < |\eta| < 1.52$) are removed due to the large amount of material in front of the first calorimeter layer, which negatively affects the electron reconstruction efficiency and increases the uncertainty on the electron momentum measurement.

In the reconstruction of an electron, it is possible for a physics process to fake the presence of a prompt electron. Such faked prompt electrons can arise from a number of different sources:

- A calorimeter shower of a hadron which mimics an electron shower.

- An electron from a photon conversion.

- The semi-leptonic decay of a heavy flavour hadron.

In the following sections, electron identification and isolation criteria designed to reduce the number of faked prompt electrons are discussed.

3.5.2.2 Identification

Electron identification algorithms are applied to separate electrons from background objects, such as hadronic jets or photon conversions [41].

A likelihood based method combines the signal and background probability density functions (PDFs) of the discriminating variables, such as the transition radiation in the TRT and shower shape, to calculate an overall probability for the object to correspond to an electron or background process. The discriminant $d_{\mathcal{L}}$ is defined as

$$d_{\mathcal{L}} = \frac{\mathcal{L}_{\mathrm{S}}}{\mathcal{L}_{\mathrm{S}} + \mathcal{L}_{\mathrm{B}}}, \tag{3.8}$$

with

$$\mathcal{L}_{S(B)}(\boldsymbol{x}) = \prod_{i=1}^{n} P_i^{S(B)}(x_i), \tag{3.9}$$

where $\boldsymbol{x}$ is the vector of n discriminating variables, and $P_i^{S(B)}(x_i)$ is the PDF of the i^{th} discriminating variable under the signal (background) hypothesis. Three working points are defined by differing cuts on $d_{\mathcal{L}}$, *ID-Loose*, *ID-Medium* and *ID-Tight*. *ID-Loose* offers the best electron acceptance, whilst *ID-Tight* offers the best hadron rejection. For an electron in the range $60 < p_{\mathrm{T}} < 80$ GeV, the *ID-Loose*, *ID-Medium*, and *ID-Tight* working points offer prompt electron identification efficiencies of 97%, 95% and 91%, with hadron rejection efficiencies of 99.7%, 99.8% and 99.9%, respectively.

3.5.2.3 Isolation

In order to further improve the purity of prompt electrons, isolation requirements are applied to help remove non-isolated electron candidates (e.g. semi-leptonic decays of heavy flavour hadrons) [41]. Two variables are defined for this purpose:

- **Track isolation**: $p_{\mathrm{T}}^{\mathrm{varcone0.2}}$ is defined as the sum of the transverse momentum of all tracks within a cone of $\Delta R = \min(0.2, 10\ \mathrm{GeV}/p_{\mathrm{T}})$ around the candidate electron track, meeting set quality requirements, where p_{T} refers to the electron's transverse momentum. The varying ΔR requirement reduces the contamination of additional tracks at high electron p_{T}.
- **Calorimeter isolation**: $p_{\mathrm{T}}^{\mathrm{cone0.2}}$ is defined as the sum of the transverse momentum of EM clusters within a ΔR cone of 0.2 from the candidate electron cluster.

A number of isolation working points are defined based on the calorimeter and track isolation variables. In several cases, the ratio of the isolation variable to the lepton p_{T} is used as the discriminating variable to improve performance over the full p_{T} spectrum. Three relevant working points are:

- *Loose-Track* uses a varying cut on $p_{\mathrm{T}}^{\mathrm{varcone0.2}}/p_{\mathrm{T}}$ to ensure 99% efficiency for prompt electrons across the full electron p_{T} range.
- *Tight-Track* requires $p_{\mathrm{T}}^{\mathrm{varcone0.2}}/p_{\mathrm{T}} < 0.06$, and has a prompt electron efficiency of $\sim 98\%$, whilst rejecting $\sim 50\%$ of all non-prompt electrons (dependent on electron p_{T} and η).
- *HighPt-Calo* requires $p_{\mathrm{T}}^{\mathrm{cone0.2}} < 3.5$ GeV, and has a prompt electron efficiency of $\sim 95\%$, whilst rejecting $\sim 90\%$ of all non-prompt electrons (dependent on electron p_{T} and η).

3.5.2.4 Simulation Correction Factors

Monte Carlo (MC) samples are reweighted to correct for imperfect detector simulation and physics modelling of the electron energy scale, reconstruction, identification, isolation and trigger efficiencies. Each of these corrections introduces systematic uncertainties, and are considered in the analyses presented in this thesis. These are evaluated using a Tag-and-Probe method on $Z \to ee$ and $J/\psi \to ee$ events. The main source of systematic uncertainty in the evaluation of the electron reconstruction, isolation and identification scale factors are from background modelling effects [41].

3.5.2.5 Combined Working Points

Considering the analysis identification and isolation requirements for electrons, four categories are defined, *Loose*, *ZH-Signal*, *WH-Signal* and *LH-Signal*. The definitions of the requirements for each category are summarised in Table 3.2, and are used in the analyses described in Chapters 6 and 7.

Electron Selection	p_{T}	Identification Quality	Isolation
Loose	> 7 GeV	*ID-Loose*	*Loose-Track*
ZH-Signal	> 27 GeV	*ID-Loose*	*Loose-Track*
WH-Signal	> 27 GeV	*ID-Tight*	*HighPt-Calo*
LH-Signal	> 27 GeV	*ID-Medium*	*Tight-Track*

Table 3.2: Summary of electron selection requirements.

3.5.3 Muons

3.5.3.1 Reconstruction

Muons are reconstructed offline using tracks in the inner detector (ID) and muon spectrometer (MS) [42,43]. Muon track candidates are first reconstructed in the MS. A χ^2 fit is used to reconstruct tracks from hits in the MS, with tracks failing a given quality criteria rejected. Tracks are also independently reconstructed in the ID, and a combined track is generated using a fit to hits in both the MS and ID.

Similarly to the offline electron reconstruction, muons are required to be consistent with the primary vertex, by also requiring $|d_0|/\sigma_{d_0} < 3$ and $|\Delta z_0 \sin\theta| < 0.5$ mm. Due to the tracking acceptance, muons are only considered for $|\eta| < 2.5$.

In the reconstruction of a muon, it is possible for a physics process to fake the presence of a prompt muon. Faked prompt muons can arise from a number of different sources:

- A charged hadron punching through the hadronic calorimeter, which is subsequently detected in the muon system.
- A muon from the inflight decay of a hadron (pion, kaon).
- The semi-leptonic decay of a heavy flavour hadron.

In the following sections, muon identification and isolation criteria designed to reduce the number of faked prompt muons are discussed.

3.5.3.2 Identification

Muons originating from in-flight decays of hadrons will have a deflection in their flight path by virtue of the displaced decay. It is therefore expected that muons originating from such sources will have a worse fit quality of the combined track between the ID and MS, compared to a prompt muon. To identify true signal muons, variables such as *q/p significance*[1] and the χ^2 of the fit are used to discriminate from background candidates in addition to requirements on the number of ID and MS hits.

Four muon quality working points are defined using differing cuts on these variables; *ID-Loose*, *ID-Medium*, *ID-Tight* and *ID-High-*p_T. *ID-Loose* offers the best muon reconstruction efficiency, whilst *ID-Tight* offers the best muon purity. *ID-High-*p_T offers the best muon resolution at high p_{T} (muons with $p_{\mathrm{T}} > 100$ GeV). For a muon in the range $20 < p_{\mathrm{T}} < 100$ GeV, the *ID-Loose*, *ID-Medium* and *ID-Tight* working points offer prompt muon identification efficiencies of 98.1%, 96.1% and 91.8%, with non-prompt (in-flight) muon rejection efficiencies of 99.2%, 99.8% and 99.9%, respectively.

3.5.3.3 Isolation

Similarly to electrons, prompt muons are expected to be isolated from other particles. Three muon isolation variables are defined:

---

[1] *q/p significance*: absolute value of the difference in the ratio of the charge and momentum of the muon candidate as measured in the ID and MS, divided by their uncertainty.

- **Calorimeter isolation**: $p_{\mathrm{T}}^{\mathrm{cone20}}$ is defined as the sum of the transverse momentum of topological clusters within a cone of radius $\Delta R = 0.2$ from the candidate muon.
- **Variable radius track isolation**: $p_{\mathrm{T}}^{\mathrm{varcone30}}$ is defined as the sum of the transverse momentum of all tracks within a cone of $\Delta R = \min(0.3, 10\ \mathrm{GeV}/p_{\mathrm{T}})$ around the candidate muon track, meeting set quality requirement, where p_{T} refers to the muon's transverse momentum.
- **Fixed radius track isolation**: $p_{\mathrm{T}}^{\mathrm{cone20}}$ is defined as the sum of the transverse momentum of all tracks within a cone of $\Delta R = 0.2$ around the candidate muon track, meeting set quality requirements.

A number of isolation working points are defined using the calorimeter and track isolation variables. In several cases, the ratio of the isolation variable to the lepton p_{T} is used as the discriminating variable to improve performance over the full p_{T} spectrum. Three relevant working points are:

- *Loose-Track* requires a varying cut on $p_{\mathrm{T}}^{\mathrm{varcone0.2}}/p_{\mathrm{T}}$, and provides a 99% efficiency for prompt muons across the full muon p_{T} range.
- *Tight-Track* requires $p_{\mathrm{T}}^{\mathrm{varcone0.3}}/p_{\mathrm{T}} < 0.06$, and has a prompt muon efficiency of $\sim 99\%$, whilst rejecting $\sim 5\%$ of all non-prompt muons (dependent on muon p_{T} and η).
- *HighPt-Track* requires $p_{\mathrm{T}}^{\mathrm{cone20}} < 1.25$ GeV, and has a prompt muon efficiency of $\sim 95\%$, whilst rejecting $\sim 70\%$ of all non-prompt muons (dependent on muon p_{T} and η).

The *HighPt-Track* isolation working point was studied and implemented with the aim of reducing multijet contamination in the SM $VH \to Vb\bar{b}$ analysis. The use of this new isolation working point required the development of a new MC-to-data isolation scale factor. The measurement of the isolation scale factor is discussed in more detail in Chapter 4.

3.5.3.4 Simulation Correction Factors

Monte Carlo samples are reweighted applied to correct for imperfect detector simulation and physics modelling for the muon energy scale, reconstruction, identification, isolation and trigger efficiencies. These are evaluated using a Tag-and-Probe method on $Z \to \mu\mu$ and $J/\psi \to \mu\mu$ events [43]. Each of these corrections introduces systematic uncertainties, and are considered in the analyses presented in this thesis.

3.5.3.5 Combined Working Points

Considering the identification and isolation requirements of muons, four categories are defined, *Loose*, *ZH-Signal*, *WH-Signal* and *LH-Signal*. The definitions of the requirements for each category are summarised in Table 3.3, and are used in the analyses described in Chapters 6 and 7.

Muon Selection	p_{T}	Identification Quality	Isolation
Loose	> 7 GeV	*ID-Loose*	*Loose-Track*
ZH-Signal	> 27 GeV	*ID-Loose*	*Loose-Track*
WH-Signal	> 25 GeV	*ID-Medium*	*HighPt-Track*
LH-Signal	> 27 GeV	*ID-Loose*	*Tight-Track*

Table 3.3: Summary of muon selection requirements.

3.5.4 Jets

3.5.4.1 Reconstruction

Topological clusters of energy deposits in calorimeter cells, calibrated to the electromagnetic scale, are formed by considering the energy significance of the energy deposited in a cell, S_{cell} [44], defined as

$$S_{\mathrm{cell}} = \frac{E_{\mathrm{cell}}}{\sigma_{\mathrm{noise,cell}}}, \tag{3.10}$$

where E_{cell} is the energy deposited and $\sigma_{\mathrm{noise,cell}}$ is the background noise level of a cell (where many sources, such as pile-up and electronic noise are considered). Three threshold parameters are defined:

- Seed threshold, $S_{\mathrm{cell}} > 4$.
- Neighbour threshold, $S_{\mathrm{cell}} > 2$.
- Principle cell filter, $S_{\mathrm{cell}} > 0$.

Topological clusters are seeded from cells that pass the seed threshold requirement, with neighbouring cells added which satisfy the neighbour or principle cell filter requirements, stopping when the last set of cells matches only the principle cell filter threshold.

Calorimeter jets are reconstructed by clustering topological clusters in the calorimeter using the *anti-k_t* jet clustering algorithm [45]. Firstly, two distance measures are defined

$$d_{ij} = \min(k_{Ti}^{2p}, k_{Tj}^{2p}) \frac{\Delta_{ij}^2}{R^2}, \tag{3.11}$$

$$d_{iB} = k_{Ti}^{2p}, \tag{3.12}$$

where k_{Ti} is the transverse momentum of cluster i, $\Delta_{ij}^2 = (y_i - y_j)^2 + (\phi_i - \phi_j)^2$, and p is a parameter set by the choice of algorithm. In the case of the *anti-k_t* algorithm, $p = -1$. The distance parameter, R, is an option of the algorithm, and is related to the radius of the jet. The parameter

d_{ij} can be interpreted as the distance between two clusters i, j, whilst d_{iB} is interpreted as the distance between a cluster i and the beam. The jet clustering algorithm is an iterative procedure.

1. Compute all distances d_{ij} and d_{iB}.
2. Find the smallest distance.
3. If the smallest distance is d_{ij}, combine the four momentum of i and j.
4. Else if smallest distance is d_{iB}, remove i and call it a “jet”.
5. Repeat until all topological clusters are clustered into jets.

In all studies presented, jets are clustered using a radius parameter of $R = 0.4$.

3.5.4.2 Jet Calibration

As discussed in Section 3.2.3, the response of the electromagnetic and hadronic calorimeters is very different. Due to the non-compensating nature of the ATLAS calorimeters, the electromagnetic detector response is not equivalent to the hadronic response. The jet energy scale (JES) is applied to reach the energy of a truth jet at the hadronic particle scale [46,47]. Jets are calibrated from the electromagnetic (EM) scale to the jet energy scale using a series of steps, correcting for a number of effects.

- The jet direction is corrected such that it points to the primary vertex.
- Pile-up effects are corrected by subtracting an average pile-up density term from the jet.
- The jet energy scale, derived from MC simulation, is applied to correct the jet energy from the EM scale to the true jet energy.
- In-situ corrections are used to account for differences between data and MC. This is evaluated using well understood physics processes. In $\gamma/Z+$jet events, the energy of the recoiling jet is determined by balancing the decay of the well understood γ or Z. The $Z+$jet balance is used to calibrate jets with $20 < p_{\mathrm{T}} < 500$ GeV, whilst the $\gamma+$jet balance is used to calibrate jets with $36 < p_{\mathrm{T}} < 950$ GeV. In order to calibrate jets above 950 GeV, a multijet balance technique is used up to $p_{\mathrm{T}} < 2$ TeV. In the multijet balance, a single high p_{T} jet is balanced against several low p_{T} jets (where the calibration of these jets has previously been determined using the $\gamma/Z+$jet balance techniques).

3.5.4.3 Systematic Uncertainties

Systematic uncertainties from the jet energy calibration arise mostly from the in-situ calibration, with sources due to the MC modelling, assumptions in the $\gamma/Z/$multijet $+$ jet event topology, and the electron, muon and photon scale uncertainties. Additional systematic uncertainties arise from pile-up effects, the jet energy scale dependence on η, and jet flavour composition are considered as part of the JES uncertainty [47]. An additional systematic uncertainty on the jet energy resolution (JER) is evaluated using a dijet balance technique [48].

3.5.4.4 Pile-up Rejection

During 2015 and 2016 data-taking, as discussed in Section 3.4, there was a mean of approximately 20 interactions per bunch crossing. There is therefore potentially a large contamination from non-hard scatter pile-up interactions. The energy deposits from these pile-up interactions in the calorimeters can be reconstructed into jets, and should be excluded from further analysis. Using a multivariate combination of jet variables, the jet vertex tagger (JVT) algorithm is used to reject low p_{T} pile-up jets [49]. The JVT selection implemented in the work presented in this thesis is 92% efficient for hard scatter jets, with a 2% fake rate from pile-up jets.

3.5.4.5 Truth Flavour Labelling

It is useful to define the flavour of the quarks from which the jet was initiated. A flavour labelling scheme is implemented where truth hadrons are assigned to jets using exclusive ΔR matching. Final state hadrons with $p_{\mathrm{T}} > 5$ GeV and within $\Delta R < 0.3$ of the jet axis are assigned to each jet. As the labelling is exclusive, each hadron is matched to only one jet, selecting the closest jet in ΔR space. The truth jet flavour is assigned using an iterative procedure:

- If a truth b-hadron is matched to the jet, the jet is labelled a b-jet.
- If a truth c-hadron is matched to the jet, and no b-hadron, the jet is labelled a c-jet.
- Else the jet is labelled as a light-flavour jet.

A heavy flavour jet/hadron is one containing a b- or c-quark.

3.5.5 Missing Transverse Momentum

From the conservation of momentum, the vectorial sum of the momentum in the transverse plane of the detector should sum to zero. The imbalance of momentum in this plane is known as missing transverse momentum, and can arise from neutrinos, detector acceptance effects, mis-measured or unreconstructed objects. The missing transverse momentum is calculated as

$$E^{\mathrm{miss}}_{x(y)} = E^{\mathrm{miss},\ e}_{x(y)} + E^{\mathrm{miss},\ \gamma}_{x(y)} + E^{\mathrm{miss},\ \tau}_{x(y)} + E^{\mathrm{miss},\ \mathrm{jets}}_{x(y)} + E^{\mathrm{miss},\ \mu}_{x(y)} + E^{\mathrm{miss},\ \mathrm{soft}}_{x(y)}, \tag{3.13}$$

where $E^{\mathrm{miss},\ \mathrm{object}}_{x(y)}$ is the x (y) component of the negative vectorial sum of the momentum of all reconstructed objects (electrons, photons, taus, jets and muons). $E^{\mathrm{miss},\ \mathrm{soft}}_{x(y)}$ is the vectorial sum of all remaining detector objects not passing the selection of the main physics objects, such as low momentum tracks in the inner detector, or calorimeter deposits not associated to hard objects [50, 51]. The missing transverse momentum is given by

$$E_{\mathrm{T}}^{\mathrm{miss}} = \sqrt{(E_x^{\mathrm{miss}})^2 + (E_y^{\mathrm{miss}})^2}. \tag{3.14}$$

3.5.6 Overlap Removal

In the offline reconstruction of objects, it is possible that a detector response may be reconstructed as multiple objects. In order to remove this double counting, a procedure known as "overlap removal" is applied, with the aim of correctly identifying the true physics object. The following algorithm is implemented, where all physics objects used are fully reconstructed and calibrated [52].

- **Electron-muon:** If a muon shares an ID track with an electron, the electron is removed (an electron can be reconstructed if a muon radiates a photon).
- **Jet-electron:** If $\Delta R(e, \mathrm{jet}) < 0.2$, the jet is removed (a jet and an electron will result from clustering an electron's calorimeter energy deposits).
- **Electron-jet:** If $\Delta R(e, \mathrm{jet}) < \min(0.4, 0.04 + 10\ \mathrm{GeV}/p_{\mathrm{T}}^{e})$, the electron is removed (the electron is likely to have originated from a semi-leptonic heavy-flavour hadron decay). The p_{T}^{e} dependence reduces the removal of prompt electrons from nearby high-p_{T} jets.
- **Jet-muon:** If $\Delta R(\mu, \mathrm{jet}) < 0.2$, and the jet has fewer than three tracks, or the muon constitutes more than half of the energy of the jet, the jet is removed (the jet is likely to have originated from bremsstrahlung or radiation effects).
- **Muon-jet:** If $\Delta R(\mu, \mathrm{jet}) < \min(0.4, 0.04 + 10\ \mathrm{GeV}/p_{\mathrm{T}}^{\mu})$, the muon is used to correct the jet energy and removed (the muon is likely to have originated from a semi-leptonic heavy-flavour hadron decay). The p_{T}^{μ} dependence reduces the removal of prompt electrons from nearby high-p_{T} jets.

3.6 Multivariate Algorithms

The work presented in this thesis includes extensive use of multivariate algorithms. An overview of these algorithms is presented in this section. A particular focus is given to Boosted Decision Trees (BDT), as these are used in a number of cases.

When classifying events as corresponding to signal or background processes, selection cuts can be applied to boost the ratio of signal to background events. By cutting on a number of weakly correlated variables, it is possible to increase the signal purity, and reject a larger portion of the background contamination. In a simple cut-based approach, cuts can be optimised manually for a number of variables to give the best signal separation. The idea behind multivariate algorithms is that multiple selections can be optimised for a large number of input variables in a more sophisticated manner than a simple cut-based approach, offering significantly better performance. An algorithm used in two instances in this thesis, Boosted Decision Trees, is discussed below [53].

3.6.1 Boosted Decision Trees

3.6.1.1 Decision Trees

A decision tree is a simple predictive model, used to classify events based on known properties of the event. A simple example is presented in Figure 3.5. Consider an event E_i, with variables $(\mathbf{x}, Y) = (x_1, x_2, \ldots, x_n, Y)$, where $\mathbf{x}$ is the vector of known variables used for classification, and Y is the target variable, which is to be predicted. Starting from the root node, an event is classified depending on whether it passes or fails the cut $x_i > c_i$, with c_i a constant. At each subsequent layer of the tree, the process is repeated, until a leaf is reached. An event is designated as "signal" (S) or "background" (B) depending on the leaf into which it is categorised. The exact details of the variables x_i, and the other criteria are described for each specific analysis in Chapters 6 and 7.

3.6.1.2 Tree Construction

In order to construct a decision tree, at each node, the optimal cut which gives the best separation must be determined. There are a number of different procedures for determining this, with the Gini index being commonly used [53]. The Gini index is defined as

$$\text{Gini} = \left(\sum_{i=1}^{N} W_i \right) p(1-p), \tag{3.15}$$

where p is the signal purity, $n_s/(n_s + n_b)$, with $n_{s(b)}$ the sum of weight of signal (background) events. W_i is the weight for event i, of the total set of N events. Events are initially normalised such that the sum of the event weights is 1. The separation gain, G, achieved by a cut is defined as

$$G = \text{Gini}_{\text{parent}} - \text{Gini}_{\text{daughter, 1}} - \text{Gini}_{\text{daughter, 2}}, \tag{3.16}$$

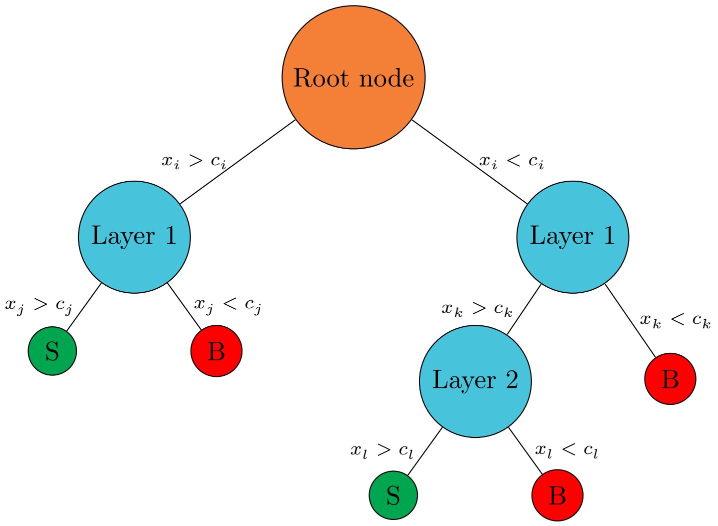

Figure 3.5: Example of a decision tree of depth 3. The "Root Node" (orange) is the initial input node, with each subsequent node (blue) labelled with the corresponding layer of the decision tree. Output leaves are denoted "S" for signal-like events (green), and "B" for background-like events (red).

where $\text{Gini}_{\text{parent}}$ is the Gini of the input node, and $\text{Gini}_{\text{daughter, 1(2)}}$ is the Gini of the two output nodes. Larger G values correspond to a greater improvement in the signal purity.

At each node, a scan of cuts is conducted for all variables, $\mathbf{x}$, with the variable and cut resulting in the largest G selected.

The growth of a node is terminated when any one of the conditions are met:

- Minimum Node Size - The number of events in a node is below a threshold, e.g. 5% of the initial number of starting events.
- Max Depth - The subsequent nodes would exceed the maximum allowed tree depth. Figure 3.5 illustrates an example decision tree with depth 3.
- Gain - The maximal G from adding an additional layer is less than 0.

If more than one half of the sum of weights on a terminating leaf corresponds to signal, the leaf is labelled a signal leaf, otherwise it is labelled a background leaf.

3.6.1.3 Boosting and Decision Forests

Whilst a decision tree provides a method for categorising data which is relatively straightforward and understandable, a single tree is highly susceptible to statistical fluctuations in the training set. A solution to this is to construct a forest of trees. Instead of using the output of a single decision tree, the outputs of all trees in the forest are averaged to give the event classification. In the simplest case, the training sample is split into n sets of random subsamples. For each subsample, a decision tree is trained, and used to construct the decision forest. Whilst individual trees will suffer from statistical fluctuations, the averaging of the trees is designed to smooth these fluctuations.

However, the procedure of randomly splitting the training set can be modified to improve the separating power of the forest. Instead of splitting the training sample, the full sample is used to train a decision tree. Misclassified events are reweighted, increasing their importance in the training. A decision tree is produced using the reweighted events, and added to the forest. This procedure is repeated, until the desired number of trees is reached.

The reweighting of events is calculated using the AdaBoost (adaptive boost) algorithm [54]. For a tree m, define

$$f_m = \frac{\sum_{Y_i \neq T_m(x_i)} W_i}{\sum_{\text{events}} W_i}, \tag{3.17}$$

where W_i is the weight of event i, Y_i is the true classification of event i ($+1$ if signal, -1 if background), $T_m(x_i)$ is the tree classification of event i ($+1$ if signal leaf, -1 if background leaf) and f_m corresponds to the total weight fraction of misclassified events by tree m. The score, α_m, is defined as

$$\alpha_m = \beta \log\left(\frac{1 - f_m}{f_m}\right), \tag{3.18}$$

with β a constant, referred to as AdaBoost beta, and can be considered as the learning rate of the forest, between 0 and 1. If the learning rate is too large, then the optimal solution may be over-shot, whilst if it is too small, the learning takes longer to converge on the optimal solution. Misclassified events are reweighted according to

$$W_i \rightarrow W_i e^{\alpha_m}, \tag{3.19}$$

and all events are renormalised to unity. A decision tree is then retrained using the updated training set, and added to the forest. The processes is repeated, where at each stage the misclassified events are reweighted according to the output of the previous tree.

The final classification output score is given by the weighted average output of all trees in the forest,

$$T(x_i) = \sum_{m=1}^{\text{NTrees}} \alpha_m T_m(x_i). \tag{3.20}$$

3.6.2 k-Fold Cross-Validation

A 2-fold cross-validation approach is used for the training and implementation of the BDT to maximise the use of the limited number of simulated events, whilst avoiding any possible training bias. Two orthogonal training sets are used, yielding two MVAs; one trained on events with only even event numbers, and one trained on events with only odd event numbers. The trainings are applied to the opposite subsets, such that the training and testing sets are fully orthogonal. This prevents possible overtraining biases when evaluating the performance of an MVA, as independent events are used for the training and statistical analysis.

Depending on the available number of training events, it is possible to use higher order cross-validation. If the number of available training events is very low, the extreme case with an $(N-1)$-fold (with N the number of training events) can be applied such that each training has a maximal number of training events. However, this comes at the cost of running N trainings and an increase in complexity. In all MVA trainings studied, a sufficient number of simulated MC events are available such that it is possible to use a 2-fold cross-validation without any loss of sensitivity.

Chapter 4

Muon Isolation Scale Factors

The use of isolation requirements, described in Sections 3.5.2 and 3.5.3, to reject fake leptons means that simulation to data scale factors need to be introduced to correct for possible mismodelling in the simulation that could result in a bias [43]. For the Run-2 version of the $VH \rightarrow Vb\bar{b}$ analysis, a new muon isolation working point, *HighPt-Track*, has been introduced to reduce the level of multijet contamination in the single muon sub-channel. New isolation scale factors and scale factor uncertainties must therefore be calculated for this working point of the form

$$\mathrm{SF}_{\mathrm{I}} = \frac{\varepsilon^{\mathrm{data}}}{\varepsilon^{\mathrm{MC}}}, \tag{4.1}$$

where $\varepsilon^{\mathrm{data(MC)}}$ is the efficiency of a muon to pass the isolation requirement, as measured in data (MC). SF_{I} can be evaluated as a function of a number of different muon variables, but in this case, the dependence on muon p_{T} and muon η is found to be sufficient to provide good closure between MC and data. The isolation efficiency in data is evaluated using a Tag-and-Probe method on $Z \rightarrow \mu\mu$ events.

4.1 Tag-and-Probe Method: Event Selection and Systematic Uncertainties

The Tag-and-Probe method aims to create a sample of events pure in muons from which the isolation efficiency in data can be extracted. Events containing two *ID-Medium* opposite charge muons with an invariant mass consistent with the Z mass are selected. Both muons are also required to be separated by $\Delta R(\mu, \mu) > 0.3$, and to have $\Delta R(\mu, \mathrm{jet}) > 0.4$ to avoid overlap between jets and muons. The tag muon is required to pass the *Loose-Track* isolation working point. The isolation efficiency of the chosen working point is extracted from measuring the efficiency of passing the isolation cut on the "probe" muon. Results are presented for the *HighPt-Track* isolation working point, as implemented in the $VH \rightarrow Vb\bar{b}$ analysis. However, the same method is used to derive the isolation efficiency in data for all other muon isolation working points.

The event selection yields a sample which is $\sim 99.9\%$ pure in $Z \to \mu\mu$ events [43]. To estimate the background contamination from $W+$jets processes and non-prompt muons from multijet events, a background model is generated assuming that the background contamination is equal in same charge and opposite charge events. Using this assumption, the background contamination model is estimated from same charge events in data, which pass the event selection, with same sign simulated $Z \to \mu\mu$ events subtracted from the estimate to account for sign flip errors,

$$N^{\mathrm{Bkg}} = T \times (N_{\mathrm{SC}}^{\mathrm{Data}} - N_{\mathrm{SC}}^{\mathrm{MC}}), \tag{4.2}$$

where $N_{\mathrm{SC}}^{\mathrm{Data(MC)}}$ is the number of same charge data (MC) events, N^{Bkg} is the total yield of background events and T is the transfer function from the same charge to opposite charge region. For the nominal case, this is 1.0, but is scaled to 0.5 and 2.0 in order to consider systematic uncertainties arising from this assumption. The efficiency in data is measured as

$$\varepsilon^{\mathrm{Data}} = \frac{N_{\mathrm{R}}^{\mathrm{Data}} - N_{\mathrm{R}}^{\mathrm{Bkg}}}{N_{\mathrm{P}}^{\mathrm{Data}} - N_{\mathrm{P}}^{\mathrm{Bkg}}}, \tag{4.3}$$

where N_{P} is the total number of probe muons, and N_{R} is the number of probe muons passing the isolation requirement.

Systematic uncertainties are evaluated by altering the event selection, aiming to determine the impact of the various selection cuts. After modifying the selection, the new isolation scale factors are calculated, and their differences are added in quadrature to estimate the total uncertainty.

A summary of the event selection and systematic uncertainties is presented in Table 4.1.

Variation	Nominal	Up	Down
Z mass ($m_{\ell\ell}$) window	$81 < m_{\ell\ell} < 101$ GeV	$86 < m_{\ell\ell} < 96$ GeV	$71 < m_{\ell\ell} < 111$ GeV
Tag isolation	*Loose-Track*	All supported isolation WPs	
Background subtraction	×1.0	×2.0	×0.5
Probe muon quality	*ID-Medium*	*ID-Tight*	*ID-Loose*
ΔR(probe,jet)	> 0.4	> 0.5	> 0.3
ΔR(probe,tag)	> 0.3	> 0.5	> 0.5
Number of vertices	> 0	< 15	≥ 15

Table 4.1: Event selection and systematic uncertainties implemented in the evaluation of the muon isolation scale factors. All the supported isolation working points (WPs) are defined in Ref. [43].

4.2 Results

Due to the dependence of the isolation efficiency on both muon p_{T} and muon η, scale factors are derived as a 2D function. Figure 4.1 presents the 2D scale factors, and their total uncertainty. Figure 4.2 compares the modelling of MC before and after the correcting for the muon isolation scale factor in 1D distributions of p_{T} and η. Good closure is seen when applying the isolation scale factors. The total scale factor uncertainty is dominated by background modelling effects for muon $p_{\mathrm{T}} < 10$ GeV, and the variation in the number of vertices for the rest of the muon p_{T} spectrum.

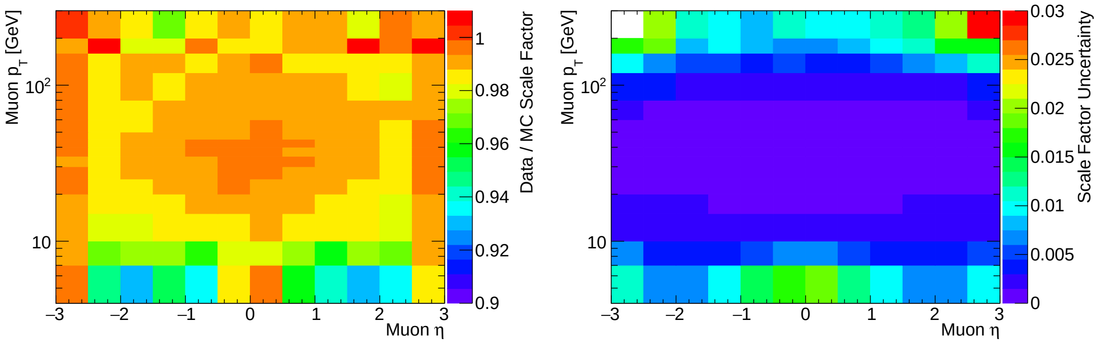

(a) **(b)**

Figure 4.1: Ratio of *HighPt-Track* muon isolation efficiency in data to MC as a function of muon p_{T} and η (a). Total uncertainty on the *HighPt-Track* muon isolation efficiency scale factor as a function of muon p_{T} and η (b).

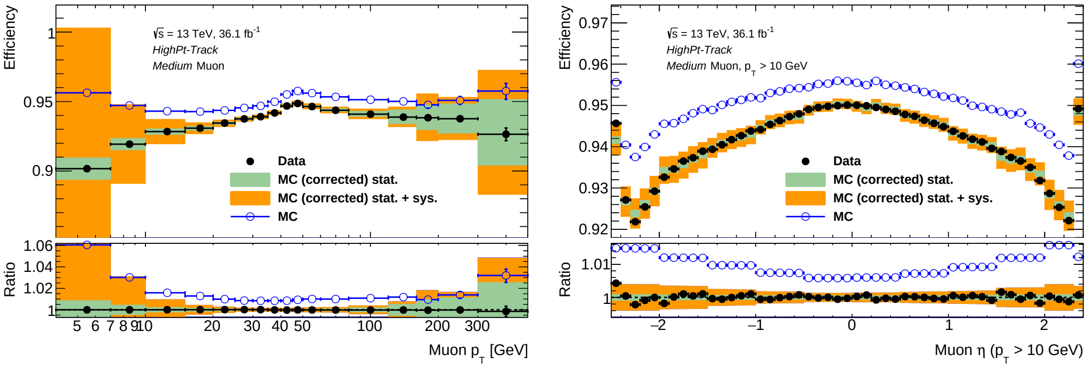

(a) **(b)**

Figure 4.2: Isolation efficiencies in data (black) and MC (blue) for the *HighPt-Track* muon isolation working point. The corrected MC after applying isolation scale factors with statistical only errors are shown in green, and the combined statistical and systematic error band is shown in orange. The bottom pad shows the ratio of the muon isolation efficiency in MC and data to the corrected MC. These are presented as a function of muon p_{T} (a) and muon η (b).

Chapter 5

b-Tagging

5.1 Overview

Identifying jets containing a b-quark, commonly referred to as b-tagging, is vital for a number of physics analyses, such as top studies[1], Higgs boson studies, SM precision measurements and new physics searches.

Three baseline b-tagging algorithms are used within ATLAS for Run-2 of the LHC. The performance of each of these algorithms is studied in Section 5.2, along with the performance of multivariate tagging algorithms, which combine these baseline algorithms to improve background rejection, in Section 5.3. Due to the similarities in the lifetime and decay of c-hadrons to b-hadrons, c-jets are categorised separately from light-flavour jets. Specific algorithmic and training considerations are used to further boost the c-jet rejection, as discussed in Section 5.3.

All performance plots in this section are produced from simulated $t\bar{t}$ events at $\sqrt{s} = 13$ TeV. Powheg [55] interfaced with Pythia6 [56] are used to simulate the hard scatter, hadronisation and fragmentation, using CT10 PDFs [57]. EvtGen is used to decay heavy flavour hadrons, which uses updated lifetime and decay tables to improve the modelling [58]. Only $t\bar{t}$ events where at least one of the subsequent W bosons decays leptonically are considered. Minimum bias interactions are generated with Pythia8 [59], and overlaid on each event. The propagation of the particles is carried out with a full simulation of the ATLAS detector using GEANT4 [60].

---

[1] $Br(t \to Wb) \sim 1.00$ by virtue of the fact that $|V_{tb}| \sim 1.00$ [6].

5.1.1 Performance of *b*-Tagging Algorithms

In order to numerically evaluate the performance of a b-tagging algorithm, the efficiency of an algorithm to select jets of flavour j is defined as

$$\varepsilon_j = \frac{\text{Number of jets of flavour } j \text{ passing cut}}{\text{Number of jets of flavour } j}, \tag{5.1}$$

with the rejection defined as $1/\varepsilon_j$. Working points for a specific b-tagging algorithm are defined by a particular selection, designed to provide a pre-defined b-jet tagging efficiency, as measured in the Powheg+Pythia6 $t\bar{t}$ sample. The performance of two or more b-tagging algorithms can be compared at a chosen working point by comparing the corresponding c- and light-flavour jet rejection. An algorithm with increased background rejection at the chosen working point, compared to another algorithm, has the better performance. Definitions of the supported working points, and their corresponding performance, used for 2015 and 2016 data-taking by ATLAS are described in more detail in Section 5.5.

Due to imperfect event modelling and simulation, it is useful to define working points such that the performance of the b-tagging algorithm in simulation can be measured in data for the specific working point, and is used to "calibrate" the MC, as discussed in more detail in Chapter 6.

5.2 Baseline *b*-Tagging Algorithms

The presence of a b-hadron can be identified in a variety of ways, but a commonly exploited property is the longer lifetime of hadrons containing a b-quark compared to other hadrons (~ 1.5 ps) [6]. For example, given a b-hadron mass of ~ 5 GeV, and momentum 50 GeV, the b-hadron will have an average decay length of ~ 5 mm, making it possible to resolve a secondary vertex from tracks recorded by the inner detector. Additional discriminating properties include the large mass of b-hadrons, large number of tracks displaced from the primary vertex, and the large momentum fraction carried by b-hadrons. In this section, algorithms designed to exploit these properties are described.

Tracks from charged particles reconstructed by the inner detector are associated to a jet based on their angular separation, ΔR(track,jet). The ΔR requirement is defined as a function of jet p_{T} in order to account for the b-hadron decay products in higher p_{T} jets becoming more collimated. Applying a varying selection reduces the contamination of tracks which do not originate from the b-hadron decay, e.g. pile-up, fragmentation or the underlying event, whilst ensuring that tracks from the b-hadron decay are associated with a high efficiency.

Tracks can only be associated to one jet, and in the case that a track can be associated to more than one jet, it is associated to the jet closest in ΔR space. Tracks are also required to pass set quality requirements, dependent on the specific b-tagging algorithm [1].

A schematic diagram of a *b*-jet is presented in Figure 5.1, with the key properties used for *b*-tagging highlighted. Each of these properties and their importance are described in Sections 5.2.1 – 5.2.3.

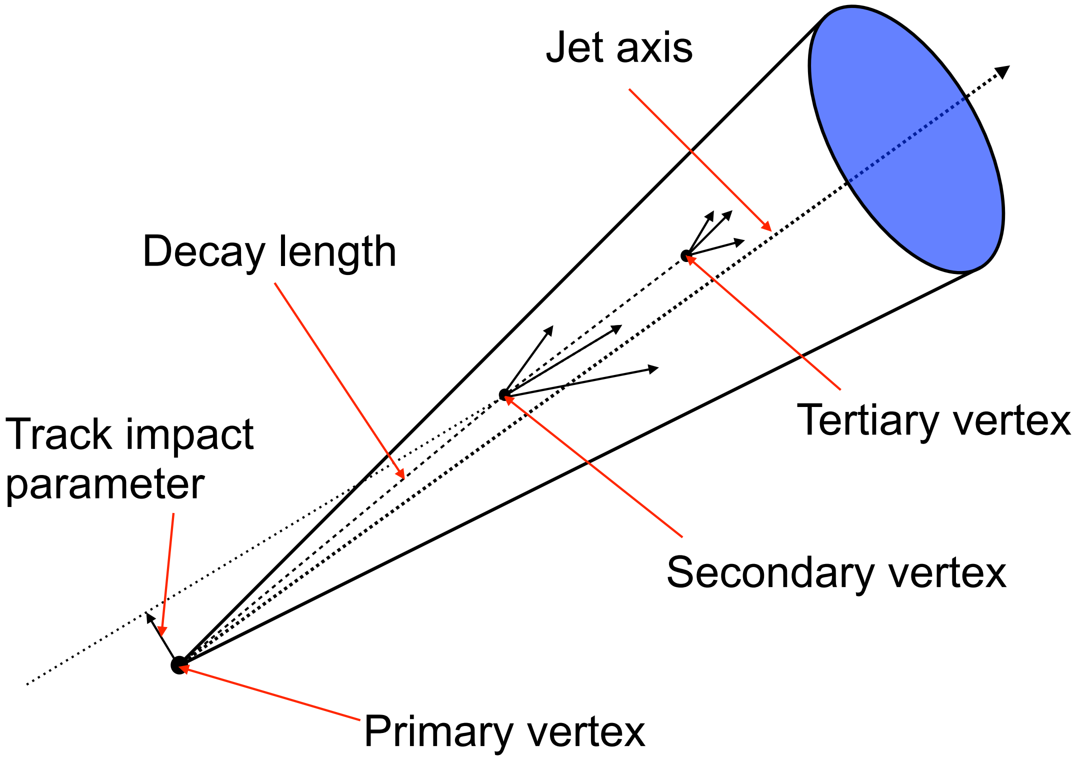

Figure 5.1: Schematic view of a *b*-hadron decay inside a jet, which results in a secondary vertex with three charged particle tracks, and a tertiary vertex with three charged particle tracks from the subsequent decay of a *c*-hadron. The secondary vertex is significantly displaced with respect to the primary vertex, thus making the decay length measurable. The track impact parameter, which is the distance of closest approach between the track and the primary vertex, is shown for one of the secondary tracks.

5.2.1 Impact Parameter Tagging Algorithms

The impact parameter of a track is defined as its point of closest approach to the primary vertex. The transverse impact parameter, d_0, is the impact parameter in the $r - \phi$ projection. The longitudinal impact parameter, z_0, is the impact parameter in the z direction. Assuming that the b-hadron decays along its flight path, impact parameters are signed, such that if the track crosses the jet direction in front of the primary vertex, it is positive, otherwise, it is assigned a negative impact parameter. The transverse and longitudinal impact parameter significances are defined as d_0/σ_{d_0} and z_0/σ_{z_0} respectively, where σ_{d_0} is the uncertainty on d_0, and σ_{z_0} is the uncertainty on z_0. Distributions of these variables are presented in Figure 5.2 for b-, c- and light-flavoured jets, where tracks originating from b-jets have a higher average decay length significance than c- and light-flavour jets. As both b- and c-jets have real displaced tracks, if the sign of the impact parameter is incorrectly assigned, this can still lead to discrimination from light-flavour jets.

The IPxD taggers use smoothed and normalised distributions of the d_0/σ_{d_0} and z_0/σ_{z_0} track parameters associated to the jet as probability distribution functions (PDFs) (with separate PDFs for b-, c- and light-flavour jets). The PDFs are used to evaluate a log-likelihood ratio (LLR) for each jet flavour combination. To simplify the procedure, it is assumed that the track impact parameters are uncorrelated. Equation 5.2 illustrates the LLR for the probability, $P_{i(j)}$, of a jet to have flavour i (j) $(i, j \in b, c, \text{light-flavour})$, and is applicable to all jet flavour combinations [61],

$$\log(P_i/P_j) = \log\left(\frac{\prod_{m=1}^{N} PDF_i(IP_m)}{\prod_{m=1}^{N} PDF_j(IP_m)}\right), \tag{5.2}$$

where IP_m is the impact parameter significance of track m, with N tracks in total associated to the jet. $PDF_{i(j)}$ is the 2D or 1D probability density function for a track from a jet of flavour i (j), and is defined as

$$PDF_{i(j)}(IP_m) = \begin{cases} PDF_{i(j)}(d_0/\sigma_{d_0}, z_0/\sigma_{z_0}), & \text{IP3D} \\ PDF_{i(j)}(d_0/\sigma_{d_0}), & \text{IP2D} \end{cases}, \tag{5.3}$$

highlighting the separate case of the IP3D tagger which uses both transverse and longitudinal impact parameters, while IP2D uses just the transverse impact parameter. The output of the LLR in Equation 5.2 provides discrimination between b-, c- and light-flavour jets, with the discriminating LLRs summarised in Table 5.1.

Additionally, the LLR allows for the use of different PDFs sets based on specific track criteria. This further boosts the separation power by utilising PDF sets for various categories of tracks [1].

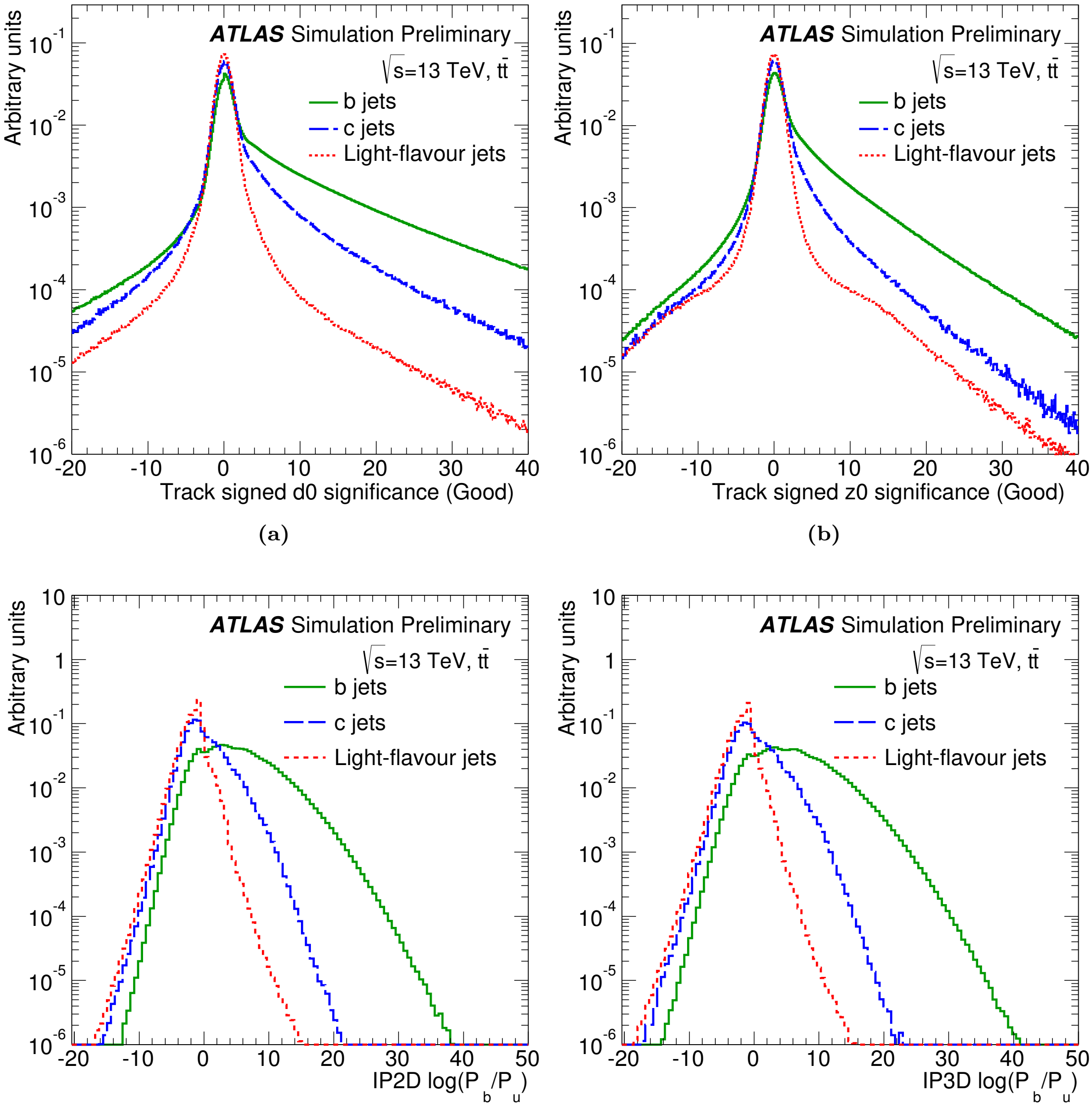

(a) **(b)**

(c) **(d)**

Figure 5.2: Track signed d_0 significance (a), z_0 significance (b), IP2D log-likelihood ratio (c) and IP3D log-likelihood ratio (d) for *b*- (solid green), *c*- (dashed blue) and light-flavour (dotted red) jets in a simulated $t\bar{t}$ sample at $\sqrt{s} = 13$ TeV [1]. The IPxD light-flavour jet probability is denoted by $\mathrm{P_u}$.

Variable	Description
$\log(P_b/P_{\text{light}})$	Likelihood ratio between the *b*- and light-flavour jet hypotheses
$\log(P_b/P_c)$	Likelihood ratio between the *b*- and *c*-jet hypotheses
$\log(P_c/P_{\text{light}})$	Likelihood ratio between the *c*- and light-flavour jet hypotheses

Table 5.1: Output variables from the IPxD algorithms.

5.2.2 Inclusive Secondary Vertex Tagging Algorithms

Inclusive secondary vertex (SV) tagging algorithms aim to reconstruct the secondary decay point [61]. Firstly, two track vertices are constructed using all selected tracks associated to a jet. Two track vertices consistent with decays originating from long lived light-flavoured hadrons, such as Λ or K_S, or detector interactions are rejected. A single vertex is constructed using the tracks from the 2-track vertices. An iterative procedure is then applied to remove the least compatible track, until the χ^2 of the vertex fit passes a suitable quality cut.

Properties of the reconstructed secondary vertex which provide discrimination between b-jets and jets of other flavours are summarised in Table 5.2. Figure 5.3 presents a number of these variables for b-, c- and light-flavour jets.

Variable	Description
$m(SV)$	Invariant mass of all tracks associated to the secondary vertex
$f_{\mathrm{E}}(SV)$	Fraction of energy in secondary vertex tracks, relative to all tracks associated to jet
$N_{\mathrm{TrkAtVtx}}(SV)$	Number of tracks associated to the secondary vertex
$N_{\mathrm{2TrkVtx}}(SV)$	Number of two track vertex candidates
$L_{xy}(SV)$	Distance between the primary and secondary vertex in the transverse plane
$L_{xyz}(SV)$	Distance between the primary and secondary vertex
$S_{xyz}(SV)$	Distance between the primary and secondary vertex, divided by its uncertainty (decay length significance)
$\Delta R(\text{jet,SV})(SV)$	ΔR between the jet axis and the secondary vertex

Table 5.2: Variables of the reconstructed secondary vertex (SV).

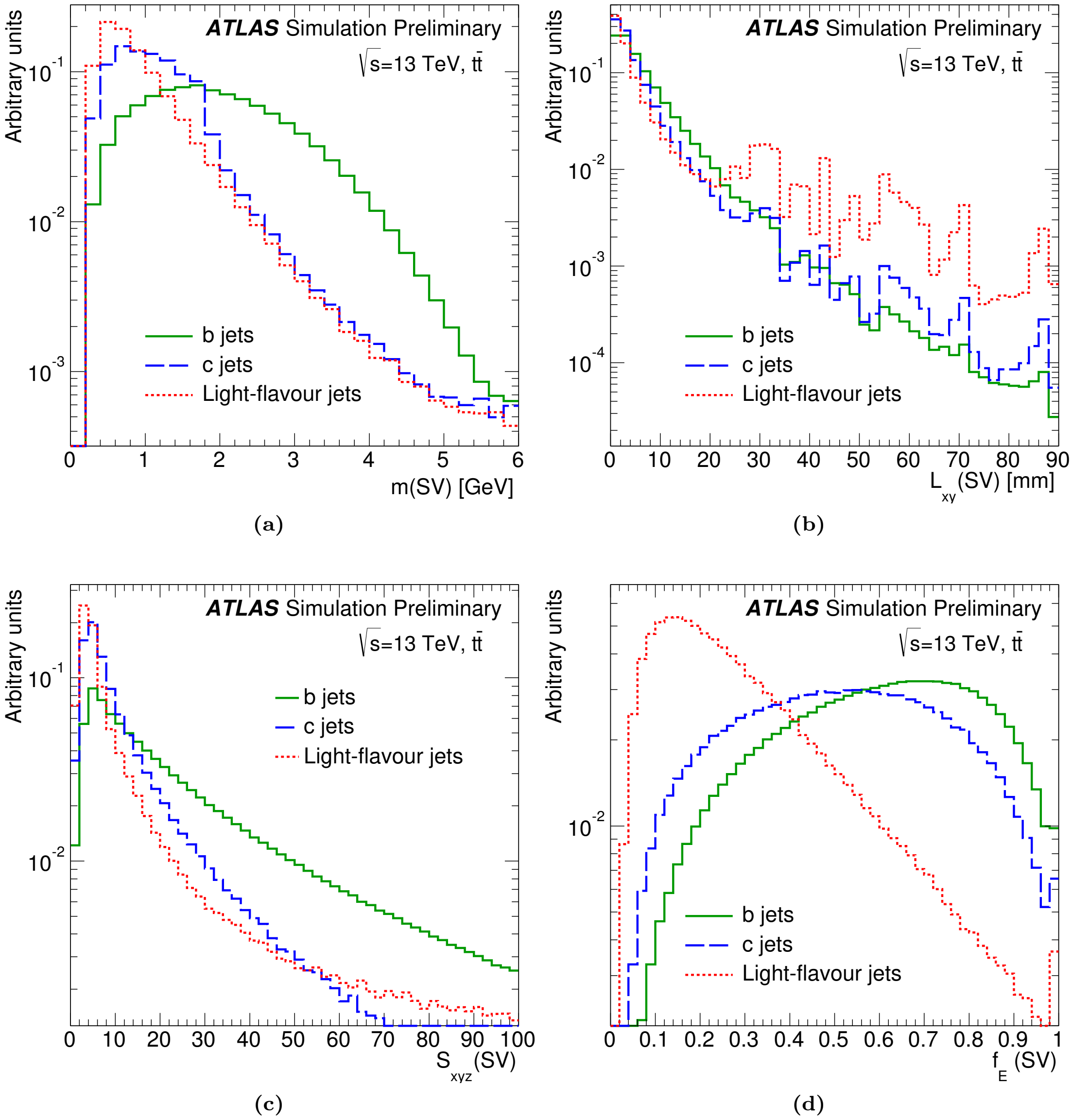

(a) **(b)**

(c) **(d)**

Figure 5.3: Reconstructed secondary vertex mass (a), transverse decay length (b), decay length significance (c) and energy fraction of secondary vertex tracks to all tracks reconstructed in the jet (d) for *b*- (solid green), *c*- (dashed blue) and light-flavour (dotted red) jets, reconstructed using the secondary vertex algorithm in a simulated $t\bar{t}$ sample at $\sqrt{s} = 13$ TeV [1]. The increased rate of light-flavour jets at high transverse decay length values is due to material interactions and long-lived particles, with the jagged structure due to vertex cleaning cuts.

5.2.3 Decay Chain Reconstruction Algorithms

The multi-vertex reconstruction algorithm, JetFitter (JF), employs a Kalman filter [62] to reconstruct the full $b \to c$ hadron decay chain [63]. As $|V_{cb}|^2 \gg |V_{ub}|^2$, a b-hadron will preferentially decay to a c-hadron, providing a distinct signature of a secondary and tertiary decay chain. Assuming that the b- and c-hadron lie along the same flight path, an iterative procedure is utilised to reconstruct the decay chain, including the position of each decay vertex. Using this procedure, it is possible to find single track vertices. Figure 5.4 presents a selection of reconstructed variables from the JF algorithm, for b-, c- and light-flavour jets. The set of discriminating output variables from the JF algorithm used in multivariate b-tagging algorithms are listed in Table 5.3.

Variable	Description
$N_{\text{2TrkVtx}}(\text{JF})$	Number of 2-track vertex candidates, prior to the decay chain fit
$m(\text{JF})$	Invariant mass of the tracks from the displaced vertices, assuming pion masses
$S_{xyz}(\text{JF})$	Significance of the average distance between the primary and displaced vertices
$f_{\text{E}}(\text{JF})$	Fraction of the charged jet energy in the displaced vertices
$N_{\text{1-trk vertices}}(\text{JF})$	Number of displaced vertices with one track
$N_{\geq\text{2-trk vertices}}(\text{JF})$	Number of displaced vertices with more than one track
$N_{\text{TrkAtVtx}}(\text{JF})$	Number of tracks from displaced vertices with at least two tracks
$\Delta R(\boldsymbol{p}_{\text{jet}}, \boldsymbol{p}_{\text{vtx}})(\text{JF})$	ΔR between the jet axis and the vectorial sum of the momenta of all tracks attached to displaced vertices

Table 5.3: Output variables from the JetFitter (JF) algorithm.

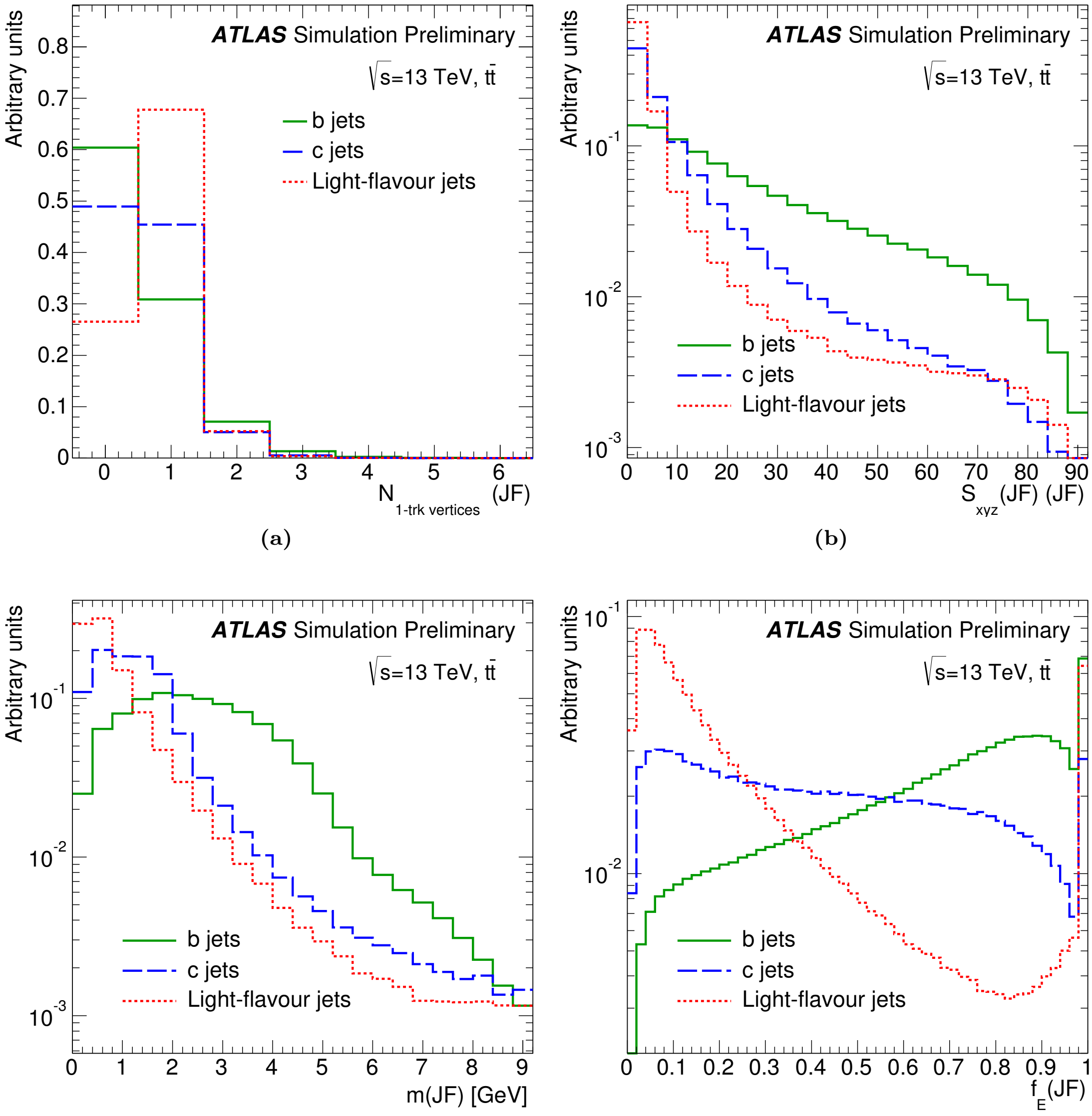

(a) (b)

(c) (d)

Figure 5.4: Number of single track vertices (a), average flight length significance of reconstructed vertices (b), invariant mass of tracks fitted to a displaced vertex (c) and the energy fraction of displaced vertex tracks relative to all tracks in the jet (d) for *b*- (solid green), *c*- (dashed blue) and light-flavour (dotted red) jets, reconstructed using the JetFitter algorithm in a simulated $t\bar{t}$ sample at $\sqrt{s} = 13$ TeV [1].

5.3 Multivariate Tagging Algorithms

Individually, each of the baseline b-tagging algorithms described in Section 5.2 provide some degree of separation of b-jets from c- and light-flavour jets. In order to enhance the rejection of c- and light-flavour jets, the outputs of each of these baseline algorithms are combined into a single discriminant using a multivariate algorithm, known as the MV2c class of algorithms.

A boosted decision tree (BDT) is trained on jets from $t\bar{t}$ events, with b-jets being considered as signal and c- and light-flavour jets being considered as background. The ratio of light-flavour jets to c-jets in the background can be modified, and the performance of the BDT can therefore be altered to improve its rejection of c-jets, at the expense of a lower light-flavour jet rejection. The naming convention of MV2c algorithms is chosen to specify the c-jet contribution of the background used in training. Given the name "MV2cXX", this corresponds to a training of the algorithm in a sample containing XX% c-jet background, with 100-XX% light-flavour jet background. The BDT training utilises the variables listed in Tables 5.2, 5.3 and 5.4, along with the jet p_{T} and η as input variables.

Figure 5.5 presents the output of the 2015 configuration of the MV2c20 multivariate b-tagging algorithm. The b-jets, confined to the higher BDT output score region, are well separated from c- and light-flavour jets. The performance curves used to assess the c- and light-flavour jet rejection for a range of b-jet efficiencies are constructed using a scan of this output, measuring the corresponding b-, c- and light-flavour jet efficiencies for jets passing the MV2c20 output cut using Equation 5.1.

Comparison plots of the light-flavour and c-jet rejection for various training configurations are presented in Figure 5.6 for the 2015 configuration of the MV2c algorithms. In each of the training configurations, a significantly different performance with respect to c-jets and light-flavour jets is observed. MV2c00 is found to provide the best light-flavour jet rejection, up to a factor of $\sim 1/2$ higher for a 70% b-jet tagging efficiency compared to MV2c20. However, this is at a significant cost in the c-jet rejection, which is reduced by a factor of $\sim 1/4$ when compared to MV2c20. As c-jet contamination is a significant background in many ATLAS analyses, and the light-flavour jet rejection is already sufficient in most cases, the training of MV2c20 is used as the default and recommended b-tagging algorithm for analyses during 2015 and provides a good balance between the performance of light-flavour and c-jet rejection.

Figure 5.7 presents the light-flavour and c-jet rejection as a function of the b-jet tagging efficiency for the 2015 configuration of the MV2c20 algorithm, and MV1c algorithm, used as the default algorithm for many Run-1 results [64]. The MV1c algorithm similarly uses a training sample composed of 20% c-jets, meaning that the difference in performance is mainly arising from updates to b-tagging algorithms and the detector upgrade for Run-2 (installation of the IBL). As the Run-1 $t\bar{t}$ sample is generated at $\sqrt{s} = 8$ TeV, with Run-1 pile-up conditions, the Run-2 $t\bar{t}$ sample is reweighted to have the same average number of interactions per bunch crossing, jet p_{T} and jet η for b-, c- and light-flavour jets to minimise the bias introduced by event kinematics.

For a 70% b-jet tagging efficiency, the inclusive light-flavour jet rejection has been improved by a factor of ~ 4, whilst the c-jet rejection has been improved by a factor of ~ 1.5 compared to the

Run-1 performance. The most significant factor driving the improvement in performance is from the installation of the IBL for Run-2.

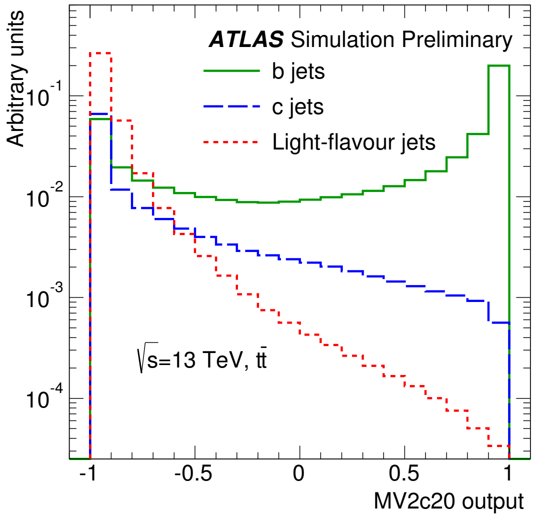

(a)

Figure 5.5: Output of the 2015 configuration of the MV2c20 b-tagging algorithm, for b- (solid green), c- (dashed blue) and light-flavour (dotted red) jets in a simulated $t\bar{t}$ sample at $\sqrt{s} = 13$ TeV [1].

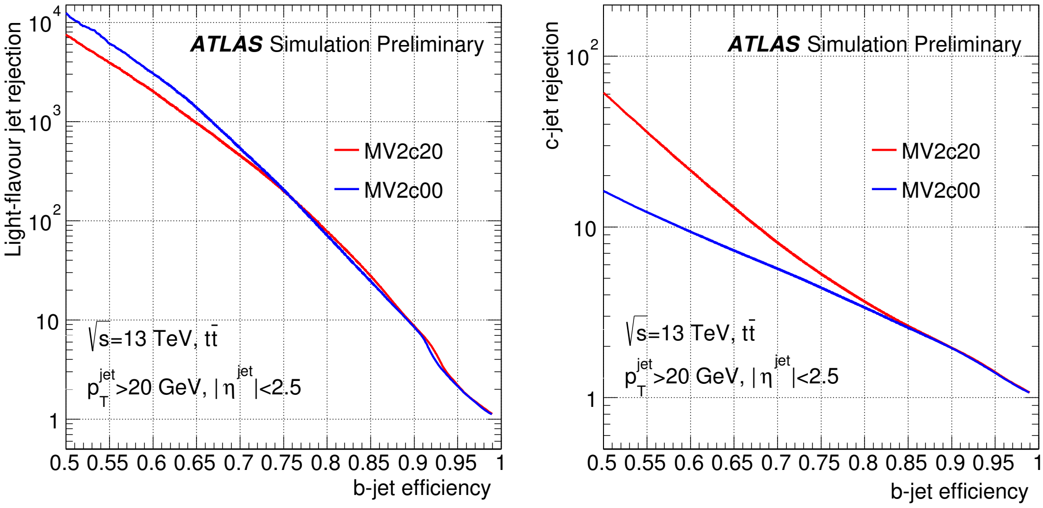

(a) **(b)**

Figure 5.6: Light-flavour (a) and c-jet (b) rejection as a function of b-jet tagging efficiency for the MV2c algorithm in a simulated $t\bar{t}$ sample at $\sqrt{s} = 13$ TeV. The red line indicates the performance of the 2015 configuration of Run-2 b-tagging algorithms, trained on a $t\bar{t}$ sample with 20% c-jet and 80% light-flavour jet background (MV2c20). The blue line indicates the performance of the same b-tagging algorithm trained on a $t\bar{t}$ sample with 0% c-jet and 100% light-flavour jet background (MV2c00).

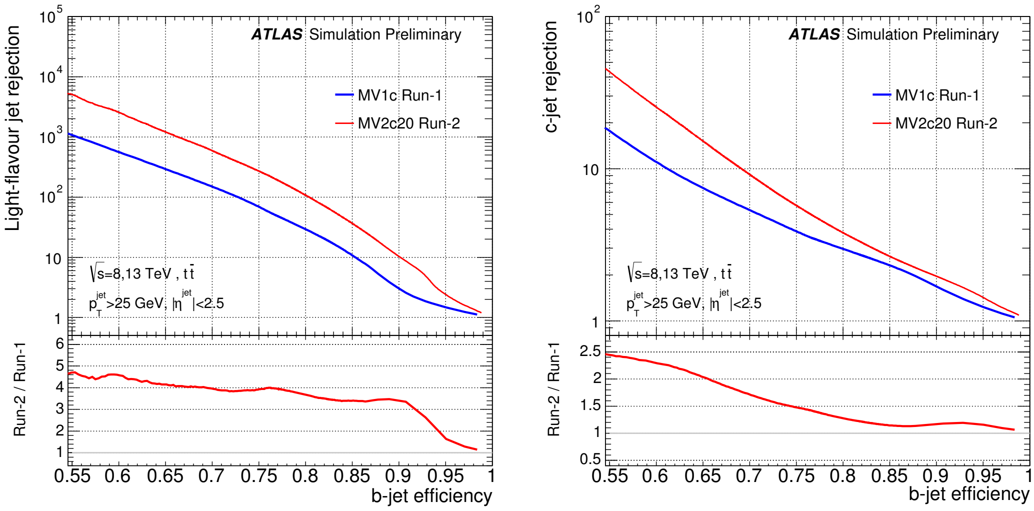

(a) (b)

Figure 5.7: Light-flavour (a) and c-jet (b) rejection as a function of b-jet tagging efficiency for the 2015 configuration of the MV2c20 algorithm (red line), and the default Run-1 algorithm (blue line), MV1c, in simulated $t\bar{t}$ samples at $\sqrt{s} = 13$ TeV and $\sqrt{s} = 8$ TeV, respectively. The MV2c20 performance takes into account the updated algorithm performance and detector upgrades. Event kinematics at $\sqrt{s} = 13$ TeV in Run-2 are reweighted to match those from Run-1 at $\sqrt{s} = 8$ TeV to avoid any bias in the comparison.

5.3.1 Differential Performance of Multivariate Tagging Algorithms

The performance of the ATLAS b-tagging algorithms has been studied as a function of several event and jet variables. Figure 5.8 presents the b-, c- and light-flavour jet efficiencies as a function of jet p_{T}, η and the average number of interactions per bunch crossing, for the 70% b-jet tagging efficiency working point.

The b-tagging efficiency is observed to decrease at both low and high jet p_{T}. For jets with lower p_{T}, the decay length of the b-hadron is shorter, and therefore harder to resolve, and the σ_{d_0} resolution is reduced for low p_{T} tracks, both reducing the b-tagging performance. At significantly higher jet p_{T}, the b-hadron will travel further from the primary vertex, and decay past the first ID layer. This therefore reduces the tracking impact parameter resolution, and subsequently degrades the b-tagging performance. Additionally, at high jet p_{T}, the tracks become more collimated, limiting the track reconstruction efficiency.

The b-jet efficiency is observed to reduce with increased jet η. The reason for this is two-fold. At high η, more material interactions result in increased multiple scattering and hadronic interactions, enhancing uncertainties on track measurements and decreasing the track reconstruction efficiency. Also, at sufficiently high η, tracks will no longer pass through all four barrel pixel layers, but instead reach the end-cap region, reducing tracking resolution.

It is also observed that the b-jet efficiency is roughly stable with the average number of interactions per bunch crossing. This is important to achieve so that the b-tagging performance is not affected by the high instantaneous luminosity delivered by the LHC. The *c*- and light-flavour jet efficiencies are also relatively stable as a function of the average number of interactions per bunch crossing, although with a slight degradation in performance at high values.

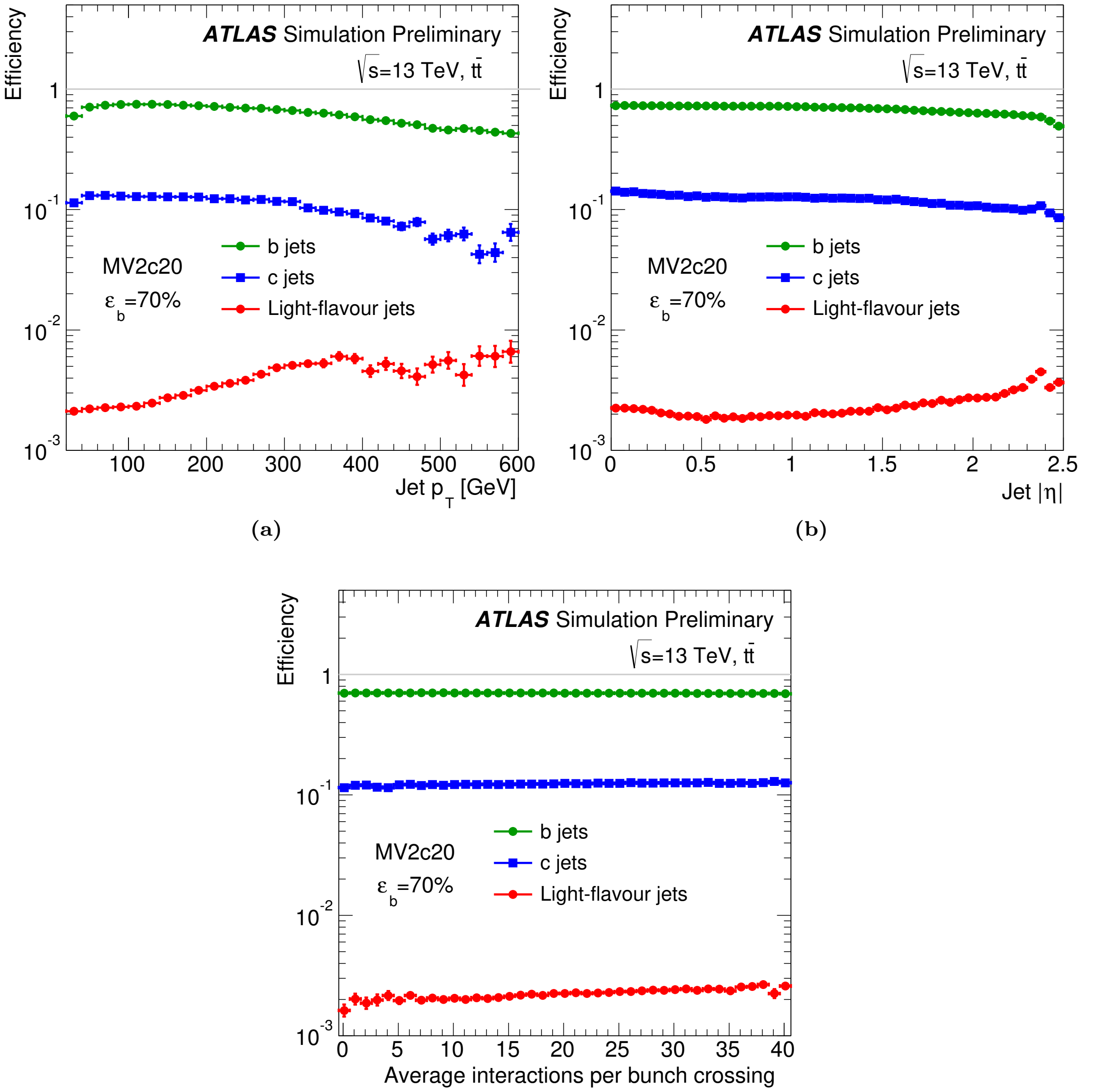

(a) **(b)** **(c)**

Figure 5.8: b- (green), c- (blue) and light-flavour (red) jet efficiencies as a function of jet p_{T} (a), jet η (b) and the average number of interactions per bunch crossing (c) at the 70% b-jet tagging efficiency working point for the 2015 configuration of the MV2c20 b-tagging algorithm in a simulated $t\bar{t}$ sample at $\sqrt{s} = 13$ TeV [1].

5.4 Enhanced Multivariate Algorithms

Since conducting studies into the performance of the MV2c b-tagging algorithm, updated versions of the baseline and multivariate algorithms have subsequently been released for 2016 data-taking [65]. Improvements to both the secondary vertex and impact parameter algorithms resulted in a significant increase in the c-jet rejection. For example, the inclusion of $Z' \to t\bar{t}$, with $m_{Z'} = 4$ TeV, events in the IPxD reference histograms results in a significant increase in performance at high jet p_{T}. Figure 5.9 presents a comparison of the performance of the 2015 configuration of the MV2c20 algorithm, and the 2016 configuration of the MV2c00, MV2c10 and MV2c20 algorithms. The MV2c10 configuration results in an improvement of $\sim 40\%$ in the c-jet rejection, for a similar light-flavour jet rejection. For the subsequent analyses presented, MV2c10 under the 2016 configuration is used as the default b-tagging algorithm, with 2015 data and MC reprocessed to utilise the improved performance from the updated algorithms.

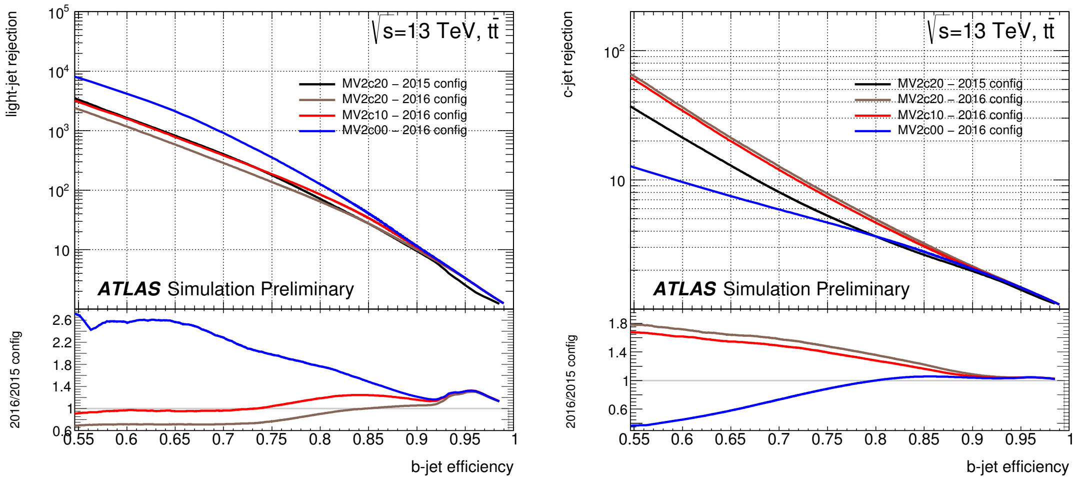

(a) (b)

Figure 5.9: Light-flavour jet (a) and c-jet (b) rejection as a function of b-jet tagging efficiency for the 2015 configuration of the MV2c20 algorithm and 2016 training configurations of the MV2cXX algorithms, as measured in a simulated $t\bar{t}$ sample at $\sqrt{s} = 13$ TeV [65].

5.5 Working Point Definitions

Table 5.4 summarises the four supported working points of the 2016 configuration of the MV2c10 algorithm. Taking the 70% b-jet tagging efficiency working point as an example, it is possible to have a light-flavour jet rejection rate of approximately 400, and a c-jet rejection rate of approximately 12 in the $t\bar{t}$ sample.

b-jet Efficiency [%]	MV2c10 Cut	c-jet Rejection	Light-flavour Jet Rejection
60	0.94	34.5	1538.8
70	0.82	12.2	381.3
77	0.65	6.2	134.3
85	0.18	3.1	33.5

Table 5.4: Working point definitions for the 2016 configuration of the MV2c10 b-tagging algorithm, as measured in a simulated $t\bar{t}$ sample at $\sqrt{s} = 13$ TeV.

5.6 Summary

The performance of the 2015 configuration of baseline and multivariate b-tagging algorithms has been validated, with a number of distributions for the baseline algorithms presented for each jet flavour. The validation of the performance of b-tagging algorithms was an essential step as part of the commissioning of b-tagging algorithms for Run-2. The overall performance was found to be as expected, with commissioning completed on time for the start of Run-2 data-taking.

The performance of the new Run-2 multivariate algorithm, MV2cXX, balances an improvement in the c-jet rejection at the cost of a reduced light-flavour jet rejection, when increasing the c-jet fraction in training. The MV2c20 algorithm was adopted as the default algorithm for 2015 data-taking. This was subsequently updated to MV2c10 for analyses using 2015 and 2016 data, which has significantly enhanced performance.

Comparisons of the b-tagging performance with algorithms used in Run-1 have been conducted, with the light-flavour (c-) jet rejection found to increase by a factor of 4 (1.5) over the performance at the end of Run-1. This is as a result of updates to the algorithms and, most importantly, the installation of the Insertable B-Layer during the long shutdown between Run-1 and Run-2. This improvement in c-jet and light-flavour jet rejection is greatly beneficial to numerous analyses throughout ATLAS, offering a significant improvement in the rejection of background events.

Chapter 6

Calibrating the *b*-Jet Tagging Efficiency

6.1 Overview

The performance of b-tagging algorithms, as discussed in Chapter 5, is evaluated using Monte Carlo (MC) samples, which may not accurately reproduce the performance in real data due to the effect of imperfect physics and detector modelling. In order to determine the effect of this, the performance of algorithms is measured in data. The performance for each b-tagging working point, as defined in Section 5.5, is evaluated for each jet flavour, b, c and light-flavour, where the simulation is corrected using a scaling factor per jet,

$$\kappa_j = \frac{\varepsilon_j^{\text{data}}}{\varepsilon_j^{\text{MC}}}, \tag{6.1}$$

where κ_j is the scale factor to be applied to b-tagged jets of flavour j in simulation and $\varepsilon_j^{\text{data (MC)}}$ is the measured tagging efficiency for jets of flavour j at a specific working point in data (MC). Typically, κ_j is evaluated as a function of jet p_{T} and η. For untagged jets, there is a corresponding inefficiency scale factor

$$w_j = \frac{1-\varepsilon_j^{\text{data}}}{1-\varepsilon_j^{\text{MC}}} = \frac{1-\kappa_j\varepsilon_j^{\text{MC}}}{1-\varepsilon_j^{\text{MC}}}, \tag{6.2}$$

which is applied to preserve the total number of events. The total scale factor for an event is the product of κ_j and w_j, as appropriate for all tagged/untagged jets in a simulated sample. Various calibration procedures exist for each jet flavour [66].

The calibration of c-jets is conducted using semi-leptonic $t\bar{t}$ events, with one W boson decaying leptonically, and the other hadronically. The c-jet efficiency in data is then extracted using events where the hadronically decaying W boson produces a c-jet, which occurs $\sim 34\%$ of the time [6]. Light-flavour jets are calibrated using a procedure referred to as the negative tag method. In this method, it is assumed that light-flavour jets are mis-tagged as a result of detector resolution effects, meaning that prompt tracks are expected to have symmetric signed impact parameter and secondary vertex decay length significances. Using the negatively signed track impact parameters and secondary vertex decay lengths, corrected to account for heavy flavour hadrons and the asymmetry between positive and negative light-flavour tags, it is possible to estimate the light-flavour jet tagging efficiency in data. The calibrations are produced as a function of jet p_{T} (and $|\eta|$ for light-flavour jets), along with associated uncertainties [66].

This chapter describes a method to extract the b-jet tagging efficiency from data using a sample enriched in top-quark pairs ($t\bar{t}$) and a likelihood formalism, referred to as the $t\bar{t}$ likelihood calibration [67]. As $Br(t \to Wb) \sim 1$, di-leptonic $t\bar{t}$ events are selected to give a high b-jet purity, using the event selection described in Section 6.2, with data and simulated samples described in Section 6.3. From this selection, the b-jet tagging efficiency is extracted from data as a function of jet p_{T} using a likelihood formalism, as described in Section 6.4. A discussion of systematic uncertainties is presented in Section 6.5, with data to MC comparison plots presented in Section 6.7. Multivariate techniques are applied to improve the b-jet purity of the event selection, with training and performance studies presented in Section 6.8. The closure of the $t\bar{t}$ likelihood calibration when fitting to MC is presented in Section 6.9, and the results from the fit to data presented in Section 6.10. Results are only presented for the *anti-*k_t $R = 0.4$ calorimeter jet collection at the 70% b-jet tagging efficiency working point. However, the procedure has also been applied to other working points and jet collections used on ATLAS.

6.2 Object and Event Selection

This calibration targets di-leptonic $t\bar{t}$ events, where both W bosons decay leptonically. Events are selected using single and di-lepton triggers. Data events are also required to pass the quality requirements of the Good Runs List, which ensures that all components of the detector are operating as expected.

Di-leptonic $t\bar{t}$ events are selected by requiring exactly two oppositely charged leptons (either electrons or muons) with $|\eta| < 2.5$, passing *LH-Signal* quality requirement cuts, as described in Sections 3.5.2 and 3.5.3. Events containing one or more additional *Loose* leptons are vetoed.

Jets are required to have $p_{\mathrm{T}} > 20$ GeV and $|\eta| < 2.5$, with the leading jet $p_{\mathrm{T}} > 30$ GeV. A tighter cut on the leading jet p_{T} is found to increase the $t\bar{t}$ purity, and therefore the b-jet purity. Events are required to contain exactly 2 or 3 jets. In the same lepton flavour channel, it is required that $E_{\mathrm{T}}^{\mathrm{miss}} > 60$ GeV, and the di-lepton invariant mass, $m_{\ell\ell}$, satisfies $50 < m_{\ell\ell} < 80$ GeV $\vee$ $m_{\ell\ell} > 100$ GeV in order to reduce the contamination from the $Z +$ jets and Drell-Yann backgrounds. This results in a b-jet purity of $\sim 70\%$, where the remaining jets are mainly composed of light-flavour jets, and very little c-jet contamination.

This event selection gives a total of four signal regions; the $e\mu$+2-jet, $e\mu$+3-jet, $ee/\mu\mu$+2-jet and $ee/\mu\mu$+3-jet channels. The same lepton flavour channels are considered jointly as they have similar background compositions and systematic uncertainties.

$Z +$ jets control regions are defined, from which the overall normalisation of the $Z +$ jets background can be extracted. A $Z +$ jets control region for the $e\mu$ channel is defined by requiring the same lepton flavour and $80 < m_{\ell\ell} < 100$ GeV, where the selection requirement on $E_{\mathrm{T}}^{\mathrm{miss}}$ is dropped to reduce the extrapolation uncertainty from the control region to the signal region. For the $ee/\mu\mu$ channel, the $Z +$ jets control region is required to satisfy $80 < m_{\ell\ell} < 100$ GeV and $E_{\mathrm{T}}^{\mathrm{miss}} > 60$ GeV.

The definitions of all the analysis regions are summarised in Table 6.1.

Process	$e\mu$	$ee/\mu\mu$
$t\bar{t}$ Signal Region (SR)	$e\mu$ lepton flavour	$ee/\mu\mu$ lepton flavour, $E_{\mathrm{T}}^{\mathrm{miss}} > 60$ GeV, $50 < m_{\ell\ell} < 80$ GeV $\vee$ $m_{\ell\ell} > 100$ GeV
$Z +$ jets Control Region (CR)	Same lepton flavour, $80 < m_{\ell\ell} < 100$ GeV	Same lepton flavour, $E_{\mathrm{T}}^{\mathrm{miss}} > 60$ GeV, $80 < m_{\ell\ell} < 100$ GeV

Table 6.1: Selections applied for the $Z +$ jets control regions and $t\bar{t}$ signal regions for the $e\mu$ and $ee/\mu\mu$ channels of the $t\bar{t}$ likelihood calibration. The 2-and 3-jet regions are defined by an additional requirement on the number of signal jets in the event.

6.3 Data and Simulated Samples

The data used in the b-jet efficiency measurement corresponds to the full $\sqrt{s} = 13$ TeV 2015 and 2016 pp datasets. After offline data quality requirements, this corresponds to an integrated luminosity of 36.1 fb^{-1}.

MC samples are used to simulate all background processes, with the exception of the multijet background which is estimated using a data-driven approach, as discussed in Section 6.3.1. Aside from the dominant $t\bar{t}$ process, there are non-negligible contributions from the production of a single top-quark in association with a W boson (Wt), $Z +$ jets and diboson processes. The MC generators and Parton Distribution Function (PDF) set used for each process are summarised in Table 6.2. EvtGen [58], which uses updated lifetime and decay tables to improve the modelling, is used to decay heavy flavour hadrons in all the parton shower generators, except for Sherpa [68]. To evaluate systematic uncertainties arising from assumptions in the event modelling, alternative MC samples are used, and are also summarised in Table 6.2. Details of the motivation for, and how these alternative MC samples are implemented to evaluate systematic uncertainties, are provided in Section 6.5. All nominal and alternative samples are passed through GEANT4 [60] for a full simulation of the ATLAS detector.

The contamination from $t\bar{t} + V$ and $H \rightarrow WW$ processes was tested, and found to have a negligible impact on both the background yields and the efficiency measurement results. For simplicity, these background processes are therefore not considered.

Process	Matrix Element	PDF Set	Parton Shower	$\sigma \times$ Br [pb]
Nominal Generators				
$t\bar{t}$	Powheg [55]	CT10 [57]	Pythia-6.428 [56]	832 [69]
Single top-quark (Wt) (diagram removal scheme)	Powheg	CT10	Pythia-6.428	71.7 [70]
$Z \rightarrow \ell\ell$+jets ($m_{\ell\ell} >$ 40 GeV)	MG5_aMC@NLO [73]	NNPDF23LO [71]	Pythia-8.186	6300 [72]
Diboson (WW,WZ,ZZ)	Sherpa 2.1.1 [68]	CT10	Sherpa 2.1.1	36.7
Alternative Generators				
$t\bar{t}$ (less radiation) [74]	Powheg	CT10	Pythia-6.428	832
$t\bar{t}$ (more radiation)	Powheg	CT10	Pythia-6.428	832
$t\bar{t}$	Powheg	CT10	Herwig++ [75]	832
$t\bar{t}$	MG5_aMC@NLO	CT10	Herwig++	832
Single top-quark (Wt) (less radiation)	Powheg	CT10	Pythia-6.428	71.7
Single top-quark (Wt) (more radiation)	Powheg	CT10	Pythia-6.428	71.7
Single top-quark (Wt)	Powheg	CT10	Herwig++	71.7
Single top-quark (Wt) (diagram subtraction) [76]	Powheg	CT10	Pythia-6.428	71.7
$Z \rightarrow \ell\ell$+jets ($m_{\ell\ell} >$ 60 GeV)	Powheg	CT10	Pythia-8.186	5850 [72]

Table 6.2: Nominal and alternative Monte Carlo samples used in the $t\bar{t}$ likelihood calibration. Alternative MC samples are used to estimate the impact of different aspects of the modelling of the various background processes by comparing the flavour composition and kinematics of the alternative sample to the nominal sample. Further details of the generation and implementation of these samples are presented in Section 6.5. Minimum bias interactions are generated with Pythia8 [59], and overlaid on each event.

6.3.1 Fake Prompt Leptons

In the reconstruction of events, it is possible for jets to be mis-identified, and fake the presence of an isolated lepton. In the case of a fake electron or muon, these can often arise from a number of different sources, as discussed in Sections 3.5.2 and 3.5.3.

Whilst the contamination of fake leptons is reduced through the use of cuts on lepton isolation and identification variables, the contribution of events with fake leptons is non-negligible. Due to difficulty in generating sufficient MC events, because of the low efficiency for a jet to fake a lepton, and the large modelling uncertainties, the contribution of events with fake leptons is estimated using a data-driven method.

In this method, it is firstly assumed that the contribution of events with fake leptons is symmetric when requiring two leptons to have the same and opposite charge. Therefore, data events where the two leptons have the same sign (SS) provide a good model for the fake lepton background, with little contamination from other processes. In order to prevent double counting of events with a fake lepton in the MC samples, the SS MC background is subtracted from the SS data events to generate the fake lepton background template. In the $e\mu$+2-jet channel, the fake lepton background is estimated to provide $\sim 2\%$ of the total background contribution. All jets in events with fake leptons are assumed to be light-flavoured. This assumption has been tested by taking the alternative hypothesis that all jets in events with fake leptons are b-jets, and was found to have a negligible impact on the results.

6.3.2 Monte Carlo to Data Normalisation Factors

Due to large theoretical uncertainties on the cross-section and acceptance effects, normalisation factors for the most important processes, $t\bar{t}$ and $Z+$jets, are derived from data using the regions summarised in Section 6.2. A comparison between the MC and data yields, used to derive the normalisation scale factors, are presented for each of the regions in Figure 6.1.

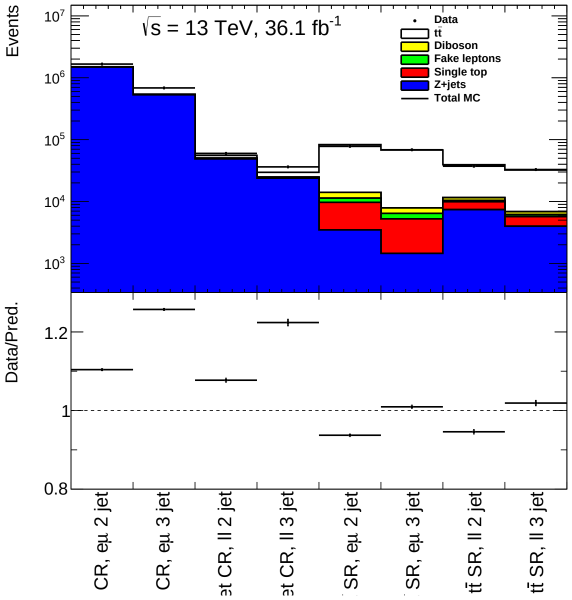

Figure 6.1: Expected yields for the various processes compared to data in the four $Z+$jets control regions and four $t\bar{t}$ signal regions, as described in Table 6.1, for the $t\bar{t}$ likelihood calibration, corresponding to 36.1 fb^{-1} of Run-2 data collected at $\sqrt{s} = 13$ TeV. Statistical uncertainty on the data points are indicated by the error bars. The ratio shows the total background prediction compared to data, prior to the application of the normalisation factor.

A maximum likelihood fit to the data yield in each of these regions is used to extract the normalisation factors for the $t\bar{t}$ and $Z+$jets background in all analysis regions. The normalisation of $t\bar{t}$ and $Z+$jets is floated independently in each channel, resulting in a total of four normalisation factors for each background. Scale factors derived from the fit are presented in Table 6.3.

Region	$t\bar{t}$ Normalisation Scale Factor	$Z+$jets Normalisation Scale Factor
$e\mu$+2-jet	0.930 ± 0.004	1.107 ± 0.001
$e\mu$+3-jet	1.016 ± 0.004	1.265 ± 0.002
$ee/\mu\mu$+2-jet	0.912 ± 0.007	1.097 ± 0.005
$ee/\mu\mu$+3-jet	0.994 ± 0.008	1.280 ± 0.008

Table 6.3: Derived normalisation factors for $t\bar{t}$ and $Z+$jets processes in each channel of the $t\bar{t}$ likelihood calibration.

6.3.3 Event Yields

In the following section, the event yield in each region is presented, together with the expected jet flavour composition. MC predictions are scaled to the data luminosity, 36.1 fb^{-1}, and the MC-to-data normalisation scale factors presented in Table 6.3 have been applied.

Tables 6.4 and 6.5 present the yields for the $e\mu$ and $ee/\mu\mu$ channels, respectively. In the $e\mu$+2- (3-) jet region, an overall b-jet purity of 71% (53%) is found. In the $ee/\mu\mu$+2- (3-) jet channel, an overall b-jet purity of 59% (46%) is found. The high b-jet purity obtained from the selection of di-leptonic $t\bar{t}$ events is vital to reduce modelling uncertainties of the light-flavour jet flavour fraction, and therefore reduce the overall uncertainties on the final scale factor values.

Sample	$t\bar{t}$	Single Top	Fake Leptons	$Z+$jets	Diboson	Total MC	Data
2 Leptons	211823 ± 282	15700 ± 68	5114 ± 72	9506 ± 195	8425 ± 55	250568 ± 361	239669
At least 2 jets	200353 ± 274	13510 ± 63	4371 ± 66	6741 ± 138	6173 ± 39	231148 ± 323	222072
Exactly 2 or 3 jets	130403 ± 219	10113 ± 54	2833 ± 53	5719 ± 127	4604 ± 34	153672 ± 266	146469
2 jets	69705 ± 161	6287 ± 43	1634 ± 40	4051 ± 109	3001 ± 27	84678 ± 205	77895
ll	1473 ± 23	341 ± 10	1634 ± 40	3320 ± 97	2582 ± 25	9351 ± 111	-
cl	220 ± 9	35 ± 3	-	393 ± 39	324 ± 9	973 ± 41	-
cc	15 ± 2	4.3 ± 1.1	-	53 ± 10	37 ± 3	109 ± 11	-
bl	20822 ± 87	3995 ± 34	-	215 ± 23	48 ± 3	25081 ± 96	-
bc	1237 ± 22	153 ± 7	-	9.3 ± 3.8	4.4 ± 1.0	1404 ± 23	-
bb	45938 ± 131	1757 ± 23	-	60 ± 15	4.8 ± 1.3	47761 ± 134	-
ll [%]	2.1	5.4	100	82.0	86.1	11.0	-
cl [%]	0.3	0.6	-	9.7	10.8	1.1	-
cc [%]	0.0	0.1	-	1.3	1.2	0.1	-
bl [%]	29.9	63.6	-	5.3	1.6	29.6	-
bc [%]	1.8	2.4	-	0.2	0.1	1.7	-
bb [%]	65.9	28.0	-	1.5	0.2	56.4	-
3 jets	60696 ± 148	3826 ± 33	1199 ± 35	1668 ± 65	1603 ± 20	68992 ± 170	68574
lll	881 ± 18	153 ± 6	1199 ± 35	1308 ± 60	1272 ± 18	4813 ± 74	-
cll	155 ± 7	30 ± 3	-	166 ± 18	230 ± 7	580 ± 21	-
ccl	22 ± 3	3.0 ± 0.9	-	66 ± 13	40 ± 3	131 ± 13	-
ccc	0.8 ± 0.4	0.2 ± 0.2	-	-	2.3 ± 0.7	3.3 ± 0.9	-
bll	13504 ± 70	1774 ± 22	-	79 ± 11	48 ± 3	15405 ± 74	-
bcl	1517 ± 23	154 ± 7	-	9.4 ± 3.7	4.7 ± 0.9	1685 ± 24	-
bcc	124 ± 7	19 ± 2	-	1.6 ± 1.1	0.3 ± 0.2	144 ± 7	-
bbl	41909 ± 123	1599 ± 21	-	32 ± 7	6.3 ± 1.2	43547 ± 125	-
bbc	1905 ± 26	69 ± 5	-	5.8 ± 3.5	0.2 ± 0.2	1980 ± 27	-
bbb	679 ± 16	26 ± 3	-	-	0.3 ± 0.3	705 ± 16	-
lll [%]	1.5	4.0	100	78.4	79.4	7.0	-
cll [%]	0.3	0.8	-	9.9	14.3	0.8	-
ccl [%]	0.0	0.1	-	3.9	2.5	0.2	-
ccc [%]	0.0	0.0	-	0.0	0.1	0.0	-
bll [%]	22.2	46.4	-	4.7	3.0	22.3	-
bcl [%]	2.5	4.0	-	0.6	0.3	2.4	-
bcc [%]	0.2	0.5	-	0.1	0.0	0.2	-
bbl [%]	69.0	41.8	-	1.9	0.4	63.1	-
bbc [%]	3.1	1.8	-	0.3	0.0	2.9	-
bbb [%]	1.1	0.7	-	0.0	0.0	1.0	-

Table 6.4: Event yields for data and simulation, along with the predicted flavour composition, in the $e\mu$ channel signal region, for 36.1 fb^{-1} of Run-2 data collected at $\sqrt{s} = 13$ TeV. The normalisation of the $t\bar{t}$ and $Z+$ jets samples are corrected using normalisation scale factors derived in Section 6.3.2. Data and fakes are not split by jet flavour. Only statistical uncertainties are considered.

Sample	$t\bar{t}$	Single Top	Fake Leptons	$Z+$jets	Diboson	Total MC	Data
2 leptons	213462 ± 283	15867 ± 68	34765 ± 186	4341949 ± 4623	16640 ± 127	4622682 ± 4638	5479903
At least 2 jets	201777 ± 276	13634 ± 63	23505 ± 153	2697571 ± 3025	11645 ± 117	2948132 ± 3044	3314172
Exactly 2 or 3 jets	131347 ± 220	10216 ± 54	19042 ± 138	2314113 ± 2787	8798 ± 112	2483517 ± 2802	2831465
Signal Region	53734 ± 140	4268 ± 35	959 ± 31	11483 ± 216	1975 ± 22	72420 ± 263	70079
2 jets	28066 ± 102	2543 ± 27	512 ± 23	7447 ± 183	1217 ± 17	39785 ± 213	37216
ll	683 ± 16	157 ± 7	512 ± 23	6182 ± 172	1051 ± 16	8586 ± 175	-
cl	94 ± 6	22 ± 2	-	614 ± 41	123 ± 6	852 ± 42	-
cc	6.1 ± 1.5	2.0 ± 0.8	-	85 ± 15	15.8 ± 1.8	109 ± 15	-
bl	8907 ± 57	1585 ± 21	-	435 ± 36	22.6 ± 2.2	10951 ± 71	-
bc	504 ± 14	55 ± 4	-	16.2 ± 5.0	1.6 ± 0.6	577 ± 15	-
bb	17872 ± 82	721 ± 14	-	115 ± 18	2.7 ± 1.0	18711 ± 85	-
ll [%]	2.4	6.2	100	83.0	86.4	21.6	-
cl [%]	0.3	0.9	-	8.2	10.1	2.1	-
cc [%]	0.0	0.1	-	1.1	1.3	0.3	-
bl [%]	31.7	62.3	-	5.8	1.9	27.5	-
bc [%]	1.8	2.2	-	0.2	0.1	1.4	-
bb [%]	63.7	28.4	-	1.5	0.2	47.0	-
2 jets	25668 ± 96	1725 ± 22	447 ± 21	4036 ± 115	758 ± 14	32635 ± 154	32863
lll	419 ± 12	67 ± 4	447 ± 21	3030 ± 103	618 ± 13	4581 ± 107	-
cll	75 ± 5	9.6 ± 1.5	-	421 ± 32	96 ± 5	601 ± 33	-
ccl	8.0 ± 1.7	1.1 ± 0.5	-	132 ± 18	19.9 ± 2.2	161 ± 19	-
ccc	0.3 ± 0.3	-	-	1.9 ± 1.3	1.2 ± 0.5	3.4 ± 1.5	-
bll	6044 ± 47	815 ± 15	-	274 ± 26	19.3 ± 2.0	7153 ± 55	-
bcl	651 ± 15	61 ± 4	-	30.0 ± 12.6	1.5 ± 0.4	744 ± 20	-
bcc	57 ± 5	4.8 ± 1.0	-	4.1 ± 2.2	-	66 ± 5	-
bbl	17368 ± 79	723 ± 14	-	141 ± 17	2.5 ± 0.6	18234 ± 82	-
bbc	760 ± 17	34 ± 3	-	0.6 ± 0.6	0.7 ± 0.4	795 ± 17	-
bbb	286 ± 10	10.3 ± 1.7	-	0.7 ± 0.7	-	297 ± 10	-
lll [%]	1.6	3.9	100	75.1	81.4	14.0	-
cll [%]	0.3	0.6	-	10.4	12.6	1.8	-
ccl [%]	0.0	0.1	-	3.3	2.6	0.5	-
ccc [%]	0.0	0.0	-	0.0	0.2	0.0	-
bll [%]	23.5	47.3	-	6.8	2.5	21.9	-
bcl [%]	2.5	3.5	-	0.7	0.2	2.3	-
bcc [%]	0.2	0.3	-	0.1	0.0	0.2	-
bbl [%]	67.7	41.9	-	3.5	0.3	55.9	-
bbc [%]	3.0	2.0	-	0.0	0.1	2.4	-
bbb [%]	1.1	0.6	-	0.0	0.0	0.9	-

Table 6.5: Event yields for data and simulation, along with the predicted flavour composition, in the $ee/\mu\mu$ channel signal region, for 36.1 fb^{-1} of Run-2 data collected at $\sqrt{s} = 13$ TeV. The normalisation of the $t\bar{t}$ and $Z+$jets samples are corrected using normalisation scale factors derived in Section 6.3.2. Data and fakes are not split by jet flavour. Only statistical uncertainties are considered. The signal region selection cuts are defined in Table 6.1.

6.4 Likelihood Fit Procedure

The b-jet tagging efficiency is extracted from data using a likelihood formalism [67]. The use of a likelihood allows per event jet correlations to be exploited, resulting in a more precise measurement of the b-jet efficiency compared to a measurement using individual jets. Efficiencies are extracted as a function of the jet p_{T}. The following likelihood function is maximised for the 2-jet case,

$$\begin{aligned}\mathcal{L}\left(p_{\mathrm{T},1}, p_{\mathrm{T},2}, w_1, w_2\right) = & \; [\quad f_{bb}\mathcal{P}_{bb}\left(p_{\mathrm{T},1}, p_{\mathrm{T},2}\right)\mathcal{P}_b\left(w_1|p_{\mathrm{T},1}\right)\mathcal{P}_b\left(w_2|p_{\mathrm{T},2}\right) \\ & + \; f_{bl}\mathcal{P}_{bl}\left(p_{\mathrm{T},1}, p_{\mathrm{T},2}\right)\mathcal{P}_b\left(w_1|p_{\mathrm{T},1}\right)\mathcal{P}_l\left(w_2|p_{\mathrm{T},2}\right) \\ & + \; f_{ll}\mathcal{P}_{ll}\left(p_{\mathrm{T},1}, p_{\mathrm{T},2}\right)\mathcal{P}_l\left(w_1|p_{\mathrm{T},2}\right)\mathcal{P}_l\left(w_2|p_{\mathrm{T},2}\right) \\ & + \; 1 \leftrightarrow 2 \;]/2,\end{aligned} \tag{6.3}$$

where f_{bb}, f_{bl} and $f_{ll} = 1 - f_{bb} - f_{bl}$ are the bb, bl and ll event flavour fractions (obtained from MC); $\mathcal{P}_j\left(w|p_{\mathrm{T}}\right)$ is the probability density function for the MV2c10 b-tagging output, w, for a jet of flavour j, given the jet p_{T} (extracted from data for b-jets and from MC for light-flavour jets); and $\mathcal{P}_{j_1 j_2}\left(p_{\mathrm{T},1}, p_{\mathrm{T},2}\right)$ is the two-dimensional probability density functions for two jets of flavour $[j_1, j_2]$ to have momenta $[p_{\mathrm{T},1}, p_{\mathrm{T},2}]$ (extracted from MC). Due to the low c-jet contamination achieved by the di-leptonic $t\bar{t}$ event selection, c-jets are considered as part of the light-flavour jet category in order to simplify the likelihood.

All the probability density functions are implemented as binned histograms, where symmetric combinations (such as bb or ll) are symmetrised to reduce statistical fluctuations. In the results presented in the following sections, six bins of jet p_{T} are considered for the calibration, with bin edges defined as $\{20, 30, 90, 140, 200, 300\}$ GeV. The choice of six calibration bins is motivated by the fact that this offers a sufficient description of the b-tagging performance over the jet p_{T} range considered, whilst also not introducing an unnecessarily large number of systematic uncertainties when applying the correction in analyses.

The b-jet tagging efficiency corresponds to

$$\varepsilon_b\left(p_{\mathrm{T}}\right) = \int_{w_{cut}}^{\infty} dw' \mathcal{P}_b\left(w'|p_{\mathrm{T}}\right), \tag{6.4}$$

where $\mathcal{P}_j\left(w|p_{\mathrm{T}}\right)$ is implemented as a histogram with two bins, with the bin above the working point cut value corresponding to ε_b. In the case of 3-jet events, the probability density functions is constructed in an analogous way to Equation 6.3. In order to simplify the fitting procedure, the following factorisation assumption is made:

$$\mathcal{P}_{j_1 j_2 j_3}\left(p_{\mathrm{T},1}, p_{\mathrm{T},2}, p_{\mathrm{T},3}\right) = \mathcal{P}_{j_1}\left(p_{\mathrm{T},1}\right)\mathcal{P}_{j_2}\left(p_{\mathrm{T},2}\right)\mathcal{P}_{j_3}\left(p_{\mathrm{T},3}\right). \tag{6.5}$$

The final result is obtained from the combined results of the four channels, $e\mu$+2-jets, $e\mu$+3-jets, $ee/\mu\mu$+2-jets and $ee/\mu\mu$+3-jets, using a χ^2 minimisation procedure. In general, it is found that the $e\mu$+2-jets channel is the most sensitive, with the lowest combined statistical and systematic uncertainty.

6.5 Systematic Uncertainties

Systematic uncertainties are evaluated by modifying the nominal MC sample according to a single systematic uncertainty. The fit is repeated, with the variation introduced by each systematic uncertainty treated as a $\pm 1\ \sigma$ variation in the central scale factor value. For each channel, the systematic uncertainties are combined in quadrature to give the overall systematic uncertainty. Under each variation, the normalisation procedure described in Section 6.3.2 is repeated. There are three types of systematic uncertainty considered; uncertainties relating to the modelling of simulated samples are described in Section 6.5.1, uncertainties on the normalisation of simulated samples are described in Section 6.5.2, and experimental uncertainties are described in Section 6.5.3.

6.5.1 Modelling Uncertainties

The modelling uncertainties considered on the $t\bar{t}$, Wt and $Z+$jets backgrounds are summarised in Table 6.6. As the background contribution from $Z+$jets is smaller than that from Wt, a simpler approach to evaluating the modelling uncertainty is taken.

- **Modelling ($t\bar{t}/Wt$):** An uncertainty on the matrix element calculations, for both $t\bar{t}$ and Wt, is estimated from samples generated using aMC@NLO+Herwig++. As this uses the Herwig++ showering generator, these samples are compared to alternative samples generated using Powheg+Herwig++, rather than the nominal Powheg+Pythia6.
- **Hadronisation ($t\bar{t}/Wt$):** The parton shower and hadronisation models used in the nominal Powheg+Pythia6 samples, for both $t\bar{t}$ and Wt, are compared using samples generated with Powheg+Herwig++.
- **More/less radiation ($t\bar{t}/Wt$):** The more and less radiation tunes, for both $t\bar{t}$ and Wt, involve the modification of the h_{damp} and renormalisation scale, μ_R, which affect the kinematics of the showering radiation. In the nominal case:
  - h_{damp} is set to the top mass, m_{top}, 172.5 GeV.
  - $\mu_R^{\mathrm{Nom}} = \sqrt{m_{\mathrm{top}}^2 + p_{\mathrm{T}}{}^2}$, where p_{T} is the transverse momentum of the top quark.

  In the more radiation configuration, these are set to $\mu_R = 0.5 \times \mu_R^{\mathrm{Nom}}$ and $h_{\mathrm{damp}} = 2 \times m_{\mathrm{top}}$, whilst in the less radiation configuration, $\mu_R = 2.0 \times \mu_R^{\mathrm{Nom}}$ and $h_{\mathrm{damp}} = m_{\mathrm{top}}$ are used [77]. The total difference in the measured efficiency scale factors between the more and less radiation samples is halved and symmetrised to estimate the variation on the nominal sample.
- **NNLO top p_{T}, $t\bar{t}$ p_{T} reweighting ($t\bar{t}$):** The uncertainties on the modelling of the top-quark p_{T} and $t\bar{t}$ p_{T} are evaluated by taking the difference between the nominal Powheg+Pythia6 $t\bar{t}$ prediction, and the nominal sample in which the top-quark p_{T} and $t\bar{t}$ p_{T} distributions are reweighted to match predictions at NNLO accuracy in QCD [78, 79].

Uncertainty	Name	Nominal Sample	Comparison Sample
$t\bar{t}$ Modelling Uncertainties			
$t\bar{t}$ hard scatter generation models	Modelling ($t\bar{t}$)	Powheg+Herwig++	aMC@NLO+Herwig++
$t\bar{t}$ parton shower and hadronisation models	Hadronisation ($t\bar{t}$)	Powheg+Pythia6	Powheg+Herwig++
$t\bar{t}$ Parton distribution function (PDF) central value	$t\bar{t}$ PDF reweighting	aMC@NLO+Herwig++ with CT10 PDF	aMC@NLO+Herwig++ with PDF4LHC15_NLO_100 PDF
$t\bar{t}$ showering radiation, modified factorisation and renormalisation scale	More/less radiation ($t\bar{t}$)	Powheg+Pythia6 with ×0.5 renormalisation scale and $h_{\text{damp}} = 2 \times m_{\text{top}}$	Powheg+Pythia6 with ×2 renormalisation scale and $h_{\text{damp}} = m_{\text{top}}$
$t\bar{t}$ NNLO reweighting of top and $t\bar{t}$ p_{T} spectra	NNLO Top p_{T}, $t\bar{t}$ p_{T} reweighting	Powheg+Pythia6	Powheg+Pythia6 reweighted to NNLO prediction
Wt Modelling Uncertainties			
Wt hard scatter generation models	Modelling (single top-quark)	Powheg+Herwig++	aMC@NLO+Herwig++
Wt parton shower and hadronisation models	Hadronisation (single top-quark)	Powheg+Pythia6	Powheg+Herwig++
Wt showering radiation, modified factorisation and renormalisation scale	More/less radiation (single top-quark)	Powheg+Pythia6 with ×0.5 renormalisation scale and $h_{\text{damp}} = 2 \times m_{\text{top}}$	Powheg+Pythia6 with ×2 renormalisation scale and $h_{\text{damp}} = m_{\text{top}}$
Wt diagram overlap	DR vs. DS (single top-quark)	Powheg+Pythia6, diagram removal scheme	Powheg+Pythia6, diagram subtraction scheme
$Z+$jets Modelling Uncertainties			
$Z+$jets hard scatter generation	Modelling ($Z+$jets)	MadGraph+Pythia8	Powheg+Pythia8
$Z+$jets p_{T}(jet) reweighting	$Z+$jets p_{T} reweighting	MadGraph+Pythia8	MadGraph+Pythia8 with p_{T}(jet) reweighting scheme derived from $Z+$jets $e\mu$ control region

Table 6.6: Summary of the systematic uncertainties evaluated for the $t\bar{t}$, Wt and $Z+$jets processes in the $t\bar{t}$ likelihood calibration. For each source of uncertainty considered, the nominal and alternative samples are indicated. To consider the effect of diagram overlap in the generation of Wt events, the diagram removal (DR) and diagram subtraction (DS) schemes are considered.

- **PDF reweighting ($t\bar{t}$):** A $t\bar{t}$ sample generated using aMC@NLO+Herwig++ with the CT10 PDF set is reweighted to the PDF4LHC15_NLO_100 PDF set, and the difference compared.
- **Diagram removal vs. diagram subtraction (Wt):** In the generation of Wt events, there is an overlap between these processes at NLO and $t\bar{t}$ generators. Two approaches to remove this overlap are used [80]
  - **Diagram Removal (DR):** Remove all diagrams in the NLO Wt process that overlap with $t\bar{t}$ events (nominal case).
  - **Diagram Subtraction (DS):** Implement a subtraction term in the matrix element to cancel events which overlap with $t\bar{t}$ events (alternative case).

The impact of using the nominal diagram removal scheme is assessed by comparing to a sample generated using the diagram subtraction technique.

- **Modelling (Z + jets):** To evaluate uncertainties in the matrix element calculation, the modelling with the nominal MadGraph+Pythia8 sample is compared to a Z + jets sample generated using Powheg+Pythia8.

- **p_{T} reweighting (Z+jets):** In the Z+jets control regions, the jet p_{T} spectrum was found to be poorly modelled by the nominal MadGraph+Pythia8 Z+jets sample. A further systematic uncertainty is considered by reweighting the Z + jets MC jet p_{T} spectrum to data in the control region, and taking the difference as a systematic uncertainty.

6.5.2 Normalisation Uncertainties

Normalisation uncertainties are considered for several processes [67]. The normalisation uncertainty of the $Z+b/c$, diboson and fake lepton backgrounds has only a small impact on the total systematic uncertainty. Therefore, large priors are assigned as conservative estimates on the normalisation uncertainties, as there would be limited benefit from further studying their size.

- **Wt:** The single top-quark normalisation is varied by ±6%, taken as an estimate on the $\sqrt{s} = 13$ TeV Wt production cross section uncertainty [70].

- **Z+jets:** The Z+jets normalisation in the signal region is varied by ±20%, as an extrapolation uncertainty from the control region where the scale factors are determined. This is determined by comparing the data to Monte Carlo agreement in the $m_{\ell\ell}$ distribution for the nominal and alternative Z + jets MC generators.

- **$Z + b/c$:** The normalisation of Z + jets events containing at least one heavy flavour (b,c) hadron is varied by ±50% to account for heavy flavour mismodelling observed in $Z + b$ measurements [81].

- **Diboson:** The diboson normalisation is varied by ±50%. An additional ±20% uncertainty is added in the 3-jet channels. This is taken as a conservative estimate on the normalisation uncertainty from the comparison with alternative MC samples.

- **Fake lepton:** The fake lepton normalisation is varied by ±50%. This is determined as a conservative estimate of the normalisation uncertainty in the same-charge control region when using alternative MC samples.

6.5.3 Detector Uncertainties

In addition, relevant detector related systematic uncertainties are considered:

- **Luminosity:** The luminosity uncertainty is 2.1% for 2015 data (3.2 fb^{-1}), and 3.4% for 2016 data (32.9 fb^{-1}). Due to correlations in these measurements, the total uncertainty for the combined 2015 and 2016 dataset is 3.2% [37].

- **Pile-up reweighting:** The MC is reweighted to describe the pile-up in data, by scaling the pile-up in MC by 1.09. The systematic uncertainty is evaluated by varying the scale factor from 1.00 to 1.18 [82].
- **Jet energy scale (JES):** Uncertainties related to the JES are studied using a globally reduced 19 nuisance parameter model. This parameterisation also includes additional nuisance parameters to account for uncertainties on the sample flavour composition, the sample flavour response, b-jets in the events, and punch-through jets [46].
- **Jet energy resolution (JER):** The nominal jet p_{T} is varied by a random smearing factor taken from a Gaussian with width equal to the JER uncertainty, parameterised as a function of the jet p_{T} and η [46].
- **Electron efficiency, resolution, scale and isolation uncertainties** are evaluated on $\sqrt{s} = 13$ TeV data and applied independently as two-sided variations [41].
- **Muon efficiency, resolution, scale and isolation uncertainties** are evaluated on $\sqrt{s} = 13$ TeV data and applied independently as two-sided variations [43].
- **Muon and electron trigger efficiencies** are evaluated on $\sqrt{s} = 13$ TeV data and applied independently as two-sided variations [35].
- **$E_{\mathrm{T}}^{\mathrm{miss}}$:** Uncertainties on the scale, resolution and efficiency of the tracks used to define the soft term in the $E_{\mathrm{T}}^{\mathrm{miss}}$ calculation [50]. The $E_{\mathrm{T}}^{\mathrm{miss}}$ is also recalculated according to all other experimental systematic variations.
- **JVT:** The uncertainty on JVT is evaluated to propagate a 2% uncertainty on the hard scatter jet efficiency [49].
- **Light-flavour and c-jet mis-tag rate:** the light-flavour jet and c-jet mis-tag rate in the MC is varied separately by the uncertainty on the Run-2 data-driven light-flavour and c-jet calibrations. These scale factors use the full uncertainty on each of the c- and light-flavour jet calibrations [66].

6.6 Combination of Channels

In the combination of the different channels (2- and 3-jets, $e\mu$ and $ee/\mu\mu$) all single systematic variations are treated as fully correlated, except for the modelling uncertainties, for which a 50% correlation is assumed. This is justified by the fact that such uncertainties rely on an estimate provided purely by the difference of two different MC generators and that the selections vary significantly among the different channels, and include a number of effects. Therefore, the correlation amongst the channels when using different modelling generators lies somewhere between 0% and 100%, and so a mid-point of 50% is used. It was checked that such an assumption leads to only minor differences in the final results after varying the correlation between channels to either 0% or 100% for modelling uncertainties, with consistent scale factor results obtained in both cases.

6.7 Data to Monte Carlo Comparisons

Good modelling of the data by the simulated samples is essential for ensuring that accurate and reliable b-jet tagging efficiencies are extracted from data. In this section, data to MC comparison distributions for a number of key variables in all analysis regions are presented. The variables of interest are: the invariant mass of the vectorial sum of the four momenta of both leptons, $m_{\ell\ell}$; the transverse momentum of the vectorial sum of the four momenta of both leptons, p_{ll}; the jet transverse momentum, jet p_{T}; and the jet pseudorapidity, jet η. The data to MC comparison distributions as a function of jet p_{T} are presented in six bins, corresponding to the number of calibration bins.

Figures 6.2 - 6.5 present plots for the $e\mu$+2-jet, $e\mu$+3-jet, $ee/\mu\mu$+2-jet and $ee/\mu\mu$+3-jet channels, respectively. In all figures, the MC normalisation correction factors, as derived in Section 6.3.2, are applied. Systematic uncertainty bands in green correspond to the addition in quadrature of normalisation, detector, MC modelling and MC statistical uncertainties. Statistical uncertainties on the data points are indicated by the error bars. In all regions, good agreement between data and simulation is observed within the statistical and systematic uncertainties.

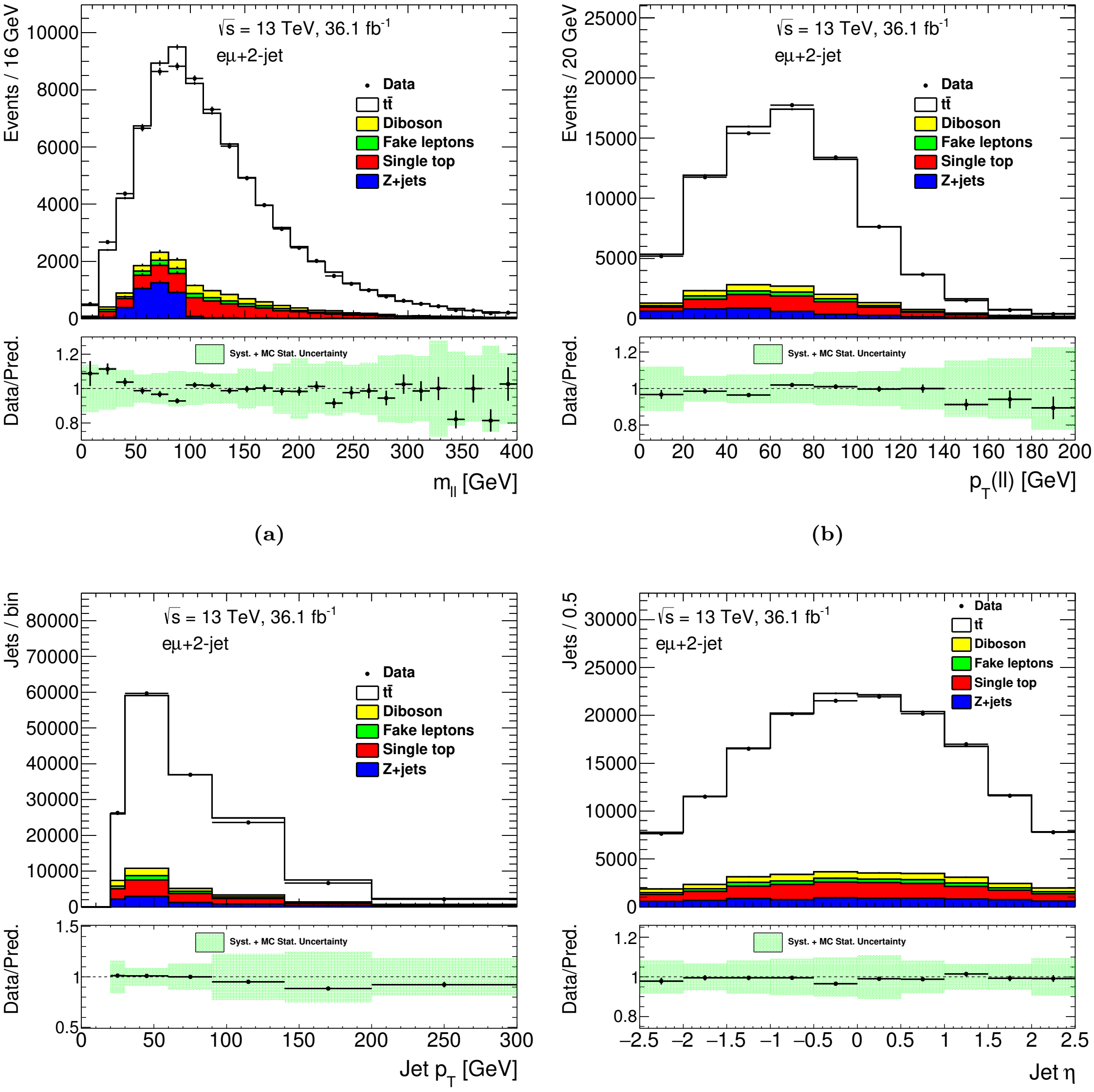

(a) (b)

(c) (d)

Figure 6.2: Distributions of the $m_{\ell\ell}$ (a), $p_{\mathrm{T}}(\ell\ell)$ (b), jet p_{T} (c) and jet η (d) for the $t\bar{t}$ $e\mu$+2-jet signal region selection, corresponding to 36.1 fb^{-1} of Run-2 data collected at $\sqrt{s} = 13$ TeV. The stacked histograms correspond to the various simulated processes, and the points to the data. Statistical uncertainties on the data points are indicated by the error bars. The bottom pad shows the ratio of data to MC, where systematic uncertainty bands (green shaded area) correspond to the normalisation, detector, MC modelling and MC statistical uncertainties.

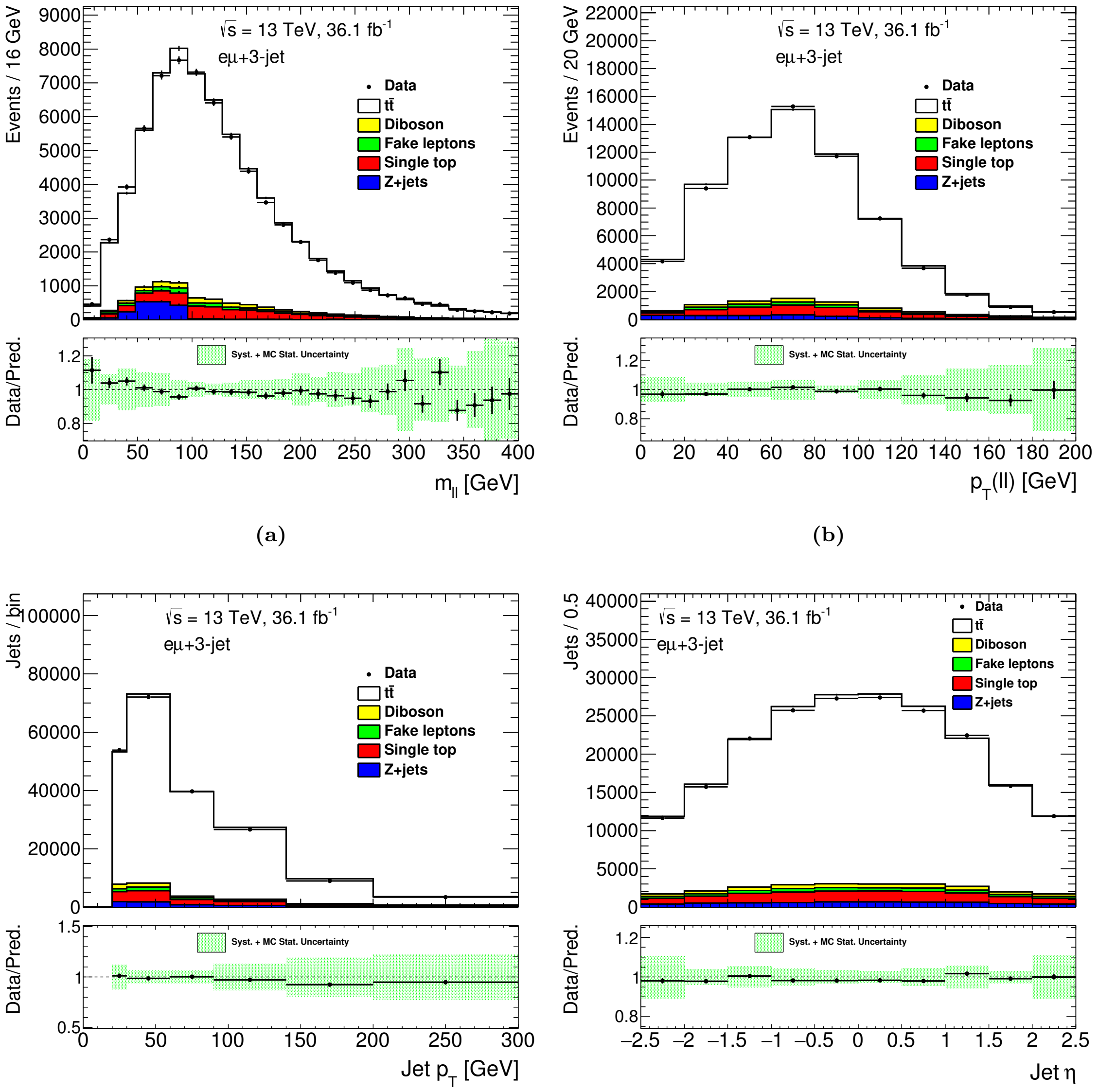

(a) (b)

(c) (d)

Figure 6.3: Distributions of the $m_{\ell\ell}$ (a), $p_{\mathrm{T}}(\ell\ell)$ (b), jet p_{T} (c) and jet η (d) for the $t\bar{t}$ $e\mu$+3-jet signal region selection, corresponding to 36.1 fb^{-1} of Run-2 data collected at $\sqrt{s} = 13$ TeV. The stacked histograms correspond to the various simulated processes, and the points to the data. Statistical uncertainties on the data points are indicated by the error bars. The bottom pad shows the ratio of data to MC, where systematic uncertainty bands (green shaded area) correspond to the normalisation, detector, MC modelling and MC statistical uncertainties.

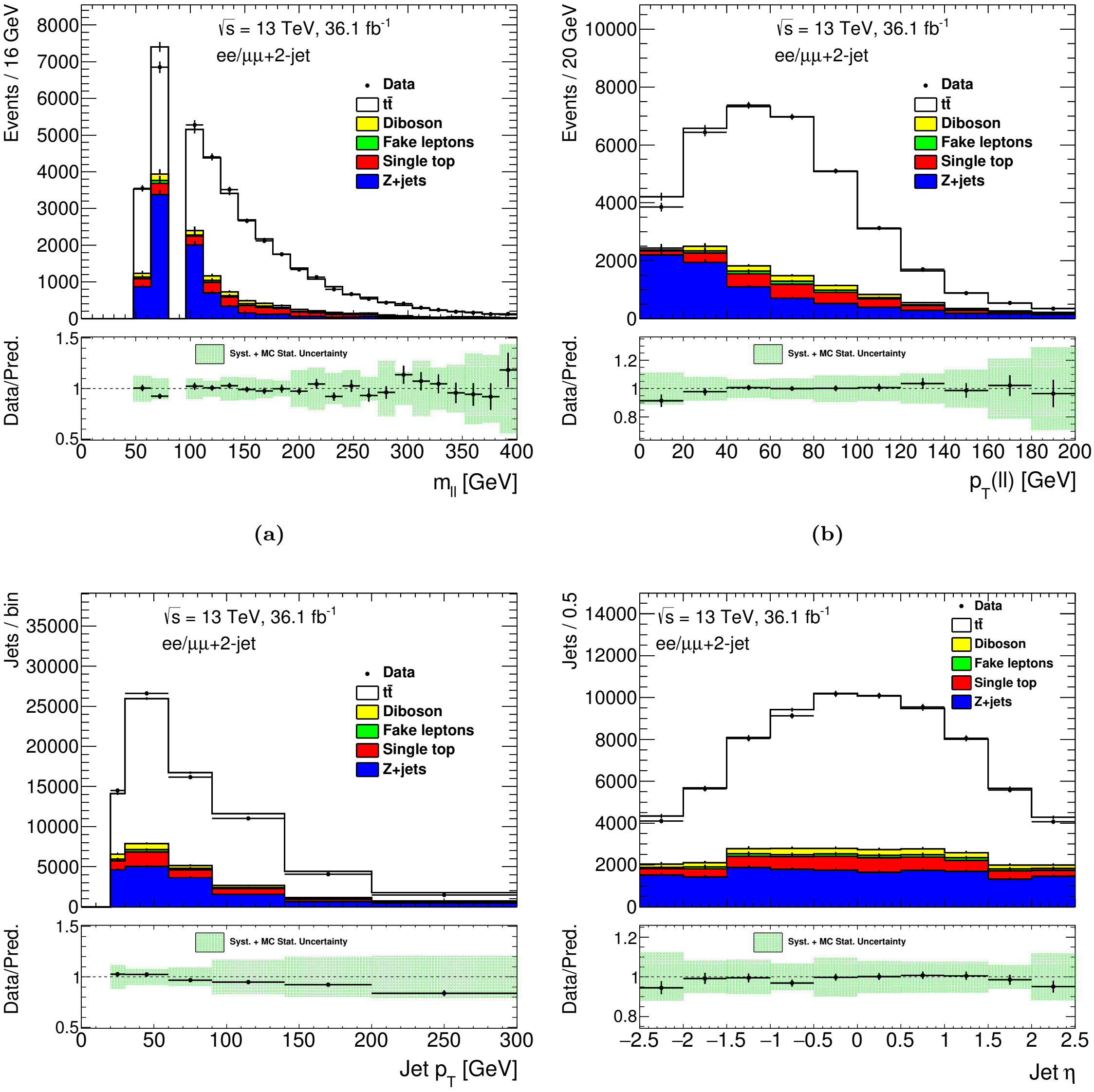

(a) (b)

(c) (d)

Figure 6.4: Distributions of the $m_{\ell\ell}$ (a), $p_{\mathrm{T}}(\ell\ell)$ (b), jet p_{T} (c) and jet η (d) for the $t\bar{t}$ $ee/\mu\mu$+2-jet signal region selection, corresponding to 36.1 fb^{-1} of Run-2 data collected at $\sqrt{s} = 13$ TeV. The stacked histograms correspond to the various simulated processes, and the points to the data. Statistical uncertainties on the data points are indicated by the error bars. The bottom pad shows the ratio of data to MC, where systematic uncertainty bands (green shaded area) correspond to the normalisation, detector, MC modelling and MC statistical uncertainties.

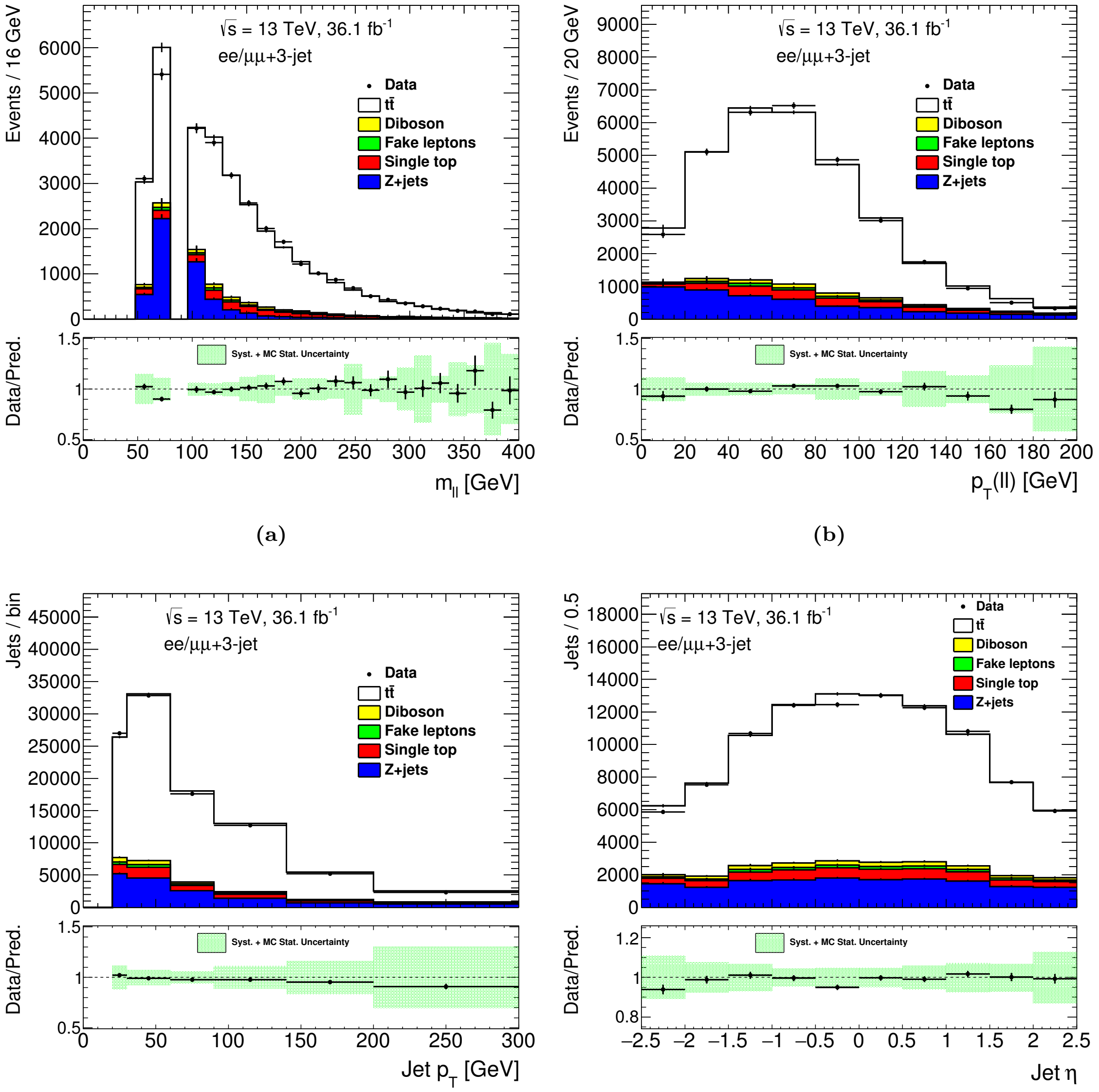

(a) (b)

(c) (d)

Figure 6.5: Distributions of the $m_{\ell\ell}$ (a), $p_{\mathrm{T}}(\ell\ell)$ (b), jet p_{T} (c) and jet η (d) for the $t\bar{t}$ $ee/\mu\mu$+3-jet signal region selection, corresponding to 36.1 fb^{-1} of Run-2 data collected at $\sqrt{s} = 13$ TeV. The stacked histograms correspond to the various simulated processes, and the points to the data. Statistical uncertainties on the data points are indicated by the error bars. The bottom pad shows the ratio of data to MC, where systematic uncertainty bands (green shaded area) correspond to the normalisation, detector, MC modelling and MC statistical uncertainties.

6.8 Multivariate Event Selection

The full 2015 and 2016 dataset yields a total integrated luminosity of 36.1 fb^{-1}, and therefore provides a sufficient number of data events such that the scale factor results are systematically dominated for all channels in the range $20 <$ jet $p_{\text{T}} < 300$ GeV. It is therefore possible to tighten the event selection in order to obtain an increased b-jet purity, and reduce the effects of modelling uncertainties from events containing light-flavour jets.

In order to achieve this enhanced event selection, a boosted decision tree (BDT) is trained using the TMVA package [53]. The BDT is trained using MC samples to select events with two b-jets from $t\bar{t}$ decays as signal, and reject all other events as background, with separate trainings for the 2-jet and 3-jet channels. The output of the BDT, denoted $\mathcal{D}_{bb}^{\text{LH}}$, provides discrimination of signal events from background events, with improved performance over a single variable. By cutting on $\mathcal{D}_{bb}^{\text{LH}}$ as part of the event selection, the purity of $b\bar{b}$ events can be significantly increased.

Each of the variables included are designed to select $t\bar{t}$ events based on their topology, and not on the b-tagging information of the jet, to minimise any bias on the b-tagging output. Table 6.7 lists each input variable utilised. The separation of $\mathcal{D}_{bb}^{\text{LH}}$ was found to increase on addition of each variable. The configuration of the BDT parameters is presented in Table 6.8. The configuration parameters were taken from the Run-1 $VH \to Vb\bar{b}$ analysis BDT, described in Ref. [83]. Variations in NCuts, NTrees and MaxDepth were tested, but found to have little impact on the performance of the BDT.

Variable	Definition
Leading jet p_{T}	-
Sub-leading jet p_{T}	-
Third-leading jet p_{T}	Only used for 3-jet events
$\Delta\phi(j_1, j_2)$	$\Delta\phi$ of leading 2 jets
$\min \Delta R(j, j)$	Minimum ΔR of all jet combinations
Imbalance	$(j_1(p_{\text{T}}) - j_2(p_{\text{T}}))/(j_1(p_{\text{T}}) + j_2(p_{\text{T}}))$
$m(lj)$	Minimal average value of all $m(lj)$ pairings
$\min \Delta R(l_1, j)$	Minimal ΔR separation of lepton 1 to all jets
$\min \Delta R(l_2, j)$	Minimal ΔR separation of lepton 2 to all jets

Table 6.7: Input training variables for the $t\bar{t}$ likelihood calibration BDT algorithm to identify events containing two b-jets from $t\bar{t}$ decays. The symbol $m(lj)$ is defined explicitly in Equation 6.6, j_1 and j_2 correspond to the leading and sub-leading jets, ordered by jet p_{T}, respectively, and l_1 and l_2 correspond to the leading and sub-leading leptons, ordered by lepton p_{T}, respectively.

Configuration	Value	Definition
BoostType	AdaBoost	Boost procedure
AdaBoostBeta	0.15	Learning rate
SeparationType	GiniIndex	Node separation gain
NTrees	200	Number of trees
MaxDepth	4	Maximum tree depth
NCuts	100	Number of equally spaced cuts tested per variable per node
NEventsMin	5%	Minimum number of events in a node

Table 6.8: The configuration parameters for the $t\bar{t}$ likelihood calibration BDT designed to select events with two b-jet from $t\bar{t}$ decays.

$m(lj)$ is defined as

$$m(lj) = \begin{cases} [\min((m(l_1,j_1)+m(l_2,j_2)),(m(l_2,j_1)+m(l_1,j_2)))]/2 & \text{2-jets} \\ [\min((m(l_1,j_1)+m(l_2,j_2)),(m(l_1,j_1)+m(l_3,j_3)),(m(l_2,j_2)+m(l_3,j_3)),(m(l_2,j_1)+m(l_1,j_2)),(m(l_1,j_3)+m(l_3,j_1)),(m(l_2,j_3)+m(l_3,j_2)))]/2 & \text{3-jets} \end{cases}, \quad (6.6)$$

where $m(l_m, j_n)$ is the invariant mass of the 4-vector sum of lepton m and jet n. In the 3-jet case, all cyclic permutations are considered.

The training samples include both the nominal $t\bar{t}$ sample and the alternative samples used for evaluating MC modelling uncertainties, as described in Table 6.2. The inclusion of these samples not only increases the number of events available for training, but also exposes the BDT to the topologies of events under these variations. It was found that the inclusion of the alternative $t\bar{t}$ samples led to a further reduction in the scale factor uncertainties. A 2-fold cross-validation approach, as described in Section 3.6.2, is used for the BDT training and implementation.

Good agreement between data and simulation for the input variables of $\mathcal{D}_{bb}^{\mathrm{LH}}$ are presented in Figure 6.6 for the $e\mu$+2-jet category. Similar agreement between data and simulation is observed in all other channels. Figures 6.7 and 6.8 present the data to MC comparison of $\mathcal{D}_{bb}^{\mathrm{LH}}$, with the stacked histograms displaying the physics processes and event flavour compositions, respectively.

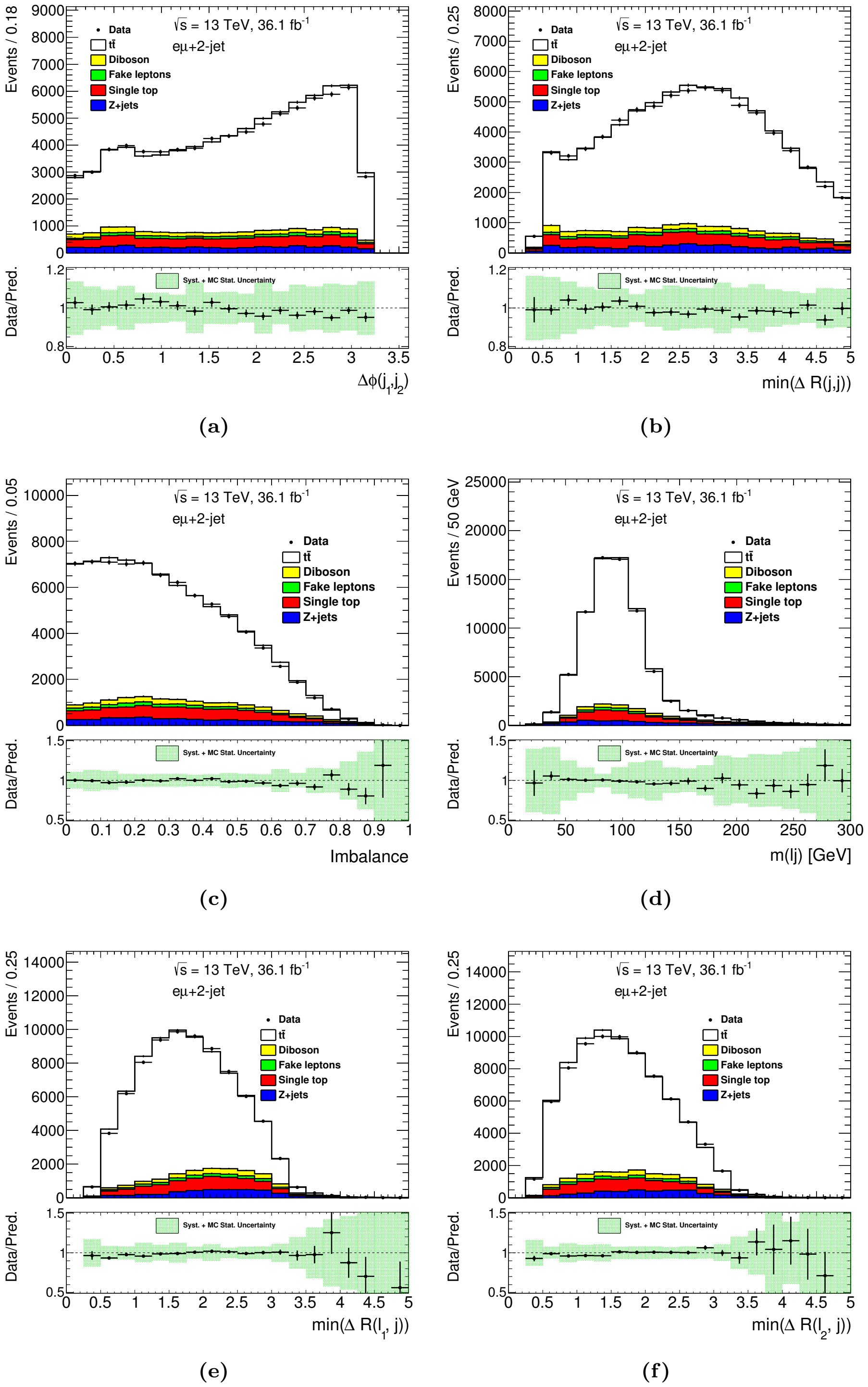

(a) (b) (c) (d) (e) (f)

Figure 6.6: Distributions of the $\mathcal{D}_{bb}^{\mathrm{LH}}$ input variables, $\Delta\phi(j_1, j_2)$ (a), $\min \Delta R(j, j)$ (b), momentum imbalance (c), $m(l, j)$ (d), $\min \Delta R(l_1, j)$ (e) and $\min \Delta R(l_2, j)$ (f) for the $t\bar{t}$ $e\mu$+2-jet signal region selection, corresponding to 36.1 fb^{-1} of Run-2 data collected at $\sqrt{s} = 13$ TeV. The stacked histograms correspond to the various simulated processes, and the points to the data. Statistical uncertainties on the data points are indicated by the error bars. The bottom pad shows the ratio of data to MC, where systematic uncertainty bands (green shaded area) correspond to the normalisation, detector, MC modelling and MC statistical uncertainties.

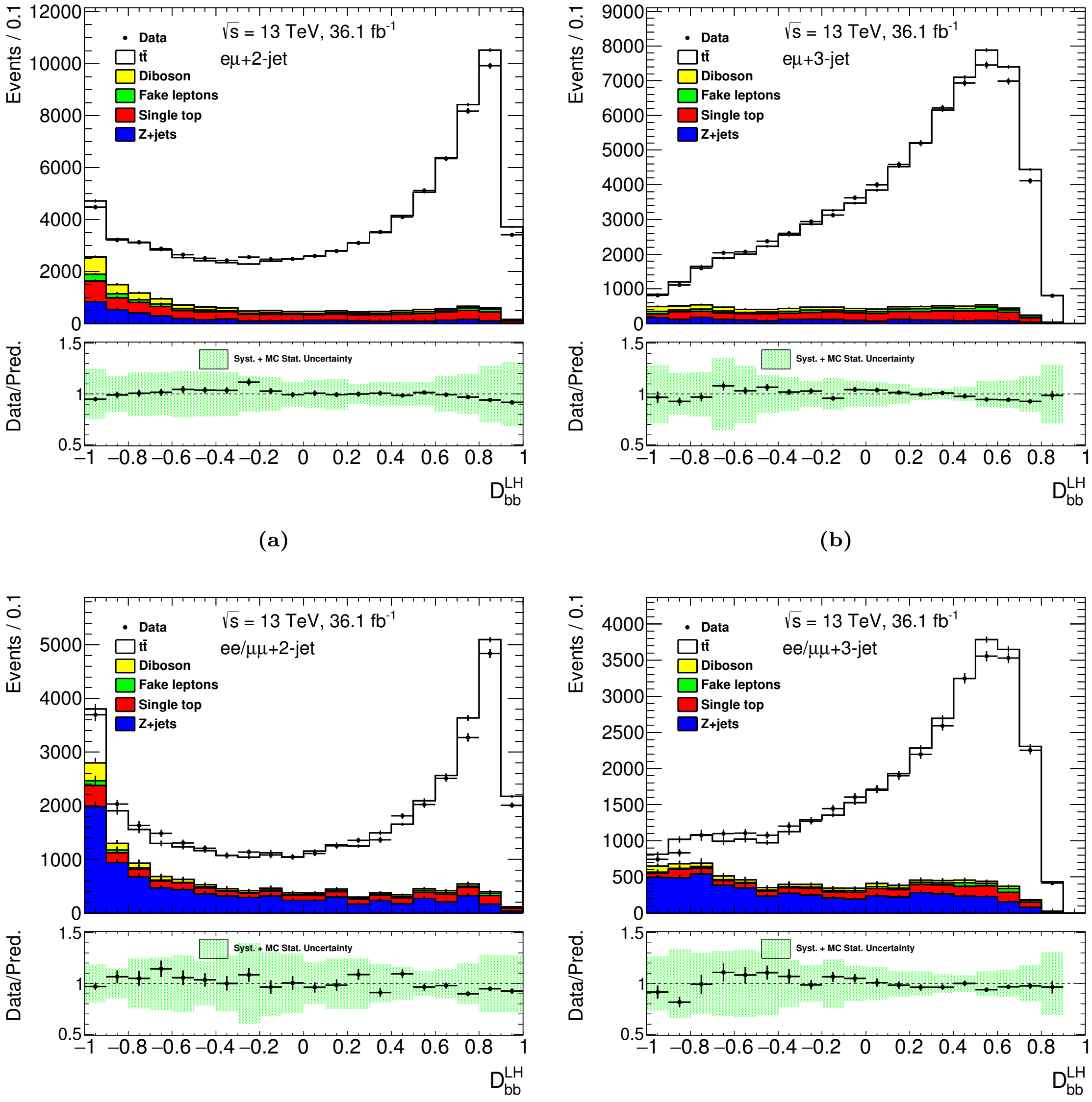

(a) **(b)**

(c) **(d)**

Figure 6.7: Distributions of the $\mathcal{D}_{bb}^{\mathrm{LH}}$ output distributions in the $t\bar{t}$ $e\mu$+2-jet (a), $e\mu$+3-jet (b), $ee/\mu\mu$+2-jet (c) and $ee/\mu\mu$+3-jet (d) signal region selections, corresponding to 36.1 fb^{-1} of Run-2 data collected at $\sqrt{s} = 13$ TeV. Systematic uncertainty bands correspond to the normalisation, detector, modelling and MC statistical uncertainties. The Statistical uncertainties on the data points are indicated by the error bars. The bottom pad shows the ratio of data to MC, where systematic uncertainty bands (green shaded area) correspond to the normalisation, detector, MC modelling and MC statistical uncertainties.

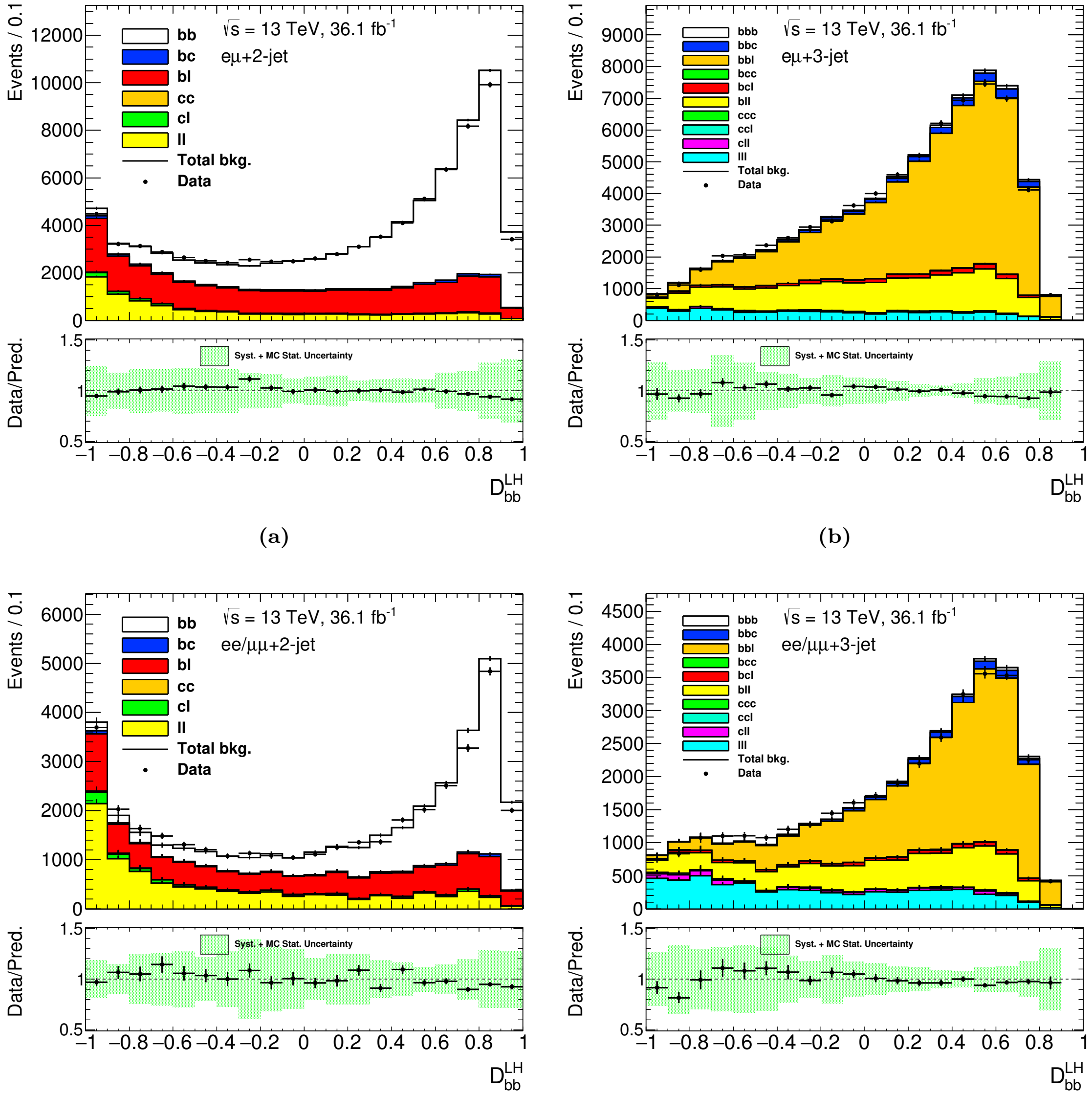

(a) (b)

(c) (d)

Figure 6.8: Distributions of the $\mathcal{D}_{bb}^{\mathrm{LH}}$ output distributions in the $t\bar{t}$ $e\mu$+2-jet (a), $e\mu$+3-jet (b), $ee/\mu\mu$+2-jet (c) and $ee/\mu\mu$+3-jet (d) signal region selections, corresponding to 36.1 fb^{-1} of Run-2 data collected at $\sqrt{s} = 13$ TeV. The stacked histograms correspond to the various jet flavours, and the points to the data. The Statistical uncertainties on the data points are indicated by the error bars. The bottom pad shows the ratio of data to MC, where systematic uncertainty bands (green shaded area) correspond to the normalisation, detector, MC modelling and MC statistical uncertainties.

6.8.1 BDT Cut Optimisation

The optimal cut value on the BDT outputs, $\mathcal{D}_{bb}^{\mathrm{LH}}$, in the 2- and 3-jet channels is determined though a scan of cut values in steps of 0.10. At each step, the b-jet calibration measurement for the 70% efficiency working point is repeated, until the total uncertainty in one calibration bin is found to increase again. The choice of this value must balance the increase in statistical uncertainty due to a reduction in the number of events passing the selection, with the simultaneous decrease in systematic uncertainty. Other b-tagging working points yield consistent results, and therefore the same cut value is used. The optimal BDT cut values are summarised in Table 6.9.

Channel	$\mathcal{D}_{bb}^{\mathrm{LH}}$ Cut Value
2-jet events ($e\mu$ and $ee/\mu\mu$)	0.10
3-jet events ($e\mu$ and $ee/\mu\mu$)	0.10

Table 6.9: Optimal $\mathcal{D}_{bb}^{\mathrm{LH}}$ cut values used for the $t\bar{t}$ likelihood calibration in the 2-jet and 3-jet channels.

6.8.2 Impact on *b*-jet Purity

The aim of applying a cut on $\mathcal{D}_{bb}^{\mathrm{LH}}$ is to increase the b-jet purity. This will subsequently reduce the impact of modelling uncertainties introduced through the modelling of the light-flavour and c-jet fractions. In order to compare the impact of the $\mathcal{D}_{bb}^{\mathrm{LH}}$ cut, Figure 6.9 presents the b-jet fractions in $e\mu$+2-jet events before the $\mathcal{D}_{bb}^{\mathrm{LH}}$ cut (a), and after the $\mathcal{D}_{bb}^{\mathrm{LH}}$ cut (b) for the nominal and alternative $t\bar{t}$ generators. The b-jet purity is greatly increased, for example in the high jet p_{T} region from $\sim 60\%$ to $\sim 85\%$. Furthermore, the differences in b-jet purity between the alternative $t\bar{t}$ generators is reduced, indicating that the impact of the systematic uncertainties will be reduced.

It was tested whether the performance of the BDTs could be further improved by introducing separate BDT trainings for events containing low p_{T} jets, $p_{\mathrm{T}} < 30$ GeV. It was hoped that this training setup would help to accommodate for the different kinematics of the low jet p_{T} region, and therefore boost the separating power. However, it was found that this offered no significant improvement in the reduction of systematic uncertainties from the overall result. Subsequently, only one training is used for the whole jet p_{T} spectrum.

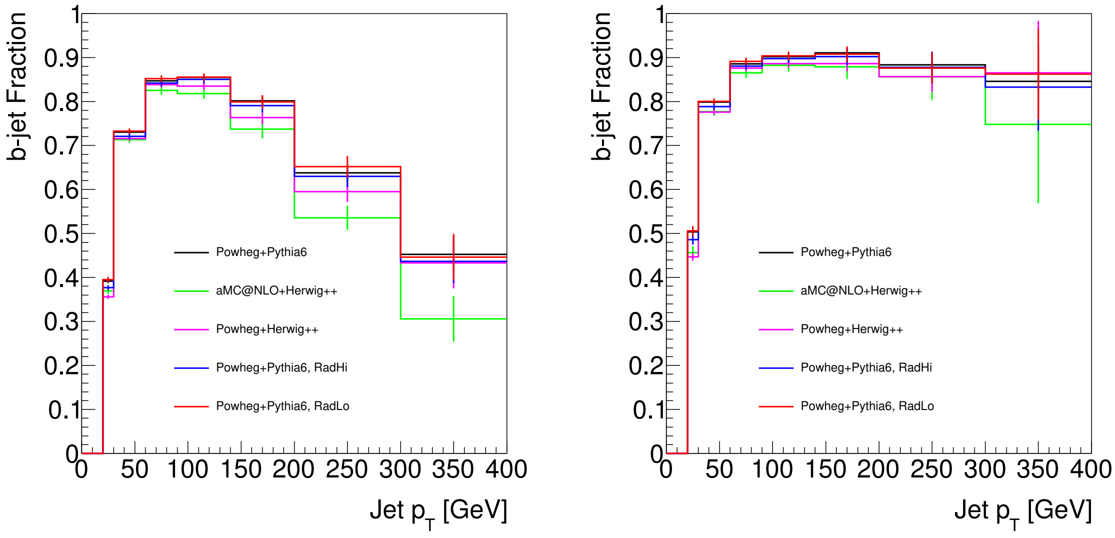

(a) **(b)**

Figure 6.9: The b-jet fractions in the $t\bar{t}$ $e\mu$+2-jet signal region before the $\mathcal{D}_{bb}^{\mathrm{LH}}$ cut (a), and after the $\mathcal{D}_{bb}^{\mathrm{LH}}$ cut (b). Purities are presented for each $t\bar{t}$ generator considered in the calibration; Powheg+Pythia6 (black), aMC@NLO+Herwig++ (green), Powheg+Herwig++ (purple), Powheg+Pythia6 RadHi (blue), and Powheg+Pythia6 RadLo (red).

6.9 Monte Carlo Closure

The likelihood procedure for extracting the b-jet tagging efficiency, as described in Section 6.4, relies on a number of assumptions to simplify the procedure, possibly yielding fitted b-jet efficiencies which differ from the true value. Additionally, the use of the $\mathcal{D}_{bb}^{\mathrm{LH}}$ cut, as described in Section 6.8, could lead to a bias. In order to test the validity of the $t\bar{t}$ likelihood calibration, the procedure is applied to MC, in an analogous way to data. The fitted b-jet tagging efficiencies should, if the fit is unbiased, yield the true b-jet efficiency extracted using the MC truth information. In an unbiased fit, scale factors as a function of jet p_{T} should be consistent with unity, within statistical uncertainties.

To simplify the procedure, the fit is conducted on just $t\bar{t}$ events, with only statistical uncertainties considered. The MC closure test is conducted for the 70% b-jet tagging efficiency working point. Table 6.10 presents the extracted scale factors in each of the four analysis channels, and the combination of all four analysis channels. Figure 6.10 summarises the combined results.

A small non-closure effect of $\sim 4\%$ is observed for $20 < p_{\mathrm{T}} < 30$ GeV in the 3-jet channels. To be conservative, an additional 4% uncertainty is therefore added in this bin for the 3-jet channels to account for this non-closure effect. The cause of this effect is believed to be due to the assumptions introduced to simplify the 3-jet likelihood fit, as described in Equation 6.5.

	b-jet Efficiency Scale Factor ± Total Error				
p_{T} Interval [GeV]	eμ		ee+$\mu\mu$		Combination
	2-jet	3-jet	2-jet	3-jet	
[20; 30]	1.000 ± 0.009	1.038 ± 0.009	1.000 ± 0.014	1.032 ± 0.013	1.018 ± 0.005
[30; 60]	1.000 ± 0.003	0.993 ± 0.004	1.000 ± 0.005	0.995 ± 0.005	0.997 ± 0.002
[60; 90]	0.999 ± 0.003	0.994 ± 0.003	0.998 ± 0.005	0.994 ± 0.005	0.996 ± 0.002
[90; 140]	0.999 ± 0.004	0.998 ± 0.004	1.000 ± 0.005	0.996 ± 0.005	0.998 ± 0.002
[140; 200]	0.995 ± 0.006	0.999 ± 0.006	0.996 ± 0.009	1.001 ± 0.009	0.997 ± 0.004
[200; 300]	1.001 ± 0.014	1.002 ± 0.013	1.012 ± 0.017	1.001 ± 0.016	1.004 ± 0.007

Table 6.10: Scale factors obtained from the $t\bar{t}$ likelihood MC closure test in the $e\mu$+2-jet, $e\mu$+3-jet, $ee/\mu\mu$+2-jet and $ee/\mu\mu$+3-jet channels and their combination, in terms of ratios of the measured to the true b-jet efficiencies, with related statistical uncertainties. The cut on $\mathcal{D}_{bb}^{\mathrm{LH}}$ is applied.

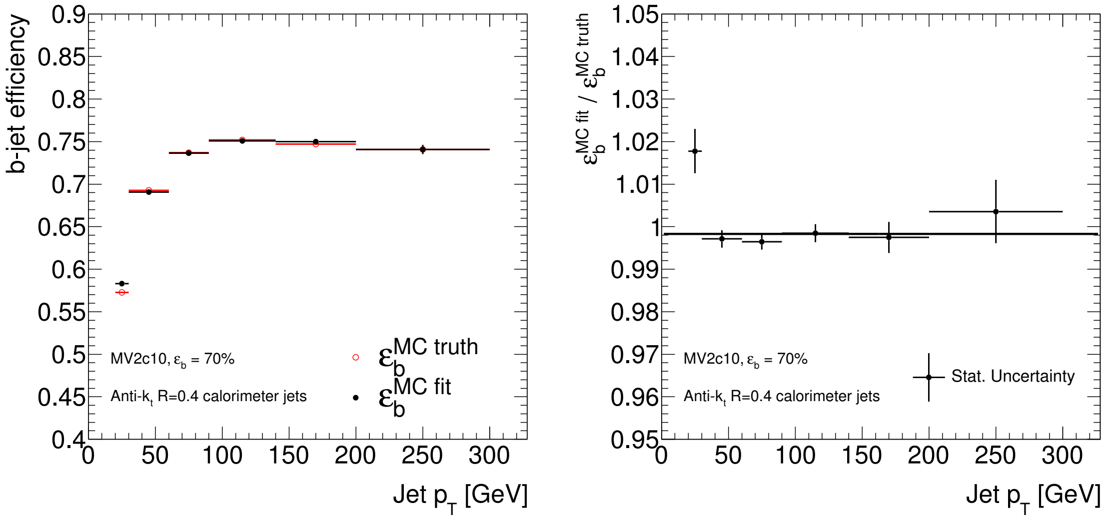

(a) (b)

Figure 6.10: $t\bar{t}$ likelihood calibration MC closure test results. Efficiencies (a) and scale factors (b) from the combination of all 4 channels, with the cut on $\mathcal{D}_{bb}^{\text{LH}}$ applied. $\varepsilon_b^{\text{MC truth}}$ corresponds to the true *b*-tagging efficiency in MC, $\varepsilon_b^{\text{MC fit}}$ corresponds to the measured *b*-tagging efficiency from fitting the likelihood to MC. A small ($\sim 4\%$) non-closure effect is seen in the lowest p_{T} bin of the 3-jet channels, and is added as an additional systematic uncertainty in the final fit to data.

6.10 Scale Factor Results

6.10.1 Calibration of the MV2c10 70% Efficiency Working Point

In the following section, results for the 70% *b*-jet tagging efficiency working point are presented. Scale factors are presented as a function of jet p_{T}, derived for six p_{T} bins. The true MC efficiencies as a function of p_{T} for the samples used in this analysis are shown for reference in Table 6.11.

Table 6.12 shows the *b*-jet tagging efficiencies measured in 2015 and 2016 collision data for all calibration channels. In Table 6.13, the data-over-MC scale factors for each channel with the total uncertainty are presented. The result of the combination of all channels is shown in Table 6.14 and in Figure 6.11. The detailed effect is shown of each systematic uncertainty on the scale factors measured for the *b*-tagging efficiency for all channels in Table 6.15.

Whilst scale factors consistent with unity are obtained, it is still necessary to apply these in analyses in order to consider the effect of systematic uncertainties, as well as to ensure consistency with the application of *c*- and light-flavour jet scale factors.

	b-jet Efficiency (%)			
p_{T} Interval	$e\mu$		$ee/\mu\mu$	
[GeV]	2-jet	3-jet	2-jet	3-jet
$[20; 30]$	58.0 ± 0.3	56.7 ± 0.3	57.4 ± 0.5	55.8 ± 0.4
$[30; 60]$	69.6 ± 0.1	68.9 ± 0.1	69.2 ± 0.3	68.8 ± 0.2
$[60; 90]$	74.0 ± 0.1	73.6 ± 0.1	74.2 ± 0.2	73.8 ± 0.2
$[90; 140]$	75.2 ± 0.2	75.0 ± 0.1	75.8 ± 0.3	75.0 ± 0.2
$[140; 200]$	75.6 ± 0.3	74.9 ± 0.2	75.6 ± 0.4	74.4 ± 0.3
$[200; 300]$	73.7 ± 0.6	74.4 ± 0.3	72.9 ± 0.8	73.9 ± 0.4

Table 6.11: True MC efficiencies (in %) for the $e\mu$+2-jet, $e\mu$+3-jet, $ee/\mu\mu$+2-jet and $ee/\mu\mu$+3-jet channels for the 70% working point, with the $\mathcal{D}_{bb}^{\mathrm{LH}}$ cut applied. The uncertainties correspond to MC statistical uncertainties only.

	b-jet Efficiency (%) ± Statistical Error ± Systematic Error (Total Error)			
p_{T} Interval	$e\mu$		$ee/\mu\mu$	
[GeV]	2-jet	3-jet	2-jet	3-jet
$[20; 30]$	58.7 ± 0.7 ± 8.5 (8.6)	58.1 ± 0.7 ± 8.2 (8.3)	57.6 ± 1.2 ± 7.3 (7.4)	60.0 ± 1.1 ± 9.2 (9.3)
$[30; 60]$	71.4 ± 0.3 ± 2.4 (2.4)	71.9 ± 0.3 ± 2.1 (2.2)	71.0 ± 0.6 ± 3.3 (3.3)	70.6 ± 0.6 ± 2.7 (2.7)
$[60; 90]$	75.7 ± 0.3 ± 1.6 (1.7)	75.3 ± 0.3 ± 1.4 (1.4)	76.9 ± 0.6 ± 2.8 (2.9)	77.7 ± 0.6 ± 1.9 (2.0)
$[90; 140]$	76.8 ± 0.4 ± 1.8 (1.8)	76.2 ± 0.4 ± 2.2 (2.3)	76.5 ± 0.6 ± 2.5 (2.6)	76.0 ± 0.7 ± 3.4 (3.5)
$[140; 200]$	74.9 ± 0.8 ± 2.4 (2.6)	74.6 ± 0.8 ± 4.7 (4.8)	74.1 ± 1.1 ± 2.0 (2.3)	73.9 ± 1.1 ± 4.7 (4.8)
$[200; 300]$	71.9 ± 1.7 ± 2.8 (3.2)	69.2 ± 1.6 ± 10.0 (10.1)	69.5 ± 2.2 ± 2.6 (3.4)	71.2 ± 2.1 ± 10.3 (10.5)

Table 6.12: Measured efficiencies in data (in %) for the $e\mu$+2-jet, $e\mu$+3-jet, $ee/\mu\mu$+2-jet and $ee/\mu\mu$+3-jet channels for the 70% working point using the $t\bar{t}$ likelihood calibration, with the $\mathcal{D}_{bb}^{\mathrm{LH}}$ cut applied. The first uncertainty is the statistical uncertainty, the second refers to the systematic uncertainty, and the total uncertainty is in parenthesis.

	b-jet Efficiency Scale Factor ± Total Error			
p_{T} Interval	$e\mu$		$ee/\mu\mu$	
[GeV]	2-jet	3-jet	2-jet	3-jet
$[20; 30]$	1.01 ± 0.15	1.02 ± 0.15	1.00 ± 0.13	1.08 ± 0.17
$[30; 60]$	1.03 ± 0.04	1.04 ± 0.03	1.03 ± 0.05	1.03 ± 0.04
$[60; 90]$	1.02 ± 0.02	1.02 ± 0.02	1.04 ± 0.04	1.05 ± 0.03
$[90; 140]$	1.02 ± 0.02	1.02 ± 0.03	1.01 ± 0.03	1.01 ± 0.05
$[140; 200]$	0.99 ± 0.03	1.00 ± 0.06	0.98 ± 0.03	0.99 ± 0.07
$[200; 300]$	0.98 ± 0.04	0.93 ± 0.14	0.95 ± 0.05	0.96 ± 0.14

Table 6.13: Measured data-over-MC scale factors for the $e\mu$+2-jet, $e\mu$+3-jet, $ee/\mu\mu$+2-jet and $ee/\mu\mu$+3-jet channels, with the total (statistical + systematic) uncertainty for the 70% working point using the $t\bar{t}$ likelihood calibration, with the $\mathcal{D}_{bb}^{\mathrm{LH}}$ cut applied.

p_{T} Interval [GeV]	Scale Factor	Statistical Error	Systematic Error	Total Error
[20; 30]	1.013	0.012	0.123	0.123
[30; 60]	1.035	0.003	0.030	0.030
[60; 90]	1.029	0.004	0.018	0.018
[90; 140]	1.019	0.004	0.021	0.022
[140; 200]	0.984	0.010	0.024	0.026
[200; 300]	0.964	0.018	0.032	0.037

Table 6.14: Scale factors obtained from combining all channels for the 70% working point using the $t\bar{t}$ likelihood calibration, with the $\mathcal{D}_{bb}^{\mathrm{LH}}$ cut applied.

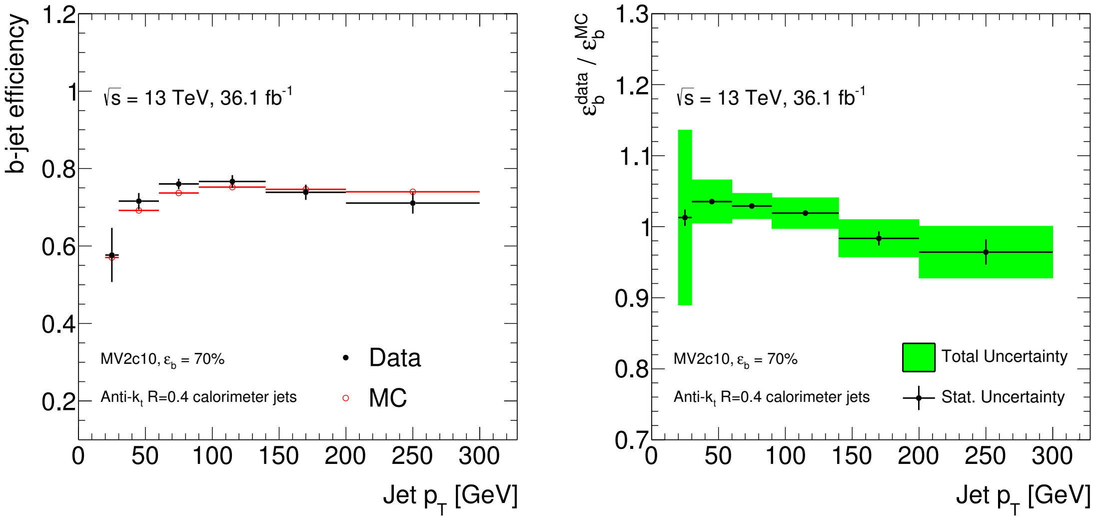

(a) (b)

Figure 6.11: The *b*-jet tagging efficiencies in data (black) and MC (red) (a) and *b*-tagging efficiency scale factors (b) obtained from the combination of all channels for the 70% working point using the $t\bar{t}$ likelihood calibration, with the $\mathcal{D}_{bb}^{\mathrm{LH}}$ cut applied. Statistical errors are indicated by the error bar, and the total uncertainty is indicated by the shaded green region.

p_{T} Interval [GeV]	20-30	30-60	60-90	90-140	140-200	200-300
Scale factor	1.013	1.035	1.029	1.019	0.984	0.964
Total uncertainty	0.123	0.030	0.018	0.022	0.026	0.037
Statistical uncertainty	0.012	0.003	0.004	0.004	0.010	0.018
Systematic uncertainty	0.123	0.030	0.018	0.021	0.024	0.032
Systematic Uncertainties [%]						
Modelling Uncertainties						
Modelling ($t\bar{t}$)	3.2	0.3	0.9	1.1	1.1	0.7
Hadronisation ($t\bar{t}$)	9.0	1.5	0.3	1.0	1.4	2.2
NNLO top p_{T}, $t\bar{t}$ p_{T} reweighting ($t\bar{t}$)	0.1	0.1	0.1	0.3	0.5	0.9
PDF reweighting ($t\bar{t}$)	0.9	0.2	0.2	0.3	0.4	0.4
More / less radiation ($t\bar{t}$)	1.7	0.9	0.4	0.3	0.6	0.4
Modelling (Wt)	0.5	0.2	0.2	0.2	0.3	0.1
Parton shower / Hadronisation (Wt)	1.1	0.1	0.1	0.0	0.1	0.2
More / less radiation (Wt)	0.0	0.0	0.0	0.1	0.1	0.1
DR vs. DS (Wt)	0.1	0.1	0.1	0.1	0.1	0.2
Modelling ($Z+\mathrm{jets}$)	0.6	0.5	0.5	0.9	0.6	1.2
p_{T} reweighting ($Z+\mathrm{jets}$)	0.0	0.1	0.0	0.1	0.1	0.1
Normalisation Uncertainties						
Wt	0.2	0.1	0.0	0.1	0.1	0.1
$Z+\mathrm{jets}$	1.8	0.5	0.5	0.4	0.5	0.5
$Z+b/c$	0.4	0.1	0.1	0.0	0.0	0.0
Diboson	1.6	1.1	0.7	0.6	0.7	0.8
Fake leptons	0.7	0.7	0.6	0.6	0.5	0.5
Experimental Uncertainties						
Pile-up reweighting	0.3	0.0	0.0	0.2	0.3	0.6
Electron efficiency/resolution/scale/trigger	0.1	0.0	0.0	0.0	0.0	0.0
Muon efficiency/resolution/scale/trigger	0.1	0.0	0.0	0.0	0.2	0.2
$E_{\mathrm{T}}^{\mathrm{miss}}$	0.1	0.0	0.0	0.0	0.1	0.1
JVT	0.1	0.0	0.1	0.1	0.0	0.1
Jet energy scale (JES)	6.8	1.4	0.5	0.4	0.5	0.7
Jet energy resolution (JER)	0.0	1.3	0.3	0.1	0.3	0.4
Light-flavour jet mis-tag rate	0.6	0.1	0.0	0.0	0.0	0.0
c-jet mis-tag rate	0.6	0.1	0.1	0.0	0.0	0.0
Luminosity	0.2	0.1	0.1	0.1	0.1	0.1
Non-Closure Uncertainty						
MC Non-Closure	1.2	0.0	0.0	0.0	0.0	0.0

Table 6.15: b-tagging efficiency scale factors measured from the combination of all channels for the working point using the $t\bar{t}$ likelihood calibration, with the $\mathcal{D}_{bb}^{\mathrm{LH}}$ cut applied. The sign of the uncertainty is determined by subtracting the nominal scale factor from the varied sample scale factor.

6.10.2 Comparison to Results Without BDT Selection

In order determine the impact of the multivariate event selection to boost the *b*-jet purity, scale factors have been calculated without the $\mathcal{D}_{bb}^{\mathrm{LH}}$ cut applied, again for the 70% *b*-jet tagging efficiency working point. The result of the combination of all channels is shown in Table 6.16 and in Figure 6.12.

A comparison of the calibration scale factors with and without the $\mathcal{D}_{bb}^{\mathrm{LH}}$ cut is shown in Figure 6.13. A large reduction in the scale factor uncertainty is achieved. More precisely, comparing Tables 6.16 and 6.14, the largest reduction in the scale factor uncertainty is in the highest jet p_{T} bin, $[200; 300]$ GeV. The total uncertainty is reduced from 0.112 to 0.037, corresponding to a factor of ~ 3 reduction, with smaller reductions across the full jet p_{T} spectrum. This is expected from the significant improvement in the *b*-jet purity from applying the $\mathcal{D}_{bb}^{\mathrm{LH}}$ selection. This is highly beneficial in reducing the impact of the systematic uncertainties associated with *b*-tagging in analyses.

p_{T} Interval [GeV]	Scale Factor	Statistical Error	Systematic Error	Total Error
$[20; 30]$	1.021	0.009	0.125	0.125
$[30; 60]$	1.050	0.004	0.033	0.033
$[60; 90]$	1.040	0.004	0.019	0.020
$[90; 140]$	1.020	0.004	0.031	0.032
$[140; 200]$	0.981	0.006	0.059	0.059
$[200; 300]$	0.936	0.014	0.111	0.112

Table 6.16: Scale factors obtained from combining all channels for the 70% working point using the $t\bar{t}$ likelihood calibration, without the $\mathcal{D}_{bb}^{\mathrm{LH}}$ cut applied.

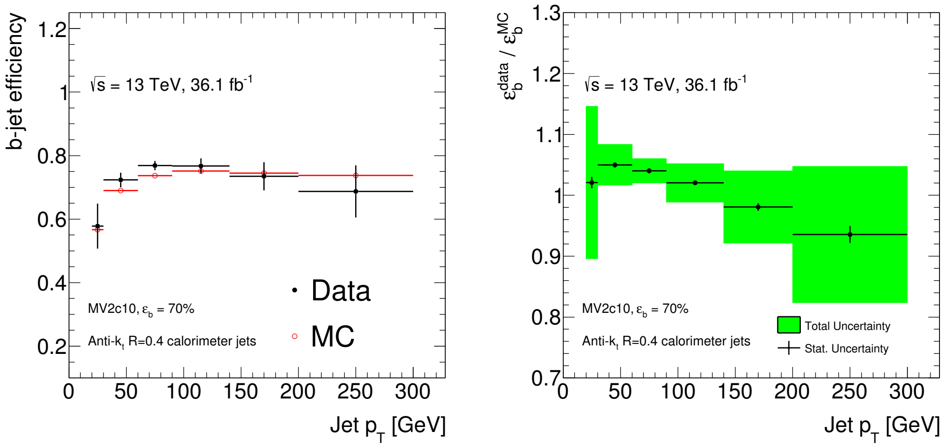

(a) (b)

Figure 6.12: The *b*-jet tagging efficiencies in data (black) and MC (red) (a) and *b*-tagging efficiency scale factors (b) obtained from the combination of all channels for the 70% working point using the $t\bar{t}$ likelihood calibration, without the $\mathcal{D}_{bb}^{\mathrm{LH}}$ cut applied. Statistical errors are indicated by the error bar, and the total uncertainty is indicated by the shaded green region.

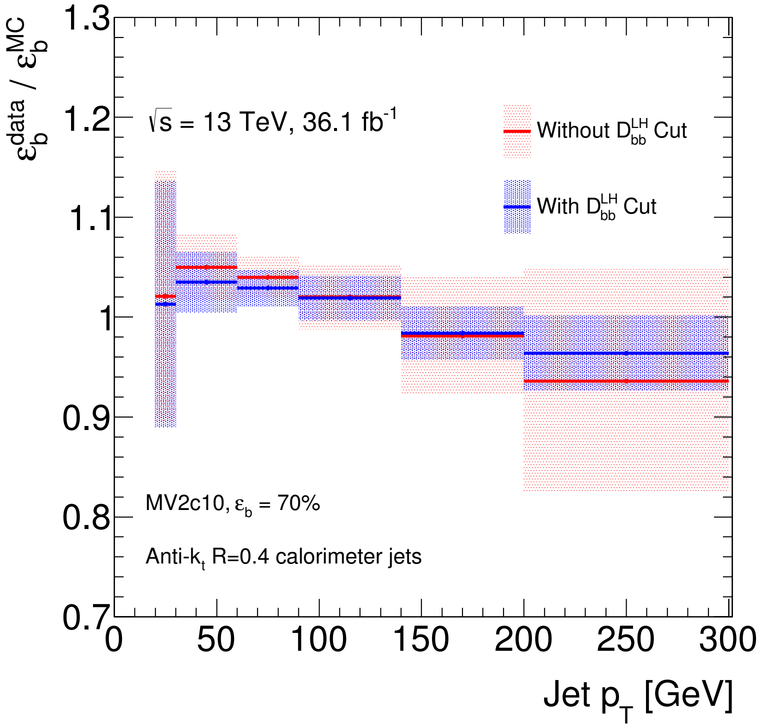

Figure 6.13: Comparison of the data-over-MC scale factors without the $\mathcal{D}_{bb}^{\mathrm{LH}}$ cut applied (shaded red), and with the $\mathcal{D}_{bb}^{\mathrm{LH}}$ cut applied (shaded blue) measured using the $t\bar{t}$ likelihood calibration. The shaded regions correspond to the total scale factor uncertainty.

6.11 Summary

The b-jet tagging efficiency in data has been calibrated using an enriched data sample of $t\bar{t}$ events, corresponding to 36.1 fb^{-1} of Run-2 data. Using a di-leptonic $t\bar{t}$ event selection, a b-jet purity between 50% and 70% is achieved, with good modelling of event variables observed. The procedure, developed during Run-1 of the LHC, has been updated to include Run-2 systematic uncertainties, and modified to include a multivariate event selection. The implementation of a BDT, trained to identify $b\bar{b}$ pairs, and reject events with other jet flavour compositions, has resulted in a significant improvement in the b-jet purity. Subsequently, the impact of uncertainties arising from the modelling of the light-flavour jet and c-jet fraction have been greatly reduced, resulting in a factor of ~ 3 reduction of the scale factor uncertainties in the highest jet p_{T} region. Whilst results have only been presented for the *anti-k_t* $R = 0.4$ calorimeter jet collection at the 70% b-jet tagging efficiency working point, the procedure has been applied to other working points and jet collections. The calibration scale factors derived using the $t\bar{t}$ likelihood calibration are used as the default b-jet tagging efficiency calibration procedure for 2015 and 2016 data in all ATLAS analyses that use b-tagging.

Chapter 7

The Search for Standard Model $VH \to Vb\bar{b}$

7.1 Overview

During Run-1 of the LHC, a new spin-0 scalar boson was observed by both the ATLAS and CMS experiments [10, 11]. In a combination of Run-2 ATLAS data from $H \to \gamma\gamma$ and $H \to ZZ^* \to 4\ell$ decays, the Higgs boson mass was measured as $m_H = 124.98 \pm 0.19(\text{stat.}) \pm 0.21(\text{syst.})$ GeV [16]. The mass corresponds to an expected branching ratio of $H \to b\bar{b}$ is $0.582^{+0.007}_{-0.007}$ [24], which is the largest decay mode of the SM Higgs boson.

However, the background $b\bar{b}$ production cross section is approximately 10^7 times larger than the gluon-gluon fusion Higgs production cross section [84]. The small signal-to-background ratio therefore makes observation extremely challenging in the gluon-gluon fusion production channel. An alternative approach is to instead search for the associated production of a Higgs boson with a vector boson ($V = W/Z$). Leptonic decays of the vector boson provide an effective way to trigger events, whilst also greatly reducing the multijet background. Three analysis channels are considered to target each of the leptonic decays of the vector boson. The 0-lepton channel targets $Z \to \nu\nu$ (where the neutrinos manifest themselves as $E_{\mathrm{T}}^{\mathrm{miss}}$), the 1-lepton channel targets $W \to l\nu$, and the 2-lepton channel targets $Z \to ll$ decays. Feynman diagrams for quark initiated $VH \to Vb\bar{b}$ production are presented in Figure 7.1, and for the gluon initiated production in Figure 7.2. In spite of the cost in production cross-section ($VH \to Vb\bar{b}$ production corresponds to $\sim 5\%$ of all Higgs production at the LHC), the $VH \to Vb\bar{b}$ production mode is one of the most sensitive in which to search for the $H \to b\bar{b}$ decay at the LHC [85].

During Run-1 of the LHC, ATLAS observed a $H \to b\bar{b}$ signal significance of 1.4 σ[1], compared to 2.6 σ expected in the VH production mode [83]. CMS observed a signal significance of 2.1 σ, compared to 2.1 σ expected [86]. The combination of both ATLAS and CMS data yielded an observed signal significance of 2.6 σ, with 3.7 σ expected [87]. Finding evidence for, and later

---

[1] The signal significance is measured in terms of the number of observed standard deviations from the background-only model, with one standard deviation corresponding to 1 σ.

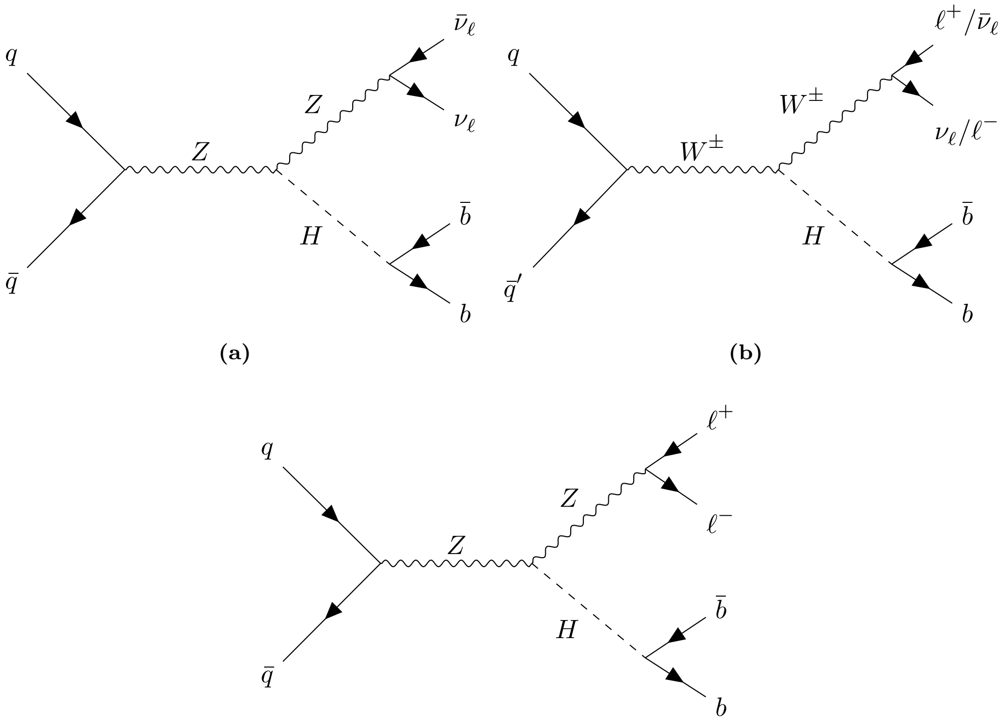

(a) **(b)**

(c)

Figure 7.1: Feynman diagrams for the leading-order quark initiated SM $VH \to Vb\bar{b}$ process in the 0- (a), 1- (b) and 2-lepton (c) channels.

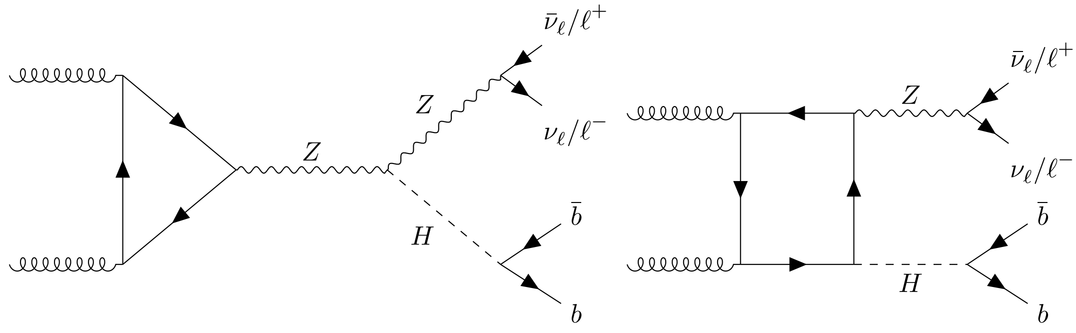

Figure 7.2: Feynman diagrams for the leading-order gluon initiated SM $VH \to Vb\bar{b}$ process in the 0- and 2-lepton channels.

observing, the $H \to b\bar{b}$ decay is one of the main physics goals of the LHC physics programme, and vital for confirming that the scalar boson observed during Run-1 is indeed the SM Higgs boson.

Whilst the multijet background is greatly reduced in the $VH \to Vb\bar{b}$ channel, a number of key backgrounds still remain. These backgrounds are significantly larger than the signal, and composed of several different processes. The main backgrounds are $t\bar{t}$ (all channels), $Z+$jets (0- and 2-lepton), $W+$jets (0- and 1-lepton) and single top-quark (1-lepton).

To reduce the large background, the analysis is performed in the 'boosted' regime, as the signal is preferentially produced with a large p_{T}. To further boost the sensitivity of the analysis to $VH \to Vb\bar{b}$ signal events, a boosted decision tree (BDT) is trained to separate signal events from background. Simulated samples are fitted to data using a global profile likelihood fit of the BDT output, referred to as the global likelihood fit or simply 'fit' throughout. The global likelihood fit incorporates a number of analysis regions to determine the ratio of the measured $VH \to Vb\bar{b}$ signal yield to the SM expectation, known as the signal strength. Analysis regions include both signal regions, which have the most sensitivity to the $VH \to Vb\bar{b}$ signal, and control regions, used to constrain the various background processes using data. In order to validate the fit to the $VH \to Vb\bar{b}$ signal using the BDT, an analogous fit is conducted to the SM $VZ \to Vb\bar{b}$ signal, using a BDT retrained to identify $VZ \to Vb\bar{b}$ events as signal. Additionally, a fit to the reconstructed dijet Higgs mass, m_{bb}, is conducted using a cut-based selection. Whilst the fit to m_{bb} has reduced sensitivity to the $VH \to Vb\bar{b}$ signal, it offers a further validation of the background model, fitting procedure and multivariate approach.

This chapter will discuss the analysis strategy and results from the Run-2 ATLAS measurement of $VH \to Vb\bar{b}$ using 36.1 fb^{-1} of data collected at $\sqrt{s} = 13$ TeV [3]. Section 7.2 presents the event selections and analysis regions. Section 7.3 presents the data and samples used. The training and performance of this BDT to separate signal events from background is presented in Section 7.4. An overview of the fit procedure is summarised in Section 7.5, with systematic uncertainties discussed in Section 7.6. Validations of the fit model are described in Section 7.7, and results are presented in Section 7.8, including those from the cross-checks of the analysis. Future prospects for the analysis beyond the current iteration are discussed in Section 7.9.

7.2 Object and Event Selection

7.2.1 Event Selection

In this section, the event selection of all channels is discussed, and summarised in Table 7.1.

Leptons: To target each of the vector boson decay modes ($Z \to \nu\nu$, $W \to \ell\nu$, $Z \to \ell\ell$), events are categorised based on the number of *Loose* leptons. Events with 0 *Loose* leptons reside in the 0-lepton channel, 1 *Loose* lepton in the 1-lepton channel, and 2 *Loose* leptons in the 2-lepton channel, as defined in Sections 3.5.2 and 3.5.3. Additionally, in the 1-lepton and 2-lepton channels, tighter requirements are placed on the signal leptons:

- **1-lepton channel**: Events are required to have exactly 1 *WH-Signal* lepton to improve the WH signal purity.
- **2-lepton channel**: Events are required to have 1 or more *ZH-Signal* leptons. The invariant mass of the two leptons, $m_{\ell\ell}$, is required to be consistent with the mass of the Z boson, m_Z; $81 < m_{\ell\ell} < 101$ GeV. In the signal region, the leptons are required to have the same flavour, such that they are consistent with the decay of a Z boson.

Trigger: Data events are collected using a $E_{\mathrm{T}}^{\mathrm{miss}}$ trigger in the 0-lepton channel and 1-lepton muon sub-channel. The $E_{\mathrm{T}}^{\mathrm{miss}}$ trigger relies on calorimeter information, meaning that high p_{T} muons manifest themselves as $E_{\mathrm{T}}^{\mathrm{miss}}$ in the calorimeter trigger system, and can therefore fire the trigger. For 2015 data, the $E_{\mathrm{T}}^{\mathrm{miss}}$ trigger threshold was set at 70 GeV, whilst for 2016 data, thresholds of 90 GeV and 110 GeV were used, depending on the data-taking period. Single lepton triggers are used for the 1-lepton electron sub-channel and 2-lepton channel. The lowest un-prescaled single electron (muon) trigger threshold was initially set at 24 GeV (20 GeV) for 2015 data, and subsequently raised to 26 GeV (24-26 GeV) for 2016 data.

Jets: Events are categorised by the number of jets. Signal jets are defined to be in the range $|\eta| < 2.5$ and $p_{\mathrm{T}} > 20$ GeV. Forward jets are defined to be in the range $2.5 < |\eta| < 4.5$ and $p_{\mathrm{T}} > 30$ GeV. Events with exactly 2 signal jets form the 2-jet category, events with exactly 3 jets form the 3-jet category, and events with 3 or more jets form the 3+-jet category. In the 0-, 1- and 2-lepton channels, the 2-jet category is used. In the 0- and 1-lepton channels, the 3-jet category is used, whilst in the 2-lepton channel, the 3+-jet category is used. This is due to a smaller $t\bar{t}$ contamination in high jet multiplicity events in the 2-lepton channel, allowing high jet multiplicity signal events to be recovered.

***b*-tagging:** Exactly two signal jets are required to be b-tagged at the 70% efficiency working point, where all signal jets are considered for b-tagging. The leading b-tagged jet is required to have $p_{\mathrm{T}} > 45$ GeV, and the two b-tagged jets are used to construct the $H \to b\bar{b}$ candidate.

Vector boson: In the 0-lepton channel, the transverse momentum of the Z boson, p_{T}^{Z}, is reconstructed as $E_{\mathrm{T}}^{\mathrm{miss}}$, with a cut placed at $p_{\mathrm{T}}^{Z} > 150$ GeV, due to the slow turn-on curve of the $E_{\mathrm{T}}^{\mathrm{miss}}$ trigger. In the 1-lepton channel, the transverse momentum of the W boson, p_{T}^{W}, is reconstructed as the vectorial sum of the lepton transverse momentum, p_{T}^{ℓ}, and $E_{\mathrm{T}}^{\mathrm{miss}}$. A cut is also placed at $p_{\mathrm{T}}^{W} > 150$ GeV, due to the large multijet contamination at low p_{T}^{W} values. In the 2-lepton channel, p_{T}^{Z} is the vectorial sum of the momentum of the two leptons, with a cut placed at $p_{\mathrm{T}}^{Z} > 75$ GeV due to low signal sensitivity in the lower p_{T}^{Z} regions. The 2-lepton channel is split into two regions, $75 < p_{\mathrm{T}}^{Z} < 150$ GeV and $p_{\mathrm{T}}^{Z} > 150$ GeV.

Multijet: In the 0-lepton channel the multijet background is reduced through a series of angular topological cuts. In the 1-lepton channel, the region with $E_{\mathrm{T}}^{\mathrm{miss}} > 30$ GeV is selected in the electron only sub-channel to reduce the multijet contamination.

Common Selections	
Jets	≥ 2 central jets
b-jets	Exactly 2 b-tagged signal jets
Leading jet p_{T}	> 45 GeV
0-Lepton	
Trigger	$E_{\mathrm{T}}^{\mathrm{miss}}$
Jets	Exactly 2 or 3 jets
Leptons	Exactly 0 *Loose* leptons
$E_{\mathrm{T}}^{\mathrm{miss}}$	> 150 GeV
H_{T}	> 120 (2-jet), >150 GeV (3-jet)
$\lvert\min(\Delta\phi(E_{\mathrm{T}}^{\mathrm{miss}}, \mathrm{jets}))\rvert$	$> 20^{\circ}$ (2-jet), $> 30^{\circ}$(3-jet)
$\lvert\Delta\phi(E_{\mathrm{T}}^{\mathrm{miss}}, bb)\rvert$	$> 120^{\circ}$
$\lvert\Delta\phi(b_1, b_2)\rvert$	$< 140^{\circ}$
$\lvert\Delta\phi(E_{\mathrm{T}}^{\mathrm{miss}}, E_{\mathrm{T,trk}}^{\mathrm{miss}})\rvert$	$< 90^{\circ}$
p_{T}^{V} regions	$[150, \infty]$ GeV
1-Lepton	
Trigger	e sub-channel: single electron μ sub-channel: $E_{\mathrm{T}}^{\mathrm{miss}}$
Jets	Exactly 2 or 3 jets
Leptons	Exactly 1 *WH-Signal* lepton Exactly 1 *Loose* lepton
$E_{\mathrm{T}}^{\mathrm{miss}}$	> 30 GeV (e sub-channel)
p_{T}^{V} regions	$[150, \infty]$ GeV
2-Lepton	
Trigger	Single lepton
Jets	Exactly 2 or ≥ 3 jets
Leptons	Exactly 2 *Loose* leptons ≥ 1 *ZH-Signal* lepton Opposite-charge for $\mu\mu$
$m_{\ell\ell}$	$81 < m_{\ell\ell} < 101$ GeV
p_{T}^{V} regions	$[75, 150]$, $[150, \infty]$ GeV

Table 7.1: Summary of the signal event selection in the 0-, 1- and 2-lepton channels of the $VH \to Vb\bar{b}$ analysis, where b_1 and b_2 are the two b-tagged jets forming the Higgs boson candidate dijet system, bb, H_{T} is the scalar sum of the p_{T} of the jets in an event and $E_{\mathrm{T,trk}}^{\mathrm{miss}}$ is defined as the missing transverse momentum calculated from the negative vector sum of the transverse momenta of tracks reconstructed in the inner detector.

7.2.1.1 Cut-Based Dijet Mass Analysis Selection

In order to boost the sensitivity of the cut-based dijet mass analysis, a number of modifications to further tighten the event selection are made, and summarised in Table 7.2. The selection cuts for the cut-based dijet mass analysis are taken from the Run-1 version of the $VH \to Vb\bar{b}$ analysis [83].

In all channels, additional requirements are placed on the separation between the 2 b-tagged jets in ΔR space, $|\Delta R(b_1, b_2)|$. The approximation for $1 \to 2$ body decays gives the following relationship

$$\Delta R \sim \frac{2m}{p_{\mathrm{T}}}, \tag{7.1}$$

with ΔR the separation in $\eta - \phi$ space of the decay products, m the mass of the parent particle and p_{T} the transverse momentum of the parent particle. Therefore, as the boost of the Higgs is increased, the separation between the decay products is reduced. Assuming the Higgs has recoiled from the V boson in the rest frame of the detector, denoting p_{T}^{H} as the Higgs transverse momentum, $p_{\mathrm{T}}^{V} \sim p_{\mathrm{T}}^{H}$. Therefore, at higher p_{T}^{V} values, the ΔR separation is reduced for signal events, but the same does not hold true for background events. Due to increased signal purity in higher p_{T}^{V} regions, the fitting regions are further separated to $150 < p_{\mathrm{T}}^{V} < 200$ GeV and $p_{\mathrm{T}}^{V} > 200$ GeV to increase signal sensitivity [83].

In the 1- and 2-lepton channels, there are further specific modifications to the event selection:

- **1-lepton channel**: To reduce the $t\bar{t}$ background, it is required that $m_{\mathrm{T}}^{W} < 120$ GeV[2].
- **2-lepton channel**: To reduce the $t\bar{t}$ background, it is required that $E_{\mathrm{T}}^{\mathrm{miss}}/\sqrt{S_{\mathrm{T}}} < 3.5\ \sqrt{\mathrm{GeV}}$, with S_{T} defined as the scalar sum of the transverse momentum of the leptons and jets in an event.

	Channel		
Selection	0-Lepton	1-Lepton	2-Lepton
m_{T}^{W}	-	< 120 GeV	-
$E_{\mathrm{T}}^{\mathrm{miss}}/\sqrt{S_{\mathrm{T}}}$	-	-	$< 3.5\ \sqrt{\mathrm{GeV}}$
	p_{T}^{V} Region		
p_{T}^{V}	[75, 150] GeV (2-lepton only)	[150, 200] GeV	$[200, \infty]$ GeV
$\Delta R(b_1,\ b_1)$	< 3.0	< 1.8	< 1.2

Table 7.2: Summary of the signal event selection in the 0-, 1- and 2-lepton channels of the cut-based dijet mass $VH \to Vb\bar{b}$ analysis.

---

[2] The W transverse mass, m_{T}^{W}, is defined in the 1-lepton channel as $m_{\mathrm{T}}^{W} = \sqrt{2p_{\mathrm{T}}^{\ell}E_{\mathrm{T}}^{\mathrm{miss}}(1-\cos(\Delta\phi(\boldsymbol{\ell}, \boldsymbol{E}_{\mathrm{T}}^{\mathrm{miss}}))}$, where p_{T}^{ℓ} is the lepton transverse momentum, $\boldsymbol{\ell}$ is the lepton momentum 4-vector, and $\boldsymbol{E}_{\mathrm{T}}^{\mathrm{miss}}$ is the 4-vector of the missing transverse momentum.

7.2.2 Analysis Regions

In the nominal version of the analysis, the signal strength and significance are measured using a global profile likelihood fit to the BDT output discriminant. The regions used in the fit are summarised in Table 7.3. A total of eight signal regions (SR), composed of the various jet multiplicity and p_{T}^{V} bins, and six control regions (CR), used to constrain the background processes, are implemented in the global profile likelihood fit. Events passing the selection described in Section 7.2.1 are used in the signal regions, except for those lying in an orthogonal control region. A $W+$HF CR is defined for the 1-lepton channel, and is described in Section 7.2.2.1. A single bin is used ("Yield") in this region, which allows the $W+$HF normalisation to be constrained from the data. In the 2-lepton channel, a top $e\mu$ CR in implemented, and is described in Section 7.2.2.2. The m_{bb} distribution is input for this region, which allows the top m_{bb} shape and normalisation to be constrained from the data.

In the dijet mass analysis, the fitting regions are modified in order to improve the analysis sensitivity. An additional division at $p_{\mathrm{T}}^{V} = 200$ GeV is made in all channels (except in the top $e\mu$ CR in order to maintain a sufficient number of data events) to exploit the larger signal sensitivity in the higher p_{T}^{V} regions. In the 1-lepton channel, the $W+$HF CR is merged into the signal region as the low m_{bb} region sufficiently constrains the $W+$HF background. The corresponding analysis regions for the cut-based dijet mass analysis are summarised in Table 7.4. There are additional regions due to the extra p_{T}^{V} division.

Channel	SR/CR	Categories			
		2 b-tagged jets			
		75 GeV $< p_{\mathrm{T}}^{V} <$ 150 GeV		$p_{\mathrm{T}}^{V} >$ 150 GeV	
		2-jet	3-jet	2-jet	3-jet
0-lepton	SR	-	-	BDT	BDT
1-lepton	SR	-	-	BDT	BDT
2-lepton	SR	BDT	BDT	BDT	BDT
1-lepton	W+HF CR	-	-	Yield	Yield
2-lepton	Top $e\mu$ CR	m_{bb}	m_{bb}	Yield	m_{bb}

Table 7.3: The distributions used in the global profile likelihood fit for the signal regions (SR) and control regions (CR) for all the categories in each channel, for the nominal $VH \to Vb\bar{b}$ analysis.

7.2.2.1 $W+$HF Control Region

In an earlier version of the Run-2 analysis using 13.2 fb^{-1} of data [2], one of the largest systematic uncertainties was identified as originating from the normalisation uncertainty on the $W+$HF background. This is one of the dominant background processes in the 1-lepton channel, which if better controlled, would improve the signal sensitivity of the analysis. A dedicated $W+$HF CR has therefore been defined and included in the analysis.

Channel	SR/CR	Categories					
		75 GeV $< p_{\mathrm{T}}^{V} <$ 150 GeV		150 GeV $< p_{\mathrm{T}}^{V} <$ 200 GeV		$p_{\mathrm{T}}^{V} >$ 200 GeV	
		2-jet	3-jet	2-jet	3-jet	2-jet	3-jet
0-lepton	SR	-	-	m_{bb}	m_{bb}	m_{bb}	m_{bb}
1-lepton	SR plus $W+$HF CR	-	-	m_{bb}	m_{bb}	m_{bb}	m_{bb}
2-lepton	SR	m_{bb}	m_{bb}	m_{bb}	m_{bb}	m_{bb}	m_{bb}
2-lepton	Top $e\mu$ CR	m_{bb}	m_{bb}	Yield*	$m_{bb}{}^{\dagger}$	Yield*	$m_{bb}{}^{\dagger}$

Table 7.4: The distributions used in the global profile likelihood fit for the dijet mass analysis, for the signal (SR) and control regions (CR), in each channel. The two regions marked with * (†) are merged into a single region, to reduce statistical uncertainties.

The aim of the $W+$HF CR is to obtain a region with a high $W+$HF purity, such that the normalisation can be better constrained when fitting to data. As the other main background in the 1-lepton channel is from $t\bar{t}$, a key challenge in isolating the $W+$HF background is to remove the $t\bar{t}$ background. This is achieved by using a cut on the reconstructed leptonically decaying top mass, m_{top} (assuming a semi-leptonic $t\bar{t}$ decay). To calculate m_{top}, it is first necessary to determine the longitudinal momentum of the neutrino, p_z^{ν}. Using the W mass hypothesis, m_W, this can be calculated using conservation of 4-momentum as

$$p_z^{\nu} = \frac{1}{2(p_{\mathrm{T}}^{l})^2}\left[p_z^l X \pm E_l\sqrt{X^2 - 4(p_{\mathrm{T}}^{l})^2(E_{\mathrm{T}}^{\mathrm{miss}})^2}\right], \tag{7.2}$$

with

$$X = m_W^2 + 2p_x^l E_x^{\mathrm{miss}} + 2p_y^l E_y^{\mathrm{miss}}, \tag{7.3}$$

where p_{T}^{l} is the lepton's transverse momentum, $p_{x,y,z}^{l}$ are the x, y and z components of the lepton's 4-momentum and $E_{x,y}^{\mathrm{miss}}$ are the x and y components of the missing transverse momentum. If p_z^{ν} has an imaginary solution (i.e. $X^2 < 4(p_{\mathrm{T}}^{l})^2(E_{\mathrm{T}}^{\mathrm{miss}})^2$), the $E_{\mathrm{T}}^{\mathrm{miss}}$ is shifted such that the discriminant is equal to zero. The m_{top} variable is finally reconstructed by selecting the jet from the two b-tagged jets which minimises m_{top}.

Figure 7.3 presents the m_{top} distributions in the 1-lepton 2-jet and 3-jet regions. The $t\bar{t}$ contribution is peaked near the SM top mass. Cutting above this value will therefore remove a large component of the $t\bar{t}$ background. An optimal cut of $m_{\mathrm{top}} > 225$ GeV was selected, which removes a large component of the $t\bar{t}$ background, whilst maintaining a significant number of $W+$HF events. To ensure that the CR has very little signal contamination, signal events are removed with $\sim 99.5\%$ efficiency by removing the region with $m_{bb} > 75$ GeV.

The combination of these cuts generates a CR which is orthogonal to the signal region, and, as presented in Figure 7.4, is found to have a $W+$HF purity of 80% (75%) in the 2-jet (3-jet) regions.

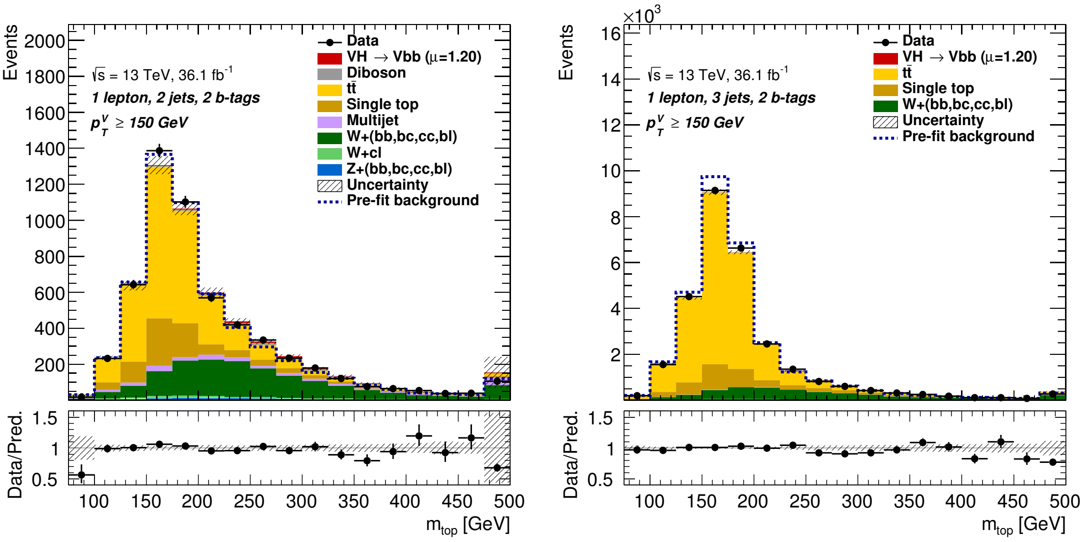

(a) (b)

Figure 7.3: Distributions of m_{top} in the 1-lepton channel of the $VH \to Vb\bar{b}$ analysis for the 2-jet (a) and 3-jet (b) regions. Data (black points with statistical error bars) are shown, corresponding to 36.1 fb^{-1} of Run-2 data collected at $\sqrt{s} = 13$ TeV, along with the simulated prediction (coloured stacked histograms), as described in Section 7.3. Simulated samples are scaled by the best fit values from the global profile likelihood fit to data, as described in Section 7.5. The unfilled dashed histogram corresponds to the prefit background prediction. The bottom pad shows the ratio of data to the combined signal and background model, while the total systematic uncertainty is indicated by the hatched band. The top background is centred near the measured top mass.

7.2.2.2 Top $e\mu$ Control Region

In the nominal selection of the 2-lepton channel, it is required that both leptons are of the same flavour (ee or $\mu\mu$), in order to target the leptonic decays of the Z boson. However, it is also possible to define a control region in the 2-lepton channel which is very pure in terms of the $t\bar{t}$ and Wt backgrounds by requiring different lepton flavours, i.e. $e\mu$. This region is called the top $e\mu$ CR, with 99% of events either $t\bar{t}$ or Wt. The remaining backgrounds are from $V+$jets, and almost 100% of the $VH \to Vb\bar{b}$ signal is rejected.

This region is kinematically extremely similar to the signal region, meaning that it can be directly used to control the $t\bar{t}$ and Wt normalisation and modelling in the 2-lepton channel. An example of the modelling of m_{bb} in the $e\mu$ CR is presented in Figure 7.5.

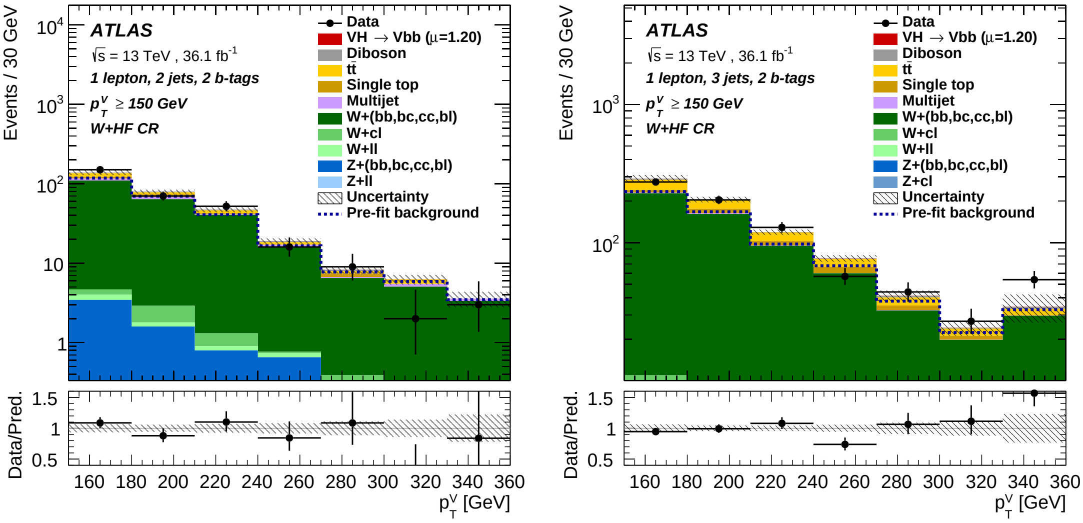

(a) (b)

Figure 7.4: Distributions of p_{T}^{V} in the 1-lepton channel of the $VH \to Vb\bar{b}$ analysis for the 2-jet (a) and 3-jet (b) $W+\mathrm{HF}$ control regions. Data (black points with statistical error bars) are shown, corresponding to 36.1 fb^{-1} of Run-2 data collected at $\sqrt{s} = 13$ TeV, along with the simulated prediction (coloured stacked histograms), as described in Section 7.3. Simulated samples are scaled by the best fit values from the global profile likelihood fit to data, as described in Section 7.5. The unfilled dashed histogram corresponds to the prefit background prediction. The bottom pad shows the ratio of data to the combined signal and background model, while the total systematic uncertainty is indicated by the hatched band.

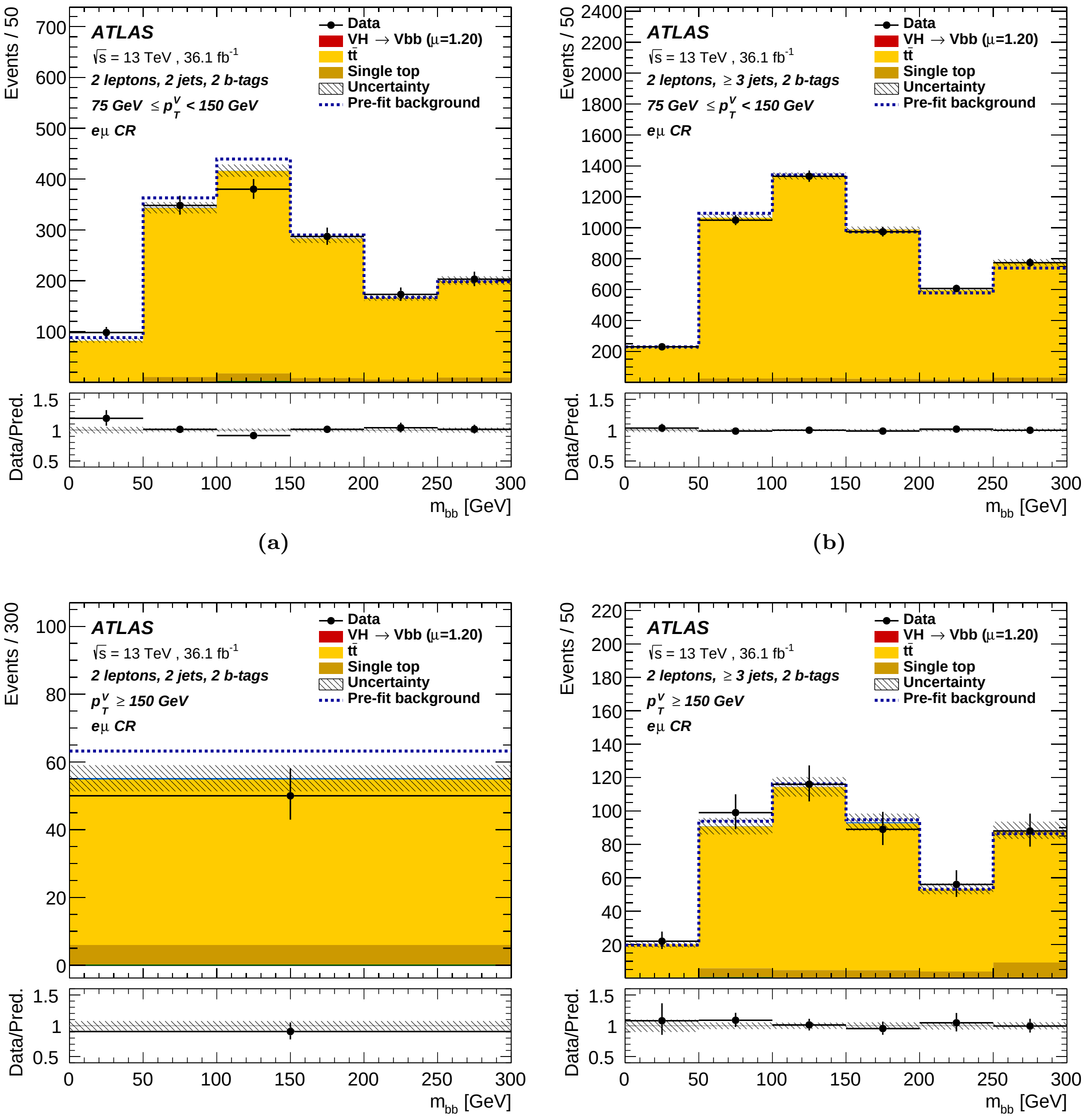

(a)

(b)

(c)

(d)

Figure 7.5: Distributions of m_{bb} in the 2-lepton channel of the $VH \to Vb\bar{b}$ analysis for the 2-jet (a) and 3-jet (b) for $75 < p_{\mathrm{T}}^{V} < 150$ GeV, and the 2-jet (c) and 3-jet (d) for $p_{\mathrm{T}}^{V} > 150$ GeV top $e\mu$ control regions. Data (black points with statistical error bars) are shown, corresponding to 36.1 fb^{-1} of Run-2 data collected at $\sqrt{s} = 13$ TeV, along with the simulated prediction (coloured stacked histograms), as described in Section 7.3. Simulated samples are scaled by the best fit values from a global profile likelihood fit to data, as described in Section 7.5. The unfilled dashed histogram corresponds to the prefit background prediction. The bottom pad shows the ratio of data to the combined signal and background model, while the total systematic uncertainty is indicated by the hatched band.

7.3 Data and Simulated Samples

Data are collected by the ATLAS detector from pp collisions at $\sqrt{s} = 13$ TeV. Data events are required to pass the quality requirements of the Good Runs List, which ensures that all components of the detector are operating as expected. The combined 2015 and 2016 dataset corresponds to 36.1 fb^{-1}.

Monte Carlo samples are used to simulate most background and signal processes, with the exception of the multijet contribution in the 1-lepton channel, which uses a data-driven method, as outlined in Section 7.3.2. Table 7.5 summarises the matrix element generators, parton showers, Parton Distribution Function (PDF) sets, and corresponding cross-sections for each process. EvtGen, which uses updated lifetime and decay tables to improve the modelling, is used to decay heavy flavour hadrons in all the parton shower generators, except for Sherpa [58]. All nominal samples are passed through GEANT4 [60] for a full simulation of the ATLAS detector.

$V+$jets samples are generated in preset slices of max($p_{\mathrm{T}}^{V}, H_{\mathrm{T}}$), where p_{T}^{V} is the truth transverse momentum of the vector boson, and H_{T} is the scalar sum of the transverse momentum of all truth particles. Due to the rapidly falling p_{T}^{V} and H_{T} distributions, it is necessary to generate samples using these slices in order to obtain a sufficient number of simulated MC events over the full spectrum. Furthermore, to obtain a sufficient number of heavy-flavour events, samples are generated with heavy flavour filters applied:

- ***b*-filter:** At least 1 b-hadron present, with $p_{\mathrm{T}} > 0$ GeV and $|\eta| < 4$.
- ***c*-filter, *b*-veto:** At least 1 c-hadron present with $p_{\mathrm{T}} > 4$ GeV and $|\eta| < 3$, and veto events which pass the b-filter.
- ***c*-veto, *b*-veto:** Veto events which pass the b-filter and c-filter.

$V+$jets processes are categorised based on the truth flavour labels of the Higgs candidate jets; $V+bb$, $V+bc$, $V+bl$, $V+cc$, $V+cl$, $V+ll$. The $V+$HF category is defined as containing $V+bb$, $V+bc$, $V+bl$, $V+cc$. Within this category, the $V+bb$ contribution is dominant, ranging from 70% to 90% of $V+$HF events depending on the channel and analysis region. Due to the large light-flavour jet rejection achieved by MV2c10, the contamination of $V+cl$ and $V+ll$ is significantly lower than the processes considered in the $V+$HF category, and are therefore considered separately.

7.3.1 Truth *b*-jet Tagging

Due to the high rejection achieved by the MV2c10 algorithm, the number of simulated MC events can become very limited for processes generated without a b-jet present (such as $V+cc$, $V+cl$, $V+ll$) when selecting events directly based upon the MV2c10 output. In order to use the full number of events of these samples, whilst also maintaining the correct normalisations and shapes due to the b-tagging selection, a procedure known as "truth tagging" is applied. In an event, all jets

Process	Matrix Element	PDF Set	Parton Shower	$\sigma \times$ Br [pb]
$qq \to ZH \to \nu\nu b\bar{b}$	Powheg-Box v2 [55] + GoSam [88]+ MiNLO [97, 98]	NNPDF3.0NLO [71]	Pythia-8.212 [89]	8.91×10^{-2} [90–96]
$qq \to WH \to \ell\nu b\bar{b}$	Powheg-Box v2 + GoSam+MiNLO	NNPDF3.0NLO	Pythia-8.212	2.69×10^{-1}
$qq \to ZH \to \ell\ell b\bar{b}$	Powheg-Box v2 + GoSam+MiNLO	NNPDF3.0NLO	Pythia-8.212	4.45×10^{-2}
$gg \to ZH \to \nu\nu b\bar{b}$	Powheg-Box v2	NNPDF3.0NLO	Pythia-8.212	1.43×10^{-2}
$gg \to ZH \to \ell\ell b\bar{b}$	Powheg-Box v2	NNPDF3.0NLO	Pythia-8.212	7.23×10^{-3} [99–103]
$Z \to \nu\nu$+jets	Sherpa 2.2.1 [68]	NNPDF3.0NLO	Sherpa 2.2.1	5700 [72]
$W \to \ell\nu$+jets	Sherpa 2.2.1	NNPDF3.0NLO	Sherpa 2.2.1	60200
$Z \to \ell\ell$+jets	Sherpa 2.2.1	NNPDF3.0NLO	Sherpa 2.2.1	6300
$t\bar{t}$	Powheg-Box v2	NNPDF3.0NLO	Pythia-8.212	832 [69]
Single top (s-channel)	Powheg-Box v2	CT10 [57]	Pythia-6.428 [56]	3.35 [104]
Single top (t-channel)	Powheg-Box v1	CT10f4	Pythia-6.428	70.4 [105]
Single top (Wt-channel)	Powheg-Box v2	CT10	Pythia-6.428	71.7 [70]
WW	Sherpa 2.1.1	CT10	Sherpa 2.1.1	45.7
WZ	Sherpa 2.2.1	NNPDF3.0NLO	Sherpa 2.2.1	21.7
ZZ	Sherpa 2.2.1	NNPDF3.0NLO	Sherpa 2.2.1	6.53

Table 7.5: The nominal Monte Carlo samples used in $VH \to Vb\bar{b}$ analysis, and the corresponding process cross-sections at $\sqrt{s} = 13$ TeV. The $t\bar{t}$ samples include a filter to require that at least one of the W bosons decay leptonically, with the top mass set to 172.5 GeV. In the $VH \to Vb\bar{b}$ signal samples, the mass of the Higgs boson is fixed to 125 GeV, and the $H \to b\bar{b}$ branching fraction is fixed to 58%. The acceptance from other Higgs boson production and decay modes has been tested to be negligible, and is therefore not considered for the purposes of this analysis. Minimum bias interactions are generated with Pythia8 [59], and overlaid on each event.

are kept, but weighted by the probability that the jet is tagged, with the probability determined as a function of the jet p_{T} and η from a $t\bar{t}$ sample. As an example, consider an event with 3-jets, where it is required that exactly 2-jets are b-tagged. Each jet i has a b-tagging efficiency ε_i (taken from MC as a function of jet p_{T} and jet η), meaning the total weight, w_{tot}, is given by

$$w_{\mathrm{tot}} = \varepsilon_1\varepsilon_2(1-\varepsilon_3) + \varepsilon_1(1-\varepsilon_2)\varepsilon_3 + (1-\varepsilon_1)\varepsilon_2\varepsilon_3. \tag{7.4}$$

The two jets to be assigned as the b-tagged jets, which is necessary when defining event level variables, are randomly selected based on their tagging efficiency probability. For example, the probability for jets 1 and 2 to be b-tagged is given by

$$P_{1,2}^{\text{tagged}} = \frac{\varepsilon_1 \varepsilon_2 (1 - \varepsilon_3)}{w_{\text{tot}}}. \tag{7.5}$$

This procedure is applied only to the $V + cc$, $V + cl$, $V + ll$ and WW samples to maintain a sufficient number of MC events. These processes constitute $< 2\%$ of the total background, and good closure is found when comparing to direct b-tagging.

7.3.2 Multijet Modelling

In the 0- and 2-lepton channels, studies have shown that the multijet contamination is negligible [3]. However, in the 1-lepton channel, there is a non-negligible contribution from multijet events, which pass the event selection due to the reconstruction of a fake lepton. This can arise from a number of different sources, as described in Sections 3.5.2 and 3.5.3.

Due to limitations of the number of simulated MC events in the mulitjet samples, the multijet background is estimated using a data driven method. A multijet enriched region, as outlined in Table 7.6, is defined by inverting the lepton isolation requirement. From this region, after subtracting the contributions from electroweak and top backgrounds from simulation, a template of the multijet background is extracted. Due to the limited number of events in the inverted isolation region, only 1 b-tag is required. To extract the normalisation of the multijet background in the isolated region, a simultaneous fit of the top ($t\bar{t}$ and single top-quark), $W +$jets and multijet normalisation is conducted to the m_{T}^{W} distribution, with a single bin included for the $W +$ HF control region.

	Isolated Region	Inverted Isolation Region
Electron	$p_{\text{T}}^{\text{cone0.2}} < 3.5$ GeV	$p_{\text{T}}^{\text{cone0.2}} > 3.5$ GeV
Muon	$p_{\text{T}}^{\text{cone20}} < 1.25$ GeV	$p_{\text{T}}^{\text{cone20}} > 1.25$ GeV

Table 7.6: Summary of the isolated and inverted isolation regions used for the estimation of the multijet background in the 1-lepton channel of the $VH \rightarrow Vb\bar{b}$ analysis.

The main assumption of the template method is that the multijet shape extracted from the inverted isolation region provides a good estimate of the multijet shape in the isolated region. Isolation extrpolation factors are derived as a function of lepton p_{T}, η and $E_{\text{T}}^{\text{miss}}$, from considering the ratio of event yields in the isolated and anti-isolated region. These correction factors are applied to the anti-isolated template to correct for any bias when extrapolating to the isolated region.

Figure 7.6 presents the modelling of the multijet contamination in the 1-lepton 2-jet electron and muon sub-channels for the m_{T}^{W} distribution. The total fake electron (muon) contamination in the 2-jet channel is estimated to be 2.3% (2.6%) and in the 3-jet channel 0.1% (0.3%). Systematic uncertainties are assigned to this procedure, as outlined in Section 7.6.1.

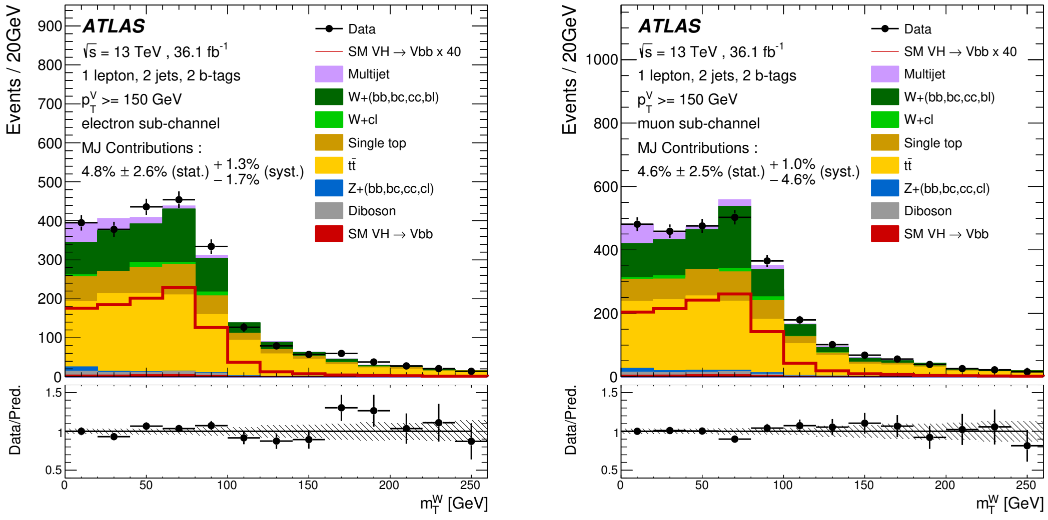

(a) (b)

Figure 7.6: Distributions of m_{T}^{W} in the 1-lepton 2-jet electron (a) and muon (b) sub-channels, illustrating the level of multijet contamination in the isolated region. Data (black points with statistical error bars) are shown, corresponding to 36.1 fb^{-1} of Run-2 data collected at $\sqrt{s} = 13$ TeV, along with the simulated prediction (coloured stacked histograms). The $t\bar{t}$, single top-quark and $W+$jets backgrounds are scaled by the normalisation factors derived in the fit to the m_{T}^{W} distribution in the isolated region. The $VH \to Vb\bar{b}$ signal is shown as a stacked red histogram, and unstacked scaled histogram to illustrate the signal shape. The bottom pad shows the ratio of data to the combined signal and background model.

7.4 Multivariate Analysis Techniques

When searching for the SM $VH \to Vb\bar{b}$ signal, the dijet mass, m_{bb}, is the variable which provides the single largest sensitivity to the signal. However, a number of other variables exist, which are only partially correlated with m_{bb}, and can be used to increase the sensitivity of the analysis, such as $\Delta R(b, b)$ or p_{T}^{V}. A number of these variables can be combined using a boosted decision tree (BDT), outlined in Section 3.6, to boost the sensitivity of the analysis. This procedure, first implemented in the Run-1 version of the $VH \to Vb\bar{b}$ analysis, offers an improvement to the analysis sensitivity of up to 15% [83].

An iterative procedure is used to select the input variables for the BDT. Starting with m_{bb}, one variable is tested at a time, selecting the variable which yields the largest improvement in sensitivity. The procedure is repeated, adding one variable at a time, until no further improvement in the sensitivity is observed [83]. Eight BDTs are trained in total, one for each signal region in each channel, as outlined in Table 7.3.

In order to compare the statistical sensitivity of a BDT training, the log-likelihood ratio sensitivity, S, is calculated on a bin-by-bin basis for a given distribution,

$$S = \sqrt{\sum_{i=1}^{n}(2 \times ((s_i + b_i) \times \log(1 + s_i/b_i) - s_i))}, \tag{7.6}$$

where n is the total number of bins in the distribution, s_i is the signal yield in bin i, and b_i is the background yield in bin i.

Good modelling is required for all input variables in order to ensure no bias is introduced through the implementation of the BDT. This was tested by comparing the MC modelling of each variable in each region. Good agreement between the simulation and data was observed in all cases. A summary of all variables used in the 0-, 1- and 2-lepton BDTs is presented in Table 7.7. The output of the BDT when trained with $VH \to Vb\bar{b}$ events as signal is denoted BDT_{VH}. As a cross-check, an additional BDT is trained using $VZ \to Vb\bar{b}$ events as signal, with the same input variables and configuration as BDT_{VH}, and the output denoted BDT_{VZ}.

Variable	Name	0-lepton	1-lepton	2-lepton
p_{T}^{V}	pTV		✓	✓
$E_{\mathrm{T}}^{\mathrm{miss}}$	MET	✓	✓	✓
$p_{\mathrm{T}}^{\mathrm{jet1}}$	pTB1	✓	✓	✓
$p_{\mathrm{T}}^{\mathrm{jet2}}$	pTB2	✓	✓	✓
m_{bb}	mBB	✓	✓	✓
$\Delta R(\mathrm{jet}_1, \mathrm{jet}_2)$	dRBB	✓	✓	✓
$\lvert\Delta\eta(\mathrm{jet}_1, \mathrm{jet}_2)\rvert$	dEtaBB	✓		
$\Delta\phi(V, H)$	dPhiVBB	✓	✓	✓
$\Delta\eta(V, H)$	dEtaVBB			✓
M_{eff}	HT	✓		
$\min(\Delta\phi(\ell, \mathrm{jet}))$	dPhiLBmin		✓	
m_{T}^{W}	mTW		✓	
$m_{\ell\ell}$	mLL			✓
$\Delta Y(W, H)$	dYWH		✓	
m_{top}	mTop		✓	
	3-jet events only			
$p_{\mathrm{T}}^{\mathrm{jet3}}$	pTJ3	✓	✓	✓
m_{bbj}	mBBJ	✓	✓	✓

Table 7.7: Variables used to train the multivariate discriminant in each leptonic channel of the $VH \to Vb\bar{b}$ analysis. The variable M_{eff} is defined as the scalar sum of the transverse momenta of all jets and $E_{\mathrm{T}}^{\mathrm{miss}}$, $p_{\mathrm{T}}^{\mathrm{jet1}}$ and $p_{\mathrm{T}}^{\mathrm{jet2}}$ are the p_{T} of the leading and sub-leading b-tagged jet, $p_{\mathrm{T}}^{\mathrm{jet3}}$ is the p_{T} of the additional jet not b-tagged in the 3-jet category and $m_{\ell\ell}$ is the invariant mass of the di-lepton system in the 2-lepton channel.

7.4.1 BDT Training in 1-lepton

7.4.1.1 BDT Optimisation in 1-lepton

Studies were carried out to determine if the BDT parameters used in the Run-1 configuration of the BDT training were still optimal for the Run-2 analysis. The nominal configuration from Run-1 is summarised in Table 7.8. A 3D scan was conducted of three BDT parameters; NTrees, MaxDepth and NEventsMin, with the ranges and steps summarised in Table 7.9. For each possible configuration, the statistical sensitivity was calculated, and compared to the nominal training setup.

Figure 7.7 presents the measured statistical sensitivity for each BDT_{VH} configuration, with MaxDepth $= 4$, for the 1-lepton 2-jet and 3-jet categories. Whilst MaxDepth $= 3$ and MaxDepth $= 5$ were also studied, only MaxDepth $= 4$ is presented as this was found to give the best performance. In the 2-jet category, a slight increase in the statistical sensitivity over the nominal configuration is observed, with an increase from 2.58 ± 0.07 to 2.67 ± 0.09 for 220 trees and a 3% minimum node size. Whilst the statistical uncertainty on the measured sensitivities is of the order 0.07 and is highly correlated between results, it was decided that, to avoid additional complications and inconsistency issues between the channels, the increase was not substantial enough to warrant changing the nominal BDT training parameters.

A similar situation is also observed for the 3-jet region. The nominal configuration yields a sensitivity of 1.53 ± 0.03, while switching to 500 trees and 1% minimum node size can increase this to 1.60 ± 0.04. This increase was again not judged to be substantial enough compared to the nominal performance to warrant changing the setup.

It was therefore concluded that no significant gain could be made in the optimisation of the parameters of the BDT_{VH} in the 1-lepton channel, and the Run-1 configuration was still sufficient for Run-2. Furthermore, even if a small gain could be achieved, it was decided that the additional complications of updating and implementing different BDT configurations for each leptonic channel meant that the nominal configuration was used in all channels and regions of the analysis.

Configuration	Value	Definition
BoostType	AdaBoost	Boost procedure
AdaBoostBeta	0.15	Learning rate
SeparationType	GiniIndex	Node separation gain
NTrees	200	Number of trees
MaxDepth	4	Maximum tree depth
NCuts	100	Number of equally spaced cuts tested per variable per node
NEventsMin	5%	Minimum number of events in a node

Table 7.8: Nominal BDT_{VH} and BDT_{VZ} configuration parameters, as implemented in the Run-1 $VH \rightarrow Vb\bar{b}$ analysis.

Configuration	Min	Max	Step
NTrees	100	500	20
MaxDepth	3	5	1
NEventsMin	1%	5%	1%

Table 7.9: Ranges and step sizes of BDT$_{VH}$ parameters tested to optimise the 1-lepton $VH \to Vb\bar{b}$ BDT$_{VH}$ performance. To avoid regions of phase space where overtraining is likely, NTrees is limited to be below 500, MaxDepth below 5, and NEventsMin above 1%. Equally, to avoid testing regions known to result in suboptimal performance, NTrees is limited to be above 100, MaxDepth above 3, and NEventsMin below 5%.

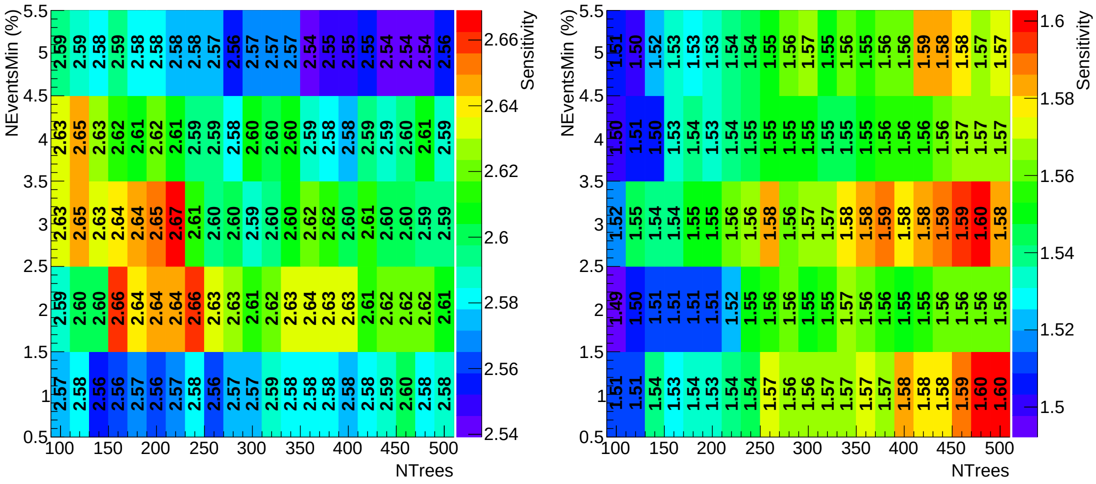

(a) (b)

Figure 7.7: The BDT$_{VH}$ statistical sensitivity for the $VH \to Vb\bar{b}$ signal in the 1-lepton 2-jet (a) and 3-jet (b) signal regions, as a function of NTrees and NEventsMin, with MaxDepth fixed to 4.

7.4.1.2 BDT Performance in the 1-lepton 2-jet Region

In order to utilise the full number of simulated MC events in the training, whilst avoiding any possible training bias, a 2-fold cross-validation approach, as described in Section 3.6.2, is implemented in the BDT training. Figure 7.8 presents the BDT$_{VH}$ output for signal and background events when trained on events with odd event numbers and tested on events with even event numbers, and when trained on events with even event numbers and tested on events with odd event numbers. Good agreement is observed in the output of BDT$_{VH}$ for both folds of the BDT training, indicating that creating orthogonal folds based on the event number does not introduce a bias in the final BDT$_{VH}$ performance.

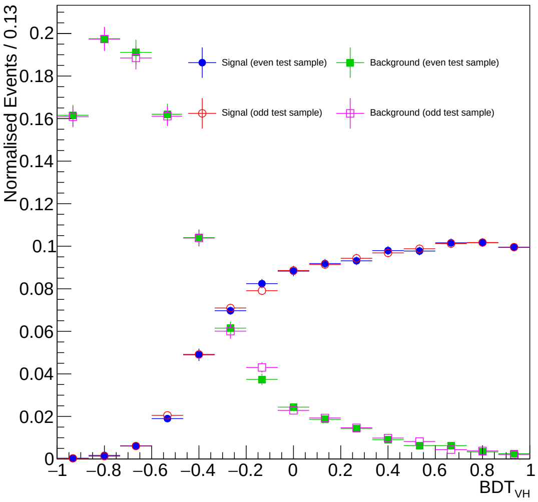

Figure 7.8: The BDT$_{VH}$ output for signal (background) events when trained on events with odd event numbers and tested on events with even event numbers, blue (green) markers, and when trained on events with even event numbers and tested on events with odd event numbers, red (pink) markers in the 1-lepton 2-jet signal region. The statistical uncertainties on the simulated samples are indicated by the error bars.

7.4.2 BDT Transformation

The output values of BDT$_{VH}$ and BDT$_{VZ}$ are arbitrary, and can be binned in many different ways. The use of more bins increases the sensitivity to signal, however this comes at the cost of increased statistical uncertainties, difficulty in parameterising smooth systematic uncertainties and increased complexity of the global likelihood fit. The re-binning of BDT$_{VH}$ and BDT$_{VZ}$ is therefore designed to provide the maximal signal sensitivity, whilst minimising the number of bins and maintaining the MC statistical uncertainty at a reasonable level. The following transformation was optimised for the analysis, and is applied in all BDT distributions. The function

$$Z(k,l) = z_s n_s(k,l)/N_s + z_b n_b(k,l)/N_b, \tag{7.7}$$

where $z_{s(b)}$ are parameters to tune the algorithm and $n_{s(b)}(k,l)$ is the number of signal (background) events in the BDT output interval from bins k to l, is used to parameterise the re-binning procedure. The re-binning is conducted using the following algorithm:

1. Starting from the last bin on the right of the original histogram, increase the range of the interval (k, last) by adding one after the other, the bins from the right to the left.
2. Calculate the value of Z at each step.
3. Once $Z(k, \text{last}) > 1$ and the MC statistical uncertainty is in the range is $< 20\%$, re-bin all the bins in the interval (k, last) into a single bin.

4. Repeat steps 1-3, starting this time from the last bin on the right, not included in the previous remap, stopping when reaching the first bin.

Sensitivity studies have found $z_s = 10$, $z_b = 5$ as optimal parameters for BDT_{VH}, leading to 15 BDT output bins after applying the transformation. Due to a limited number of simulated MC events in the $VZ \to Vb\bar{b}$ signal samples, BDT_{VZ} is set to have 10 output bins after applying the transformation, with $z_s = 5$, $z_b = 5$.

7.5 Global Profile Likelihood Fit Procedure

In order to extract the signal significance and strength, a global profile likelihood fit is used. In this section, an overview of the global likelihood fit procedure is described, with key terms and nomenclature introduced.

7.5.1 Likelihood Function

The statistical analysis of the data uses a binned likelihood function, defined as a product of Poisson probability terms [106, 107]. Considering the case of statistical only uncertainties, the likelihood function is defined as

$$\mathcal{L}(\mu) = \prod_{i=1}^{\mathrm{nbins}} \frac{(\mu s_i + b_i)^{n_i}}{n_i!} e^{-(\mu s_i + b_i)}, \tag{7.8}$$

where μ is the measured signal strength ($\sigma_{\mathrm{obs}}/\sigma_{\mathrm{SM}}$), s_i (b_i) the expected number of signal (background) events in bin i, n_i is the number of observed data events in bin i, and nbins the total number of bins. Due to systematic uncertainties in the MC simulation of the data, owing to sources such as imperfect simulation of the detector and the finite accuracy of MC generators, it is necessary to introduce a vector of nuisance parameters (NP), $\boldsymbol{\theta}$, to the likelihood function and allow for additional degrees of freedom in the likelihood. Each systematic uncertainty θ_i corresponds to an element of $\boldsymbol{\theta}$, and modifies the likelihood function as

$$\mathcal{L}(\mu, \boldsymbol{\theta}) = \prod_{i=1}^{\mathrm{nbins}} \frac{(\mu s_i(\boldsymbol{\theta}) + b_i(\boldsymbol{\theta}))^{n_i}}{n_i!} e^{-(\mu s_i(\boldsymbol{\theta}) + b_i(\boldsymbol{\theta}))} \times \mathcal{L}_{\mathrm{aux}}(\boldsymbol{\theta}), \tag{7.9}$$

where $\mathcal{L}_{\mathrm{aux}}(\boldsymbol{\theta})$ is the Gaussian auxiliary likelihood function of the prior uncertainty on each NP θ. The auxiliary term is defined as

$$\mathcal{L}_{\mathrm{aux}}(\boldsymbol{\theta}) = \prod_{j=1}^{\mathrm{nsyst}} \frac{1}{\sqrt{2\pi}\sigma_j} e^{\frac{-\left(\tilde{\theta}_j - \theta_j\right)^2}{2\sigma_j^2}}, \tag{7.10}$$

where $\tilde{\theta}_j$ is the central value of the Gaussian, corresponding to the nominal value of systematic uncertainty j, nsyst is the total number of systematic uncertainties being considered, θ_j is the corresponding best fit value, and σ_j is the prior uncertainty of θ_j. The priors and the auxiliary function therefore act to constrain the NPs within their uncertainties by penalising large deviations in the likelihood. Prior uncertainties are obtained from physics studies. In the case of floating NPs, such as a floating normalisation uncertainty, no prior uncertainty, and therefore no penalty cost, is assigned. Statistical uncertainties of simulated MC samples are introduced through an additional Poisson auxiliary term in the likelihood [108].

The profile likelihood test statistic q_μ is defined as

$$q_\mu = -2\log\left(\frac{\mathcal{L}\left(\mu, \hat{\hat{\boldsymbol{\theta}}}\right)}{\mathcal{L}\left(\hat{\mu}, \hat{\boldsymbol{\theta}}\right)}\right), \tag{7.11}$$

where $\hat{\mu}$ and $\hat{\theta}$ are the parameters that maximise the likelihood, meaning $\mathcal{L}\left(\hat{\mu}, \hat{\boldsymbol{\theta}}\right)$ corresponds to the global maximum likelihood value, and $\hat{\hat{\boldsymbol{\theta}}}$ is the value of $\boldsymbol{\theta}$ that maximises $\mathcal{L}$ for a given μ value.

In the search for $VH \to Vb\bar{b}$, one can use the test statistic q_0 to determine the significance of discovery of a signal, and the compatibility of the observed data with the background-only model. If one considers the probability distribution function of q_μ for a given signal strength μ',

$$f\left(q_\mu|\mu'\right), \tag{7.12}$$

then the distribution of $f\left(q_0|\mu' = 0\right)$ can be approximated using an analytical function [109]. In order to evaluate the expected p-value of the measurement, the mean value of $f\left(q_0|\mu' = 1\right)$, is evaluated, which can again be obtained from an analytic function, and is denoted by $q_{0,\mathrm{exp}}$. The expected p-value of a measurement from simulation is

$$p_0 = \int_{q_{0,\mathrm{exp}}}^{\infty} f\left(q_0|\mu' = 0\right) dq_0. \tag{7.13}$$

The determination of the expected p-value is illustrated in Figure 7.9.

The corresponding observed p-value from the fit to data is given by

$$p_0 = \int_{q_{0,\mathrm{obs}}}^{\infty} f\left(q_0|\mu' = 0\right) dq_0, \tag{7.14}$$

where $q_{0,\mathrm{obs}}$ is the observed q_0 value from the fit to data in Equation 7.11. A small q_0 therefore corresponds to a low false positive probability, and can be converted into standard deviations (σ) of the Gaussian distribution using the normal inverse cumulative distribution function. A q_0 value of 1.35×10^{-2} % corresponds to a 3 σ deviation from the background-only model. A q_0 value of 2.87×10^{-5} % corresponds to a 5 σ deviation from the background-only model, and is generally used as the benchmark deviation required for discovery in high energy physics.

Also quoted are expected significances from a conditional fit to data. These are obtained by the following procedure

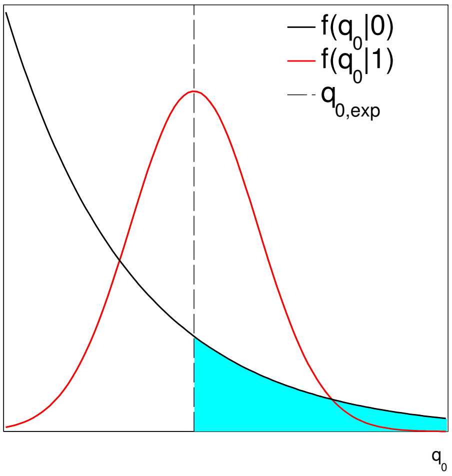

Figure 7.9: Diagram illustrating the extraction of the expected p-value from the distribution of q_0 with an expected signal strength of $\mu' = 1$. The p-value corresponds to the integral of the cyan area.

1. Conduct the global likelihood fit, with $\mu = 1$, to data.
2. Apply the results of the global likelihood fit to data to the Asimov dataset, Section 7.5.3.
3. Extract q_0 from the Asimov dataset using Equation 7.13, and the corresponding p_0 value.

7.5.2 Correlations

When constructing the likelihood, it is possible that two NPs, θ_i and θ_j can be correlated. It is important to study this behaviour to ensure that the model is reasonable, and to understand if a pull in one NP is related to another. The correlation between two NPs is first evaluated by constructing the Hessian matrix

$$\boldsymbol{H} = \begin{bmatrix} \frac{\partial^2 \mathcal{L}}{\partial\theta_1\partial\theta_1} & \frac{\partial^2 \mathcal{L}}{\partial\theta_1\partial\theta_2} & \cdots & \frac{\partial^2 \mathcal{L}}{\partial\theta_1\partial\theta_n} \\ \frac{\partial^2 \mathcal{L}}{\partial\theta_2\partial\theta_1} & \frac{\partial^2 \mathcal{L}}{\partial\theta_2\partial\theta_2} & \cdots & \frac{\partial^2 \mathcal{L}}{\partial\theta_2\partial\theta_n} \\ \vdots & \vdots & \ddots & \vdots \\ \frac{\partial^2 \mathcal{L}}{\partial\theta_n\partial\theta_1} & \frac{\partial^2 \mathcal{L}}{\partial\theta_n\partial\theta_2} & \cdots & \frac{\partial^2 \mathcal{L}}{\partial\theta_n\partial\theta_n} \end{bmatrix}. \tag{7.15}$$

The covariance matrix is obtained from the inversion of the Hessian matrix, $\boldsymbol{H}^{-1}$. The postfit uncertainties on each NP and the correlation matrix are extracted from the covariance matrix.

7.5.3 Asimov Dataset

The Asimov dataset is defined as a representative dataset, constructed from the simulation. As the Asimov dataset corresponds to the nominal simulated dataset, all NPs should remain at their nominal value, although it is possible that they can be constrained. In the Asimov dataset, it is also possible to determine the presence of correlations in NPs. This is useful when examining the fit to data, to determine if the fit is performing as expected.

7.5.4 Signal Strength

Whilst extracting the signal significance, which is one of the main aims of the analysis, it is interesting to measure the compatibility of the signal strength μ with the Standard Model. The best fit μ value, denoted by $\hat{\mu}$ in Equation 7.11, is simply the value for which the likelihood is maximal. The uncertainty on μ is evaluated by profiling $\mathcal{L}(\mu, \boldsymbol{\theta})$ as a function of μ near the best fit value (i.e re-evaluating $\mathcal{L}$ for fixed μ values), refitting $\boldsymbol{\theta}$ in each case. The point where $\log(\mathcal{L}(\mu, \boldsymbol{\theta})) - \log(\mathcal{L}(\hat{\mu}, \hat{\boldsymbol{\theta}})) = \pm 1/2$ corresponds to the ± 1 σ uncertainty on μ.

7.5.5 Impact of a Systematic on $\boldsymbol{\mu}$

When studying the fit model, an important consideration is the impact of each NP, θ, on the measured value of μ. Two possible methods to evaluate the impact of a systematic are used:

- **Breakdown method**: Evaluate the error on μ without a systematic (or group of systematics) uncertainty included in the fit, and subtract the resulting error quadratically from the full error.
- **Ranking method**: Pull a systematic by 1 σ, and re-evaluate μ. The difference between the nominal and varied value, $\Delta\mu$, is used as an estimate of the impact of the systematic uncertainty.

7.5.6 Postfit Distributions

When studying the result of the global likelihood fit, it is useful to consider the postfit agreement between simulation and data. After determining the best fit μ and $\boldsymbol{\theta}$ values, data to MC comparisons are made, applying these values to the simulated distributions. When applying the postfit μ and $\boldsymbol{\theta}$ values in a different variable to the variable which was used to fit to data, the nuisance parameters arising from MC statistical uncertainties are not included. This is due to the complexity in translating the MC statistical uncertainties from one distribution to another.

7.6 Systematic Uncertainties

7.6.1 Background Modelling Uncertainties

For the three dominant backgrounds, $t\bar{t}$, $Z+$jets and $W+$jets, unconstrained floating normalisations are applied, such that the overall normalisation of these processes can be constrained using data where possible. Acceptance uncertainties within the fit model then allow for the normalisations of these processes to vary between each region. The general model for these processes is as follows:

- **$Z+$jets:** $Z+$HF is a dominant background in the 0- and 2-lepton channels. Two floating normalisation factors for the overall $Z+$HF background are used for the 2-jet and 3-jet regions ($Z+bb$ normalisation). The 2-lepton channel has the best constraining power on the $Z+$HF background, with extrapolation uncertainties applied to the normalisation in the 0-lepton region (0-to-2-lepton ratio). Additional uncertainties on the $Z+$HF composition (ratio of bb-to-$bc/bl/cc$ events) are also derived and implemented ($Z+bc$-to-$Z+bb$ ratio, $Z+cc$-to-$Z+bb$ ratio, $Z+bl$-to-$Z+bb$ ratio). Due to the small contribution of the $Z+cl$ and $Z+ll$ backgrounds, only a single prior normalisation uncertainty is considered for each process ($Z+cl$ normalisation, $Z+ll$ normalisation).

- **$W+$jets:** $W+$HF is a dominant background in the 0- and 1-lepton channels. Two floating normalisation factors for the overall $W+$HF background are used for the 2-jet and 3-jet regions ($W+bb$ normalisation). The 1-lepton channel $W+$HF CR has the best constraining power on the $W+$HF background, with extrapolation uncertainties applied to the normalisation in the 1-lepton signal region ($W+$HF CR to SR ratio), and to the normalisation in the 0-lepton region (0-to1-lepton ratio). Additional uncertainties on the $W+$HF composition (ratio of bb-to-$bc/bl/cc$ events) are also derived and implemented implemented ($W+bc$-to-$W+bb$ ratio, $W+cc$-to-$W+bb$ ratio, $W+bl$-to-$W+bb$ ratio). Due to the small contribution of the $W+cl$ and $W+ll$ backgrounds, only a single prior normalisation uncertainty is considered for each process ($W+cl$ normalisation, $W+ll$ normalisation).

- **$t\bar{t}$:** $t\bar{t}$ is a dominant background in all three channels. The characteristics of the contribution of $t\bar{t}$ to the 0- and 1-lepton regions is very different to that in the 2-lepton channel. Generally, in 0- and 1-lepton events, there needs to be an object which has been missed or not reconstructed from the $t\bar{t}$ decay. In the 2-lepton channel, di-leptonic $t\bar{t}$ is the main contribution, with the event being fully reconstructed. For this reason, in 0- and 1-lepton, a single common floating $t\bar{t}$ normalisation is implemented, with extrapolation uncertainties applied to the normalisation in the 0-lepton region (0-to-1-lepton ratio). As the 3-jet region has the best constraining power on the $t\bar{t}$ normalisation, an extrapolation uncertainty is applied to the normalisation in the 2-jet region (2-to-3-jet ratio). In the 2-lepton channel, two floating normalisations are used for the 2-jet and 3+-jet regions, as each region has a corresponding top $e\mu$ CR, which can strongly constrain the $t\bar{t}$ normalisation.

- For other sub-dominant background processes (single top-quark, diboson and multijet), as the data are less able to constrain the normalisation, prior normalisation uncertainties are derived from MC studies, along with acceptance and shape uncertainties.

Acceptance and shape uncertainties on the background model are evaluated in data using dedicated control regions where possible, and in simulation at truth-level using the Rivet framework [110] from comparisons to alternative generators. Studying these effects at truth level offers a reduction in the statistical uncertainty from an increased number of events compared to using fully reconstructed events. Shape uncertainties are parameterised as a function of m_{bb} and p_{T}^{V}. As m_{bb} and p_{T}^{V} are the highest ranked variables in the BDT_{VH} performance, and are only weakly correlated, the variations in these variables approximate the full systematic uncertainty in the BDT_{VH} shape [83].

Acceptance uncertainties are calculated as double ratios

$$\frac{\mathrm{Acceptance}[\mathrm{Category}_{\mathrm{A}}(\mathrm{nominalMC})]}{\mathrm{Acceptance}[\mathrm{Category}_{\mathrm{B}}(\mathrm{nominalMC})]} \bigg/ \frac{\mathrm{Acceptance}[\mathrm{Category}_{\mathrm{A}}(\mathrm{alternativeMC})]}{\mathrm{Acceptance}[\mathrm{Category}_{\mathrm{B}},(\mathrm{alternativeMC})]}, \tag{7.16}$$

where $\mathrm{Acceptance}[\mathrm{Category}_{\mathrm{i}}(\mathrm{nominalMC})]$ is the yield for the nominal MC in region i (either A or B).

For each process, there is often more than one systematic effect to consider (such as the parton shower and matrix element calculations for $t\bar{t}$). In order to accommodate this, without the introduction of numerous nuisance parameters, the acceptance effect is evaluated for each systematic uncertainty, and the quadratic sum of the double ratios calculated. For shape only systematics, only the systematic uncertainty resulting in the largest shape effect is considered.

$V+$jets: Variations in the acceptance and shape uncertainties are considered from a number of sources from comparing the nominal sample (Sherpa) to alternative generators:

- Alternative MC generator: MadGraph+Pythia8 [111].
- Factorisation (μ_F) and renormalisation (μ_R) scales: Doubled and halved in a correlated and independent manner. (Six variations: $0.5\times\mu_F, 1\times\mu_R$; $0.5\times\mu_F, 2\times\mu_R$; $1\times\mu_F, 0.5\times\mu_R$; $1\times\mu_F, 2\times\mu_R$; $2\times\mu_F, 0.5\times\mu_R$; $2\times\mu_F, 1\times\mu_R$.)
- Resummation scale: Doubled and halved.
- CKKW merging scale: Varied from 15 GeV to 30 GeV (nominal 20 GeV) [112].

Shape uncertainties on the $W+$jets background are derived using truth level analysis of the simulated samples. Shape uncertainties on the $Z+$jets background are also derived in control regions pure in $Z+$jets. In the 2-lepton channel, an additional cut on the $E_{\mathrm{T}}^{\mathrm{miss}}$ significance is applied, $E_{\mathrm{T}}^{\mathrm{miss}}/\sqrt{H_{\mathrm{T}}} < 3.5\sqrt{\mathrm{GeV}}$ to reduce $t\bar{t}$ contamination, with the m_{bb} region around the Higgs boson mass also excluded. The $Z+$jets background is then scaled to data after subtracting the remaining backgrounds. The data-based shape uncertainties are found to be consistent with those derived in the truth level analysis in all regions. The m_{bb} and p_{T}^{V} shape uncertainties are correlated across all regions.

The acceptance and shape variations for $V+$jets processes are summarised in Table 7.10.

$Z+$jets	
$Z+ll$ normalisation	18%
$Z+cl$ normalisation	23%
$Z+bb$ normalisation	Floating (2-jet, 3-jet)
$Z+bc$-to-$Z+bb$ ratio	30-40%
$Z+cc$-to-$Z+bb$ ratio	13-15%
$Z+bl$-to-$Z+bb$ ratio	20-25%
0-to-2-lepton ratio	7%
p_{T}^{V}, m_{bb}	S
$W+$jets	
$W+ll$ normalisation	32%
$W+cl$ normalisation	37%
$W+bb$ normalisation	Floating (2-jet, 3-jet)
$W+bl$-to-$W+bb$ ratio	26% (0-lepton) and 23% (1-lepton)
$W+bc$-to-$W+bb$ ratio	15% (0-lepton) and 30% (1-lepton)
$W+cc$-to-$W+bb$ ratio	10% (0-lepton) and 30% (1-lepton)
0-to-1-lepton ratio	5%
W+HF CR to SR ratio	10% (1-lepton)
p_{T}^{V}, m_{bb}	S

Table 7.10: Summary of the systematic uncertainties in the background modelling for $Z+$jets and $W+$jets production in the $VH \to Vb\bar{b}$ analysis. An “S” symbol is used when only a shape uncertainty is assessed. The regions in which the normalisations are floated independently are listed in brackets.

$t\bar{t}$: Variations in the acceptance and shape uncertainties are considered from a number of sources in $t\bar{t}$ production from comparing the nominal sample (Powheg+Pythia8) to alternative generators:

- Alternative matrix element generation: MadGraph5_aMC@NLO+Pythia8.
- Alternative parton shower generation: Powheg+Herwig7 [75, 113].
- Variable showering radiation: Powheg+Pythia8 with increased shower radiation tunes and Powheg+Pythia8 with reduced shower radiation tunes [74].

The acceptance and shape variations for $t\bar{t}$ processes are summarised in Table 7.11, and are decorrelated between the uncertainties in the 0- and 1-lepton channels and the 2-lepton channel. The shape uncertainties on p_{T}^{V} and m_{bb} are estimated in the combined 0- and 1-lepton region and the 2-lepton region separately.

Single top-quark: As a sub-dominant background, single top-quark production is treated using a slightly simpler scheme compared to the $t\bar{t}$ and $V+$jets backgrounds. The single top-quark background is composed of 3 processes, t-channel, s-channel and Wt production. Normalisation uncertainties are taken from the NNLO cross section calculations. The s-channel is sufficiently sub-dominant in all channels that no further acceptance or shape uncertainties are considered. Variations in the acceptance and shape uncertainties are considered from a number of sources in single top-quark production for the Wt- and t-channels from comparing the nominal samples (Powheg+Pythia6) to alternative generators:

- Alternative matrix element generation: MadGraph5_aMC@NLO+Herwig++ [75, 111].
- Alternative parton shower generation: Powheg+Herwig++.
- Variable showering radiation: Powheg+Pythia6 with increased shower radiation tunes and Powheg+Pythia6 with reduced shower radiation tunes [74].
- Diagram double counting: Powheg+Pythia6, diagram subtraction scheme (Wt-channel only) [76], as NLO Wt production diagrams overlap with $t\bar{t}$ production.

The acceptance and shape variations for single top-quark processes are summarised in Table 7.11, and are decorrelated between each single top-quark process, but correlated across all channels.

$t\bar{t}$ (all are decorrelated between the 0+1 and 2-lepton channels)	
$t\bar{t}$ normalisation	Floating (0+1 lepton, 2-lepton 2-jet, 2-lepton 3-jet)
0-to-1-lepton ratio	8%
2-to-3-jet ratio	9% (0+1-lepton only)
W+HF CR to SR ratio	25%
p_T^V, m_{bb}	S
Single top-quark	
Cross-section	4.6% (s-channel), 4.4% (t-channel), 6.2% (Wt)
Acceptance 2-jet	17% (t-channel), 35% (Wt)
Acceptance 3-jet	20% (t-channel), 41% (Wt)
m_{bb}, p_T^V	S (t-channel, Wt)

Table 7.11: Summary of the systematic uncertainties in the background modelling for $t\bar{t}$ and single top-quark production in the $VH \to Vb\bar{b}$ analysis. An "S" symbol is used when only a shape uncertainty is assessed. The regions in which the normalisations are floated independently are listed in brackets.

Diboson: Variations in the acceptance and shape uncertainties are considered from a number of sources, and are derived by comparing the nominal samples (Sherpa) to alternative generators:

- Matrix element generation: Sherpa to Powheg+Pythia8 comparison.
- Parton shower (PS) and underlying event (UE) variations: Powheg+Pythia8 parton shower tune variations, and comparison to Powheg+Herwig++.

- Factorisation and renormalisation scales: Doubled and halved in a correlated and independent way. (Six variations: $0.5 \times \mu_F, 1 \times \mu_R$; $0.5 \times \mu_F, 2 \times \mu_R$; $1 \times \mu_F, 0.5 \times \mu_R$; $1 \times \mu_F, 2 \times \mu_R$; $2 \times \mu_F, 0.5 \times \mu_R$; $2 \times \mu_F, 1 \times \mu_R$.)

The WW background is sub-dominant, and contributes $< 0.1\%$ of the total background in all channels, and so is only treated with a normalisation uncertainty. For acceptance uncertainties, the Stewart–Tackmann jet binning method [114] is employed. As diboson events are considered as signal events in the $VZ \to Vb\bar{b}$ analysis, a more complete model of the modelling systematic uncertainties is implemented. Shape variations are calculated for the scale variations, PS/UE, in both m_{bb} and p_{T}^{V}. The matrix element shape uncertainty is only considered for m_{bb} in the WZ and ZZ processes, as the uncertainty was found to have a negligible impact on the p_{T}^{V} shape. These are fully correlated between WZ and ZZ processes. The systematic uncertainties on diboson production are summarised in Table 7.12.

ZZ	
Normalisation	20%
0-to-2 lepton ratio	6%
Acceptance from scale variations (var.)	10.3% - 18.2% (Stewart–Tackmann jet binning method)
Acceptance from PS/UE var. for 2 or more jets	5.6% (0-lepton), 5.8% (2-lepton)
Acceptance from PS/UE var. for 3 jets	7.3% (0-lepton), 3.1% (2-lepton)
m_{bb}, p_{T}^{V}, from scale var.	S (correlated with WZ uncertainties)
m_{bb}, p_{T}^{V}, from PS/UE var.	S (correlated with WZ uncertainties)
m_{bb}, from matrix element var.	S (correlated with WZ uncertainties)
WZ	
Normalisation	26%
0-to-1-lepton ratio	11%
Acceptance from scale var.	12.7% - 21.2% (Stewart–Tackmann jet binning method)
Acceptance from PS/UE var. for 2 or more jets	3.9%
Acceptance from PS/UE var. for 3 jets	10.8%
m_{bb}, p_{T}^{V}, from scale var.	S (correlated with ZZ uncertainties)
m_{bb}, p_{T}^{V}, from PS/UE var.	S (correlated with ZZ uncertainties)
m_{bb}, from matrix element var.	S (correlated with ZZ uncertainties)
WW	
Normalisation	25%

Table 7.12: Summary of the systematic uncertainties in the background modelling for diboson production in the $VH \to Vb\bar{b}$ analysis. "PS/UE" indicates parton shower/underlying event. An "S" symbol is used when only a shape uncertainty is assessed. When determining the $(W/Z)Z$ diboson production signal strength, the normalisation uncertainties in ZZ and WZ production are removed.

Multijet (1-lepton only): Systematic uncertainties are considered in two categories for the multijet background; normalisation only and shape and normalisation uncertainties. Normalisation uncertainties are uncorrelated between the electron and muon sub-channels and the 2-jet and 3-jet regions. Shape uncertainties are uncorrelated between the electron and muon sub-channels, and are evaluated directly on BDT_{VH} and BDT_{VZ}. The following systematic uncertainties are considered in evaluating the multijet normalisation and shape uncertainties.

Shape and normalisation uncertainties:

- A different electron trigger is used to test for bias from the trigger isolation requirements (electron sub-channel only).
- The 2 b-tag requirement is applied to the inverted isolation region to evaluate the impact of using the 1 b-tag requirement to derive the nominal multijet template.
- The isolation requirement in the inverted isolation region is tightened to evaluate an uncertainty on the extrapolation from the inverted isolation region to the signal region.
- Not applying the isolation extrapolation factors to evaluate the impact of the isolation extrapolation factors.
- Applying the fitted normalisation of the top and W+jets background, described in Section 7.3.2, to the anti-isolated region to determine the impact on the nominal multijet template.

Normalisation uncertainties:

- Impact of applying $t\bar{t}$ m_{bb} and p_{T}^{V} shape systematics in the inverted isolation region. The m_{bb} uncertainty changes the relative background composition in the isolated and inverted isolation regions, and can therefore vary the multijet estimate.
- Deriving the multijet template including the $E_{\mathrm{T}}^{\mathrm{miss}} < 30$ GeV region (electron sub-channel only), as this significantly alters the m_{T}^{W} distribution and increases the multijet contamination.
- Fit multijet normalisation to $E_{\mathrm{T}}^{\mathrm{miss}}$ distribution instead of m_{T}^{W} to determine any effect from using m_{T}^{W} to extract the normalisation factors.

The normalisation component of the above systematic uncertainties are added in quadrature to the following normalisation only systematic uncertainties to give the total normalisation uncertainty for each 1-lepton region. Shape systematic uncertainties are normalised such that only the shape of the BDT output is changed. The normalisation and shape systematic uncertainties are summarised in Table 7.13. Whilst the total multijet normalisation uncertainty is very large, due to the relatively small multijet contamination in the 1-lepton channel, this does not have a large impact on the signal sensitivity.

Multijet (1-lepton)	
Normalisation	60-100% (2-jet), 100-500%(3-jet)
BDT template	S

Table 7.13: Summary of the systematic uncertainties in the multijet background for the $VH \to Vb\bar{b}$ analysis. An "S" symbol is used when only a shape uncertainty is assessed. The regions in which the normalisations are floated independently are listed in brackets.

7.6.2 Signal Modelling Uncertainties

Variations in the cross-section, acceptance and shape uncertainties are considered from a number of sources in the $VH \to Vb\bar{b}$ signal production production:

- $H \to b\bar{b}$ branching ratio [115–117].
- Factorisation and renormalisation scales: Scaled to one third and triple their nominal values in a correlated and independent manner [3]. (Six variations: $0.33 \times \mu_F, 1 \times \mu_R$; $0.33 \times \mu_F, 3 \times \mu_R$; $1 \times \mu_F, 0.33 \times \mu_R$; $1 \times \mu_F, 3 \times \mu_R$; $3 \times \mu_F, 0.33 \times \mu_R$; $3 \times \mu_F, 1 \times \mu_R$.)
- PDF+α_s uncertainty from the uncertainties of the PDF4LHC15_30 PDF set [118].
- Parton shower (PS) and underlying event (UE): MadGraph5_aMC@NLO+Pythia8 A14 tune variations [119] and comparison to Powheg+MiNLO+Herwig7.

For the cross-section uncertainties, effects from the $H \to b\bar{b}$ branching ratio, factorisation and renormalisation scales and PDF+α_s variations are considered. Acceptance effects between categories are evaluated for the scale variations, PDF+α_s variations, and the PS and UE variations. For the PS and UE variations, the sum in quadrature of all tune variations and the PS comparison gives the final acceptance variation from the PS/UE variation. Shape only uncertainties are evaluated for m_{bb} and p_{T}^{V} separately for the scale variations, PDF+α_s and PS/UE variations. Uncertainties on the signal modelling are summarised in Table 7.14.

7.6.3 Experimental Systematic Uncertainties

Several sources of experimental systematic uncertainty, similar to those described in the $t\bar{t}$ likelihood calibration, are considered in the $VH \to Vb\bar{b}$ analysis at both the object and event level, as outlined below.

Luminosity: The luminosity uncertainty is 2.1% for 2015 data (3.2 fb^{-1}), and 3.4% for 2016 data (32.9 fb^{-1}). Due to correlations in these measurements, the total uncertainty for the combined 2015 and 2016 dataset is 3.2% [37].

Signal	
Cross-section (scale)	0.7% (qq), 27% (gg)
Cross-section (PDF)	1.9% ($qq \to WH$), 1.6% ($qq \to ZH$), 5% (gg)
Branching ratio	1.7 %
Acceptance from scale variations (var.)	2.5% – 8.8% (Stewart–Tackmann jet binning method)
Acceptance from PS/UE var. for 2 or more jets	10.0% – 13.9% (depending on lepton channel)
Acceptance from PS/UE var. for 3 jets	12.9%–13.4% (depending on lepton channel)
Acceptance from PDF+α_s var.	0.5%–1.3%
m_{bb}, p_{T}^{V}, from scale var.	S
m_{bb}, p_{T}^{V}, from PS/UE var.	S
m_{bb}, p_{T}^{V}, from PDF+α_s var.	S
p_{T}^{V} from NLO EW correction	S

Table 7.14: Summary of the systematic uncertainties in the signal modelling for the $VH \to Vb\bar{b}$ analysis. "PS/UE" indicates parton shower and underlying event. An "S" symbol is used when only a shape uncertainty is assessed.

Pile-up reweighting: The MC is reweighted to describe the pile-up in data, by scaling the pile-up in MC by 1.09. The systematic uncertainty is evaluated by varying the scale factor from 1.00 to 1.18 [82].

Leptons: Uncertainties are considered on the lepton trigger, reconstruction, identification and isolation efficiencies, in addition to uncertainties on the lepton energy scale and resolution [41, 43].

$E_{\mathrm{T}}^{\mathrm{miss}}$: Uncertainties on the scale, resolution and efficiency of the tracks used to define the soft term in the $E_{\mathrm{T}}^{\mathrm{miss}}$ calculation [50]. The $E_{\mathrm{T}}^{\mathrm{miss}}$ is also recalculated according to all other experimental systematic variations.

Jets: Jet energy scale (JES) are decomposed into 21 decorrelated nuisance parameters using an eigenvector decomposition [46]. The nominal jet p_{T} is varied by a random smearing factor taken from a Gaussian with width equal to the JER uncertainty, parameterised as a function of the jet p_{T} and η. The uncertainty on JVT is evaluated to propagate a 2% uncertainty on the hard scatter jet efficiency [49].

***b*-tagging:** The dominant experimental systematic uncertainties arise from the use of b-tagging. As described in Chapters 5 and 6, data-over-MC scale factors are applied in order to correct for mismodelling in the output of the b-tagging algorithm. These scale factors are derived separately for b-, c- and light-flavour jets [64, 66]. Using an eigenvector decomposition, these uncertainties are decomposed into 3, 3 and 5 components for b-, c- and light-flavour jets respectively (each eigenvector is numbered $\{0, 1, ...\}$ etc.), with additional extrapolation uncertainties for high p_{T} jets.

7.7 Fit Model Cross-Checks

Before conducting the full unblinded fit to data to measure the $VH \rightarrow Vb\bar{b}$ signal strength, it was first necessary to run a number of checks to determine the stability of the background and fit model. To run these tests, the conditional fit to data, with $\mu = 1$, was repeated under a number of conditions and with changes to the fit model. The tested fit model is compared to the nominal model by examining the changes in the pulls, constraints and correlations of the fitted nuisance parameters, and the effect on the background model. The following tests were conducted:

- The nuisance parameters from the conditional BDT_{VH} $VH \rightarrow Vb\bar{b}$ fit to data were propagated to the BDT_{VZ} analysis and vice versa to evaluate the impact and consistency of using the fitted background model from the other variant of the analysis. This test is designed to show that any difference in the pulls between these different analyses has negligible impact on the background model and results. In both cases, a consistent agreement was observed, demonstrating that the fit model was robust to using different discriminating varaibles.

- In the first version of the fit model, both $W + \text{HF}$ and $Z + \text{HF}$ had one floating normalisation parameter, with a prior extrapolation uncertainty on the 2-to-3-jet normalisation. Rather than using a prior uncertainty, it is preferable to use data to constrain the normalisation, as this is a more data-based approach, removing the need to extract priors from the MC. This fit model was compared to the now-nominal model using two decorrelated floating normalisation parameters for the 2-jet and 3-jet regions. No significant change in the pulls or constraints of the nuisance parameters were observed, and the model was therefore updated.

- The $W + \text{HF}$ shape systematic is driven by the comparison between the nominal Sherpa 2.2.1 and MadGraph+Pythia8 samples, with similar shape effects observed in all regions. This systematic is correlated across the 0- and 1-lepton channels, and the 2-jet and 3-jet regions. To test the impact of this assumption, the conditional fit was re-run such that the uncertainty was decorrelated between regions. Consistent pulls, correlations and background model were observed in both cases.

- The pulls, constraints and correlations of the nuisance parameters are compared in the conditional and unconditional fits. Consistent results were observed for both the BDT_{VH} $VH \rightarrow Vb\bar{b}$ and BDT_{VZ} $VZ \rightarrow Vb\bar{b}$ fits.

7.8 Results

7.8.1 $VH \rightarrow Vb\bar{b}$

In this section, results from the $VH \rightarrow Vb\bar{b}$ BDT$_{VH}$ global likelihood fit to data are presented.

7.8.1.1 Postfit Distributions

Postfit distributions of a number of key variables for the BDT$_{VH}$ global likelihood fit to data are presented in this section. Figures 7.10 - 7.16 present the postfit BDT$_{VH}$, m_{bb} and p_{T}^{V} distributions in the 0-, 1- and 2-lepton channels. Good postfit agreement between data and MC is achieved for all these variables in all regions. This demonstrates a robust validataion, and indicates that both BDT$_{VH}$ and the fit model are behaving as expected and in a robust fashion.

Tables 7.15 and 7.16 presents the postfit yields in each signal and control region, respectively, for the unconditional global likelihood fit to data.

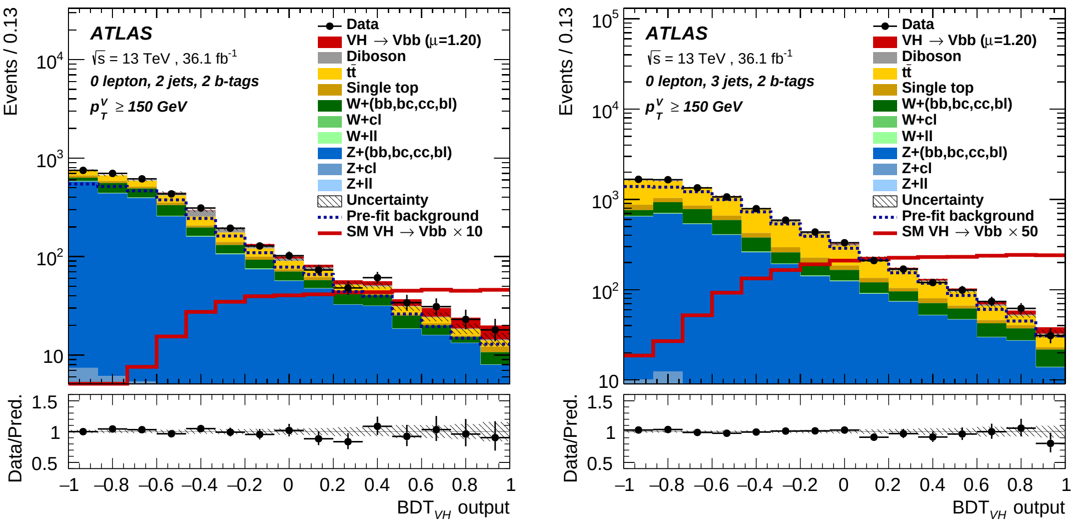

(a) (b)

Figure 7.10: Postfit BDT$_{VH}$ distributions in the 0-lepton signal regions, 2-jet (a) and 3-jet (b) for $p_{\mathrm{T}}^{V} > 150$ GeV, after the unconditional BDT$_{VH}$ global likelihood fit to data. Data (black points with statistical error bars) are shown, corresponding to 36.1 fb^{-1} of Run-2 data collected at $\sqrt{s} = 13$ TeV, along with the simulated prediction (coloured stacked histograms). The $VH \rightarrow Vb\bar{b}$ signal is scaled to the postfit value ($\mu = 1.20$), and shown as a stacked red histogram, and unstacked scaled histogram to illustrate the signal shape. The unfilled dashed histogram corresponds to the prefit background prediction. The bottom pad shows the ratio of data to the combined postfit signal and background model, while the total systematic uncertainty is indicated by the hatched band.

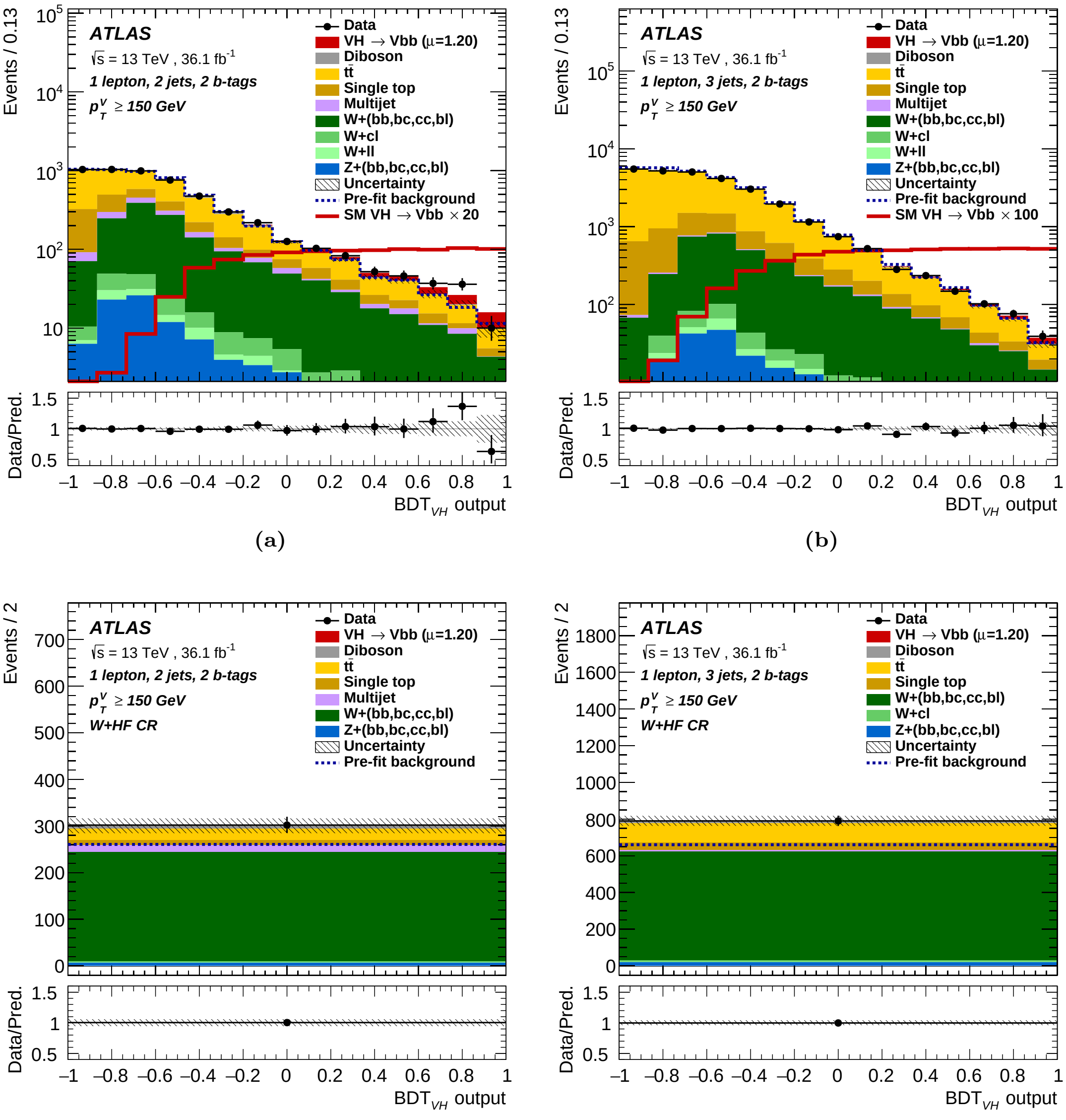

(a) (b)

(c) (d)

Figure 7.11: Postfit BDT$_{VH}$ distributions in the 1-lepton signal regions, 2-jet (a) and 3-jet (b) for $p_{\mathrm{T}}^{V} > 150$ GeV, and $W+\mathrm{HF}$ control regions, 2-jet (c) and 3-jet (d) for $p_{\mathrm{T}}^{V} > 150$ GeV, after the unconditional BDT$_{VH}$ global likelihood fit to data. Data (black points with statistical error bars) are shown, corresponding to 36.1 fb^{-1} of Run-2 data collected at $\sqrt{s} = 13$ TeV, along with the simulated prediction (coloured stacked histograms). The $VH \to Vb\bar{b}$ signal is scaled to the postfit value ($\mu = 1.20$), and shown as a stacked red histogram, and unstacked scaled histogram to illustrate the signal shape. The unfilled dashed histogram corresponds to the prefit background prediction. The bottom pad shows the ratio of data to the combined postfit signal and background model, while the total systematic uncertainty is indicated by the hatched band.

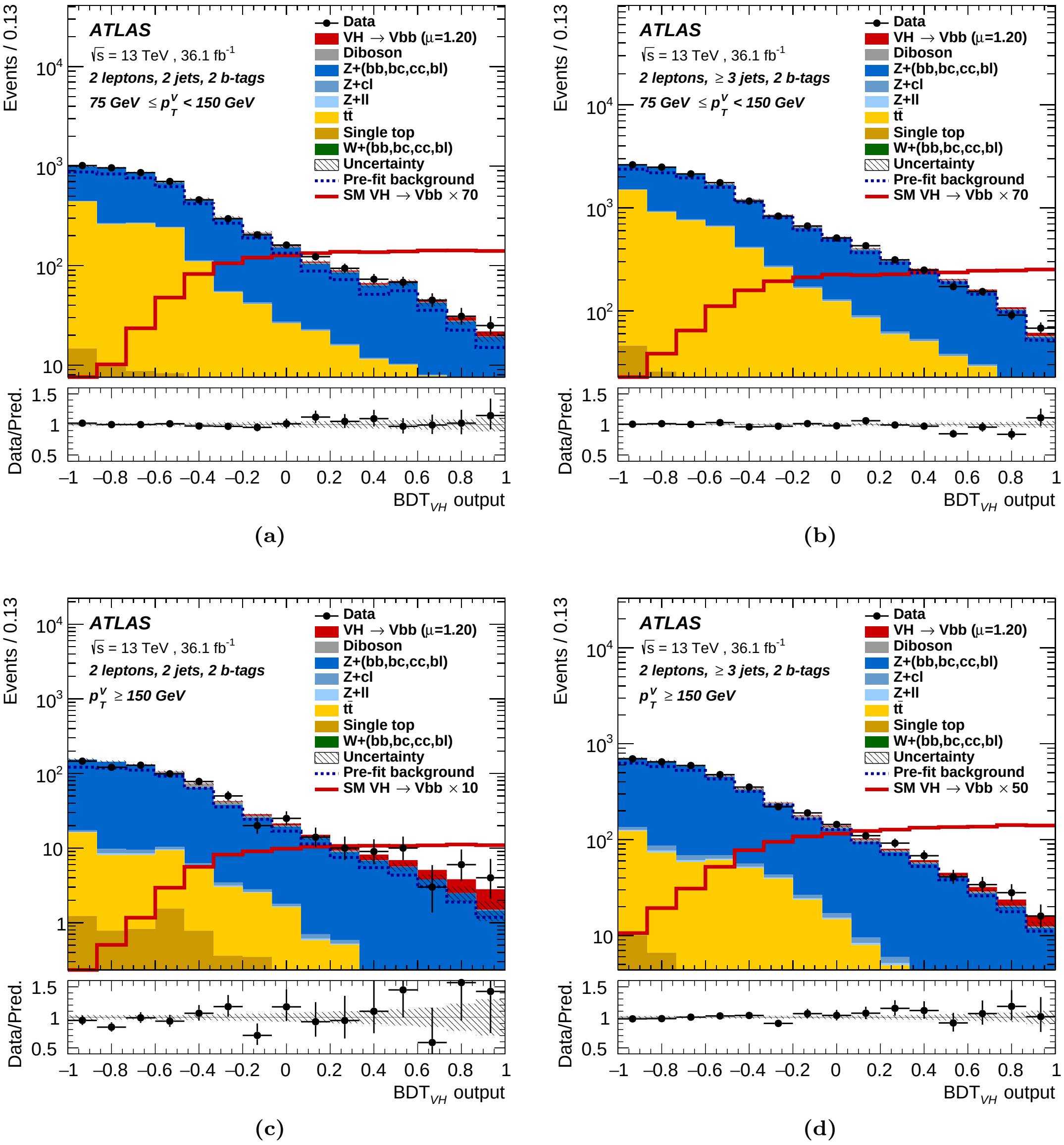

Figure 7.12: Postfit BDT$_{VH}$ distributions in the 2-lepton signal regions, 2-jet (a) and 3-jet (b) for $75 < p_{\mathrm{T}}^{V} < 150$ GeV, and the 2-jet (c) and 3-jet (d) for $p_{\mathrm{T}}^{V} > 150$ GeV, after the unconditional BDT$_{VH}$ global likelihood fit to data. Data (black points with statistical error bars) are shown, corresponding to 36.1 fb^{-1} of Run-2 data collected at $\sqrt{s} = 13$ TeV, along with the simulated prediction (coloured stacked histograms). The $VH \to Vb\bar{b}$ signal is scaled to the postfit value ($\mu = 1.20$), and shown as a stacked red histogram, and unstacked scaled histogram to illustrate the signal shape. The unfilled dashed histogram corresponds to the prefit background prediction. The bottom pad shows the ratio of data to the combined postfit signal and background model, while the total systematic uncertainty is indicated by the hatched band.

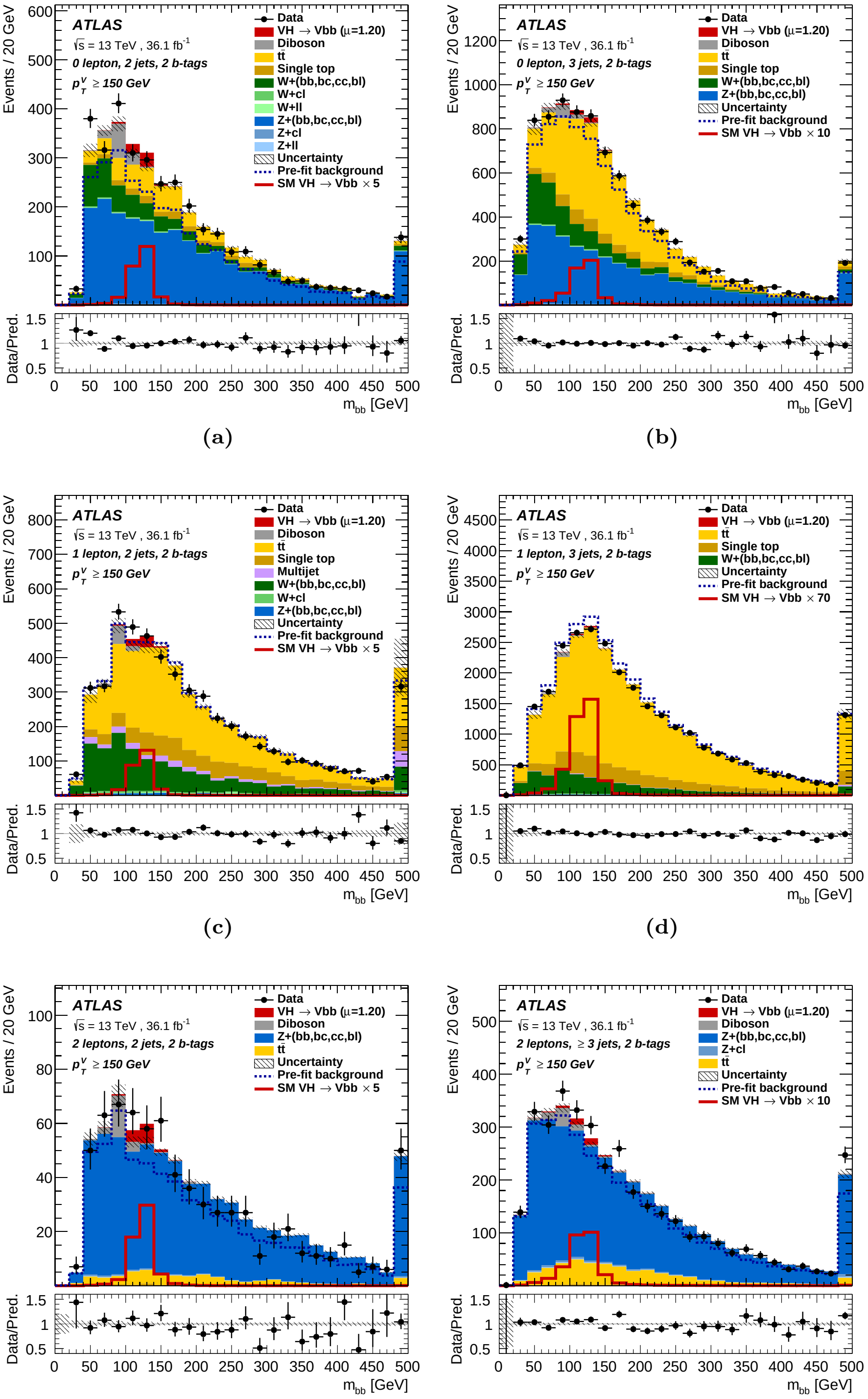

(a) (b) (c) (d) (e) (f)

Figure 7.13: Postfit m_{bb} distributions in the 0-lepton, 2-jet (a) and 3-jet (b), 1-lepton, 2-jet (c) and 3-jet (d) and 2-lepton, 2-jet (e) and 3+-jet (f) signal regions for $p_{\mathrm{T}}^{V} > 150$ GeV, after the unconditional BDT$_{VH}$ global likelihood fit to data. Data (black points with statistical error bars) are shown, corresponding to 36.1 fb^{-1} of Run-2 data collected at $\sqrt{s} = 13$ TeV, along with the simulated prediction (coloured stacked histograms). The $VH \to Vb\bar{b}$ signal is scaled to the postfit value ($\mu = 1.20$), and shown as a stacked red histogram, and unstacked scaled histogram to illustrate the signal shape. The unfilled dashed histogram corresponds to the prefit background prediction. The bottom pad shows the ratio of data to the combined postfit signal and background model, while the total systematic uncertainty is indicated by the hatched band.

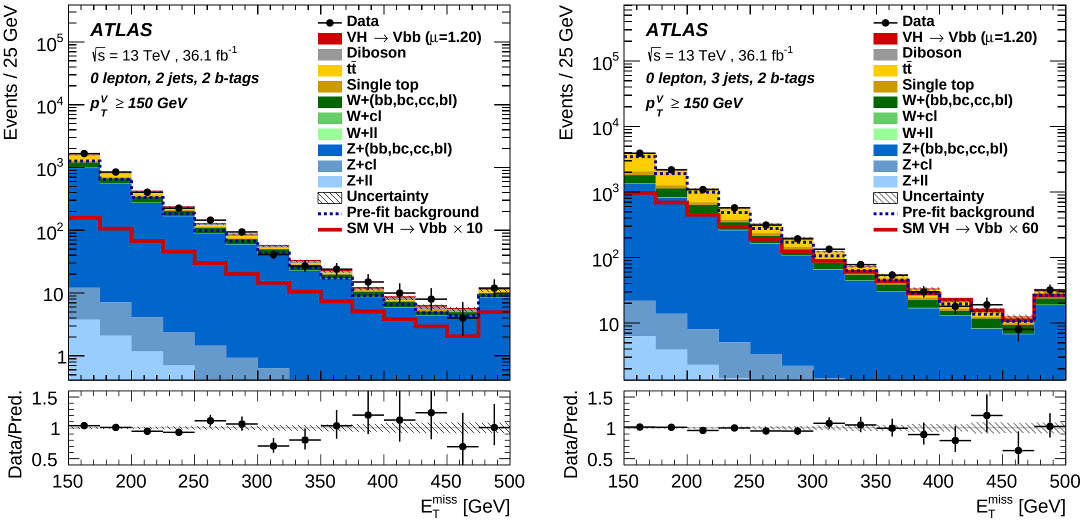

(a) (b)

Figure 7.14: Postfit $E_{\mathrm{T}}^{\mathrm{miss}}$ distributions in the 0-lepton signal regions, 2-jet (a) and 3-jet (b) for $p_{\mathrm{T}}^{V} > 150$ GeV, after the unconditional BDT$_{VH}$ global likelihood fit to data. Data (black points with statistical error bars) are shown, corresponding to 36.1 fb^{-1} of Run-2 data collected at $\sqrt{s} = 13$ TeV, along with the simulated prediction (coloured stacked histograms). The $VH \to Vb\bar{b}$ signal is scaled to the postfit value ($\mu = 1.20$), and shown as a stacked red histogram, and unstacked scaled histogram to illustrate the signal shape. The unfilled dashed histogram corresponds to the prefit background prediction. The bottom pad shows the ratio of data to the combined postfit signal and background model, while the total systematic uncertainty is indicated by the hatched band.

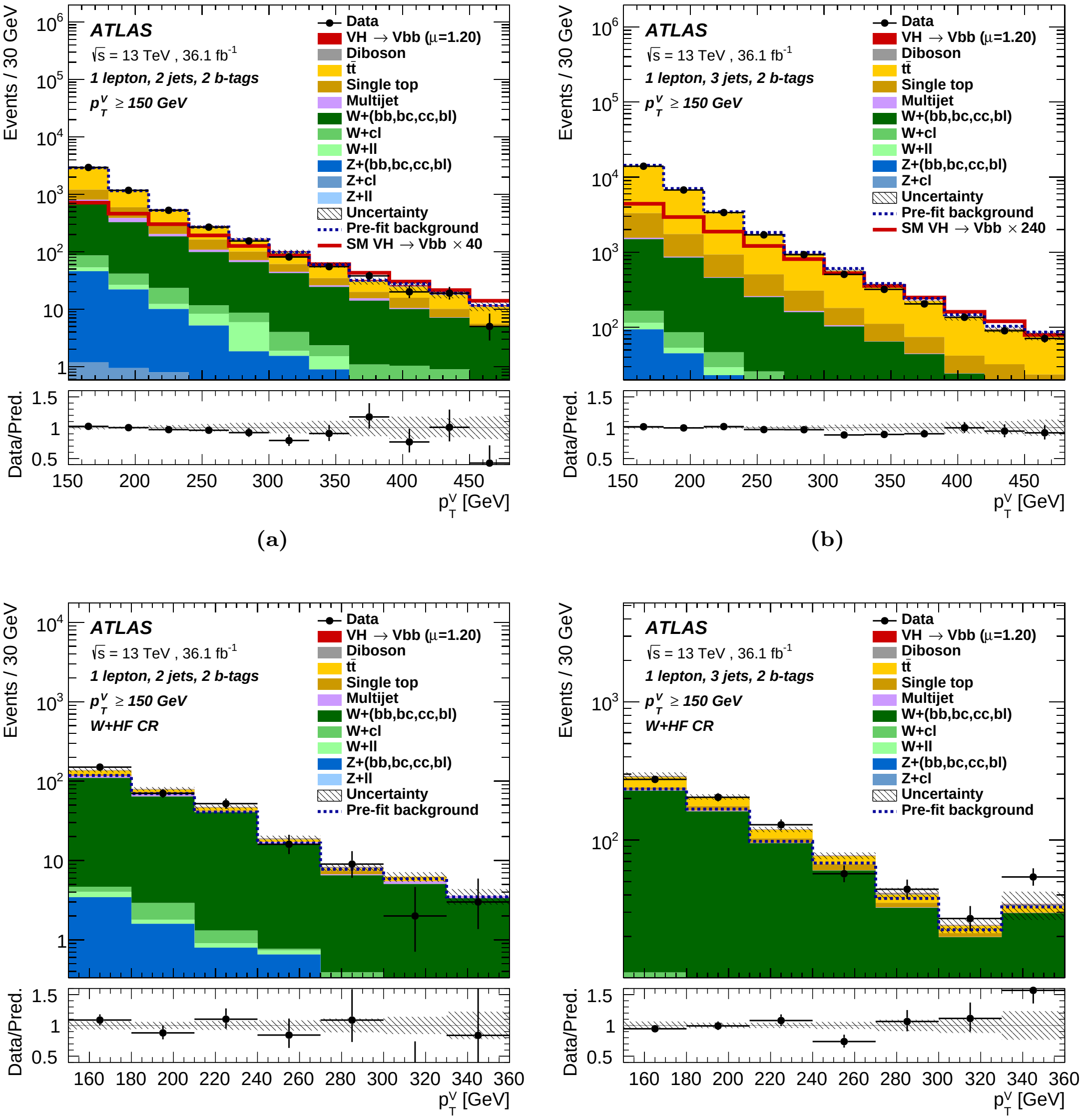

(a) (b)

(c) (d)

Figure 7.15: Postfit p_{T}^{V} distributions in the 1-lepton signal regions, 2-jet (a) and 3-jet (b), and $W+\mathrm{HF}$ control regions, 2-jet (c) and 3-jet (d) for $p_{\mathrm{T}}^{V} > 150$ GeV, after the unconditional BDT_{VH} global likelihood fit to data. Data (black points with statistical error bars) are shown, corresponding to 36.1 fb^{-1} of Run-2 data collected at $\sqrt{s} = 13$ TeV, along with the simulated prediction (coloured stacked histograms). The $VH \to Vb\bar{b}$ signal is scaled to the postfit value ($\mu = 1.20$), and shown as a stacked red histogram, and unstacked scaled histogram to illustrate the signal shape. The unfilled dashed histogram corresponds to the prefit background prediction. The bottom pad shows the ratio of data to the combined postfit signal and background model, while the total systematic uncertainty is indicated by the hatched band.

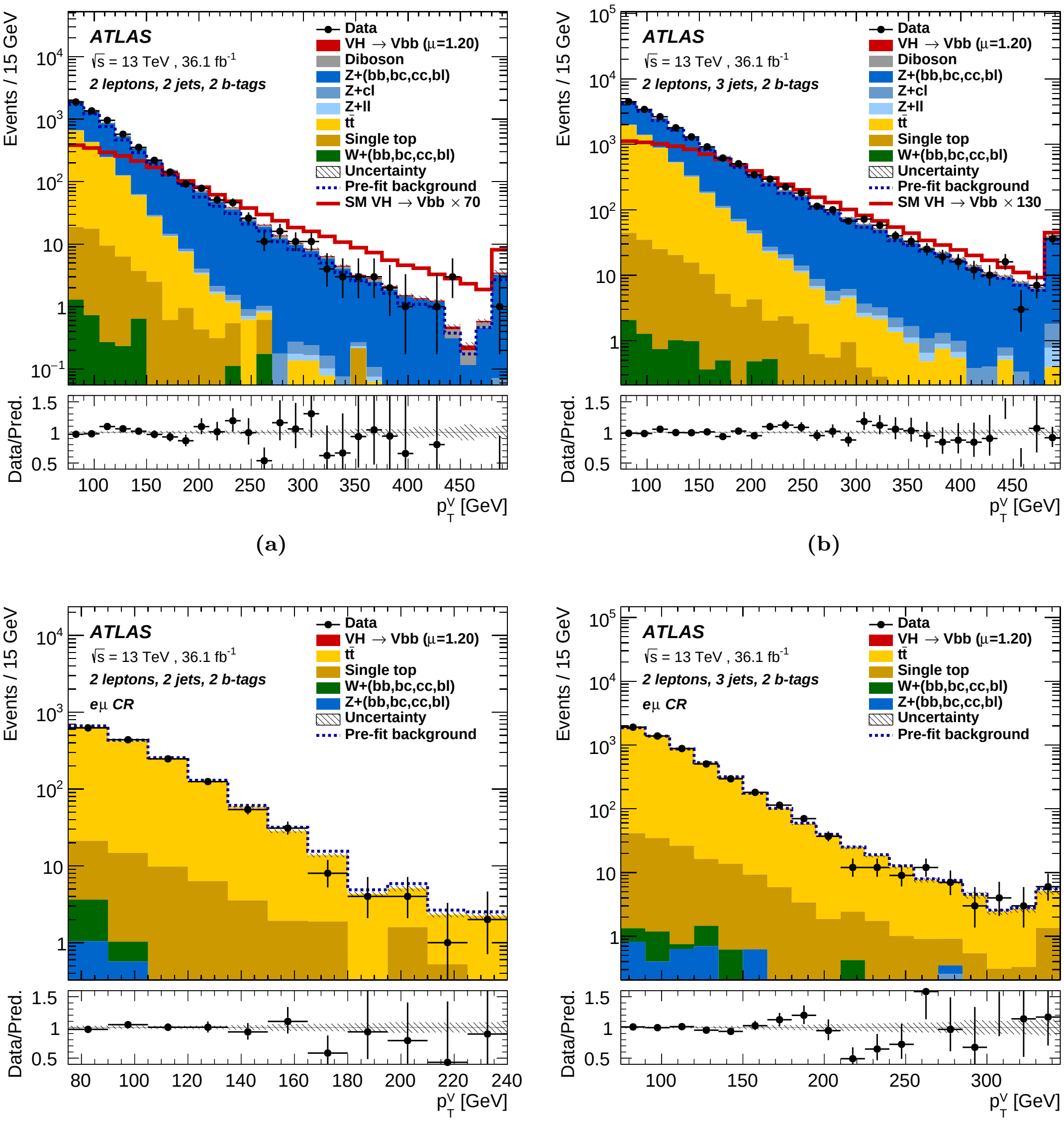

(a) (b) (c) (d)

Figure 7.16: Postfit p_{T}^{V} distributions in the 2-lepton signal regions, 2-jet (a) and 3-jet (b) and top $e\mu$ control regions, 2-jet (c) and 3-jet (d) for $p_{\mathrm{T}}^{V} > 75$ GeV, after the unconditional BDT_{VH} global likelihood fit to data. Data (black points with statistical error bars) are shown, corresponding to 36.1 fb^{-1} of Run-2 data collected at $\sqrt{s} = 13$ TeV, along with the simulated prediction (coloured stacked histograms). The $VH \to Vb\bar{b}$ signal is scaled to the postfit value ($\mu = 1.20$), and shown as a stacked red histogram, and unstacked scaled histogram to illustrate the signal shape. The unfilled dashed histogram corresponds to the prefit background prediction. The bottom pad shows the ratio of data to the combined postfit signal and background model, while the total systematic uncertainty is indicated by the hatched band.

Signal Regions	0-Lepton		1-Lepton		2-Lepton			
	$p_{\mathrm{T}}^{V} > 150$ GeV		$p_{\mathrm{T}}^{V} > 150$ GeV		75 GeV $< p_{\mathrm{T}}^{V} <$ 150 GeV		$p_{\mathrm{T}}^{V} > 150$ GeV	
Sample	2-jet	3-jet	2-jet	3-jet	2-jet	≥3-jet	2-jet	≥3-jet
$Z+ll$	9.0 ± 5.1	15.5 ± 8.1	< 1	–	9.2 ± 5.4	35 ± 19	1.9 ± 1.1	16.4 ± 9.3
$Z+cl$	21.4 ± 7.7	42 ± 14	2.2 ± 0.1	4.2 ± 0.1	25.3 ± 9.5	105 ± 39	5.3 ± 1.9	46 ± 17
Z+HF	2198 ± 84	3270 ± 170	86.5 ± 6.1	186 ± 13	3449 ± 79	8270 ± 150	651 ± 20	3052 ± 66
$W+ll$	9.8 ± 5.6	17.9 ± 9.9	22 ± 10	47 ± 22	< 1	< 1	< 1	< 1
$W+cl$	19.9 ± 8.8	41 ± 18	70 ± 27	138 ± 53	< 1	< 1	< 1	< 1
W+HF	460 ± 51	1120 ± 120	1280 ± 160	3140 ± 420	3.0 ± 0.4	5.9 ± 0.7	< 1	2.2 ± 0.2
Single top-quark	145 ± 22	536 ± 98	830 ± 120	3700 ± 670	53 ± 16	134 ± 46	5.9 ± 1.9	30 ± 10
$t\bar{t}$	463 ± 42	3390 ± 200	2650 ± 170	20640 ± 680	1453 ± 46	4904 ± 91	49.6 ± 2.9	430 ± 22
Diboson	116 ± 26	119 ± 36	79 ± 23	135 ± 47	73 ± 19	149 ± 32	24.4 ± 6.2	87 ± 19
Multijet	–	–	235 ± 119	117 ± 147	–	–	–	–
Total bkg.	3443 ± 57	8560 ± 91	5255 ± 80	28110 ± 170	5065 ± 66	13600 ± 110	738 ± 19	3664 ± 56
Signal (fit)	58 ± 17	60 ± 19	63 ± 19	65 ± 21	25.6 ± 7.8	46 ± 15	13.6 ± 4.1	35 ± 11
Data	3520	8634	5307	28168	5113	13640	724	3708

Table 7.15: The postfit Higgs boson signal and background yields for all signal regions in each channel after the full selection of the BDT_{VH} $VH \to Vb\bar{b}$ analysis has been applied. All postfit systematic uncertainties are included in the indicated uncertainties. An entry of "-" indicates that a specific background component is negligible in a certain region, or that no simulated events are left after the analysis selection.

Control Regions	1-Lepton		2-Lepton			
	$p_{\mathrm{T}}^{V} > 150$ GeV		75 GeV $< p_{\mathrm{T}}^{V} <$ 150 GeV		$p_{\mathrm{T}}^{V} > 150$ GeV	
Sample	2-jet	3-jet	2-jet	≥3-jet	2-jet	≥3-jet
$Z + ll$	< 1	< 1	< 1	< 1	< 1	< 1
$Z + cl$	–	< 1	< 1	< 1	< 1	< 1
Z+HF	6.6 ± 0.7	19.3 ± 1.4	2.1 ± 0.2	2.8 ± 0.2	< 1	1.2 ± 0.1
$W + ll$	1.1 ± 0.1	2.9 ± 0.1	–	–	–	–
$W + cl$	2.6 ± 1.1	8.7 ± 3.7	–	–	–	–
W+HF	234 ± 21	594 ± 45	3.0 ± 0.3	2.7 ± 0.3	< 1	< 1
Single top-quark	10.3 ± 2.8	40 ± 14	50 ± 15	127 ± 45	5.8 ± 1.8	27.9 ± 9.8
$t\bar{t}$	24.8 ± 7.8	107 ± 29	1437 ± 41	4852 ± 85	48.8 ± 3.8	431 ± 21
Diboson	5.6 ± 1.9	12.1 ± 4.2	–	< 1	–	–
Multijet	15.0 ± 7.4	5.9 ± 7.8	–	–	–	–
Total bkg.	300 ± 16	791 ± 27	1492 ± 37	4985 ± 68	55.2 ± 3.9	461 ± 19
Signal (fit)	< 1	1.2 ± 0.4	< 1	< 1	< 1	< 1
Data	302	790	1489	4967	50	470

Table 7.16: The postfit Higgs boson signal and background yields for all control regions in each channel after the full selection of the BDT$_{VH}$ $VH \to Vb\bar{b}$ analysis has been applied. All postfit systematic uncertainties are included in the indicated uncertainties. An entry of "-" indicates that a specific background component is negligible in a certain region, or that no simulated events are left after the analysis selection.

7.8.1.2 Signal Significance and Best Fit μ

The expected significance from the Asimov dataset, expected significance from data and observed significance from data are presented in Table 7.17. Results are presented from the global likelihood fit to individual channels, along with the global likelihood fit to all regions. In terms of expected significance, each channel has a similar sensitivity to the $VH \to Vb\bar{b}$ signal. From the global likelihood fit to all analysis regions, an observed (expected) signal significance of 3.54 σ (3.03 σ) is measured. This corresponds to an observed signal strength of $\mu = 1.20^{+0.24}_{-0.23}(\text{stat.})^{+0.34}_{-0.28}(\text{syst.})$, and provides evidence that the VH production and the $H \to b\bar{b}$ decay are consistent with the prediction of the SM.

Channel	Expected Significance (Asimov)	Expected Significance (Data)	Observed Significance (Data)
0-lepton (SR)	1.99	1.73	0.53
1-lepton (SR+CR)	1.81	1.81	2.30
2-lepton (SR+CR)	1.95	1.86	3.55
0-, 1-, 2-lepton (SR+CR)	3.19	3.03	3.54

Table 7.17: Expected significances from the BDT_{VH} global likelihood fit to the Asimov dataset and data, and observed significance from the unconditional fit to the data, corresponding to 36.1 fb^{-1} of Run-2 data collected at $\sqrt{s} = 13$ TeV. Significances for individual channels are evaluated when conducting the global profile likelihood using regions from that channel only.

In Figure 7.17 (a), the signal strength from the unconditional BDT_{VH} global likelihood fit to data with a combined signal strength parameter is presented, and compared to the case where a signal strength parameter is floated independently for each lepton channel, and Figure 7.17 (b) where a signal strength parameter is floated independently for each signal process (WH/VH). Good agreement between the signal strengths in each lepton channel is observed, with a compatibility of 11.6%. Additionally, consistent signal strengths between the WH and ZH channels are observed, with a compatibility of 75%.

Figure 7.18 presents the postfit data to MC comparison for all analysis bins, ordered by $\log(S/B)$, with S (B) the signal (background) yield in each bin. The $VH \to Vb\bar{b}$ signal contribution is scaled to the fitted signal strength, $\mu = 1.20$. The pull corresponds to the difference between data and the background-only model, divided by the statistical uncertainty. The full line indicates the pull of the prediction for signal and background with respect to the background-only prediction. Good agreement between data and simulation is observed over the full range of S/B bins.

Example event displays for candidate signal events in the 0-, 1- and 2-lepton channels are presented in Figure 7.19.

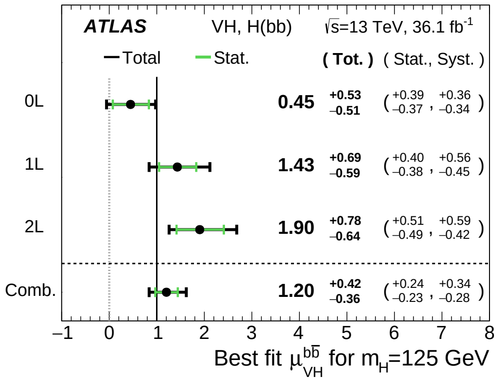

(a) (b)

Figure 7.17: The unconditional BDT_{VH} global likelihood fit to data with a combined signal strength parameter, compared to the case where a signal strength parameter is floated independently for each lepton channel (a), and where a signal strength parameter is floated independently for each signal process (WH/ZH) (b). The green error bar indicates the statistical uncertainty on μ, while the black error bar indicates the total (statistical + systematic) uncertainty on μ.

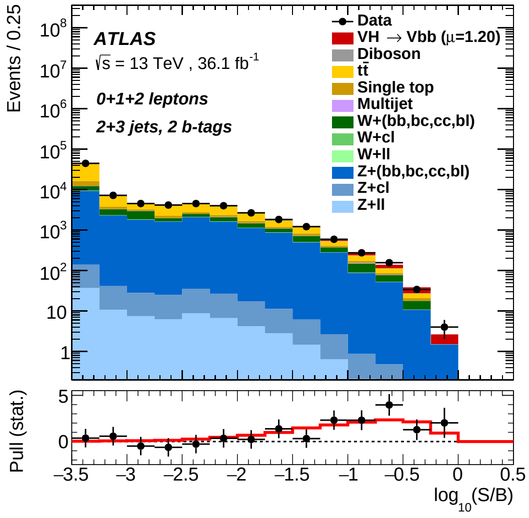

(a)

Figure 7.18: Postfit data to MC comparison for all analysis bins, ordered by $\log(S/B)$, with S (B) the signal (background) yield in each bin, for the BDT_{VH} $VH \to Vb\bar{b}$ analysis. The $VH \to Vb\bar{b}$ signal contribution is scaled to the fitted signal strength, $\mu = 1.20$. Data (black points with statistical error bars) are shown, corresponding to 36.1 fb^{-1} of Run-2 data collected at $\sqrt{s} = 13$ TeV, along with the simulated prediction (coloured stacked histograms). The pull corresponds to the difference between data and the background-only model, divided by the statistical uncertainty. The solid red line indicates the pull of the prediction for signal and background with respect to the background-only prediction.

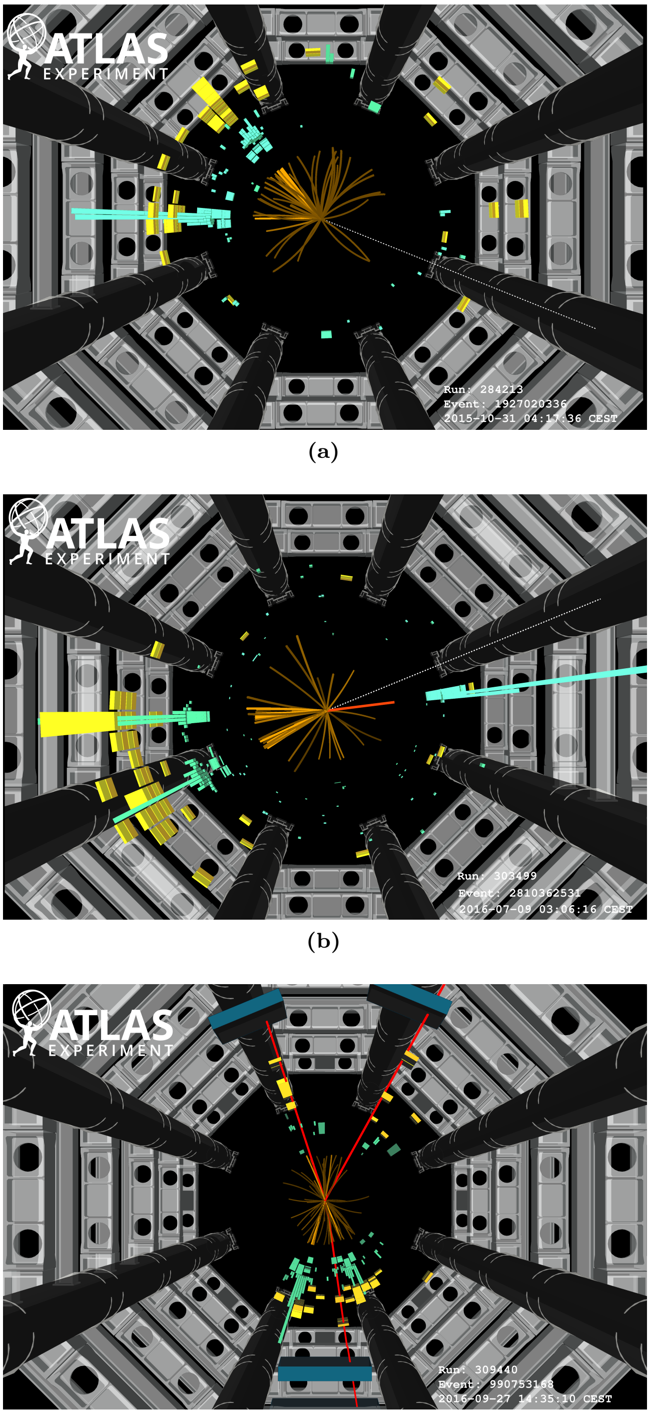

(a)

(b)

(c)

Figure 7.19: Event displays of candidate $VH \rightarrow Vb\bar{b}$ signal events in the $r - \phi$ plane of the ATLAS detector. In all cases, two b-tagged jets are represented by the green and yellow blocks corresponding to the energy depositions in the electromagnetic and hadronic calorimeters. Reconstructed tracks in the inner detector are represented by dark orange tracks, whilst light orange tracks are associated to the b-tagged jets, and are consistent with the decay of a b-hadron. The two b-tagged jets are used to construct the Higgs candidate. In the 0-lepton channel (a), the Higgs candidate can be seen recoiling off $E_{\mathrm{T}}^{\mathrm{miss}}$ (dashed track), corresponding to $p_{\mathrm{T}}^{V} = 294$ GeV. In the 1-lepton channel (b), the Higgs candidate can be seen recoiling off an electron (red track) and $E_{\mathrm{T}}^{\mathrm{miss}}$ (dashed track), corresponding the $p_{\mathrm{T}}^{V} = 450$ GeV. In the 2-lepton channel (c), the Higgs candidate can be seen recoiling off two muons (red tracks), corresponding to $p_{\mathrm{T}}^{V} = 204$ GeV. An additional muon is also found within $\Delta R < 0.4$ of a jet, and likely originates from the leptonic decay of a b-hadron.

7.8.1.3 Nuisance Parameter Ranking

The total statistical uncertainty on μ is 0.24, whilst the total systematic uncertainty on μ is 0.31. This indicates that the sensitivity of the analysis to the $VH \rightarrow Vb\bar{b}$ signal is now systematically limited, and the total uncertainty may no longer decrease proportionally as $L^{-\frac{1}{2}}$, with L the integrated luminosity.

The impact of each group of systematics on the uncertainty of the fitted signal strength, μ, is presented in Table 7.18, calculated using the breakdown method. Those arising from signal modelling, MC statistical and b-tagging uncertainties provide the largest contribution. Whilst the b-jet scale factor has the largest single experimental systematic contribution, this has greatly benefited from the work presented in Chapter 6.

In Figure 7.20, the nuisance parameters are presented, ordered by their postfit impact on μ, evaluated using the ranking method. The dominant uncertainty originates from the acceptance effects of the modelling of the underlying event (UE) and parton shower (PS) in the signal samples. The next set of nuisance parameters are more closely ranked, and include modelling effects on the $W +$ jets, $t\bar{t}$, and single top-quark processes. The largest contribution of MC statistical uncertainty can be seen to be in bins 12 and 13 of the 1-lepton 2-jet signal region BDT_{VH} distribution, and is largely driven by large statistical uncertainties on the simulated $t\bar{t}$ background. The largest contribution of experimental systematic uncertainties arise from the use of b-tagging, in particular the b-jet scale factor uncertainties.

Source of Uncertainty		σ_μ
Total		0.39
Statistical		0.24
Systematic		0.31
Experimental Uncertainties		
Jets		0.03
$E_{\mathrm{T}}^{\mathrm{miss}}$		0.03
Leptons		0.01
b-tagging	b-jets	0.09
	c-jets	0.04
	light-flavour jets	0.04
	extrapolation	0.01
Pile-up		0.01
Luminosity		0.04
Theoretical and Modelling Uncertainties		
Signal		0.17
Floating normalisations		0.07
$Z + \mathrm{jets}$		0.07
$W + \mathrm{jets}$		0.07
$t\bar{t}$		0.07
Single top-quark		0.08
Diboson		0.02
Multijet		0.02
MC statistical		0.13

Table 7.18: Contributions to the uncertainty on μ for the BDT_{VH} global likelihood fit to data, estimated using the breakdown method. The sum in quadrature of the systematic uncertainties attached to the categories differs from the total systematic uncertainty due to correlations.

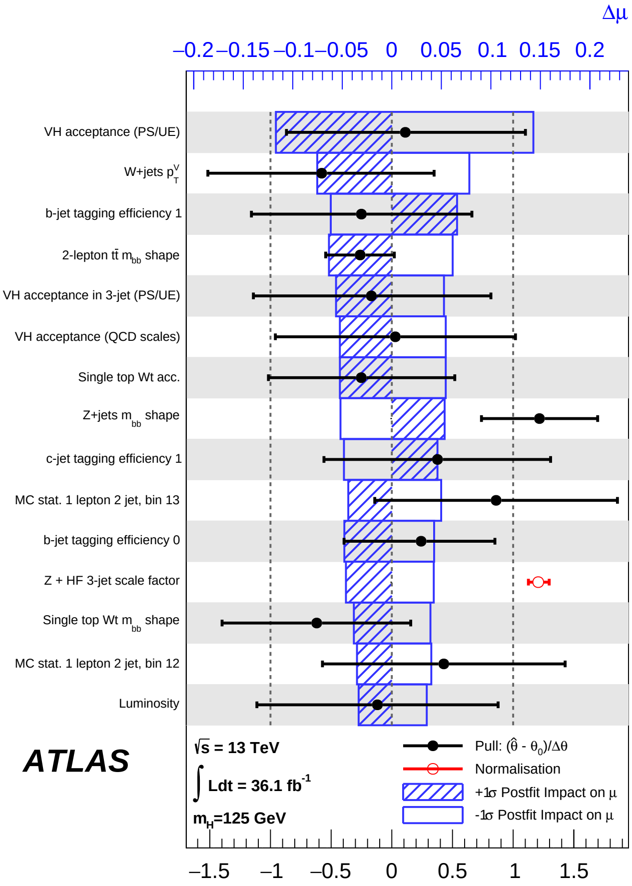

Figure 7.20: Impact of systematic uncertainties on the fitted signal-strength parameter μ in the BDT$_{VH}$ global likelihood fit to data in the $VH \to Vb\bar{b}$ analysis. The systematic uncertainties are listed in decreasing order of their impact on μ, when evaluated using the ranking method. The blue hatched and open areas correspond to the upwards and downwards variations, respectively, with the impact referring to the upper x-axis. The filled circles show the pull of the corresponding nuisance parameter in the fit, referring to the lower x-axis. The constraint of the nuisance parameter is represented by the black error bar.

7.8.2 $VZ \to Vb\bar{b}$

In this section, results from the $VZ \to Vb\bar{b}$ BDT$_{VZ}$ global likelihood fit to data are presented. An identical event selection to the BDT$_{VH}$ $VH \to Vb\bar{b}$ event selection is applied, with analogous fit regions. Due to a limited number of simulated MC events in the diboson signal samples, the BDT transformation is set to reduce the number of bins from 15 to 10.

7.8.2.1 Postfit Distributions

Postfit distributions of a number of key variables for the BDT$_{VZ}$ global likelihood fit are presented in this section. Figures 7.21 - 7.23 present the postfit $VZ \to Vb\bar{b}$ distributions in the 0-, 1- and 2-lepton channels. Good agreement between data and MC is observed in all regions.

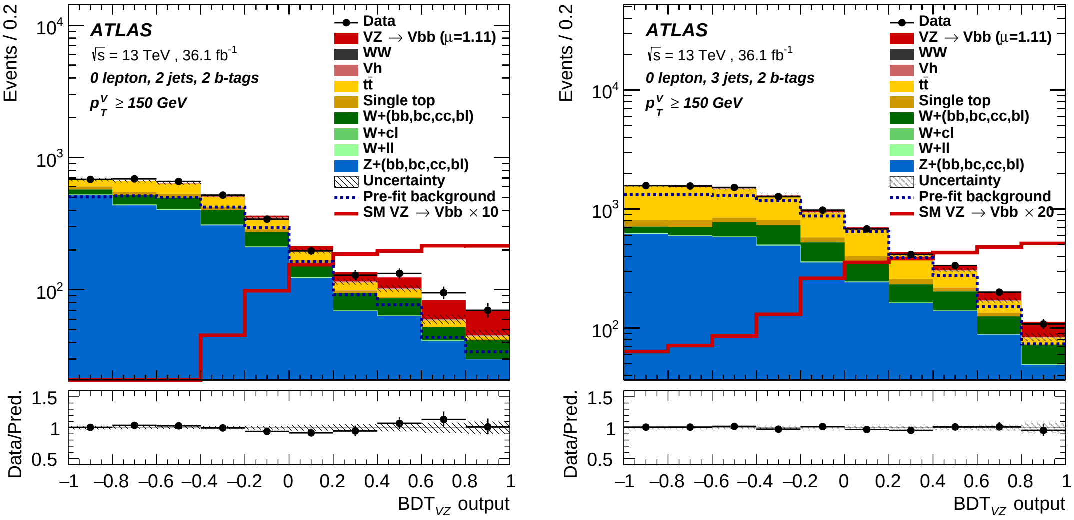

(a) (b)

Figure 7.21: Postfit BDT$_{VZ}$ distributions in the 0-lepton signal regions, 2-jet (a) and 3-jet (b) for $p_{\mathrm{T}}^{V} > 150$ GeV, after the unconditional BDT$_{VZ}$ global likelihood fit to data. Data (black points with statistical error bars) are shown, corresponding to 36.1 fb^{-1} of Run-2 data collected at $\sqrt{s} = 13$ TeV, along with the simulated prediction (coloured stacked histograms). The $VZ \to Vb\bar{b}$ signal is scaled to the postfit value ($\mu = 1.11$), and shown as a stacked red histogram, and unstacked scaled histogram to illustrate the signal shape. The unfilled dashed histogram corresponds to the prefit background prediction. The bottom pad shows the ratio of data to the combined postfit signal and background model, while the total systematic uncertainty is indicated by the hatched band.

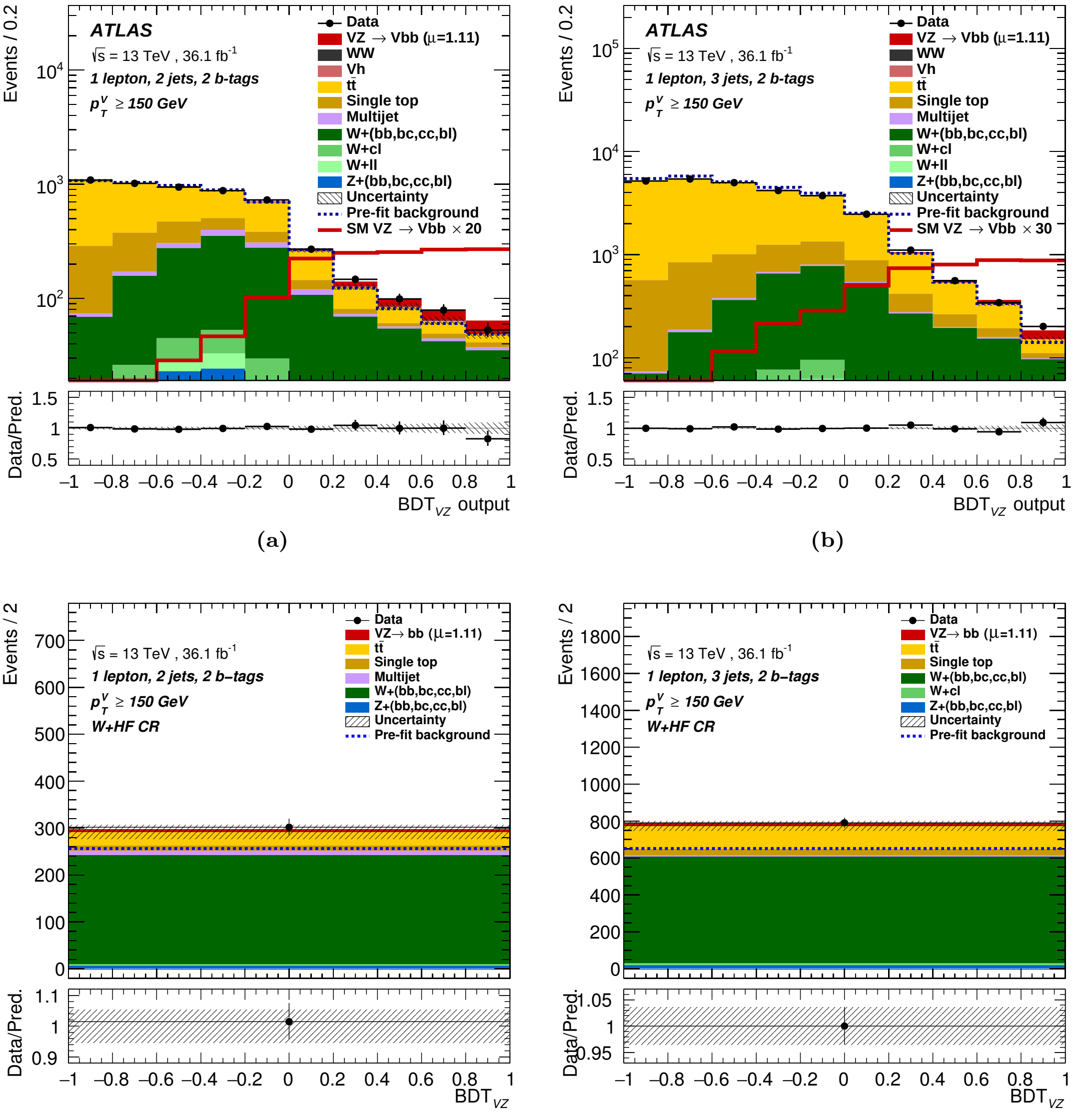

(a) (b)

(c) (d)

Figure 7.22: Postfit BDT_{VZ} distributions in the 1-lepton signal regions, 2-jet (a) and 3-jet (b) for $p_{\mathrm{T}}^{V} > 150$ GeV, and $W+\mathrm{HF}$ control regions, 2-jet (c) and 3-jet (d) for $p_{\mathrm{T}}^{V} > 150$ GeV, after the unconditional BDT_{VZ} global likelihood fit to data. Data (black points with statistical error bars) are shown, corresponding to 36.1 fb^{-1} of Run-2 data collected at $\sqrt{s} = 13$ TeV, along with the simulated prediction (coloured stacked histograms). The $VZ \to Vb\bar{b}$ signal is scaled to the postfit value ($\mu = 1.11$), and shown as a stacked red histogram, and unstacked scaled histogram to illustrate the signal shape. The unfilled dashed histogram corresponds to the prefit background prediction. The bottom pad shows the ratio of data to the combined postfit signal and background model, while the total systematic uncertainty is indicated by the hatched band.

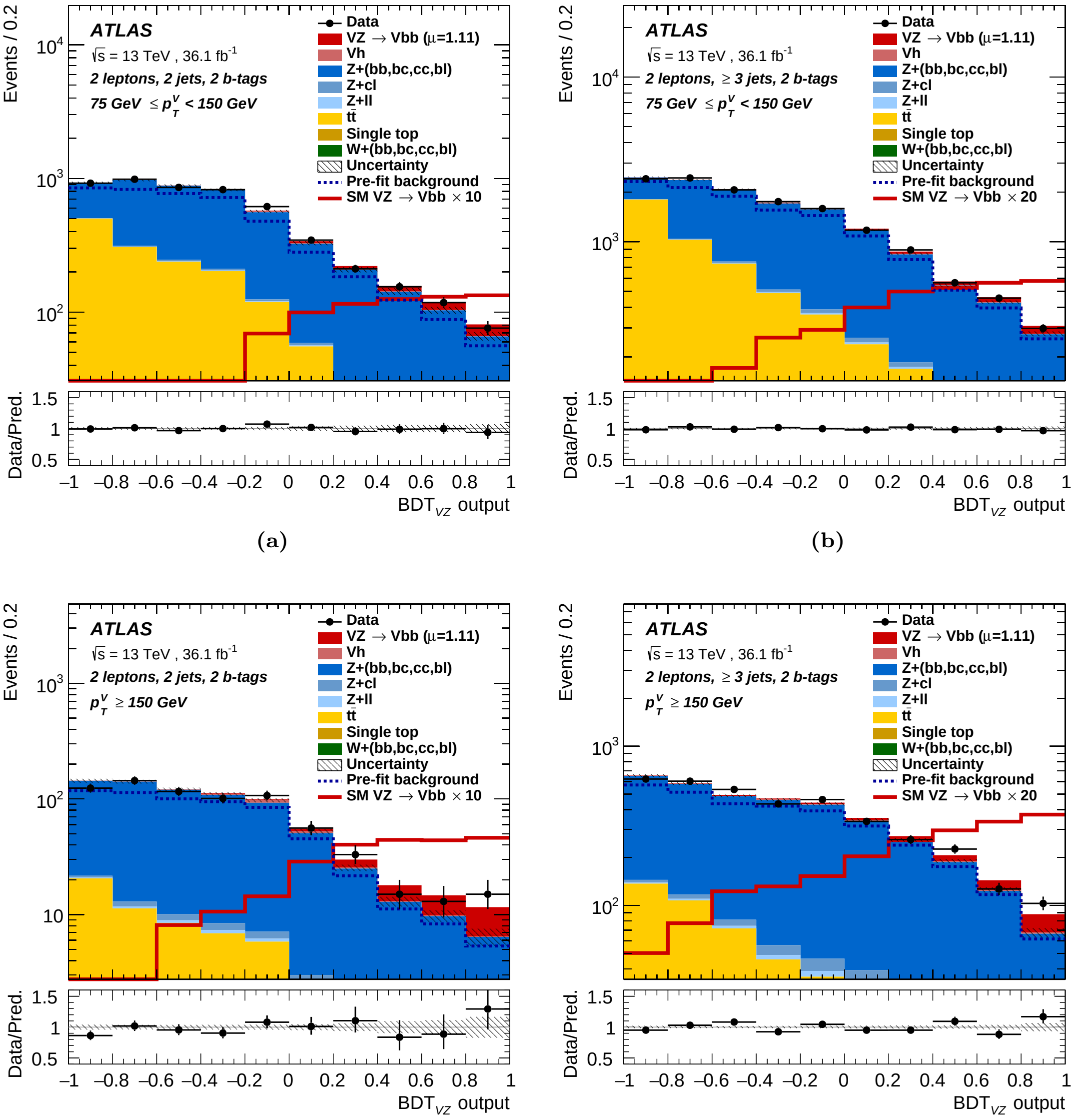

(a) (b) (c) (d)

Figure 7.23: Postfit BDT$_{VZ}$ distributions in the 2-lepton signal regions, 2-jet (a) and 3-jet (b) for $75 < p_{\mathrm{T}}^{V} < 150$ GeV, and the 2-jet (c) and 3-jet (d) for $p_{\mathrm{T}}^{V} > 150$ GeV, after the unconditional BDT$_{VZ}$ global likelihood fit to data. Data (black points with statistical error bars) are shown, corresponding to 36.1 fb^{-1} of Run-2 data collected at $\sqrt{s} = 13$ TeV, along with the simulated prediction (coloured stacked histograms). The $VZ \rightarrow Vb\bar{b}$ signal is scaled to the postfit value ($\mu = 1.11$), and shown as a stacked red histogram, and unstacked scaled histogram to illustrate the signal shape. The unfilled dashed histogram corresponds to the prefit background prediction. The bottom pad shows the ratio of data to the combined postfit signal and background model, while the total systematic uncertainty is indicated by the hatched band.

7.8.2.2 Signal Significance and Best Fit μ

The expected significance from the Asimov dataset, expected significance from data and observed significance from data are presented in Table 7.19. Results are presented from the global likelihood fit to individual channels, along with the global likelihood fit to all regions. In terms of expected significance, the 0- and 2-lepton channels are the most sensitive to the $VZ \to Vb\bar{b}$ signal. In the 1-lepton channel, the sensitivity to the $VZ \to Vb\bar{b}$ process is reduced due to the large W + HF background under the diboson signal. From the global likelihood fit to all analysis regions, an observed (expected) signal significance of 5.76 σ (5.25 σ) is measured. This corresponds to an observed signal strength of $\mu_{VZ} = 1.11^{+0.12}_{-0.11}(\text{stat.})^{+0.22}_{-0.19}(\text{syst.})$.

Channel	Expected Significance (Asimov)	Expected Significance (Data)	Observed Significance (Data)
0-lepton (SR)	3.77	3.61	4.16
1-lepton (SR+CR)	1.89	1.79	1.69
2-lepton (SR+CR)	3.79	3.48	3.45
0-, 1-, 2-lepton (SR+CR)	5.86	5.25	5.76

Table 7.19: Expected significances from the BDT$_{VZ}$ global likelihood fit to the Asimov dataset and data, and observed significance from the unconditional fit to the data, corresponding to 36.1 fb^{-1} of Run-2 data collected at $\sqrt{s} = 13$ TeV. Significances for individual channels are evaluated when conducting the global profile likelihood using regions from that channel only.

In Figure 7.24 (a), the signal strength from the unconditional BDT$_{VZ}$ global likelihood fit to data with a combined signal strength parameter is presented, compared to the case where a signal strength parameter is floated independently for each lepton channel, and Figure 7.17 (b) where a signal strength parameter is floated independently for each signal process (WZ/VZ). Good agreement between the signal strengths in each lepton channel is observed, with a measured compatibility at the level of 99.8%. Additionally, consistent signal strengths between the WZ and ZZ channels are observed, with a measured compatibility at the level of 88%.

Figure 7.25 presents the postfit data to MC comparison for all analysis bins, ordered by $\log(S/B)$, with S (B) the signal (background) yield in each bin. The $VZ \to Vb\bar{b}$ signal contribution is scaled to the fitted signal strength, $\mu = 1.11$. The pull corresponds to the difference between data and the background-only model, divided by the statistical uncertainty. The full line indicates the pull of the prediction for signal and background with respect to the background-only prediction. Good agreement between data and simulation is observed over the full range of S/B bins.

The results from the BDT$_{VZ}$ global likelihood fit to data provide strong evidence that the analysis strategy, background modelling and associated uncertainties, BDT approach and fitting procedure are robust and working as expected. The measured signal strength in each channel, and in the combination, is consistent with the SM, along with pulls and constraints of the nuisance parameters, which are all well understood. The degree of compatibility of the measured signal strength between each channel is another strong verification that the global likelihood fit and background model are behaving as expected.

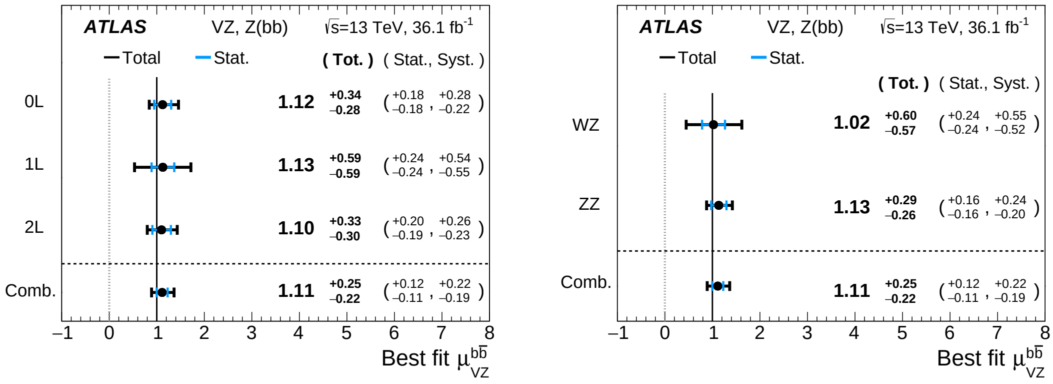

(a) (b)

Figure 7.24: The unconditional BDT$_{VZ}$ global likelihood fit to data with a combined signal strength parameter, compared to the case where a signal strength parameter is floated independently for each lepton channel (a), and where a signal strength parameter is floated independently for each signal process (WZ/ZZ) (b). The blue error bar indicates the statistical uncertainty on μ, while the black error bar indicates the total (statistical + systematic) uncertainty on μ.

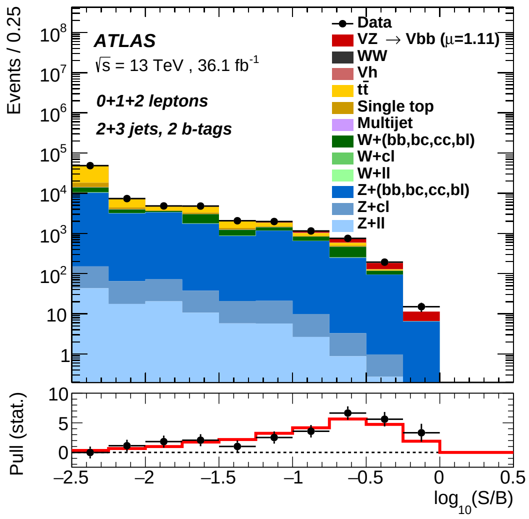

(a)

Figure 7.25: Postfit data to MC comparison for all analysis bins, ordered by $\log(S/B)$, with S (B) the signal (background) yield in each bin, for the BDT$_{VZ}$ $VZ \to Vb\bar{b}$ analysis. The $VH \to Vb\bar{b}$ signal contribution is scaled to the fitted signal strength, $\mu = 1.11$. Data (black points with statistical error bars) are shown, corresponding to 36.1 fb^{-1} of Run-2 data collected at $\sqrt{s} = 13$ TeV, along with the simulated prediction (coloured stacked histograms). The pull corresponds to the difference between data and the background-only model, divided by the statistical uncertainty. The solid line indicates the pull of the prediction for signal and background with respect to the background-only prediction.

7.8.3 $VH \rightarrow Vb\bar{b}$ Cut-Based Dijet Mass Cross-Check

In this section, results from the $VH \rightarrow Vb\bar{b}$ dijet mass (m_{bb}) global likelihood fit to data are presented. This fit provides a cross-check of the multivariate techniques used in the results presented in Section 7.8.1, by using a cut-based event selection. Whilst the analysis sensitivity is lower than that when applying a BDT, consistency between the background model and fit results can provide further validation of the BDT results.

7.8.3.1 Postfit Distributions

Postfit distributions of a number of key variables for the dijet mass global likelihood fit are presented in this section. Figures 7.26 - 7.28 present the postfit m_{bb} distributions in the 0-, 1- and 2-lepton channels. Good agreement between data and simulation is achieved in all cases.

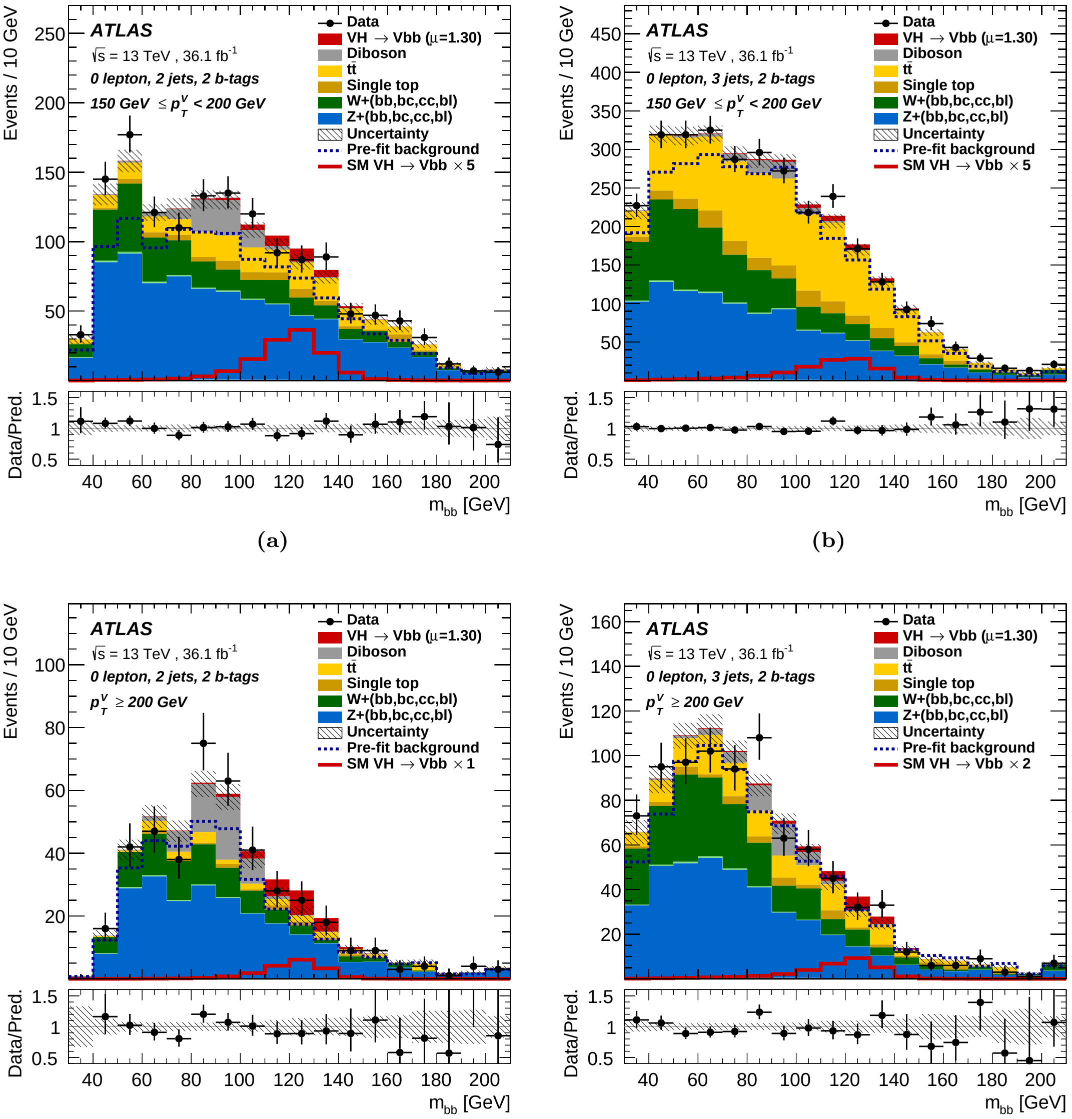

(a) (b)

(c) (d)

Figure 7.26: Postfit m_{bb} distributions in the 0-lepton signal regions, 2-jet (a) and 3-jet (b) for $150 < p_{\mathrm{T}}^{V} < 200$ GeV, and 2-jet (c) and 3-jet (d) for $p_{\mathrm{T}}^{V} < 200$ GeV, after the unconditional cut-based dijet mass global likelihood fit to data. Data (black points with statistical error bars) are shown, corresponding to 36.1 fb^{-1} of Run-2 data collected at $\sqrt{s} = 13$ TeV, along with the simulated prediction (coloured stacked histograms). The $VH \to Vb\bar{b}$ signal is scaled to the postfit value ($\mu = 1.30$), and shown as a stacked red histogram, and unstacked scaled histogram to illustrate the signal shape. The unfilled dashed histogram corresponds to the prefit background prediction. The bottom pad shows the ratio of data to the combined postfit signal and background model, while the total systematic uncertainty is indicated by the hatched band.

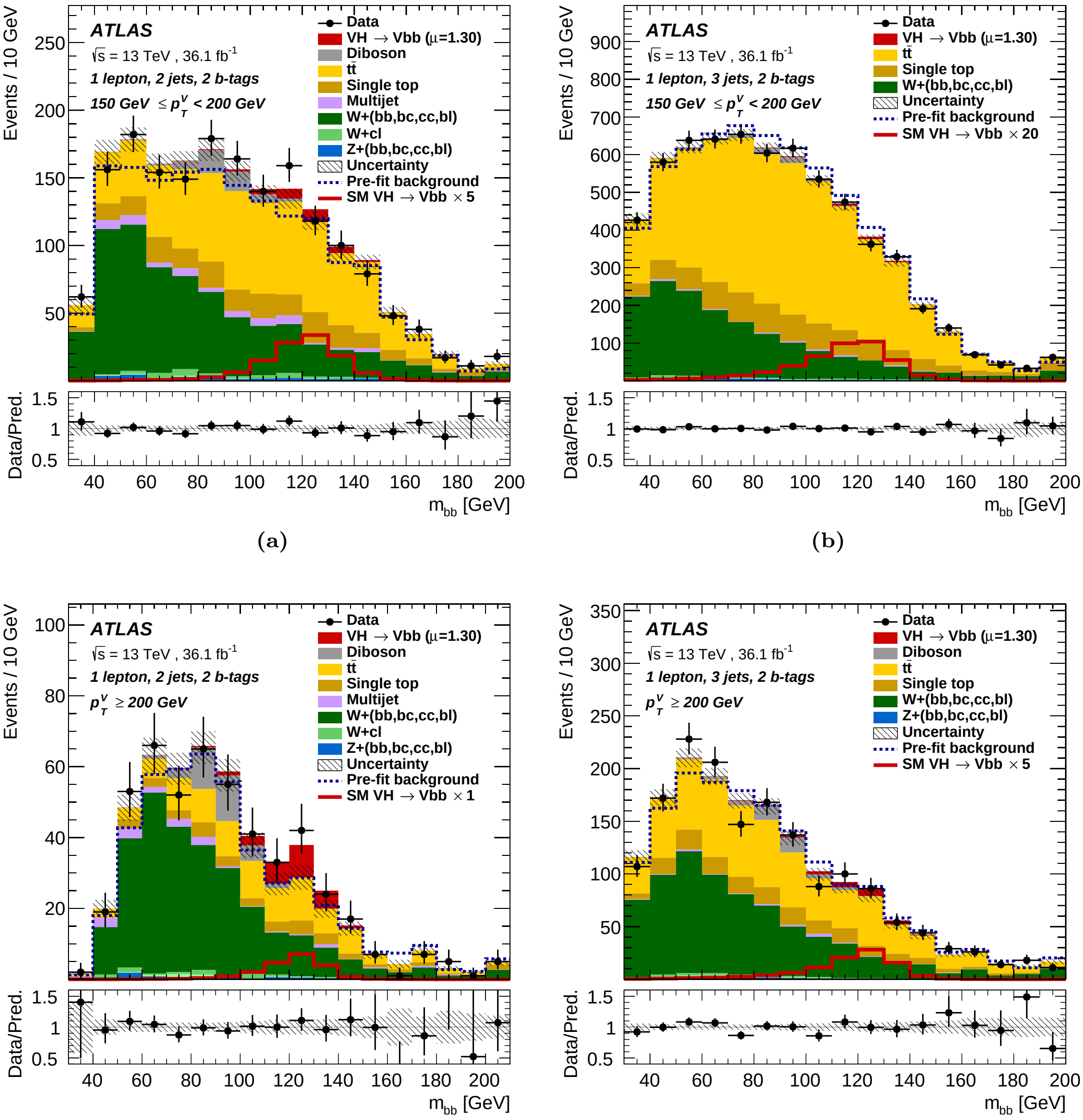

(a) (b) (c) (d)

Figure 7.27: Postfit m_{bb} distributions in the 1-lepton signal regions, 2-jet (a) and 3-jet (b) for $150 < p_{\mathrm{T}}^{V} < 200$ GeV, and 2-jet (c) and 3-jet (d) for $p_{\mathrm{T}}^{V} < 200$ GeV, after the unconditional cut-based dijet mass global likelihood fit to data. Data (black points with statistical error bars) are shown, corresponding to 36.1 fb^{-1} of Run-2 data collected at $\sqrt{s} = 13$ TeV, along with the simulated prediction (coloured stacked histograms). The $VH \to Vb\bar{b}$ signal is scaled to the postfit value ($\mu = 1.30$), and shown as a stacked red histogram, and unstacked scaled histogram to illustrate the signal shape. The unfilled dashed histogram corresponds to the prefit background prediction. The bottom pad shows the ratio of data to the combined postfit signal and background model, while the total systematic uncertainty is indicated by the hatched band.

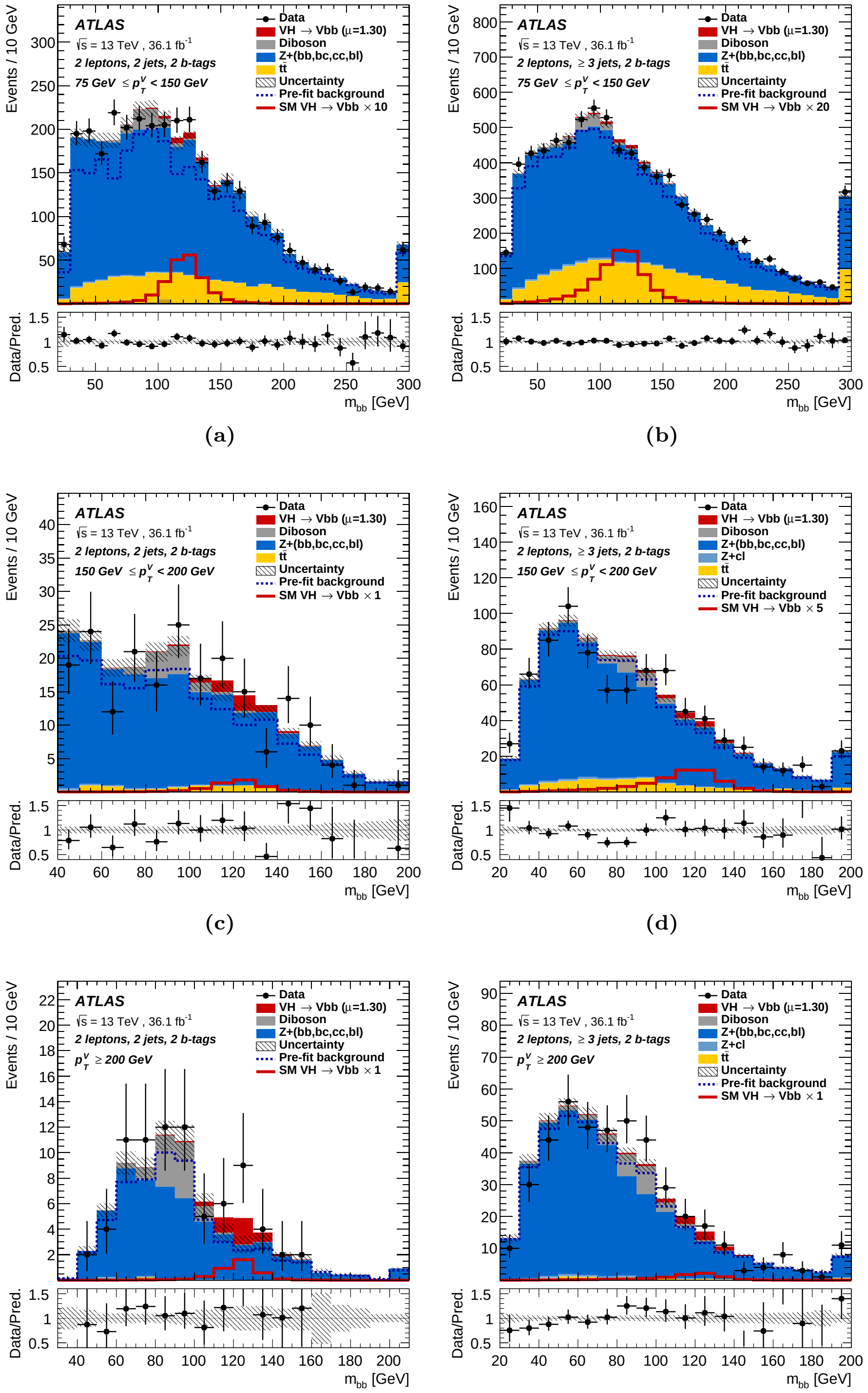

(a) (b)

(c) (d)

(e) (f)

Figure 7.28: Postfit m_{bb} distributions in the 2-lepton signal regions, 2-jet (a) and 3-jet (b) for $75 < p_{\mathrm{T}}^{V} < 150$ GeV, 2-jet (c) and 3-jet (d) for $150 < p_{\mathrm{T}}^{V} < 200$ GeV, and 2-jet (e) and 3-jet (f) for $p_{\mathrm{T}}^{V} < 200$ GeV, after the unconditional cut-based dijet mass global likelihood fit to data. Data (black points with statistical error bars) are shown, corresponding to 36.1 fb^{-1} of Run-2 data collected at $\sqrt{s} = 13$ TeV, along with the simulated prediction (coloured stacked histograms). The $VH \to Vb\bar{b}$ signal is scaled to the postfit value ($\mu = 1.30$), and shown as a stacked red histogram, and unstacked scaled histogram to illustrate the signal shape. The unfilled dashed histogram corresponds to the prefit background prediction. The bottom pad shows the ratio of data to the combined postfit signal and background model, while the total systematic uncertainty is indicated by the hatched band.

In Figure 7.29, the postfit, summed background subtracted m_{bb} distribution is presented. The background subtracted m_{bb} distribution for each region is added, weighted by the ratio of the fitted signal yield to background yield, S/B, for that region. The $VH \to Vb\bar{b}$ signal can be visually seen as a shoulder on the side of the diboson peak, in good agreement with the data points.

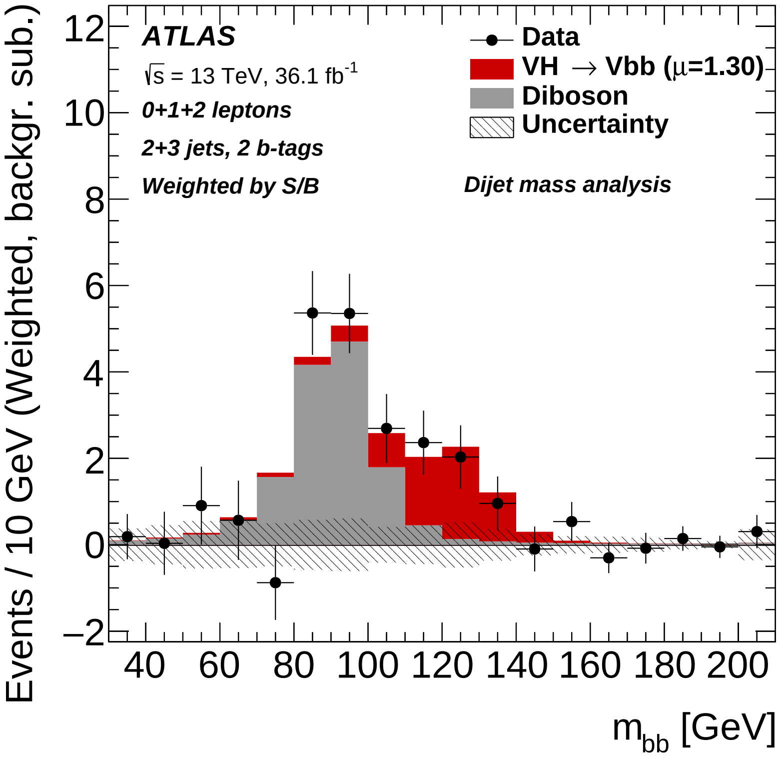

Figure 7.29: Postfit, summed background subtracted m_{bb} distribution from the cut-based dijet mass global likelihood fit to data. Each region is added, weighted by its fitted S/B and all backgrounds except for $VZ \to Vb\bar{b}$ are subtracted. The expected $VH \to Vb\bar{b}$ signal contribution is scaled by the measured signal strength ($\mu = 1.30$), and corresponds to the red filled histogram. The grey filled histogram corresponds to the postfit $VZ \to Vb\bar{b}$ contribution. Data are shown as black points with statistical error bars, corresponding to 36.1 fb^{-1} of Run-2 data collected at $\sqrt{s} = 13$ TeV. The size of the combined statistical and systematic uncertainty for the fitted background is indicated by the hatched band.

7.8.3.2 Signal Significance and Best Fit μ

The expected significance from the Asimov dataset, expected significance from data and observed significance from data are presented in Table 7.20. Results are presented from the global likelihood fit to individual channels, along with the global likelihood fit to all regions. In terms of expected significance, each channel has a similar expected sensitivity to the $VH \to Vb\bar{b}$ signal. From the global likelihood fit to all analysis regions, an observed (expected) signal significance of 3.51 σ (2.78 σ) is measured. This corresponds to an observed signal strength of $\mu = 1.30^{+0.28}_{-0.27}(\text{stat.})^{+0.37}_{-0.29}(\text{syst.})$. Whilst the larger statistical uncertainty in the cut-based analyses compared to the BDT$_{VH}$ analysis is expected, the larger systematic uncertainty arises as a result of reduced constraints on systematic uncertainties.

Channel	Expected Significance (Asimov)	Expected Significance (Data)	Observed Significance (Data)
0-lepton (SR)	1.75	1.55	0.38
1-lepton (SR+CR)	1.43	1.49	2.02
2-lepton (SR+CR)	1.60	1.60	3.45
0-, 1-, 2-lepton (SR+CR)	2.78	2.78	3.51

Table 7.20: Expected significances from the global likelihood fit to the Asimov dataset and data, and observed significance from the unconditional fit to the data, corresponding to 36.1 fb^{-1} of Run-2 data collected at $\sqrt{s} = 13$ TeV in the dijet mass analysis, for the $VH \to Vb\bar{b}$ signal. Significances for individual channels are evaluated when conducting the global profile likelihood using regions from that channel only.

In Figure 7.30, the $VH \to Vb\bar{b}$ signal strength parameter from the unconditional global likelihood fit to data is compared for the BDT$_{VH}$ and cut-based dijet mass fits with one signal strength parameter, as well as the case where a signal strength parameter is floated independently for each lepton channel. A high degree of compatibility between the dijet mass and BDT$_{VH}$ signal strengths is observed, acting as a further validation of the robustness of this result.

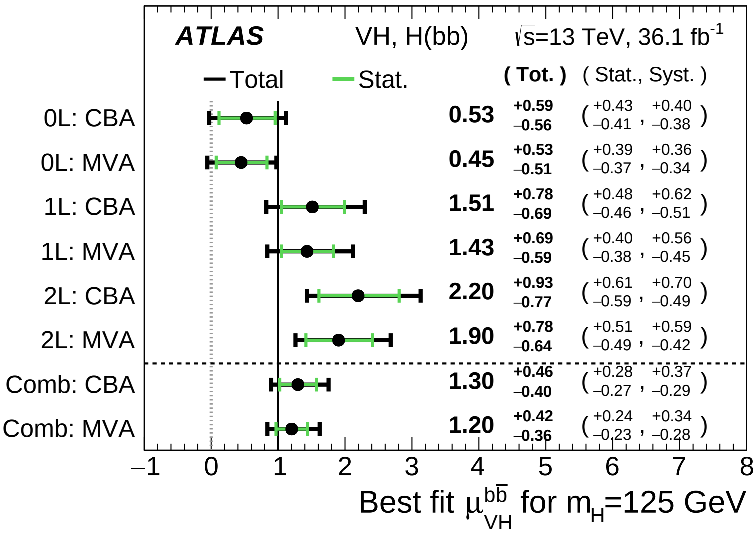

(a)

Figure 7.30: Comparison of the fitted signal strength parameters from the BDT_{VH} $VH \to Vb\bar{b}$ (MVA) fit, and the cut-based dijet mass $VH \to Vb\bar{b}$ (CBA) fit, for the cases with one signal strength parameter, as well as the case where a signal strength parameter is floated independently for each lepton channel. The green error bar indicates the statistical uncertainty on μ, while the black error bar indicates the total (statistical + systematic) uncertainty on μ.

7.8.4 Combination with Run-1 Data

The Run-2 $VH \rightarrow Vb\bar{b}$ analysis has also been combined with the Run-1 result [83]. The Run-1 result includes 4.7 fb^{-1} of data collected at $\sqrt{s} = 7$ TeV, and 20.3 fb^{-1} collected at $\sqrt{s} = 8$ TeV between 2011 and 2012.

An extremely important aspect of the combination is the correlation of systematics between each data period. Due to significant differences in the ways the systematic uncertainties were evaluated, there is not a strong motivation to correlate systematic uncertainties between the data-taking periods. This hypothesis was tested using a number of different correlation schemes. The correlation of the jet energy scale systematic uncertainties was found to have a negligible impact on the measured μ value, whilst the correlation of the b-tagging systematics introduced up to a $\sim 5\%$ variation in the measured μ value. Similarly, for background modelling systematics, the correlation between Run-1 and Run-2 was varied from fully decorrelated to fully correlated for the $t\bar{t}$, $W+\text{HF}$ and $Z+\text{HF}$ normalisation and shape uncertainties. This was found to have a negligible impact on the signal strength measurement. Therefore, it was decided not to correlate the majority of the systematic uncertainties, and only signal modelling and b-jet-specific jet energy scale uncertainties are correlated across the $\sqrt{s} = 7$ TeV, $\sqrt{s} = 8$ TeV and $\sqrt{s} = 13$ TeV analyses.

From the combination of Run-1 and Run-2 data, a signal strength of $\mu = 0.90 \pm 0.18(\text{stat.})^{+0.21}_{-0.19}(\text{syst.})$ is measured. This corresponds to an observed significance of 3.6 σ, compared to an expected significance of 4.0 σ. Figure 7.31 (a) presents the signal strength from the combined Run-1 and Run-2 unconditional BDT_{VH} global likelihood fit to data with one signal strength parameter, compared to the case where a signal strength parameter is floated independently for each signal process (WH/VH), and Figure 7.31 (b) where a signal strength parameter is floated independently for each centre of mass energy dataset. Consistent signal strengths between the WH and ZH channels are observed, with the level of compatibility at 34%. The compatibility between the signal strengths measured in each centre-of-mass dataset is at the level of 21%.

Figure 7.32 presents the postfit data to MC comparison for all analysis bins, ordered by $\log(S/B)$, with S (B) the signal (background) yield in each bin from the combined Run-1 and Run-2 analyses. The $VH \rightarrow Vb\bar{b}$ signal contribution is scaled to the fitted signal strength, $\mu = 0.90$. The pull corresponds to the difference between data and the background-only model, divided by the statistical uncertainty. The full line indicates the pull of the prediction for signal and background with respect to the background-only prediction. Good agreement between data and simulation is observed over the full range of S/B bins.

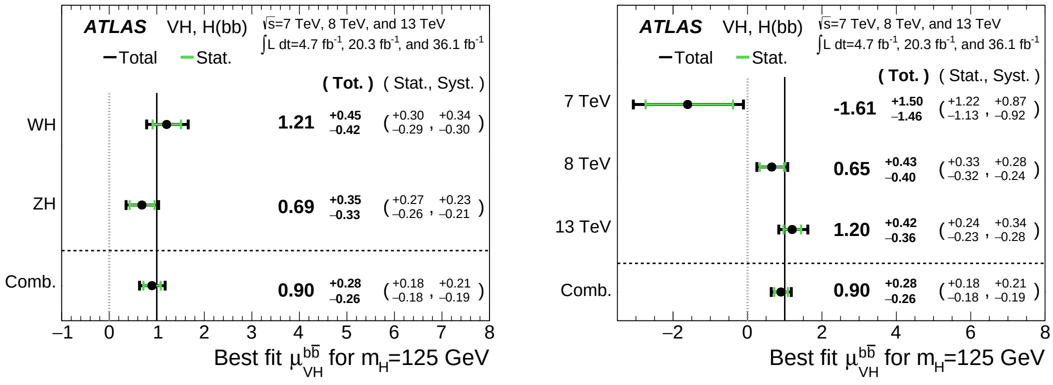

(a) (b)

Figure 7.31: The combined Run-1 and Run-2 unconditional BDT$_{VH}$ global likelihood fit to data with a single signal strength parameter, compared to the case where the signal strength parameter is floated independently for each signal process (WZ/ZZ) (a) and where the signal strength parameter is floated independently for each centre of mass energy dataset (b). The green error bar indicates the statistical uncertainty on μ, while the black error bar indicates the total (statistical + systematic) uncertainty on μ.

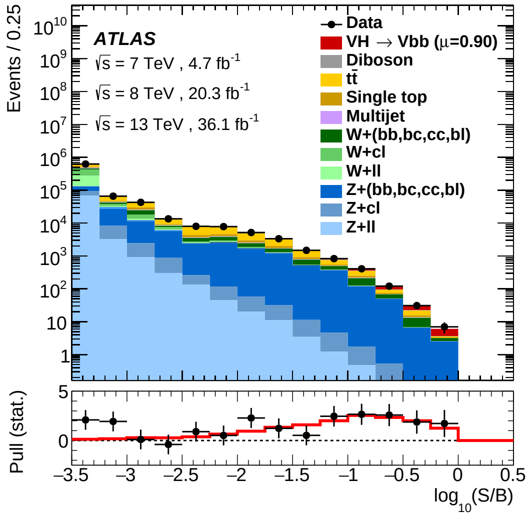

(a)

Figure 7.32: Postfit data to MC comparison for all analysis bins, ordered by $\log(S/B)$, with S (B) the signal (background) yield in each bin, for the BDT$_{VH}$ $VH \rightarrow Vb\bar{b}$ analysis. The $VH \rightarrow Vb\bar{b}$ signal contribution is scaled to the fitted signal strength, $\mu = 0.90$. Data (black points with statistical error bars) are shown, corresponding to 4.7 fb^{-1}, 20.3 fb^{-1} and 36.1 fb^{-1} of Run-1 and Run-2 data collected at $\sqrt{s} = 7$ TeV, $\sqrt{s} = 8$ TeV and$\sqrt{s} = 13$ TeV, along with the simulated prediction (coloured stacked histograms). The pull corresponds to the difference between data and the background-only model, divided by the statistical uncertainty. The solid red line indicates the pull of the prediction for signal and background with respect to the background-only prediction.

7.9 Future Prospects

The measured SM $VH \to Vb\bar{b}$ signal significance of 3.5 σ from the background-only model is the first single-experiment evidence for the $H \to b\bar{b}$ decay mode, along with the first evidence for the $H \to b\bar{b}$ decay at an LHC experiment. However, looking to the future, it is useful to study the impact of the full Run-2 dataset ($\sim$ 150 fb^{-1}) on the expected significance, and estimate what is necessary to achieve a 5 σ observation.

In evaluating the future prospects, a slightly modified fit is implemented on the Asimov dataset. The background normalisation factors from the unconditional global likelihood fit to data are first applied to the Asimov dataset, and all other nuisance parameters are kept at their nominal value. The expected significance is then extracted from this Asimov dataset, scaled to the appropriate luminosity. Table 7.21 summarises the expected significance in this Asimov dataset for 36.1 fb^{-1}, 60 fb^{-1} and 150 fb^{-1}. Table 7.22 presents the expected uncertainties on μ for each channel when altering the dataset luminosity. These projections are an ATLAS "work in progress", based upon the current ATLAS results. Therefore, the presented values only take into account the increase of the number of data events, and do not consider any potential improvements to the analysis strategy. Furthermore, the same number of MC events are used, meaning that MC statistical uncertainty represents a strong limitation in these projections.

Luminosity / fb^{-1}	Expected significance
36.1	2.9 σ
60.0	3.4 σ
150.0	4.4 σ

Table 7.21: Expected significances from a conditional $\mu = 1$ BDT$_{VH}$ global likelihood fit to an Asimov dataset, scaled to 36.1 fb^{-1}, 60 fb^{-1} and 150 fb^{-1}. Normalisation factors from the unconditional fit to 36.1 fb^{-1} of data are applied, whilst all other nuisance parameters are kept at their nominal values. These projections are an ATLAS "work in progress", based upon the current ATLAS results.

Channel	36.1 fb^{-1}	60.0 fb^{-1}	150.0 fb^{-1}
0-lepton	0.52	0.45	0.36
1-lepton	0.59	0.51	0.43
2-lepton $p_{\mathrm{T}}^{V} < 150$ GeV	1.23	1.05	0.83
2-lepton $p_{\mathrm{T}}^{V} > 150$ GeV	0.65	0.53	0.39
Combination	0.39	0.33	0.27

Table 7.22: Expected uncertainty on μ from a conditional $\mu = 1$ BDT$_{VH}$ fit to an Asimov dataset scaled to 36.1 fb^{-1}, 60 fb^{-1} and 150 fb^{-1} for each channel and the combination. Normalisation factors from the unconditional fit to 36.1 fb^{-1} of data are applied, whilst all other nuisance parameters are kept at their nominal values. These projections are an ATLAS "work in progress", based upon the current ATLAS results.

An expected $VH \to Vb\bar{b}$ significance of 4.4 σ can be achieved simply with the addition of the full Run-2 dataset. The inclusion of more data will improve the analysis sensitivity both through the reduction of statistical uncertainties, but also in the reduction of the uncertainty on floating normalisation parameters and the background modelling uncertainties, due to increased constraints from the larger dataset. However, as the analysis is becoming systematically limited, work to improve the understanding of background modelling and systematic uncertainties will be vital to achieve a 5 σ observation. Possible areas of work are discussed in more detail in Chapter 8.

7.10 Summary

A search for the SM $VH \to Vb\bar{b}$ process has been conducted with 36.1 fb^{-1} of Run-2 ATLAS data collected at $\sqrt{s} = 13$ TeV. Multivariate analysis techniques have been implemented to boost the analysis sensitivity over a global likelihood fit to the dijet mass by $\sim 10\%$. An observed signal strength of $\mu = 1.20^{+0.24}_{-0.23}(\text{stat.})^{+0.34}_{-0.28}(\text{syst.})$, corresponding to a 3.5 σ (3.0 σ) observed (expected) significance from the background-only model.

This result has been validated using two cross checks. Using an analogous global likelihood fit of the output of a BDT trained to select SM $VZ \to Vb\bar{b}$ events as signal, a signal strength of $\mu_{VZ} = 1.11^{+0.12}_{-0.11}(\text{stat.})^{+0.22}_{-0.19}(\text{syst.})$ has been observed, corresponding to a 5.8 σ (5.3 σ) observed (expected) significance from the background-only model. This fit is in good agreement with the Standard Model, and furthermore shows good agreement between the three analysis channels, providing a robust validation of the background model, BDT performance and fitting procedure.

A further cross-check of the fit model has been carried out using a fit to the dijet mass, m_{bb}. A signal strength of $\mu = 1.30^{+0.28}_{-0.27}(\text{stat.})^{+0.37}_{-0.29}(\text{syst.})$ has been measured, corresponding to a 3.5 σ (2.8 σ) observed (expected) significance from the background-only model. Again, this shows good agreement with the BDT_{VH} $VH \to Vb\bar{b}$ fit result, in terms of both the measured signal strength and background modelling, and acts as a further validation of the background fit models and BDT approach.

Finally, a combination with the Run-1 ATLAS result has been carried out. A signal strength of $\mu = 0.90 \pm 0.18(\text{stat.})^{+0.21}_{-0.19}(\text{syst.})$ has been measured, corresponding to a 3.6 σ (4.0 σ) observed (expected) significance from the background-only model.

The observed $VH \to Vb\bar{b}$ signal significance is the first evidence for VH production and $H \to b\bar{b}$ by a single experiment. The results are also consistent with the value of the Yukawa coupling to bottom quarks in the Standard Model, with robust validations carried out.

Chapter 8

Conclusions

8.1 Summary

The announcement of the discovery of the Higgs boson in 2012 by the ATLAS and CMS experiments at the LHC was a ground breaking moment in the understanding of the SM. The work of this thesis has been towards further understanding the properties of this unique particle through examining the SM $H \rightarrow b\bar{b}$ decay.

A key aspect of observing the $H \rightarrow b\bar{b}$ decay is being able to identify jets which contain a b-quark. The ATLAS b-tagging algorithms for use during Run-2 of the LHC were studied, and the performance validated. The installation of the IBL during Long-Shutdown 1, between Run-1 and Run-2, introduced an additional pixel layer to the ATLAS inner-detector, situated at a radius of approximately 30 mm. This, along with improvements to the b-tagging algorithms, has resulted in a factor of 4 improvement to the light-flavour jet rejection, and a factor of 1.5 improvement to the c-jet rejection for the same b-jet tagging efficiency. These improvements have a direct impact on all analyses which use b-tagging, significantly enhancing the sensitivity of a large portion of the ATLAS physics programme.

The performance of the b-tagging algorithms have been calibrated to data for b-jets using the $t\bar{t}$ likelihood calibration, carried out using 36.1 fb^{-1} of Run-2 data. In-depth studies on the background modelling were conducted to ensure reasonable modelling of the data by simulation. Due to both the large Run-2 dataset and $t\bar{t}$ cross-section at $\sqrt{s} = 13$ TeV, calibration results were systematically limited, mostly from the modelling uncertainties on the $t\bar{t}$ background. The implementation of a boosted decision tree to improve the b-jet purity resulted in a factor of 3 reduction in the systematic uncertainty of the b-jet scale factor for jets in the range $200 < p_{\mathrm{T}} < 300$ GeV, with smaller reductions across the full p_{T} spectrum.

The search for SM $VH \rightarrow Vb\bar{b}$ has been carried out using 36.1 fb^{-1} of Run-2 ATLAS data. Based on results presented at ICHEP 2016 [2], extensive work to improve the understanding of the dominant systematic uncertainties has been carried out. Work has also been carried out to improve the understanding of the normalisation of the $W+$HF background in the 1-lepton channel of the $VH \rightarrow Vb\bar{b}$ analysis, with the introduction of an orthogonal control region, in addition to work improving the b-jet tagging efficiency measurement. The introduction of this region provides an effective way to better constrain the $W + \text{HF}$ background normalisation, and is also used as a validation region of the fit model. This has been combined with work on validating and updating the MVA training, adding additional data, updated background uncertainties, and extensive fit studies to ensure the validity of the background model and associated uncertainties.

A combined MVA fit to all channels results in a $VH \to Vb\bar{b}$ signal significance of 3.5 σ, compared to 3.0 σ expected. This result has been cross-checked with a fit to the SM $VZ \to Vb\bar{b}$ signal, and also a cut-based dijet mass analysis. The $VZ \to Vb\bar{b}$ signal was observed with a significance of 5.8 σ, compared to 5.3 σ expected, and the $VH \to Vb\bar{b}$ signal was observed with a significance of 3.5 σ in the cut-based dijet mass analysis, compared to 2.8 σ expected. In a combination with the Run-1 analysis, an observed signal significance of 3.6 σ of the $VH \to Vb\bar{b}$ process over the background-only model has been measured, compared to an expectation of 4.0 σ. This corresponds to a measured signal strength of $\mu = 0.90 \pm 0.18(\text{stat.})^{+0.21}_{-0.19}(\text{syst.})$, and provides the first evidence for VH production and $H \to b\bar{b}$ by a single experiment.

8.2 Future Work

With future iterations of the analysis, improvements to the modelling of background processes will be vital to continue to improve the analysis sensitivity. Among the most highly ranked systematic uncertainties are those arising from signal modelling, and this will be a key area to target to further improve the sensitivity. Modelling uncertainties from $V + \text{jets}$, $t\bar{t}$ and single top-quark are all found to result in a similar overall contribution to the systematic uncertainty.

There is also a large contribution arising from the MC statistical uncertainties. Studies have indicated that this mostly arises from a limited number of simulated MC $t\bar{t}$ events in the most sensitive BDT regions of the 1-lepton channel. In this iteration of the $VH \to Vb\bar{b}$ analysis, a $t\bar{t}$ sample size of 60 M events was used, where events are generated with just a single lepton filter. A large scale production, requiring an increase in the number of simulated MC events by several factors, will be required to decrease the significant MC statistical uncertainty. Alternatively, studies are also being carried out to determine the possibility of slicing the samples, so as to target the region of phase space which is most sensitive to the $VH \to Vb\bar{b}$ signal.

Looking to the future, this is just another step in our understanding of the Standard Model, and the recently discovered Higgs boson. Whilst the $H \to b\bar{b}$ branching ratio has been measured to be consistent with the SM, this is still with large ($\sim 30\%$) uncertainties, meaning that couplings of the Higgs boson beyond those predicted by the SM are far from ruled out. As the dataset increases in size and our understanding of systematic uncertainties improves, we can now look towards precision measurements of differential distributions in all channels as possible gateways to physics beyond the Standard Model. The Higgs p_{T} spectrum is highly sensitive to new physics [120], with the sensitivity increasing with higher Higgs p_{T}. The inclusion of more data and boosted analysis techniques offers an exciting opportunity to probe this extreme region of phase space.

In identifying $H \rightarrow b\bar{b}$ candidates in the high Higgs p_{T} region, reductions in the systematic uncertainties arising from b-tagging of high p_{T} jets is essential to maintain the sensitivity of the analysis. The $t\bar{t}$ likelihood calibration provides data driven b-jet tagging efficiency measurements for jets with $p_{\mathrm{T}} < 300$ GeV, with a MC based extrapolation to estimate systematic uncertainties in the higher p_{T} region. The $t\bar{t}$ likelihood calibration is limited by systematic variations in the modelling in the higher jet p_{T} region, and therefore developing a technique to derive data-driven b-jet efficiency measurements in this region will be vital to reduce the size of b-tagging related systematic uncertainties. One possibility is to study the event selection of the $t\bar{t}$ likelihood calibration to improve the $t\bar{t}$ purity in the high jet p_{T} region. An alternative possibility is to use semi-leptonic $t\bar{t}$ events, where modelling uncertainties can be reduced by fully reconstructing the $t\bar{t}$ system [121].

The current picture of the Standard Model is far from complete, with a range of physical phenomena unexplained by current theory. Precision measurements of the coupling and decay of the Higgs boson provides an effective way to search for physics beyond the Standard Model, and will be a rapidly developing field of development for the remainder of LHC-era physics and beyond.

Colophon

This thesis was made in LaTeX 2_ε using the “hepthesis” class [122].

Bibliography

[1] ATLAS Collaboration, *Expected performance of the ATLAS b-tagging algorithms in Run-2*, Tech. Rep. ATL-PHYS-PUB-2015-022, CERN, Geneva, Jul, 2015. `https://cds.cern.ch/record/2037697`.

[2] ATLAS Collaboration, *Search for the Standard Model Higgs boson produced in association with a vector boson and decaying to a $b\bar{b}$ pair in pp collisions at 13 TeV using the ATLAS detector*, Tech. Rep. ATLAS-CONF-2016-091, CERN, Geneva, Aug, 2016. `http://cds.cern.ch/record/2206813`.

[3] ATLAS Collaboration, *Evidence for the $H \to b\bar{b}$ decay with the ATLAS detector*, `arXiv:1708.03299 [hep-ex]`.

[4] F. Halzen and A. D. Martin, *Quarks and Leptons: An Introductory Course in Modern Particle Physics*. 1984.

[5] P. G. Ratcliffe, *An Introduction to Elementary Particle Phenomenology*. 2053-2563. IOP Publishing, 2014.

[6] Particle Data Group Collaboration, *Review of Particle Physics*, Chin. Phys. **C40** (2016) no. 10, 100001.

[7] CDF Collaboration, *Observation of top quark production in $\bar{p}p$ collisions*, Phys. Rev. Lett. **74** (1995) 2626–2631, `arXiv:hep-ex/9503002 [hep-ex]`.

[8] D0 Collaboration, *Observation of the top quark*, Phys. Rev. Lett. **74** (1995) 2632–2637, `arXiv:hep-ex/9503003 [hep-ex]`.

[9] DONUT Collaboration, *Observation of tau neutrino interactions*, Phys. Lett. **B504** (2001) 218–224, `arXiv:hep-ex/0012035 [hep-ex]`.

[10] ATLAS Collaboration, *Observation of a new particle in the search for the Standard Model Higgs boson with the ATLAS detector at the LHC*, Phys. Lett. **B716** (2012) 1–29, `arXiv:1207.7214 [hep-ex]`.

[11] CMS Collaboration, *Observation of a new boson at a mass of 125 GeV with the CMS experiment at the LHC*, Phys. Lett. **B716** (2012) 30–61, `arXiv:1207.7235 [hep-ex]`.

[12] E. Komatsu et al., *Seven-year Wilkinson Microwave Anisotropy Probe (WMAP) Observations: Cosmological Interpretation*, ApJS **192** (2011) 18, `arXiv:1001.4538`

[astro-ph.CO].

[13] Super-Kamiokande Collaboration, Y. Fukuda et al., *Evidence for oscillation of atmospheric neutrinos*, Phys. Rev. Lett. **81** (1998) 1562–1567, arXiv:hep-ex/9807003 [hep-ex].

[14] L. Canetti, M. Drewes, and M. Shaposhnikov, *Matter and Antimatter in the Universe*, New J. Phys. **14** (2012) 095012, arXiv:1204.4186 [hep-ph].

[15] M. Thomson, *Modern particle physics.* Cambridge University Press, New York, 2013. http://www-spires.fnal.gov/spires/find/books/www?cl=QC793.2.T46::2013.

[16] ATLAS Collaboration, *Measurement of the Higgs boson mass in the* $H \to ZZ^* \to 4\ell$ *and* $H \to \gamma\gamma$ *channels with* $\sqrt{s}$*=13TeV pp collisions using the ATLAS detector*, Tech. Rep. ATLAS-CONF-2017-046, CERN, Geneva, Jul, 2017. https://cds.cern.ch/record/2273853.

[17] C. S. Wu, E. Ambler, R. W. Hayward, D. D. Hoppes, and R. P. Hudson, *Experimental Test of Parity Conservation in Beta Decay*, Phys. Rev. **105** (1957) 1413–1414.

[18] F. Englert and R. Brout, *Broken Symmetry and the Mass of Gauge Vector Mesons*, Phys. Rev. Lett. **13** (1964) 321–323.

[19] P. W. Higgs, *Broken Symmetries and the Masses of Gauge Bosons*, Phys. Rev. Lett. **13** (1964) 508–509.

[20] P. Higgs, *Broken symmetries, massless particles and gauge fields*, Phys. Lett. **12** (1964) 132 – 133.

[21] G. S. Guralnik, C. R. Hagen, and T. W. B. Kibble, *Global Conservation Laws and Massless Particles*, Phys. Rev. Lett. **13** (1964) 585–587.

[22] P. W. Higgs, *Spontaneous Symmetry Breakdown without Massless Bosons*, Phys. Rev. **145** (1966) 1156–1163.

[23] T. W. B. Kibble, *Symmetry Breaking in Non-Abelian Gauge Theories*, Phys. Rev. **155** (1967) 1554–1561.

[24] LHC Higgs Cross Section Working Group, *Handbook of LHC Higgs Cross Sections: 4. Deciphering the Nature of the Higgs Sector*, CERN-2017-002 (2016) , arXiv:1610.07922 [hep-ph].

[25] L. Evans and P. Bryant, *LHC Machine*, Journal of Instrumentation **3** (2008) no. 08, S08001. http://stacks.iop.org/1748-0221/3/i=08/a=S08001.

[26] CERN, *LEP design report.* CERN, Geneva, 1984. https://cds.cern.ch/record/102083.

[27] F. Marcastel, *CERN's Accelerator Complex. La chaîne des accélérateurs du CERN*, Tech. Rep. OPEN-PHO-CHART-2013-001, CERN, Geneva, Oct, 2013. http://cds.cern.ch/record/1621583.

[28] G. Apollinari, I. Béjar Alonso, O. Brüning, M. Lamont, and L. Rossi, *High-Luminosity Large Hadron Collider (HL-LHC): Preliminary Design Report*. CERN Yellow Reports: Monographs. CERN, Geneva, 2015. `https://cds.cern.ch/record/2116337`.

[29] ALICE Collaboration, *The ALICE experiment at the CERN LHC*, JINST **3** (2008) S08002.

[30] CMS Collaboration, *The CMS Experiment at the CERN LHC*, JINST **3** (2008) S08004.

[31] LHCb Collaboration, *The LHCb Detector at the LHC*, JINST **3** (2008) S08005.

[32] ATLAS Collaboration, *The ATLAS Experiment at the CERN Large Hadron Collider*, JINST **3** (2008) S08003. `http://iopscience.iop.org/1748-0221/3/08/S08003`.

[33] ATLAS Collaboration, *ATLAS Insertable B-Layer Technical Design Report*, CERN-LHCC-2010-013. ATLAS-TDR-19. `https://cds.cern.ch/record/1291633`.

[34] A. Salvucci, *Measurement of muon momentum resolution of the ATLAS detector*, EPJ Web Conf. **28** (2012) 12039, `arXiv:1201.4704 [physics.ins-det]`.

[35] ATLAS Collaboration, *Performance of the ATLAS Trigger System in 2015*, Eur. Phys. J. **C77** (2017) no. 5, 317, `arXiv:1611.09661 [hep-ex]`.

[36] S. van der Meer, *Calibration of the effective beam height in the ISR*, Tech. Rep. CERN-ISR-PO-68-31, CERN, Geneva, 1968. `http://cds.cern.ch/record/296752`.

[37] ATLAS Collaboration, M. Aaboud et al., *Luminosity determination in pp collisions at* $\sqrt{s} = 8$ *TeV using the ATLAS detector at the LHC*, Eur. Phys. J. **C76** (2016) no. 12, 653, `arXiv:1608.03953 [hep-ex]`.

[38] ATLAS Collaboration, *Luminosity Public Results Run-2*, `https://twiki.cern.ch/twiki/bin/view/AtlasPublic/LuminosityPublicResultsRun2`, July, 2017.

[39] ATLAS Collaboration, *Performance of the ATLAS Track Reconstruction Algorithms in Dense Environments in LHC Run 2*, Eur. Phys. J. **C77** (2017) no. 10, 673, `arXiv:1704.07983 [hep-ex]`.

[40] ATLAS Collaboration, *Reconstruction of primary vertices at the ATLAS experiment in Run 1 proton-proton collisions at the LHC*, Eur. Phys. J. **C77** (2017) no. 5, 332, `arXiv:1611.10235 [physics.ins-det]`.

[41] ATLAS Collaboration, *Electron efficiency measurements with the ATLAS detector using the 2015 LHC proton-proton collision data*, Tech. Rep. ATLAS-CONF-2016-024, CERN, Geneva, Jun, 2016. `https://cds.cern.ch/record/2157687`.

[42] ATLAS Collaboration, *Muon reconstruction performance in early* $\sqrt{s} = 13$ *TeV data*, Tech. Rep. ATL-PHYS-PUB-2015-037, CERN, Geneva, Aug, 2015. `https://cds.cern.ch/record/2047831`.

[43] ATLAS Collaboration, *Muon reconstruction performance of the ATLAS detector in proton-proton collision data at* $\sqrt{s}$ *=13 TeV*, Eur. Phys. J. **C76** (2016) no. 5, 292, `arXiv:1603.05598 [hep-ex]`.

[44] ATLAS Collaboration, *Topological cell clustering in the ATLAS calorimeters and its performance in LHC Run 1*, Eur. Phys. J. **C77** (2017) 490, `arXiv:1603.02934 [hep-ex]`.

[45] M. Cacciari, G. P. Salam, and G. Soyez, *The anti-*k_t *jet clustering algorithm*, JHEP 063, `arXiv:0802.1189 [hep-ph]`.

[46] ATLAS Collaboration, *Jet Calibration and Systematic Uncertainties for Jets Reconstructed in the ATLAS Detector at* $\sqrt{s} = 13$ *TeV*, Tech. Rep. ATL-PHYS-PUB-2015-015, CERN, Geneva, Jul, 2015. `https://cds.cern.ch/record/2037613`.

[47] ATLAS Collaboration, M. Aaboud et al., *Jet energy scale measurements and their systematic uncertainties in proton-proton collisions at* $\sqrt{s} = 13$ *TeV with the ATLAS detector*, Phys. Rev. **D96** (2017) no. 7, 072002, `arXiv:1703.09665 [hep-ex]`.

[48] ATLAS Collaboration, G. Aad et al., *Jet energy resolution in proton-proton collisions at* $\sqrt{s} = 7$ *TeV recorded in 2010 with the ATLAS detector*, Eur. Phys. J. **C73** (2013) no. 3, 2306, `arXiv:1210.6210 [hep-ex]`.

[49] ATLAS Collaboration, *Tagging and suppression of pileup jets with the ATLAS detector*, Tech. Rep. ATLAS-CONF-2014-018, CERN, Geneva, May, 2014. `http://cds.cern.ch/record/1700870`.

[50] ATLAS Collaboration, *Expected performance of missing transverse momentum reconstruction for the ATLAS detector at* $\sqrt{s} = 13$ *TeV*, Tech. Rep. ATL-PHYS-PUB-2015-023, CERN, Geneva, Jul, 2015. `https://cds.cern.ch/record/2037700`.

[51] ATLAS Collaboration, *Performance of missing transverse momentum reconstruction for the ATLAS detector in the first proton-proton collisions at at* $\sqrt{s}$*= 13 TeV*, Tech. Rep. ATL-PHYS-PUB-2015-027, CERN, Geneva, Jul, 2015. `https://cds.cern.ch/record/2037904`.

[52] ATLAS Collaboration, *Recommendations of the Physics Objects and Analysis Harmonisation Study Groups 2014*, Tech. Rep. ATL-COM-PHYS-2014-451, CERN, Geneva, May, 2014. `https://cds.cern.ch/record/1700874`.

[53] A. Hoecker et al., *TMVA - Toolkit for Multivariate Data Analysis*, 2007. `arXiv:physics/0703039 [physics.data-an]`.

[54] Y. Freund and R. E. Schapire, *A Decision-Theoretic Generalization of On-Line Learning and an Application to Boosting*, Journal of Computer and System Sciences **55** (1997) no. 1, 119 – 139. `http://www.sciencedirect.com/science/article/pii/S002200009791504X`.

[55] S. Alioli, P. Nason, C. Oleari, and E. Re, *A general framework for implementing NLO calculations in shower Monte Carlo programs: the POWHEG BOX*, JHEP **1006** (2010) 043,

arXiv:1002.2581 [hep-ph].

[56] T. Sjostrand, S. Mrenna, and P. Z. Skands, *PYTHIA 6.4 Physics and Manual*, JHEP **05** (2006) 026, arXiv:hep-ph/0603175 [hep-ph].

[57] H.-L. Lai, M. Guzzi, J. Huston, Z. Li, P. M. Nadolsky, J. Pumplin, and C. P. Yuan, *New parton distributions for collider physics*, Phys. Rev. **D82** (2010) 074024, arXiv:1007.2241 [hep-ph].

[58] D. Lange, *The EvtGen particle decay simulation package*, Nucl.Instrum.Meth. **A462** (2001) 152–155. http://www.sciencedirect.com/science/article/pii/S0168900201004533.

[59] T. Sjöstrand, S. Mrenna, and P. Z. Skands, *A Brief Introduction to PYTHIA 8.1*, Comput.Phys.Commun. **178** (2008) 852–867, arXiv:0710.3820 [hep-ph]. http://arxiv.org/abs/0710.3820.

[60] GEANT4 Collaboration, S. Agostinelli et al., *GEANT4: A simulation toolkit*, Nucl. Instrum. Meth. **A506** (2003) 250–303.

[61] ATLAS Collaboration, *Commissioning of the ATLAS high-performance b-tagging algorithms in the 7 TeV collision data*, ATLAS-CONF-2011-102. http://cds.cern.ch/record/1369219.

[62] P. Zarchan and H. Musoff, *Fundamentals of Kalman Filtering: A Practical Approach*. No. v. 190 in Fundamentals of Kalman filtering: a practical approach. American Institute of Aeronautics and Astronautics, Incorporated, 2000. https://books.google.co.uk/books?id=AQxRAAAAMAAJ.

[63] ATLAS Collaboration, *Expected Performance of the ATLAS Experiment - Detector, Trigger and Physics*, arXiv:0901.0512 [hep-ex].

[64] ATLAS Collaboration, *Performance of b-Jet Identification in the ATLAS Experiment*, JINST **11** (2016) no. 04, P04008, arXiv:1512.01094 [hep-ex].

[65] ATLAS Collaboration, *Optimisation of the ATLAS b-tagging performance for the 2016 LHC Run*, Tech. Rep. ATL-PHYS-PUB-2016-012, CERN, Geneva, Jun, 2016. https://cds.cern.ch/record/2160731.

[66] ATLAS Collaboration, *Calibration of the performance of b-tagging for c and light-flavour jets in the 2012 ATLAS data*, Tech. Rep. ATLAS-CONF-2014-046, CERN, Geneva, Jul, 2014. https://cds.cern.ch/record/1741020.

[67] ATLAS Collaboration, *Calibration of b-tagging using dileptonic top pair events in a combinatorial likelihood approach with the ATLAS experiment*, Tech. Rep. ATLAS-CONF-2014-004, CERN, Geneva, Feb, 2014. https://cds.cern.ch/record/1664335.

[68] T. Gleisberg, S. Höche, F. Krauss, M. Schönherr, S. Schumann, et al., *Event generation with*

SHERPA 1.1, JHEP **02** (2009) 007, `arXiv:0811.4622 [hep-ph]`.

[69] M. Czakon and A. Mitov, *Top++: A Program for the Calculation of the Top-Pair Cross-Section at Hadron Colliders*, Comput. Phys. Commun. **185** (2014) 2930, `arXiv:1112.5675 [hep-ph]`.

[70] N. Kidonakis, *Two-loop soft anomalous dimensions for single top quark associated production with a W- or H-*, Phys. Rev. **D82** (2010) 054018, `arXiv:1005.4451 [hep-ph]`.

[71] NNPDF Collaboration, *Parton distributions for the LHC Run II*, JHEP **04** (2015) 040, `arXiv:1410.8849 [hep-ph]`.

[72] S. Catani, L. Cieri, G. Ferrera, D. de Florian, and M. Grazzini, *Vector boson production at hadron colliders: a fully exclusive QCD calculation at NNLO*, Phys. Rev. Lett. **103** (2009) 082001, `arXiv:0903.2120 [hep-ph]`.

[73] J. Alwall et al., *The automated computation of tree-level and next-to-leading order differential cross sections, and their matching to parton shower simulations*, JHEP **2014** (2014) 158, `arXiv:1405.0301 [hep-ph]`.

[74] ATLAS Collaboration, *Studies on top-quark Monte Carlo modelling for Top2016*, Tech. Rep. ATL-PHYS-PUB-2016-020, CERN, Geneva, Sep, 2016. `https://cds.cern.ch/record/2216168`.

[75] M. Bahr et al., *Herwig++ Physics and Manual*, Eur. Phys. J. **C58** (2008) 639–707, `arXiv:0803.0883 [hep-ph]`.

[76] C. D. White, S. Frixione, E. Laenen, and F. Maltoni, *Isolating Wt production at the LHC*, JHEP **11** (2009) 074, `arXiv:0908.0631 [hep-ph]`.

[77] ATLAS Collaboration, *Comparison of Monte Carlo generator predictions to ATLAS measurements of top pair production at 7 TeV*, Tech. Rep. ATL-PHYS-PUB-2015-002, CERN, Geneva, Jan, 2015. `https://cds.cern.ch/record/1981319`.

[78] M. Czakon, D. Heymes, and A. Mitov, *Dynamical scales for multi-TeV top-pair production at the LHC*, JHEP **04** (2017) 071, `arXiv:1606.03350 [hep-ph]`.

[79] M. Czakon, D. Heymes, and A. Mitov, *High-precision differential predictions for top-quark pairs at the LHC*, Phys. Rev. Lett. **116** (2016) no. 8, 082003, `arXiv:1511.00549 [hep-ph]`.

[80] S. Frixione, E. Laenen, P. Motylinski, B. R. Webber, and C. D. White, *Single-top hadroproduction in association with a W boson*, JHEP **07** (2008) 029, `arXiv:0805.3067 [hep-ph]`.

[81] ATLAS Collaboration, G. Aad et al., *Measurement of the cross-section for b-jets produced in association with a Z boson at $\sqrt{s} = 7$ TeV with the ATLAS detector*, Phys. Lett. **B706** (2012) 295–313, `arXiv:1109.1403 [hep-ex]`.

[82] ATLAS Analysis Software Group, *Extended Pileup Reweighting*, `https:`

//twiki.cern.ch/twiki/bin/view/AtlasProtected/ExtendedPileupReweighting, October, 2017.

[83] ATLAS Collaboration, G. Aad et al., *Search for the $b\bar{b}$ decay of the Standard Model Higgs boson in associated $(W/Z)H$ production with the ATLAS detector*, JHEP **01** (2015) 069, `arXiv:1409.6212 [hep-ex]`.

[84] N. Cartiglia, *Measurement of the proton-proton total, elastic, inelastic and diffractive cross sections at 2, 7, 8 and 57 TeV*, `arXiv:1305.6131 [hep-ex]`.

[85] J. M. Butterworth, I. Ochoa, and T. Scanlon, *Boosted Higgs $\rightarrow b\bar{b}$ in vector-boson associated production at 14 TeV*, Eur. Phys. J. **C75** (2015) no. 8, 366, `arXiv:1506.04973 [hep-ph]`.

[86] CMS Collaboration, *Search for the standard model Higgs boson produced in association with a W or a Z boson and decaying to bottom quarks*, Phys. Rev. **D89** (2014) no. 1, 012003, `arXiv:1310.3687 [hep-ex]`.

[87] ATLAS Collaboration, *Measurements of the Higgs boson production and decay rates and constraints on its couplings from a combined ATLAS and CMS analysis of the LHC pp collision data at $\sqrt{s}$ = 7 and 8 TeV*, Tech. Rep. ATLAS-CONF-2015-044, CERN, Geneva, Sep, 2015. http://cds.cern.ch/record/2052552.

[88] G. Cullen, N. Greiner, G. Heinrich, G. Luisoni, P. Mastrolia, G. Ossola, T. Reiter, and F. Tramontano, *Automated One-Loop Calculations with GoSam*, Eur. Phys. J. **C72** (2012) 1889, `arXiv:1111.2034 [hep-ph]`.

[89] T. Sjostrand, S. Mrenna, and P. Z. Skands, *A Brief Introduction to PYTHIA 8.1*, Comput.Phys.Commun. **178** (2008) 852–867, `arXiv:0710.3820 [hep-ph]`.

[90] J. M. Campbell, R. K. Ellis, and C. Williams, *Associated production of a Higgs boson at NNLO*, JHEP **06** (2016) 179, `arXiv:1601.00658 [hep-ph]`.

[91] G. Ferrera, M. Grazzini, and F. Tramontano, *Associated ZH production at hadron colliders: the fully differential NNLO QCD calculation*, Phys. Lett. **B740** (2015) 51–55, `arXiv:1407.4747 [hep-ph]`.

[92] G. Ferrera, M. Grazzini, and F. Tramontano, *Higher-order QCD effects for associated WH production and decay at the LHC*, JHEP **04** (2014) 039, `arXiv:1312.1669 [hep-ph]`.

[93] O. Brein, R. Harlander, M. Wiesemann, and T. Zirke, *Top-Quark Mediated Effects in Hadronic Higgs-Strahlung*, Eur. Phys. J. **C72** (2012) 1868, `arXiv:1111.0761 [hep-ph]`.

[94] G. Ferrera, M. Grazzini, and F. Tramontano, *Associated WH production at hadron colliders: a fully exclusive QCD calculation at NNLO*, Phys. Rev. Lett. **107** (2011) 152003, `arXiv:1107.1164 [hep-ph]`.

[95] O. Brein, A. Djouadi, and R. Harlander, *NNLO QCD corrections to the Higgs-strahlung processes at hadron colliders*, Phys. Lett. **B579** (2004) 149–156, `arXiv:hep-ph/0307206`

[hep-ph].

[96] M. L. Ciccolini, S. Dittmaier, and M. Kramer, *Electroweak radiative corrections to associated WH and ZH production at hadron colliders*, Phys. Rev. **D68** (2003) 073003, `arXiv:hep-ph/0306234 [hep-ph]`.

[97] K. Hamilton, P. Nason, and G. Zanderighi, *MINLO: Multi-Scale Improved NLO*, JHEP **10** (2012) 155, `arXiv:1206.3572 [hep-ph]`.

[98] G. Luisoni, P. Nason, C. Oleari, and F. Tramontano, *$HW^{\pm}/HZ$ + 0 and 1 jet at NLO with the POWHEG BOX interfaced to GoSam and their merging within MiNLO*, JHEP **10** (2013) 083, `arXiv:1306.2542 [hep-ph]`.

[99] O. Brein, R. V. Harlander, and T. J. E. Zirke, *vh@nnlo - Higgs Strahlung at hadron colliders*, Comput. Phys. Commun. **184** (2013) 998–1003, `arXiv:1210.5347 [hep-ph]`.

[100] R. V. Harlander, S. Liebler, and T. Zirke, *Higgs Strahlung at the Large Hadron Collider in the 2-Higgs-Doublet Model*, JHEP **02** (2014) 023, `arXiv:1307.8122 [hep-ph]`.

[101] R. V. Harlander, A. Kulesza, V. Theeuwes, and T. Zirke, *Soft gluon resummation for gluon-induced Higgs Strahlung*, JHEP **11** (2014) 082, `arXiv:1410.0217 [hep-ph]`.

[102] B. Hespel, F. Maltoni, and E. Vryonidou, *Higgs and Z boson associated production via gluon fusion in the SM and the 2HDM*, JHEP **06** (2015) 065, `arXiv:1503.01656 [hep-ph]`.

[103] L. Altenkamp, S. Dittmaier, R. V. Harlander, H. Rzehak, and T. J. E. Zirke, *Gluon-induced Higgs-strahlung at next-to-leading order QCD*, JHEP **02** (2013) 078, `arXiv:1211.5015 [hep-ph]`.

[104] N. Kidonakis, *NNLL resummation for s-channel single top quark production*, Phys. Rev. **D81** (2010) 054028, `arXiv:1001.5034 [hep-ph]`.

[105] N. Kidonakis, *Next-to-next-to-leading-order collinear and soft gluon corrections for t-channel single top quark production*, Phys. Rev. **D83** (2011) 091503, `arXiv:1103.2792 [hep-ph]`.

[106] L. Moneta et al., *The RooStats Project*, 2010. `arXiv:1009.1003 [physics.data-an]`.

[107] W. Verkerke and D. Kirkby, *The RooFit toolkit for data modeling*, 2003. `arXiv:physics/0306116 [physics.data-an]`.

[108] R. J. Barlow and C. Beeston, *Fitting using finite Monte Carlo samples*, Comput. Phys. Commun. **77** (1993) 219–228.

[109] G. Cowan et al., *Asymptotic formulae for likelihood-based tests of new physics*, Eur. Phys. J. **C71** (2011) 1554, `arXiv:1007.1727 [physics.data-an]`.

[110] A. Buckley, J. Butterworth, L. Lonnblad, D. Grellscheid, H. Hoeth, J. Monk, H. Schulz, and F. Siegert, *Rivet user manual*, Comput. Phys. Commun. **184** (2013) 2803–2819, `arXiv:1003.0694 [hep-ph]`.

[111] J. Alwall, R. Frederix, S. Frixione, V. Hirschi, F. Maltoni, O. Mattelaer, H. S. Shao, T. Stelzer, P. Torrielli, and M. Zaro, *The automated computation of tree-level and next-to-leading order differential cross sections, and their matching to parton shower simulations*, JHEP **07** (2014) 079, `arXiv:1405.0301 [hep-ph]`.

[112] N. Lavesson and L. Lonnblad, *Merging parton showers and matrix elements: Back to basics*, JHEP **04** (2008) 085, `arXiv:0712.2966 [hep-ph]`.

[113] J. Bellm et al., *Herwig 7.0/Herwig++ 3.0 release note*, Eur. Phys. J. **C76** (2016) no. 4, 196, `arXiv:1512.01178 [hep-ph]`.

[114] I. W. Stewart and F. J. Tackmann, *Theory Uncertainties for Higgs and Other Searches Using Jet Bins*, Phys. Rev. **D85** (2012) 034011, `arXiv:1107.2117 [hep-ph]`.

[115] LHC Higgs Cross Section Working Group, *Handbook of LHC Higgs Cross Sections: 1. Inclusive Observables*, CERN-2011-002 (2011) , `arXiv:1101.0593 [hep-ph]`.

[116] LHC Higgs Cross Section Working Group, *Handbook of LHC Higgs Cross Sections: 2. Differential Distributions*, CERN-2012-002 (2012) , `arXiv:1201.3084 [hep-ph]`.

[117] LHC Higgs Cross Section Working Group, *Handbook of LHC Higgs Cross Sections: 3. Higgs Properties*, CERN-2013-004 (2013) , `arXiv:1307.1347 [hep-ph]`.

[118] J. Butterworth et al., *PDF4LHC recommendations for LHC Run II*, J. Phys. **G43** (2016) 023001, `arXiv:1510.03865 [hep-ph]`.

[119] ATLAS Collaboration, *ATLAS Run 1 Pythia8 tunes*, Tech. Rep. ATL-PHYS-PUB-2014-021, CERN, Geneva, Nov, 2014. `https://cds.cern.ch/record/1966419`.

[120] A. Biekötter, A. Knochel, M. Krämer, D. Liu, and F. Riva, *Vices and virtues of Higgs effective field theories at large energy*, Phys. Rev. **D91** (2015) 055029, `arXiv:1406.7320 [hep-ph]`.

[121] ATLAS Collaboration, *Calibration of ATLAS b-tagging algorithms in dense jet environments*, Tech. Rep. ATLAS-CONF-2016-001, CERN, Geneva, Feb, 2016. `https://cds.cern.ch/record/2127958`.

[122] A. Buckley, *A class for typesetting academic theses*, 2010.